Electro-Optic Excitations in van der Waals Materials for Active Nanophotonics

Thesis by

Souvik Biswas

In Partial Fulfillment of the Requirements for

the Degree of

Doctor of Philosophy

CALIFORNIA INSTITUTE OF TECHNOLOGY

Pasadena, California

2023

(Defended March 30, 2023)

Souvik Biswas
ORCID: 0000-0002-8021-7271

ACKNOWLEDGEMENTS

Over the course of the last 2017 days, starting from 2017, I have experienced an amazing journey and I sincerely appreciate the assistance, direction, and motivation that have brought me to my current position. Although it's difficult to convey my appreciation in words, I would like to try my best to express it.

Foremost, I express my gratitude to my academic advisor, Professor Harry A. Atwater, whose mentorship has been invaluable. I have been fortunate to work with such a successful and accomplished individual who also possesses remarkable humility and approachability. Our scientific conversations, particularly in one-on-one settings, were a pleasure and provided a wealth of new ideas that will keep me occupied for years to come. His unwavering passion for exploring new concepts, alongside his patience when faced with failed experiments in the lab, is unmatched. As a result of his guidance, my graduate school journey has been immensely fulfilling. Above all else, he is a benevolent and empathetic person who prioritizes the well-being of his students and researchers — a quality that I aspire to emulate should I have the chance.

I express my deep gratitude to my thesis committee at Caltech for generously providing their time and invaluable feedback. From the outset of my time at Caltech, Professor Dave Hsieh has been a constant source of support, inspiring me to explore innovative ideas while patiently working alongside me to decipher complex ARPES data obtained at the ALS beamline in Berkeley. Additionally, throughout my time at Caltech, Professors Stevan Nadj-Perge and Andrei Faraon have regularly offered invaluable insights into my research.

I would like to express my deepest gratitude to a remarkable group of scientists and professors who have made an indelible impact throughout my PhD journey. First and foremost, I extend my sincere appreciation to the group of Professor Jeffrey Neaton (Berkeley) - specifically Aurelie Champagne and Jonah Haber - for engaging in regular discussions with me on the theoretical aspects of excitons in layered materials. Professor Felipe Jornada (Stanford) has been an exceptional mentor, providing invaluable support to me through scientific discussions and guidance on job searches, in addition to his presence

on my thesis committee. Working alongside Supavit Pokawanvit (in Felipe's group at Stanford) has been a tremendous privilege.

I am thankful for the opportunity to be mentored by an exceptional group of scientists at Caltech, and I hold them in high regard. My first mentor, William Whitney, introduced me to black phosphorus, while Joeson Wong, my close associate, trained me on 2D materials, optics, and automating measurements, among other non-academic pursuits, ranging from Ed Sheeran to midnight food tours. Professor Zakaria Al Balushi has been a close confidant since my first year of graduate school, introducing me to the world of TMDCs and phase transition. Meir Grajower, my closest collaborator for over three years, is an outstanding teammate, with extensive knowledge of solid-state physics and electronics, coupled with strong criticism about the "real" impact of scientific work, which struck a perfect balance for me. I learned a lot about experiments, honesty, and ethics in scientific claims from him. I am also grateful to Professor Muhammad Alam for our discussions during my early days of PhD. Additionally, Professors Artur Davoyan and Deep Jariwala have provided me with excellent feedback and support on my work and career from time to time.

I will also miss the group of professors and colleagues who formed our 'boba' squad, including Professor Pin Chieh Wu, Professor Wen Hui (Sophia) Cheng, Wei-Hsiang Lin, and Sisir Yalamanchilli. I must say that Professor Benji Vest is one of the most enjoyable professors I have encountered, and I am envious of his students for having such an excellent advisor. His expertise in optics is unmatched and something to aspire to.

I had the opportunity to conduct experiments outside of Caltech and was fortunate to collaborate with a remarkable group of scientists who provided me with invaluable support. I would like to express my heartfelt appreciation to Dr. Hans Bechtel for his expertise in infrared spectroscopy; Dr. Chris Jozwiack, Dr. Aaron Bostwick, and Dr. Eli Rotenberg for their valuable contributions to ARPES; Dr. Huairuo Zhang, Dr. Wei Chang Yang, Dr. Sergiy Krylyuk, and Dr. Albert Davydov for their assistance with crystals and electron microscopy; and Irene Lopez and Professor Rainer Hillenbrand for their expertise in near-field spectroscopy.

I must acknowledge the contribution of Hamidreza Akbari, who has been an excellent collaborator and a dear friend. During our coffee breaks, I learned a lot about quantum optics from him. I also worked closely with Melissa Li and Komron Shayegan, who taught me a great deal about metasurfaces in visible and thermal radiation engineering. Samuel Seah is entrusted with the responsibility of carrying forward the legacy of black phosphorus. Given his intelligence and dedication, I am confident that the future of black phosphorus metasurfaces is promising. I have thoroughly enjoyed working with Morgan Foley on various aspects of metasurfaces and photonics. I am also grateful to Claudio Hail, Ramon Gao, and Lior Michaeli for discussions on optics, metasurfaces, and opto-mechanics.

I would like to express my gratitude to a wonderful group of colleagues whom I had the pleasure of interacting with in the Atwater group. These include Mike Kelzenberg, Ruzan Sokhoyan, Marianne Aellen, Aisulu Aitbekova, Areum Kim, Arun Nagpal, Jared Sisler (also for squash), Prachi Thureja, Kyle Virgil, Parker Wray, Ghazaleh Shirmanesh, Laura Kim, Yonghwi Kim, Kelly Mauser, Cora Went, Qin (Arky) Yang, Nina Vaidya, Haley Bauser, and Jeremy Brouillet. I am also grateful to Sumit Goel (my sports buddy), Adrian Tan (my gossip buddy), Ubamanyu Kanthsamy, Pranav Kulkarni, Jash Banker, and the entire "Indian gang" for their constant support.

During my PhD journey, I was fortunate to have a supportive group of friends from both my high school and undergraduate days who helped me during my struggles. From my high school days, I am grateful for the support of Abhishek Gupta, Soura Mondal, Chirantan Batabyal, Sohanjit Mallick, Meghadri Sen, Nirjhar Roy, Soumya Basu, Saikat Gupta, Soham Biswas, Rudrashish Bose, and Srirup Bagchi. From my college days, I owe a debt of gratitude to (in random order) Samrat Halder, Sayantan Dutta, Sayantan Bhadra, Aranya Goswami, Subhojit Dutta, Tathagata Srimani, Anusheela Das, Biswajit Paria, Mouktik Raha, Abhisek Datta, Prof. Avik Dutt, Aniruddhe Pradhan, and Subhrajit Mukherjee (my undergraduate mentor).

I express my gratitude to the KNI community for their assistance and administrative support, as well as to the International Student Programs at Caltech. I would like to extend a special thanks to Laura and Daniel for their invaluable help.

Without a doubt, every individual requires the unflinching support of their family to fully realize their potential. I am no exception to this indisputable truth. I am deeply grateful to my beloved parents, Santanu Biswas and Dipa Biswas, for their invaluable guidance and support, which have been instrumental in shaping my life. It is with certainty that I can declare that without their selfless contributions, I would not have achieved the level of success that I currently enjoy. From my childhood until now, I am fully cognizant of the numerous sacrifices they have made to ensure my education was smooth, and for that, I am forever grateful. Their constant encouragement and blessings serve as a driving force for me to continue striving for greater accomplishments. I am grateful to my paternal grandmother (Kalyani Biswas), late maternal grandparents (Heramba K. Biswas and Nilima Biswas), and late paternal grandfather (Sunil K. Biswas) for their love and blessings. On my maternal side, my (late) uncles (Amit Biswas and Sumit Biswas) have left an indelible mark on my life; I miss them dearly.

Since the year 2015, my best friend, Pallavi, has been my unwavering pillar of strength, and I am exceedingly proud to have her as my life partner. Through all the ups and downs, she has remained steadfastly by my side, and for her resolute affection and unwavering inspiration, I shall remain eternally thankful. I would also like to express my gratitude to my in-laws, Prabir Banerjee and Suparna Banerjee, for welcoming me into their family.

Throughout the preceding years, I have been blessed with some truly extraordinary instances that shall undoubtedly be forever etched in my memory as moments of immense significance and joy.

Dedicated to Ma, Bapi, and Pallavi

ABSTRACT

van der Waals materials are emerging due to their unique properties such as atomic thickness, diverse quasiparticle optical resonances, and no requirement for lattice matching. While there is a vast variety of materials, semiconductors hold a special place for opto-electronic and linear/non-linear optical studies. Black phosphorus (BP), a 2D quantum-well with direct bandgap and puckered crystal structure, is a compelling platform for this research direction. In this thesis, we investigate fundamental optical excitations in novel low-dimensional quantum materials to achieve strong light-matter interaction and integrate with nanophotonic motifs for low-footprint, reconfigurable optical technology, focusing primarily on black phosphorus and transition metal dichalcogenides.

The thesis begins with the 'thin film limit' of van der Waals materials, between 5 and 20 nm thickness range. Chapters 2 and 3 explore how few-layer black phosphorus hosts interband and intraband optical excitations that can be strongly modified with gate-controlled doping and electric field, displaying epsilon near zero and hyperbolic behavior in the mid and far-infrared. As the material approaches atomic thickness, strongly bound excitonic quasiparticles dominate the optical response. In Chapter 4, we investigate electrically tunable excitons in tri-layer black phosphorus, demonstrating a reconfigurable birefringent material that, when coupled with a Fabry-Perot cavity, enables the realization of a versatile and broadband polarization modulator.

In Chapter 5, we examine the ultimate limit of a monolayer, studying $MoTe_2$ via photoluminescence measurements and first-principles GW+BSE calculations, highlighting the Rydberg series associated with the exciton and its gate-tunability to understand strong electron-exciton interactions. In Chapter 6, we show how such excitons in monolayer black phosphorus can be strongly quantum confined at natural edges of exfoliated flakes, leading to highly temporally coherent emission. This emission is gate-tunable and understood via transmission electron microscopy and first-principles GW+BSE calculations of phosphorene nanoribbons to be originating from atomic reconstructions of the edge coupled with strain and screening effects.

Overall, our work highlights the potential of van der Waals materials for various electro-optical excitations and their applications in active nanophotonics.

PUBLISHED CONTENT AND CONTRIBUTIONS

*indicates equal contribution

- Michelle C. Sherrott*, William S. Whitney*, Deep M. Jariwala, **Souvik Biswas**, Cora M. Went, Joeson Wong, George R. Rossman, Harry A. Atwater. *Anisotropic Quantum Well Electro-Optics in Few-Layer Black Phosphorus*. Nano Letters (2019), 19, 1, 269-276. doi: 10.1021/acs.nanolett.8b03876.

S.B. participated in the device fabrication and measurements with M.C.S. and W.S.W. S.B. helped with the preparation of the manuscript.

- **Souvik Biswas**, William S. Whitney, Meir Y. Grajower, Kenji Watanabe, Takashi Taniguchi, Hans A. Bechtel, George R. Rossman, Harry A. Atwater. *Tunable intraband optical conductivity and polarization dependent epsilon-near-zero behaviour in black phosphorus*. Science Advances (2021), 7, 2, eabd4623. doi:10.1126/sciadv.abd4623.

S.B. conceived the experiment with inputs from H.A.A. S.B. fabricated the devices, performed the measurements, analyzed the data, did analytical calculations, and prepared the manuscript.

- **Souvik Biswas***, Meir Y. Grajower*, Kenji Watanabe, Takashi Taniguchi, Harry A. Atwater. *Broadband electro-optic polarization conversion with atomically thin black phosphorus*. Science (2021), 374, 6566, 448-453. doi:10.1126/science.abj7053.

S.B. conceived the experiment with inputs from M.Y.G. and H.A.A. S.B. fabricated the devices, performed the measurements, analyzed the data, did analytical calculations and numerical simulations, and prepared the manuscript.

- **Souvik Biswas**, Aurelie Champagne, Jonah B. Haber, Supavit Pokawanvit, Joeson Wong, Sergiy Krylyuk, Hamidreza Akbari, Kenji Watanabe, Takashi Taniguchi, Albert V. Davydov, Zakaria Y. Al Balushi, Diana Y. Qiu, Felipe H. da Jornada, Jeffrey B. Neaton, Harry A. Atwater. *Rydberg excitons and trions in monolayer $MoTe_2$*. In revisions, ACS Nano (2022), arxiv. doi:10.48550/arXiv.2302.03720.

S.B. conceived the experiment with inputs from H.A.A. S.B. fabricated the devices, performed the measurements, analyzed the data, did analytical calculations, and prepared the manuscript.

- **Souvik Biswas***, Joeson Wong*, Supavit Pokawanvit, Huairuo Zhang, WeiChang D. Yang, Kenji Watanabe, Takashi Taniguchi, Hamidreza Akbari, Albert V. Davydov, Felipe H. da Jornada, Harry A. Atwater. *Signatures of edge-confined excitons in monolayer black phosphorus*. Submitted (2023).

S.B. conceived the experiment with inputs from J.W. and H.A.A. S.B. fabricated the devices, performed the measurements, analyzed the data, did analytical calculations, and prepared the manuscript with input from J.W.

This thesis contains excerpts from the aforementioned published/submitted manuscripts.

TABLE OF CONTENTS

LIST OF ILLUSTRATIONS

LIST OF TABLES

Chapter 1. INTRODUCTION

1.1 VAN DER WAALS MATERIALS

A new class of materials, called van der Waals materials[1,2], has recently excited widespread interest because of their novel and unique properties. They are essentially layered materials, where each layer is held together by van der Waals forces of attraction–which are much weaker compared to chemical or ionic bonds. This allows isolation of individual layers via different methods of 'exfoliation'–such as mechanical[3] (Scotch-tape being one of the most popular choices of a handle layer) and chemical methods involving sonication and intercalation[4,5]. The fact that in-plane bonds are chemical and hence, in general, stronger than the van der Waals bonds makes exfoliation a reliable technique to generate large area high-quality samples. Although van der Waals materials have been studied back in 1960s via optical and electrical characterization[6], the field rapidly exploded in 2004 when Novoselov and Geim were able to isolate graphene in the form of a few layers and eventually a monolayer[7]. 2D materials appear in different phases of matter such as metals, semiconductors, insulators and also exhibit unusual and exotic topological properties in Dirac and Weyl semi-metals, charge density waves, etc[8–10]. Furthermore, since these materials can be cleaved and then stacked without lattice matching requirements (due to van der Waals attraction), one can create so-called 'heterostructures' which may have completely different properties from their parent layers[11,12]. Taken together, the possibility of exploring phases of matter in 2D materials and their heterostructures is endless and can be studied for decades.

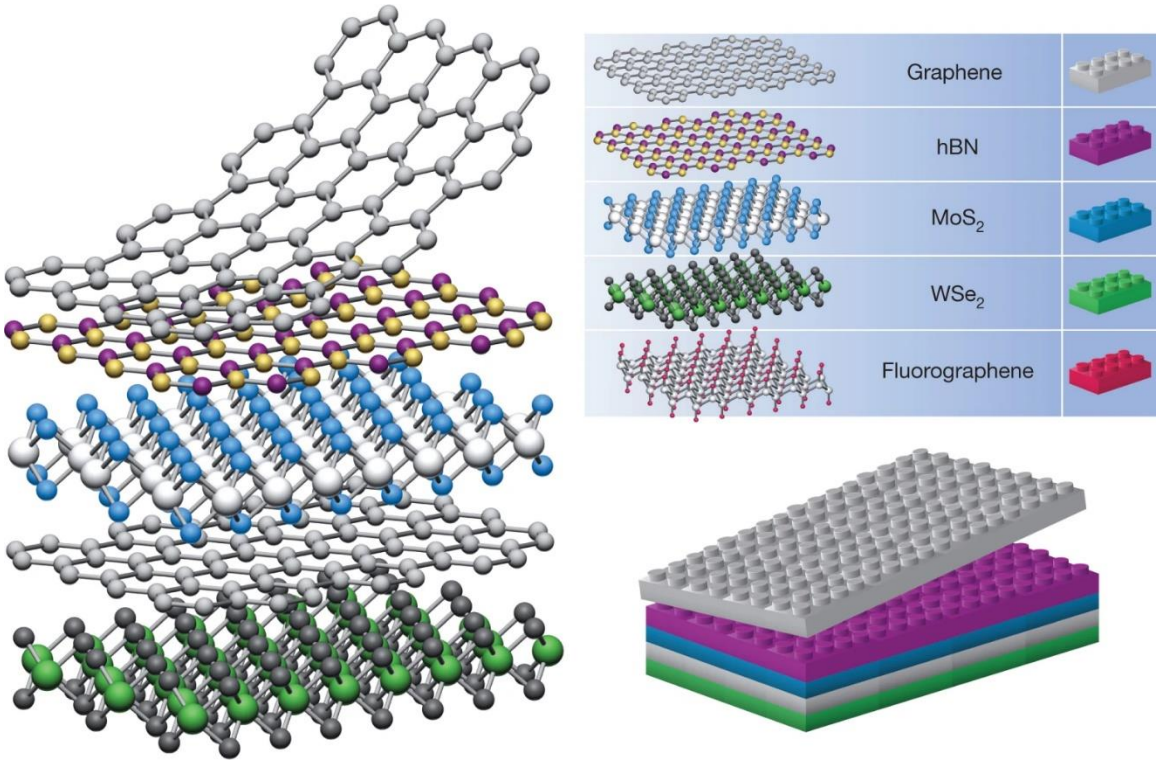

Figure 1.1. Conceptual schematic of Lego-like behavior in van der Waals heterostructures. Different materials can be stacked to form new materials with different properties compared to their parent. Figure taken from Ref. [1]

Of considerable interest in the context of opto-electronics is graphene, the family of TMDCs, and black phosphorus. This thesis will mainly focus on the opto-electronics of black phosphorus and one candidate TMDC–$MoTe_2$.

1.2 EXCITONS

When a (negatively charged) electron and a (positively charged) hole are attracted to each other through Coulomb forces of interaction, a stable quasiparticle is formed called the exciton[13,14]. While such states exhibit significant similarities to the hydrogen atom, they also show interesting deviations due to the two-dimensional nature of the host[15]. Usually, they result from photo-excited charge oscillations in semiconductors and are redshifted from the band-edge by the exciton binding energy (E_B). Excitons display an unusually large oscillator strength and thus host strong light-matter interactions enabling efficient optical excitation and read-out capabilities.

Exciton behaves like an atom (impurity) in the background of a crystal lattice and displays a fine-structure akin to a hydrogen atom. These states appear as resonances of finite width in the optical spectrum and are known as the Rydberg series[15]. The width of each state is related to the quantum yield of the transition as well as other competing non-radiative processes like phonon scattering, electron scattering, etc.

Thus far, excitons have remained practically elusive, since in typical bulk semiconductors, the binding energy is on the order of ~1-10 meV due to strong self-screening[16]. This makes it very difficult to observe such states at room temperature due to thermal fluctuations ($k_BT \sim 25$ meV) and only allows visualization at very low temperatures ($k_BT < \sim 1$ meV), limiting its use for practical technology.

From this point of view, some of the transition metal dichalcogenides (TMDCs) and black phosphorus, offer a way out. They host excitons with binding energy on the order of 100s of meV, making them attractive for practical and viable room-temperature operation[13,14,17]. This is enabled by the strong Coulomb attraction between the electron and hole due to low dimension and reduced dielectric screening in atomically thin sheets. Naturally, monolayers exhibit the largest binding energy and strongest resonances, in general.

Group VIB TMDCs such as molybdenum and tungsten based diselenides, ditellurides, and disulfides: MoS_2, $MoSe_2$, WS_2, WSe_2 and $MoTe_2$ occur in semiconducting phase (2H) and can be exfoliated down to a monolayer[13,14,17–20]. Black Phosphorus is another candidate which occurs in the semiconducting phase[21]. Both these systems host strong excitons, especially at the monolayer limit. In TMDCs an indirect to direct bandgap transition takes place at the monolayer thickness due to the lack of interlayer interactions which play a role in band structure renormalization. Such reduced interactions manifest as a lower valence band maximum resulting in a direct band gap–high absorption and intense photoluminescence. Black phosphorus is unique since due to its crystal structure, it remains a direct bandgap at all thickness with changes in the binding energy (detailed later)[22,23]. Such properties are attractive for light emission and absorption applications.

Another interesting aspect is the dipole orientation in these layered materials. Due to thickness constraints, most excitons are in-plane dipoles allowing maximal interaction with normally incident light radiation. Next, we discuss strategies to engineer excitons in different ways.

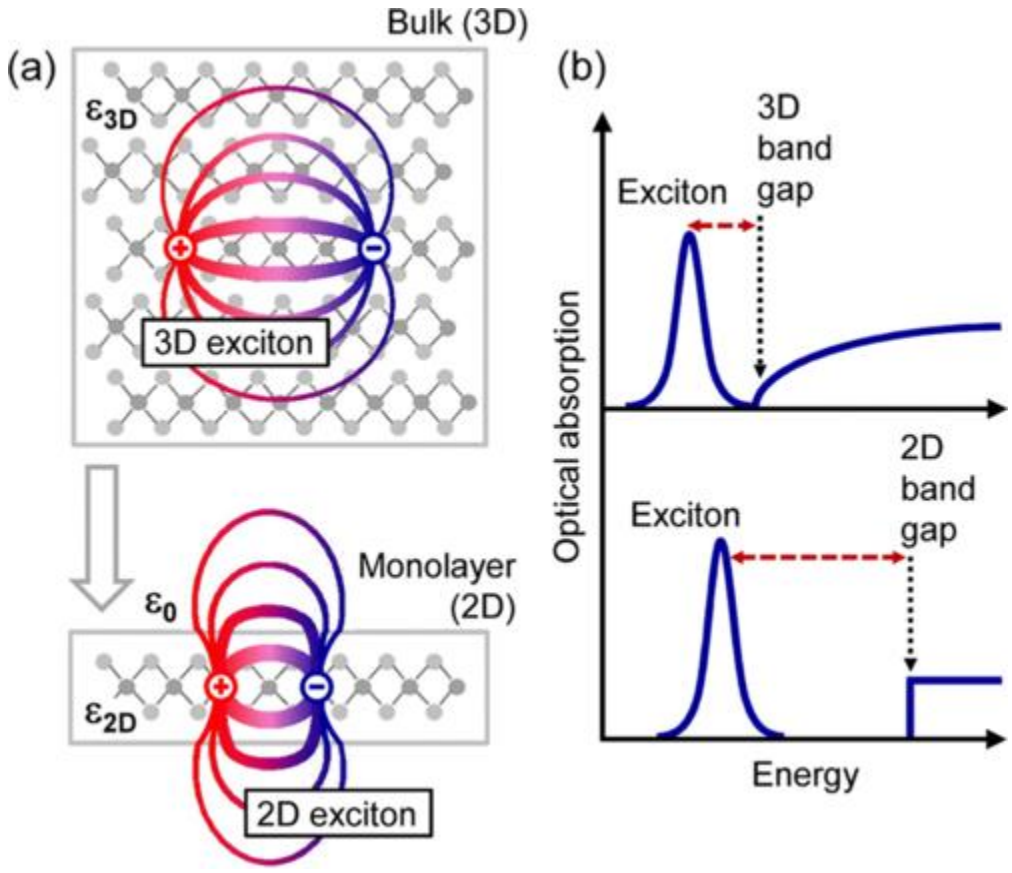

Figure 1.2. Schematic of exciton and absorption. (a) Coulomb field lines for an exciton in a 3D bulk semiconductor and monolayer 2D semiconductor showing reduced screening from the environment. (b) Optical absorption showing excitonic state and quasiparticle gap for 2D and 3D case. Figure taken from Ref. [15]

1.3 ELECTRICAL TUNING OF EXCITONS

2D materials offer attractive opportunities for electrical tuning of their properties. For example, MoS_2 monolayers and few-layers were demonstrated to have excellent transistor like characteristics which rapidly exploded the field in that direction[24]. As these materials are atomically thin, encapsulating them in a field-effect heterostructure enables electrostatic doping of the active layer.

This allows tuning of the charge density and the current in the active layer as well, thus modulating its electrical and optical properties.

One of the first efforts in that direction include Mak and Xu's efforts to dope a monolayer and observe in absorption and PL the emergence of trions–a quasiparticle which consists of an exciton bound to an electron or hole[20,25]. Trions also possess a relatively high binding energy (~20-30 meV) and hence can be observed at room temperatures. Further studies by Chernikov reported more detailed characterization of the exciton and trion as a function of gate voltage, not only for the ground state but also for the higher energy Rydberg states for a select few TMDCs[26–29].

Another important aspect is that 2D materials, near excitonic resonances, show enhanced refractive properties upon incident light radiation. This is mainly due to high scattering and strong light-matter interaction on resonance. Excitons can be modelled approximately as a Lorentzian function with finite amplitude, resonance energy and linewidth, as mentioned before[30,31]. Upon electrical gating the Lorentzian function can be heavily modified which forms the basis for actively tunable refractive element. Such elements can be cascaded to construct complex metasurfaces, which is what a section of this thesis highlights.

1.4 ELECTRIC-FIELD EFFECTS ON EXCITONS

Depending upon the electrostatic geometry, 2D materials can be made to purely experience displacement-field effects while keeping the charge density neutral or constant. Such geometry usually involves dual gates with symmetric doping condition and has the largest effects on thicknesses beyond a monolayer (due to in-plane dipole of a monolayer). Stark effect has been heavily explored in natural bilayers as well as monolayer-monolayer heterostructures[32–34]. At higher thicknesses other quantum effects kick in such as Burstein-Moss shifts and band-gap reduction/normalization[35]. Detailed discussion of different effects dominating at different thicknesses is presented later in the thesis.

1.5 MECHANICAL TUNING OF EXCITONS

Upon mechanical straining the electronic band structure can be modified since it is related to the lattice structure. Optical properties such as excitons (in monolayer or few-layers) and interband transitions can be modulated with strain[36–39]. 2D Materials are placed on flexible substrates which

allows dynamic modulation of the strain. Changing temperature can also modify the lattice constant which can be another mechanism for changing strain. Additionally, the phonon spectrum (manifested in Raman spectroscopy) can also be tuned via strain. Strain engineering in multilayers not only modifies lattice constant but also tunes interlayer coupling. Such a strategy has been proved to be very effective for tuning optical properties in black phosphorus as shown by Yan[38]. A similar strategy was also adopted by us to tune interlayer interactions between MoS_2 and WSe_2 on a flexible substrate[40].

Other forms of tuning include applying magnetic fields or optical pumping which are beyond the scope of this thesis.

1.6 PLASMONS

Plasmons are quantized charge oscillations in a semiconductor or a metal. Such oscillations are induced by virtue of Drude-like absorption from free carriers and are termed as intraband absorption– as the carriers do not change their band index. The absorption process is accompanied by a phonon since it is not momentum conserving. In terms of the optical response of a plasmonic system, the real part of the dielectric function becomes negative (thus allowing excitation of confined modes), and the imaginary part becomes positive (meaning the material becomes lossy). Plasmonic materials thus suffer a trade-off between being able to confine light to sub-wavelength volumes and intrinsic loss/efficiency. While mostly explored in graphene, other doped semiconductors, and metals in the library of 2D materials offer interesting alternatives[41–46]. For example, black phosphorus is a highly anisotropic system which has been theorized to be in-plane hyperbolic–meaning plasmonic along one crystal axes and dielectric along another[47–50]. Thus far, experiments demonstrating direct evidence of plasmonic behavior have remained elusive. In this thesis, we establish this fact in chapter 3 and show gate-tunability of the same.

1.7 PHONONS

Phonons are quantized vibrations of the atomic lattice. Usually, they are observed in optical spectroscopy for polar materials since there is a permanent charge separation which allows the dipoles to interact strongly with incident light. Hexagonal boron nitride and molybdenum trioxide are two examples of the most studied phonon systems due to high anisotropy and high-quality

phonon resonances[51,52]. Mathematical modelling of phonons is similar to excitons in that they can be described by a Lorentzian lineshape.

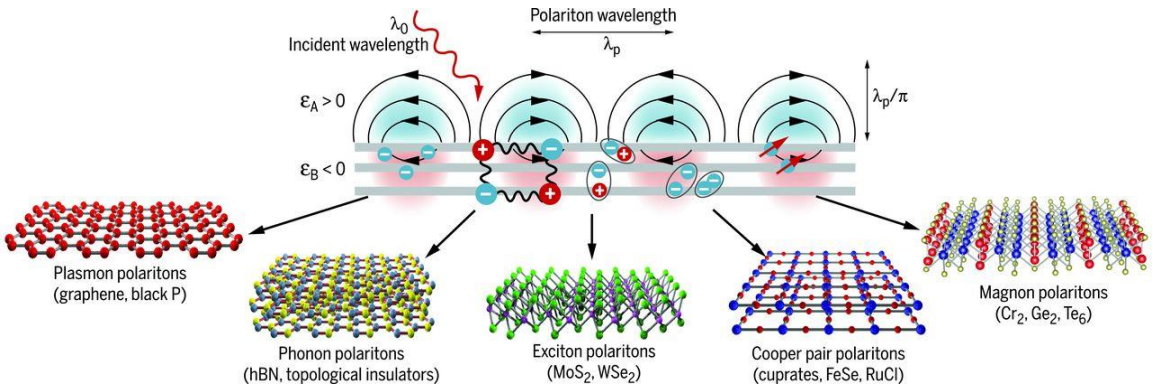

Figure 1.3. An overview of possible material resonances in the van der Waals library. Each quasiparticle induces a susceptibility resonance in the optical response of the material that can interact with light strongly, creating hybrid light-matter modes–polaritons. From left to right– electrons/holes in graphene and black phosphorus, lattice vibrations in hBN and topological insulators, electron-hole quasiparticles in semiconductors, cooper pairs in superconductors and magnons in magnetic materials. This figure is taken from Ref. [53]

1.8 BLACK PHOSPHORUS

Black phosphorus (BP) is a relatively new member of the 2D materials family and is the layered allotrope of phosphorus. It has a distinct crystal structure as compared to the TMDCs and graphene family. It possesses a highly buckled lattice structure which renders strong anisotropy between different crystalline directions which manifests as anisotropic optical, electrical, thermal, and mechanical properties. Despite such exciting properties, BP remains relatively poorly explored especially in the mono/few layer limit because of highly sensitive nature to oxidation and degradation requiring inert processing atmosphere and immediate encapsulation after isolation for best quality devices. This is because in-plane bonds in BP are weaker as compared to graphene or TMDCs and hence in-plane oxidation is much faster than out-of-plane.

BP is a direct band gap semiconductor and has varying bandgap with number of layers–behaving like a quantum well. As the material becomes thicker, the quantum confinement changes in the vertical direction which modulates the energy spacing of the intersubband levels. In the monolayer

limit, BP has a band gap of ~2 eV which gradually reduces to a value of ~0.3 eV in the bulk limit. In stark contrast to TMDCs, no indirect-to-direct transition happens in the bandgap for BP since the band-minimum occurs at the Γ point of the Brillouin zone–which is strongly affected by interlayer interactions. Such properties make BP attractive for infrared photonics as it bridges the gap between graphene (in the mid to far-infrared) and TMDCs (which have band-gaps in the visible frequencies).

The most compelling property of BP (within the scope of this thesis) is the anisotropy and the strong electrical tunability of its optical properties. It is a unique quantum-well like system with large in-plane birefringence, not seen usually in other materials. Thus quantum-well effects like quantum-confined Stark effect, Pauli blocking, Burstein-Moss shifts are expected to be observed in gated structures for multilayer BP. As one approaches the atomic limit, excitonic effects are expected to kick in. BP, in fact, possesses one of the highest binding energy for excitons in its monolayer limit in a free-standing film (~0.8 eV) which gradually decreases for thicker films, until the free-carrier continuum (quasi-particle band gap) merges with the excitonic resonance, i.e., the exciton Coulomb field is heavily screened by the BP layers.

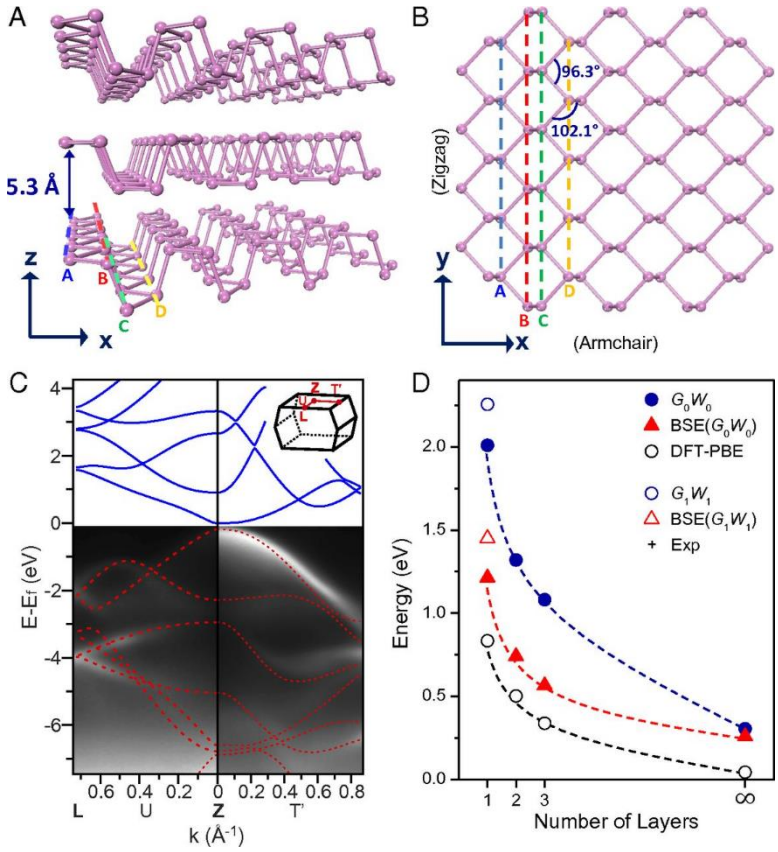

Figure 1.4. Overview of black phosphorus. (a) Side view of anisotropic puckered crystal structure of layer BP. (b) Top view of a monolayer BP crystal structure. (c) Angle resolved photoemission spectroscopy measurement of band structure in bulk BP with the band minima being at the Γ (Z)point. (d) Layer dependent band gap of BP showing strong interlayer interactions. This figure is taken from Ref. [54]

This anisotropy inspires compelling new physics, such as in-plane hyperbolic plasmons, and technology applications, such as polarization modulation and generation.

1.9 LIGHT-MATTER COUPLING

Matter interaction with electromagnetic radiation is one of the most widely studied subjects in solid-state physics and perhaps the most promising for future technology. Strong interaction is usually achieved when the optical density of states of a system is very high which is reflected in the complex refractive index or dielectric function of the system. There are two broad ways of achieving the same.

1. Material resonance

This involves working around a quasi-particle resonance such as those described previously– excitons, plasmons and phonons, where each susceptibility resonance can be simply modelled with a Lorentzian lineshape: $I(\omega) = \frac{\frac{A\Gamma}{2}}{(\omega-\omega_0)^2+\left(\frac{\Gamma}{2}\right)^2}$, where A is the intensity of the resonance, Γ is the broadening and ω_0 is the resonant energy.

2. Geometric resonance

This involves utilizing a structure which can be thought to induce a mode (electric or magnetic dipole, quadrupole, or higher order) that interacts strongly with light. This is achieved by using optical cavities like Fabry-Perot or nanostructures that acts as subwavelength antenna elements[55–57].

Light-Matter coupling can be further broadly classified into the following categories:

A. Strong coupling

This is achieved when a material is brought in close proximity with an optical resonator and their resonances are aligned. Mathematically, if the coupling strength between the material and resonator is denoted by g, and their respective dissipation rates are denoted as κ and γ, then the condition for strong coupling is given $g > \frac{|\kappa-\gamma|}{2}$.

B. Weak coupling

This regime is achieved when the matter acts as a weak perturbation and the optical response is governed by the optical resonator ($g \leq \frac{|\kappa-\gamma|}{2}$). Despite being weak, such regimes are useful for building amplitude and phase modulators whereby shifting the resonance to different energies, a large modulation depth can be achieved. In this regime, three kinds of coupling can be accessed– critical coupling, under coupling and over coupling–all exhibiting Purcell enhancement of certain degree. If the total response (r_{tot}) of a system is dominated by non-resonant (r_{nr}) and resonant (r_r) processes, it can be mathematically expressed as–$r_{tot} = r_r + r_{nr}$. Critical coupling is achieved when $r_{nr} \sim r_r$ and a π phase shift exists between the two channels–thereby allowing complete absorption

of light. In a complex plane representation of the total scattering channel the real and imaginary part of r_{tot} lie at the center. However, as the resonant channel begins dominating the non-resonant part ($r_{nr} > r_r$), the system goes into under-coupling whereas it goes into over-coupling for the reverse case.[58] An illustrative figure for a ring-resonator system where t is the transmission of the system, a is the absorption in the ring and k is coupling between the waveguide and the ring for the different regimes and their optical output is shown.

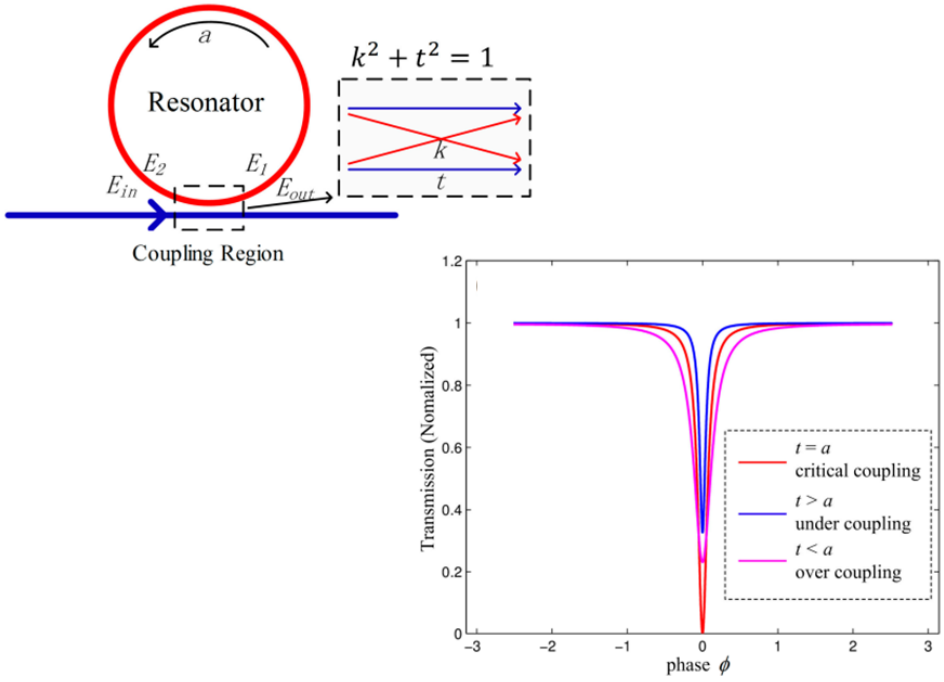

Figure 1.5. Different regimes of weak coupling. A ring-resonator system is shown for illustrative purposes with three regimes identified–critical coupling (t = a), over-coupling (t < a) and under-coupling (t > a). Their optical response (transmission) is also plotted. This figure is taken from Ref. [59]

1.10 METASURFACES

Subwavelength photonic structures have restructured our understanding of classical Snell's law, which is written as:

$$\frac{sin\theta_1}{sin\theta_2} = \frac{v_1}{v_2} = \frac{\lambda_1}{\lambda_2} = \frac{n_2}{n_1}$$

where $\theta_{1,2}$ are the incident and refracted angle, $v_{1,2}$ are the speed of light, $\lambda_{1,2}$ are the wavelengths of light, $n_{1,2}$ are the refractive indices of each medium, respectively.

At an interface when a phase gradient is imposed, this equation needs to be reframed to account for the spatial dependence of the accumulated phase. A generalized law of reflection and refraction then emerges as follows:

$$n_t \sin(\theta_t) - n_i \sin(\theta_i) = \frac{1}{k_0}\frac{d\Phi}{dx}$$

$$\cos(\theta_t)\sin(\phi_t) = \frac{1}{n_t k_0}\frac{d\Phi}{dy}$$

$$\sin(\theta_r) - \sin(\theta_i) = \frac{1}{n_i k_0}\frac{d\Phi}{dx}$$

$$\cos(\theta_r)\sin(\phi_r) = \frac{1}{n_t k_0}\frac{d\Phi}{dy}$$

where $\frac{d\Phi}{dx}$ and $\frac{d\Phi}{dy}$ are phase gradients along x and y directions, $\theta_t, \theta_i, \theta_t$ are the transmitted, incident, and reflected angles in the x-direction, and ϕ_t, ϕ_r are the transmitted and reflected angles in the y-direction. Incident plane is defined to be x-z. Provided a full 2π phase space is accessible, light can be directed or manipulated in arbitrary ways. Via careful engineering of the phase gradient and polarization at each element, novel applications will benefit like beam steering, spatial light modulation, focusing or lensing and holography.

A convenient approach to designing phase gradients is by controlling the shape or geometry of each nanophotonic element, as first demonstrated in previous reports[60,61]. Since then, the field has exploded via various ways of engineering such as changing materials of the antenna or their surrounding.

1.11 ACTIVE NANOPHOTONICS

While modifying geometry provides a way to control phase, amplitude, and polarization of each metasurface element, it also has certain restrictions which limit functionality–such as lack of real

time reconfiguration. Geometric elements are fixed at the time of fabrication and thus, their response is static. Active nanophotonics offers attractive schemes to tune different properties of light as a function of time, in a controlled fashion.

Dynamic control at the near-field and far-field level in real time opens up a number of promising applications such as fast LIDARs and detectors, displays for augmented and virtual reality (AR/VR), LiFi and thermal radiation engineering. It can also impact computing, information transfer and processing.

There now exist many approaches to dynamically control optical properties of materials and careful attention must be paid to the different metrics required for each application–such as speed, energy, robustness, and cost. Mechanical strain tuning, piezo effects, and thermally-induced phase change materials[62–65] can be useful in generating large tunability at the cost of slow speed. In contrast, semiconductor charge injection[66,67] or electric-field based effects like the Stark[68] or Pockels shift[69] can provide much faster operation at the cost of lower refractive index modulation. Thus, a judicious combination of a dynamic tuning mechanism and nanophotonic element can enable the "universal metasurface" with independent control knobs for different properties of light–amplitude, phase, polarization, wavevector and wavelength.

1.12 OPTICAL MODULATORS

At the heart of active nanophotonics lies optical modulators[66,70–72]. The fundamental working principle involves a dynamically tunable element whose complex refractive indices can be changed with an external stimulus - such as temperature, electric field, magnetic field, electronic doping, strain, or optical pumping–which in turn modulates the phase or amplitude of the incident light, either in reflection or transmission mode (depending upon the application). Usually, such tunable elements are coupled with optical resonators such as Fabry-Pérot cavities, ring resonators, waveguides, metasurfaces to amplify the dynamic tunability. Since this thesis is focused on electro-optic effects–graphene, TMDC and black phosphorus are attractive candidates for the same. While graphene has a very broad-band response thanks to its zero bandgap, black phosphorus and TMDCs exhibit complementary response to graphene due to their direct/indirect bandgap nature. In graphene, two major mechanisms are at play upon charge injection–Drude absorption at long wavelengths (mid to far-infrared) and Pauli blocking (in the near to mid-infrared). For black phosphorus, a much more

complex picture emerges upon charge injection, depending upon the thickness (which is discussed in detail in this thesis).

1.13 SCOPE OF THIS THESIS

This thesis explores the emerging field of van der Waals nanophotonics which combines the study of atomically thin materials and optics at the subwavelength scale. We leverage the material resonances of quantum-confined, atomically thin semiconductors as active elements for existing and novel photonic designs. This enables real time reconfiguration of different properties of light at subwavelength scales. Furthermore, optical spectroscopy of such quantum materials also reveals key insights into their fundamental properties.

Chapter 2 introduces electro-optic effects in few-layer black phosphorus under symmetric and asymmetric gating. By using a dual gate, the charge density as well as the electric field can be independently controlled in black phosphorus. This allows isolation of the two effects: 1. Doping (Pauli-blocking) and 2. Field (quantum-confined Stark effect and modification of selection rules of optical transitions). Both regimes present ways to alter the refractive indices of BP which are attractive for mid-infrared photonics. In Chapter 3, we focus on the mid to far-infrared properties of similar structures and investigate the free-carrier optical response. We find highly anisotropic absorption which can be modulated by injecting charge in BP. Such absorption is Drude-like and induces a metallic behavior (seen as epsilon-near-zero) along one of the crystal axis (armchair), while the other axis (zigzag) remains dielectric. This marks the first observation of in-plane electrically tunable hyperbolicity in BP and opens avenues for plasmon switching, beam steering, etc.

Chapter 4 builds on this work and expands its scope by studying electrically tunable excitons in tri-layer black phosphorus (significantly thinner than previous studies) which leads to tuning of the complex refractive index on the order of 1 (orders of magnitude higher than lithium niobate, barium titanate, etc.). Such large tuning happens only along the armchair axis due to symmetry arguments and thus a highly tunable birefringence material emerges. By combining with an optical resonator (Fabry-Perot cavity), large changes in amplitude and phase can be enabled to create different polarization states of light across the Poincare sphere across the entire telecommunication band. This constitutes the first demonstration of an electrically tunable polarization modulator using van der Waals materials.

Since excitons form the basis of strong optical modulation, a careful fundamental investigation of the same is of utmost importance. In Chapter 5, we approach the ultimate limit of a monolayer, since they host excitons with the highest binding energy, and focus on the fundamental optical properties. We study $MoTe_2$, a semiconductor of the TMDC family, using photoluminescence measurements to investigate the Rydberg series associated with the exciton. Combing it with gate-tunable heterostructure we find that the emission can be strongly tuned between the neutral excitonic and charged excitonic (trionic) state. We further perform GW+BSE calculations to support our understanding of excitons and exciton-electron interactions. Finally, in Chapter 6, we study excitons in monolayer black phosphorus and strong quantum confinement at natural edges of exfoliated flakes (which happened to be a serendipitous finding). Such confinement results in highly temporally coherent emission which is polarized and also tunable in a gated heterostructure. Through transmission electron microscopy we study how edges of phosphorene reconstruct to minimize energy and using first-principles GW+BSE calculations of phosphorene nanoribbons we understand how some configurations, in conjunction with strain, lead to formation of edge (localized) states, appearing as additional peaks in our experiments.

Overall, our work highlights the opportunities presented by van der Waals materials through various electro-optical excitations for applications in active nanophotonics.

Chapter 2. INTERBAND EXCITATIONS IN MULTILAYER BLACK PHOSPHORUS

2.1 ABSTRACT

The incorporation of electrically tunable materials into photonic structures such as waveguides and metasurfaces enables dynamic, electrical control of light propagation at the nanoscale. Few-layer black phosphorus is a promising material for these applications due to its in-plane anisotropic, quantum well band structure, with a direct band gap that can be tuned from 0.3 eV to 2 eV with number of layers and subbands that manifest as additional optical transitions across a wide range of energies. In this work, we report an experimental investigation of three different, anisotropic electro-optic mechanisms that allow electrical control of the complex refractive index in few-layer black phosphorus from the mid-infrared to the visible: Pauli-blocking of intersubband optical transitions (the Burstein-Moss effect); the quantum-confined Stark effect; and the modification of quantum well selection rules by a symmetry-breaking, applied electric field. These effects generate near-unity tuning of the BP oscillator strength for some material thicknesses and photon energies, along a single in-plane crystal axis, transforming absorption from highly anisotropic to nearly isotropic. Lastly, the anisotropy of these electro-optical phenomena results in dynamic control of linear dichroism and birefringence, a promising concept for active control of the complex polarization state of light, or propagation direction of surface waves.

2.2 INTRODUCTION

Dynamic control of the near and far-field propagation of light is critical for next-generation optoelectronic devices. Ultra-thin, layered materials are promising building blocks for this functionality, as they are easily incorporated into atom-scale structures, and their optical properties can be changed dramatically under applied electric fields[73,74]. Few-layer black phosphorus (BP) is particularly compelling due to its high electronic mobility, in-plane anisotropy, and thickness-tunable quantum well band structure, with a direct band gap that varies from 0.3 eV in bulk to 2 eV for monolayers[54,75]. Recent work using electrostatic gating and potassium ions has further shown that the electronic band gap of BP may be tuned by an electric field.[35,76–78] These unique

attributes have already enabled the realization of novel and high-performance optoelectronic devices, including waveguide-integrated photodetectors[79–83].

One of the most unusual features of BP is its large in-plane structural anisotropy, which generates to a polarization-dependent optical response[21,49,84] as well as mechanical[85], thermal[86], and electrical transport characteristics[87,88] that vary with in-plane crystallographic orientation[89]. This optical anisotropy corresponds to a large, broadband birefringence[90], wherein the distinct optical index of refraction along each axis leads to a phase delay between polarization states of light. Moreover, mirror-symmetry in the x-z plane forbids intersubband optical transitions along the zigzag axis, and as a result, BP exhibits significant linear dichroism, wherein the material absorption depends strongly on the polarization state of exciting light[84,91].

In this work, we use multiple field-effect device configurations to isolate and characterize three distinct, anisotropic electro-optic effects that allow significant control of the complex refractive index in BP. These effects are Pauli-blocking of intersubband optical transitions, also known as a Burstein-Moss or band-filling effect; the quantum confined Stark effect; and modification of quantum well selection rules by a symmetry-breaking electric field. The resulting response approaches near-unity tunability of the BP oscillator strength for some BP thicknesses and photon energies and tunes along one in-plane crystal axis. As a result, we are able to electrically control dichroism and birefringence in BP. In some cases, we observe tuning of the black phosphorus optical response from highly anisotropic to nearly isotropic. We observe this anisotropic tunability from the visible to mid-infrared (mid-IR) spectral regimes, behavior not seen in traditional electro-optic materials such as graphene[92], transparent conducting oxides[58,93], silicon[67], and quantum wells[94]. This opens up the possibility of realizing novel photonic structures in which linear dichroism in the van der Waals plane can be continuously tuned with low power consumption, because the switching is electrostatic in nature. By controlling optical losses in the propagation plane, for example, efficient in-plane beam steering of surface plasmon polaritons or other guided modes is enabled. Moreover, an electrically tunable polarizer could be realized by modulating the polarization state of light absorbed in a resonant structure containing BP. Because this tunability is strongest at infrared wavelengths, it could also enable control of the polarization state of thermal radiation[95–97].

2.3 EXPERIMENTAL MEASUREMENTS OF THE BLACK PHOSPHORUS OPTICAL RESPONSE WITH AN APPLIED ELECTRIC FIELD

In order to probe and distinguish the electro-optical tuning mechanisms evident in few-layer BP, we used a combination of gating schemes wherein the BP either floats in an applied field or is contacted, as shown in Fig. 2.1a. Samples for infrared measurements were fabricated by mechanically exfoliating few-layer BP onto 285 nm SiO_2/Si in a glove box environment. Contacts of 20 nm Ni/200 nm Au were fabricated by electron beam lithography, electron beam evaporation, and liftoff. A top gate dielectric of 45 nm Al_2O_3 was deposited by atomic layer deposition (ALD) following the technique in Ref. [98], and a semi-transparent top contact of 5 nm Ni was deposited by electron beam evaporation and liftoff. Measurements were performed in a Fourier Transform Infrared Spectrometer coupled to a microscope.

Polarization-dependent optical measurements are taken aligned to the crystal axes, in order to probe the structural anisotropy shown in Fig. 2.1b. This enables us to isolate the contribution of charge-carrier density effects–i.e., a Burstein-Moss shift–and external field-effects–i.e.: the quantum-confined Stark effect and control of forbidden transitions in the infrared–to the tunability of linear dichroism, qualitatively illustrated in Figures 2.1c and 2.1d[36,65,99]. In the anisotropic Burstein-Moss (BM) shift, the optical band gap of the material is changed as a result of band filling and the consequent Pauli-blocking of intersubband transitions. As the carrier concentration of the sample is changed, the Fermi level moves into (out of) the conduction or valence band, resulting in a decrease (increase) of absorptivity due to the disallowing (allowing) of optical transitions[100–102]. Because intersubband optical transitions are only allowed along the armchair axis of BP, this tunability occurs only for light polarized along this axis. In the quantum-confined Stark Effect, the presence of a strong electric field results in the leaking of electron and hole wave functions into the band gap as Airy functions, red-shifting the intersubband transitions energies[77]. In quantum well structures, this red-shifting is manifested for multiple subbands, and therefore can be observed over a wide range of energies above the band gap. To assess the gate-tunable anisotropy of the optical response of BP, the armchair and zigzag axes, illustrated in Fig. 2.1b, of the samples considered are identified by a combination of cross-polarized visible microscopy–where the incident light passes through a linear polarizer, then the sample, and finally through a second,

orthogonal linear polarizer and by rotating the sample, the fast and slow optical axes (and hence crystal axes) are identified[100]–and either polarization-dependent Raman spectroscopy or infrared measurements, described below. Representative Raman spectra are presented for the visible frequency sample on $SrTiO_3$ in Figure 2.1e. The optically active armchair axis exhibits a maximum intensity of the A_g^2 resonant shift at 465 cm^{-1}, whereas this is a minimum for the zigzag axis[103,104].

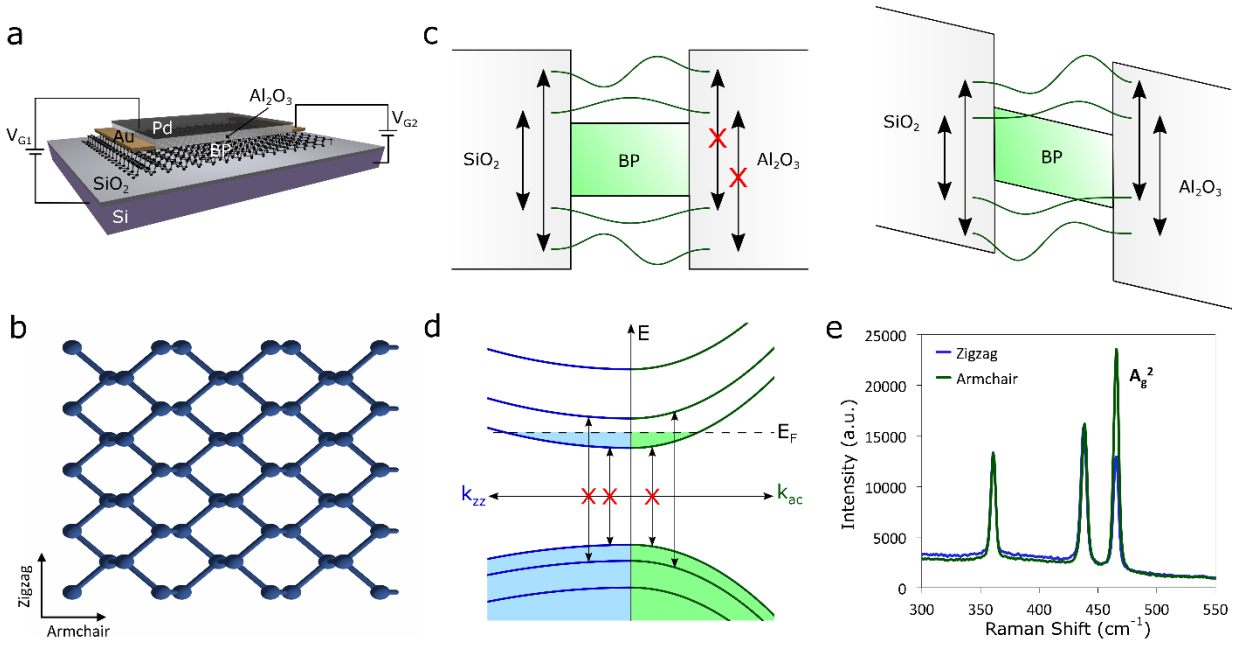

Figure 2.1. Anisotropic electro-optical effects in few-layer BP. Anisotropic electro-optical effects in few-layer BP. (a) Schematic figure of infrared tunability devices. Few-layer BP is mechanically exfoliated on 285 nm SiO_2/Si and then capped with 45 nm Al_2O_3 by ALD. A semitransparent top contact of 5 nm Pd is used to apply field (V_{G1}) while the device floats and 20 nm Ni/200 nm Au contacts are used to gate (V_{G2}) the contacted device. (b) Crystal structure of BP with armchair and zigzag axes indicated. (c) Illustration of two field-driven electro-optical effects: the quantum-confined Stark effect, and symmetry-breaking modification of quantum well selection rules. In the quantum-confined Stark effect, an external field tilts the quantum well energy levels, causing a red-shifting of the intersubband transition energies. In the observed modification of selection rules, this field breaks the symmetry of the quantum well and orthogonality of its wavefunctions, allowing previously forbidden transitions to occur. (d) Illustration of anisotropic Pauli-blocking (Burstein-Moss effect) in BP. Intersubband transitions are blocked due to the filling of the

conduction band. Along the ZZ axis, all optical transitions are disallowed regardless of carrier concentration. (e) Raman spectra with excitation laser polarized along AC and ZZ axes. The strength of the A_g^2 peak is used to identify crystal axes.

2.4 MEASUREMENTS ON A 3.5 NM FLAKE

To illustrate the mechanisms of tunable dichroism of BP in the mid-infrared, we measure tunability of transmittance using Fourier-Transform Infrared (FTIR) microscopy as a function of externally (V_{G1}) or directly applied bias (V_{G2}), presented for a 3.5 nm thick flake, as determined from atomic force microscopy (AFM), in Figure 2.2. Fig. 2.2b presents the raw extinction of the flake along the armchair axis at zero bias, obtained by normalizing the armchair axis extinction to that of the optically inactive zigzag axis. A band edge of approximately 0.53 eV is measured, consistent with a thickness of 3.5nm. A broad, weak shoulder feature is observed at approximately 0.75 eV. The corresponding calculated optical constants for the flake are presented in Figure 2.2c for comparison.

Calculations of the optical constants of BP are based on the formalism developed in Ref.[101]. Optical conductivity σ is calculated using the Kubo formula within an effective low-energy Hamiltonian for different thicknesses. The permittivity is calculated as $\varepsilon(\omega) = \varepsilon_\infty + i\sigma/\omega\delta$ where δ is the thickness of the BP, and the high-frequency permittivity ε_∞ is taken from Ref.[105]. Gate-dependent optical properties used for Figure 2.5 are from Ref.[102].

Figures 2.2d and 2.2e illustrate the influence of an external field on the extinction of BP with carrier concentration held constant (i.e., the BP is left floating). The extinction data for each voltage is normalized to the zero bias case and to the peak BP extinction seen in Figure 2.2b, to obtain a tuning strength percentage that quantifies the observed tunability of the BP oscillator strength. We note that this normalization scheme underestimates the tuning strength away from the band edge, where BP extinction is maximal.

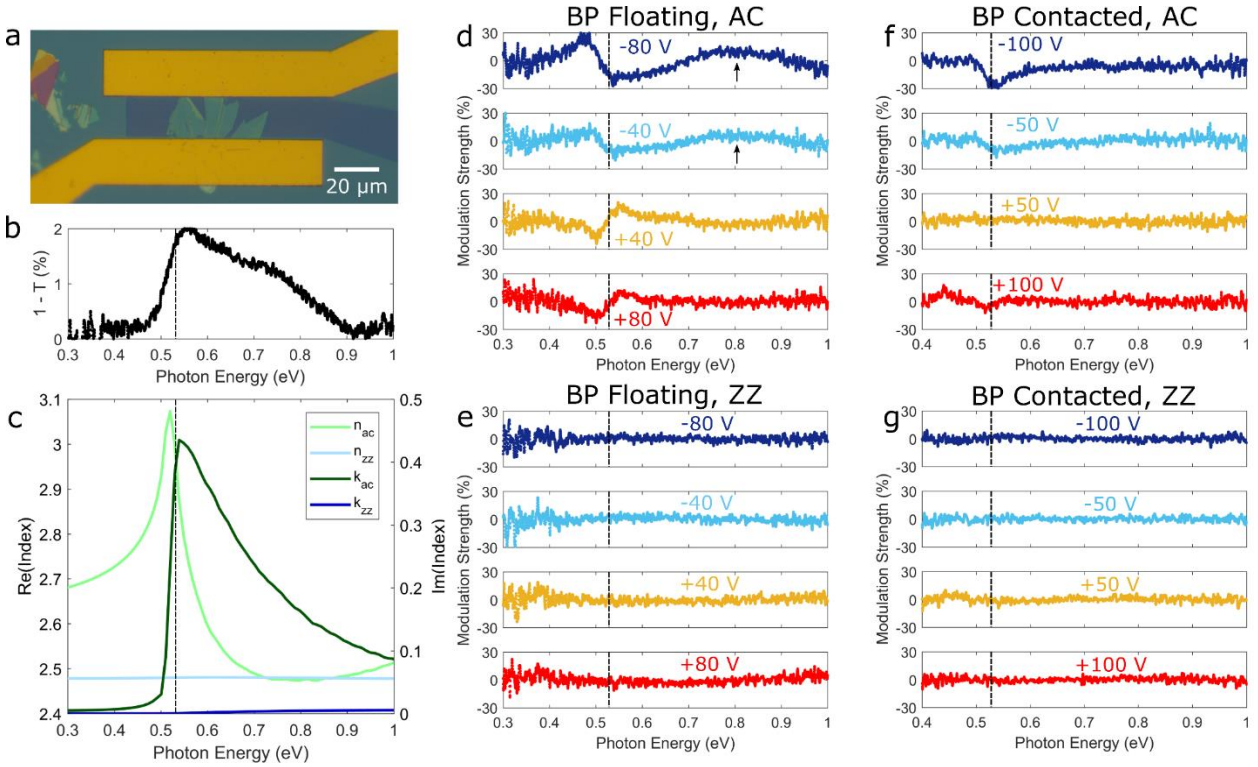

Figure 2.2. Electrically tunable linear dichroism: quantum-confined Stark and Burstein-Moss effects and forbidden transitions. (a) Optical image of fabricated sample; (b) Zero-bias infrared extinction of 3.5 nm flake, polarized along armchair (AC) axis. (c) Calculated index of refraction for 3.5 nm thick BP with a Fermi energy at mid-gap. (d) Tunability of BP oscillator strength with field applied to floating device, for light polarized along the AC axis. (e) Corresponding tunability for light polarized along the zigzag (ZZ) axis. (f) Tunability of BP oscillator strength with gating of contacted device, for light polarized along the AC axis. (g) Corresponding tunability for light polarized along the ZZ axis.

Along the armchair axis, presented in Fig. 2.2d, two tunable features are measured near photon energies of 0.5 and 0.8 eV. We explain the first feature at 0.5 eV as arising from a shifting of the BP band edge due to the quantum-confined Stark effect. At negative bias, the band gap effectively shrinks, and this is manifest as a redistribution of oscillator strength near the band edge to lower energies. As a result, an increase in absorptance is measured below the zero-bias optical band gap,

and a decrease is seen above it. At positive bias, this trend is weakened and reversed. We propose two explanations for this asymmetry: the first is the influence of electrical hysteresis, and the second is the presence of a small internal field in the BP at zero bias, which has been observed in previous works on the infrared optical response of few-layer BP[84].

The second, higher energy feature observed in the measured spectrum does not correspond to any predicted intersubband transition. Rather, we propose it arises due to the modification of quantum well selection rules that limit the allowed intersubband optical transitions in black phosphorus by the applied electric field. In a symmetric quantum well, only transitions between states with equal quantum numbers are allowed, as other states have orthogonal wavefunctions with zero overlap integrals[101]. However, a strong applied field breaks the symmetry of the quantum well and the orthogonality of its wavefunctions, eliminating this selection rule. We note that this feature is present in the 0 V extinction spectrum, consistent with a zero-bias internal field. As the symmetry is further broken with an externally-applied electric field, this transition is strengthened. Under positive bias, the internal and external fields are in competition, resulting in minimal change. This suppressed tunability can also be attributed to hysteresis, as before.

In Figure 2.2e, no tunability is measured for any applied bias for light polarized along the zigzag axis. This can be well understood due to the dependence of the Stark effect on the initial oscillator strength of an optical transition; because no intersubband optical transitions are allowed along this axis, the field effect is weak. Similar behavior has been observed in excitons in ReS_2 based on an optical Stark effect[106]. Moreover, while the externally applied field can allow 'forbidden' transitions along the armchair axis by breaking the out-of-plane symmetry of the quantum well, in-plane symmetry properties and thus the selection rule precluding all zig-zag axis intersubband transitions are unaffected. This selection rule and the corresponding symmetry properties have been previously described[107].

In Figures 2.2f and 2.2g, we present the complementary data set of tunable dichroism measurements due to a directly applied gate bias with electrical contact made to the BP in a standard field-effect transistor (FET) geometry. Here, we observe tunability dominated by carrier concentration effects. At the band gap energy of approximately 0.53 eV, a simple decrease in absorptance is observed at negative and large positive biases, consistent with an ambipolar BM shift. Unlike the results of applying field while the BP floats, no tunability of the forbidden

transition at 0.75 eV is observed; this is explained in part due to the screening of the electric field due to the carrier concentration tunability. We additionally may consider the possibility that this optical transition is disallowed by Pauli-blocking effects, negating the symmetry-breaking effect of the directly applied field. As in the case for the floating BP measurement, no tunability is observed along the zigzag axis.

2.5 MEASUREMENTS ON A 8.5 NM FLAKE

The anisotropic electro-optical effects described above change character rapidly as the BP thickness–and hence band gap and band structure–is varied. Figure 2.3 presents analogous results on a flake of 8.5 nm thickness, determined by AFM, for which an optical image is presented in Fig. 2.3a. Due to the increased thickness, the energy separation between subbands is smaller, resulting in a narrower free-spectral range between absorptance features measured in the zero-bias spectrum, presented in Fig. 2.3b and for which corresponding calculated optical constants are presented in Fig. 2.3c. Results for tunability by an external field with the BP left floating are presented in Fig. 2.3d. As in the thin flake, substantial tuning of the absorptance at each intersubband transition is observed due to the quantum-confined Stark effect (QCSE) red-shifting the energy of the subbands. Due to the large Stark coefficient in BP–which increases with thickness in the few-layer limit–absorption is nearly 100% suppressed, resulting in an approximately isotropic optical response from the material[35,108]. Unlike the previous sample, tuning of forbidden transitions is not apparent; all features correspond to transitions measured in the 0 V normalization scheme as well as the calculated optical constants for a thickness of 8.5 nm. As before, no tuning is seen along the zigzag axis, as shown in Figure 2.4. In Fig. 2.3e, the tunability for directly gated, contacted BP is shown. The observed tuning–a reduction in extinction centered at each of the calculated intersubband transition energies–is relatively weak and does not persist to high photon energies. This suggests that the dominant tunability mechanism is the ambipolar BM shift, rather than the QCSE.

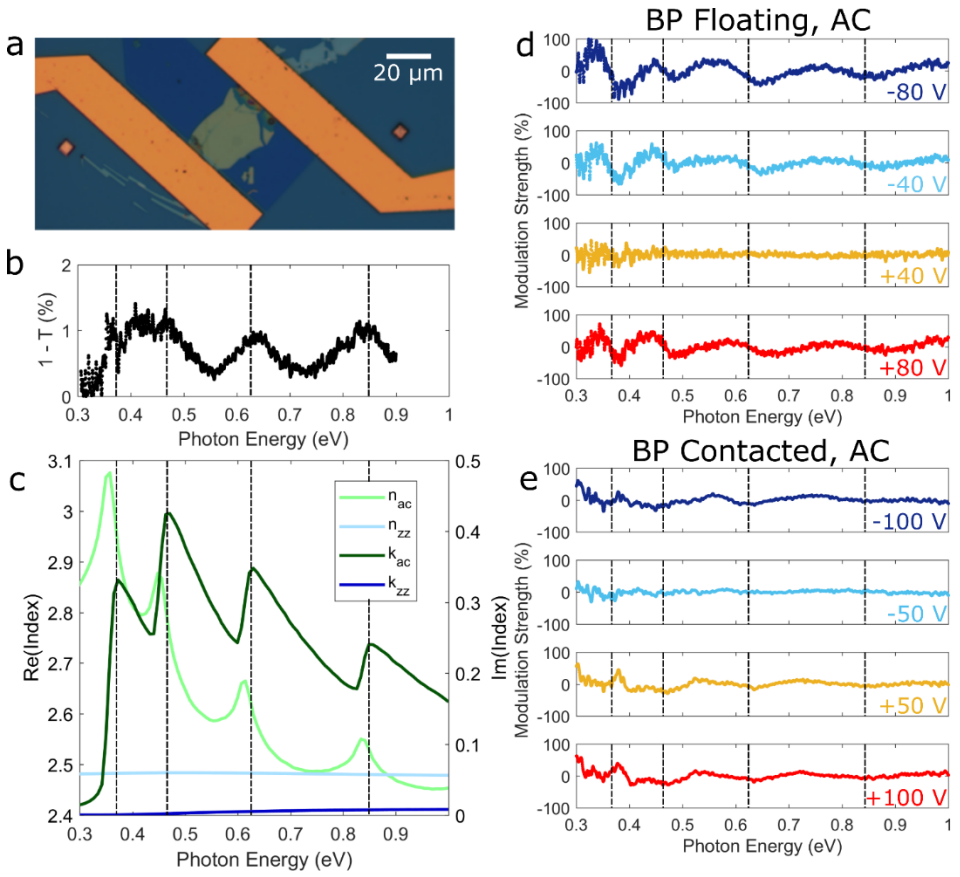

Figure 2.3. Variation of Tunability with BP Thickness. (a) Optical image of fabricated 8.5 nm sample. (b) Zero-bias extinction of 8.5 nm flake, polarized along AC axis. (c) Calculated index of refraction for 8.5 nm thick BP. (d) Tuning of BP oscillator strength with field applied to floating device, for light polarized along the AC axis. (e) Tuning of BP oscillator strength with gating of contacted device, for light polarized along the AC axis.

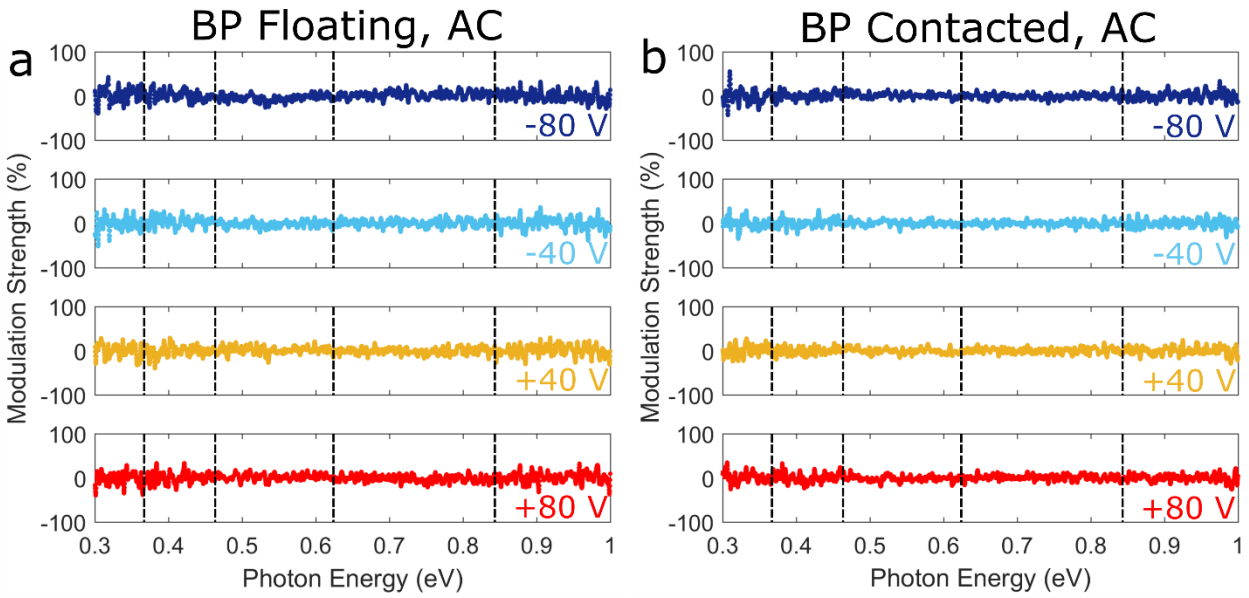

Figure 2.4. Tunability for 8.5 nm Flake along Zigzag Axis. (a) Tunability of BP oscillator strength with field applied to floating device, for light polarized along the ZZ axis. (b) Tunability of BP oscillator strength with gating of contacted device, for light polarized along the ZZ axis.

Additional measurements at lower energies are presented in Figure 2.5.

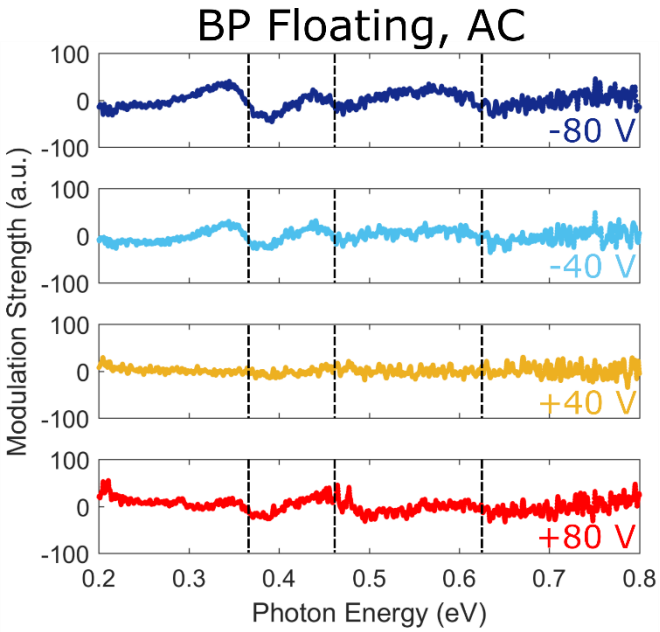

Figure 2.5. Tunability for 8.5 nm Flake at Lower Energies. Tunability of BP oscillator strength with field applied to floating device, for light polarized along the ZZ axis, measured at lower photon energies.

2.6 VISIBLE FREQUENCY MODULATION

In Figure 2.6, we present results of gate-tunable dichroism at visible frequencies in a 20 nm thick flake, comparable to those considered for infrared tunability. A new device geometry is used to enable transmission of visible light, shown schematically in Fig. 2.6a and in an optical image in Fig. 2.6b. In this configuration, a $SrTiO_3$ substrate is utilized to allow transmission-mode measurements at visible wavelengths. A symmetric gating scheme is devised based on semi-transparent top and back gate electrodes of 5 nm Ni. Samples for visible measurements were fabricated by depositing a 5 nm thick semi-transparent back contact of Ni, followed by 45 nm Al_2O_3 by ALD on a 0.5 mm thick $SrTiO_3$ substrate. Few-layer BP was then mechanically exfoliated and electrical contacts were fabricated as above. Measurements are performed in a visible spectrometer. Nickel was selected as the optimum metallic contact through Finite-Difference Time Domain simulations. Only an applied field, floating BP measurement is utilized, as band-filling effects should be negligible at this energy range. In Fig. 2.6c, we present tunability results from 1.3 to 2 eV. Due to the QCSE, tunability is observed up to 1.8 eV, corresponding to red light. Thus, we demonstrate that electro-optic tuning of linear dichroism is possible across an

extraordinarily wide range of wavelengths in a single material system, enabling multifunctional photonic devices with broadband operation.

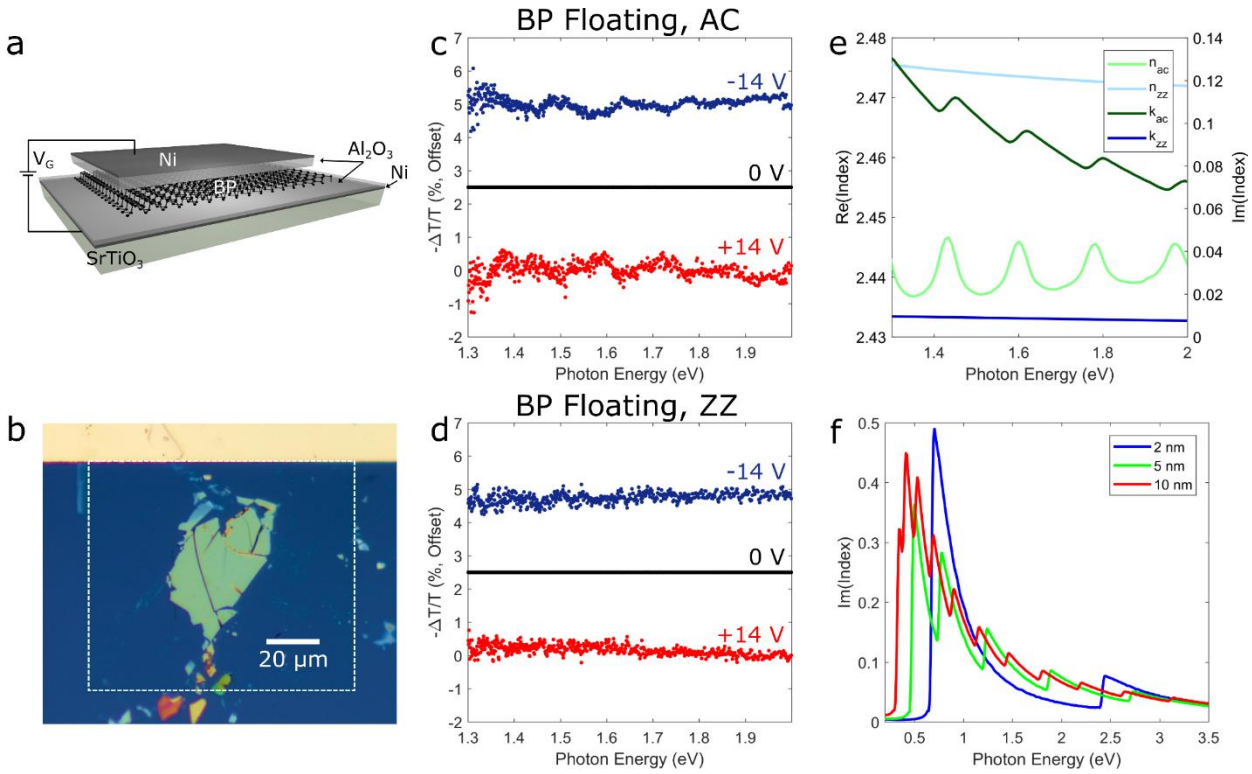

Figure 2.6. Tunability in the Visible. (a) Schematic figure of visible tuning device. Few-layer BP is mechanically exfoliated on 45 nm Al_2O_3/5 nm Ni on $SrTiO_3$ and then coated with 45 nm Al_2O_3. A 5 nm thick semitransparent Ni top contact is used. (b) Optical image of fabricated sample with 20 nm thick BP. Dashed white line indicates the boundary of the top Ni contact. (c) Tuning of extinction with field applied to floating device, for light polarized along the AC axis. (d) Corresponding tuning for light polarized along the ZZ axis. (e) Calculated index of refraction for 20 nm thick BP for the measured energies. (f) Calculated imaginary index of refraction of several thicknesses of BP from the infrared to visible.

The decay of BP intersubband oscillator strength at higher photon energies provides a spectral cutoff for QCSE-based tunability, but for 5 nm BP or thinner this oscillator strength is strong through the entire visible regime, as illustrated in Fig. 2.6f. We thus suggest that in very thin BP,

strong tuning of absorption and dichroism is possible to even higher energies. By selecting a flake of 2 nm, for example, tunable linear dichroism is possible up to 3 eV from the band gap energy of 0.75 eV. A higher density of features, beginning at lower energies, may be introduced by utilizing a thicker flake, with slightly decreased tuning strength, as seen for 5 and 10 nm thickness flakes. We also note that by substituting graphene top and bottom contacts or utilizing nanophotonic techniques to focus light on the BP, higher absolute tuning strength could be easily realized.

This phenomenon is in stark contrast to the gate-tunability of the optical response of other 2D materials, where substantial tunability is typically constrained to the narrowband energy of the primary exciton, as in MoS_2 and WS_2[26,73]. In another van der Waals materials system, monolayer graphene, tunability is accessible over a broader wavelength range due to the Pauli-blocking of optical transitions at $2E_F$; however, this is limited to the range over which electrostatic gating is effective, typically between $E_F \sim 0$ to $E_F \sim 0.5$ eV[44,74]. Moreover, these materials are not dichroic or birefringent in-plane, and so BP offers a novel phenomenon that can be taken advantage of to realize previously challenging or impossible photonic devices. The same restriction is true of bulk tunable materials such as quantum wells, transparent conducting oxides, and transition metal nitrides.

2.7 CONCLUSIONS

In summary, we have observed and isolated three competing, anisotropic electro-optical effects in few-layer black phosphorus: the Pauli-blocking of intersubband transitions (Burstein-Moss effect), the quantum-confined Stark effect, and the modification of quantum well selection rules by a symmetry breaking electric field. These effects, which produce near-unity changes in the black phosphorus oscillator strength for some material thicknesses and photon energies, can be tuned to a broad range of frequencies, from the mid infrared to the visible, by controlling the thickness and thus band structure of the black phosphorus. Further, these are strongly anisotropic electro-optical effects, and we thus observe them to allow electrical control of both linear dichroism and birefringence. We observe that absorption in BP can be tuned from anisotropic to nearly isotropic. We suggest that these phenomena and this material are a promising platform for controlling the in-plane propagation of surface or waveguide modes, as well as for polarization-switching, phase and amplitude control, and reconfigurable far-field metasurfaces. As with van der Waals materials as a whole, few layer black phosphorus provides a route not only to an improved material platform

for optoelectronics, but also to new physics, and the potential new technology paradigms that follow.

Chapter 3. INTRABAND EXCITATIONS IN MULTILAYER BLACK PHOSPHORUS

3.1 ABSTRACT

Black phosphorus (BP) offers considerable promise for infrared and visible photonics. Efficient tuning of the bandgap and higher subbands in BP by modulation of the Fermi level or application of vertical electric fields has been previously demonstrated, allowing electrical control of its above bandgap optical properties. Here, we report modulation of the optical conductivity below the band-gap (5-15 μm) by tuning the charge density in a two-dimensional electron gas (2DEG) induced in BP, thereby modifying its free carrier dominated intraband response. With a moderate doping density of $7x10^{12}$ cm^{-2} we were able to observe a polarization dependent epsilon-near-zero behavior in the dielectric permittivity of BP. The intraband polarization sensitivity is intimately linked to the difference in effective fermionic masses along the two crystallographic directions, as confirmed by our measurements. Our results suggest the potential of multilayer BP to allow new optical functions for emerging photonics applications.

3.2 INTRODUCTION

Hyperbolic photonic materials, in which the dielectric permittivities associated with different polarization directions have opposite signs, present a unique platform to engineer extremely strong anisotropic light-matter interactions and tailor novel topological properties of light[109,110]. They can enable a wide range of phenomena such as near field enhancement and modification of the local density of states of emitters[111], negative refraction[112], hyperlensing[113], super-Planckian thermal emission[114], sub diffraction light confinement[115], canalization of incident energy[47], and more. Such a wide range of novel functionalities are achieved easily with a relatively new class of materials known as epsilon-near-zero (ENZ) materials[116,117]. In addition to passive artificial metamaterial ENZ-based structures based on periodically arranged metal-dielectric stacks[118], hyperbolic dispersion has also been explored for a wide range of natural materials such as graphite, h-BN, WTe_2 in different spectral ranges [46,51,119]. Despite many advances in the ability to engineer ENZ or hyperbolic metamaterials, the idea of an electrically or optically tunable on-demand hyperbolic

material still remains experimentally fairly unexplored and is highly attractive for study of fundamental phenomena such as achieving active control of optical topological transitions, as well as applications in optical information processing and switching, and other functions[51,119].

Two-dimensional electron gases (2DEG) in atomically thin materials with strong electro-optic susceptibility offer an ideal platform to achieve highly tunable light-matter interactions[42,43,120,121]. These systems have established critical metrological standards in the field of condensed matter physics (such as the fine structure constant[122] and conductance quanta[123]) and have contributed to advances in photonics[124–126]. Black phosphorus (BP), among other two-dimensional materials, has been heavily explored as an electronic platform for high mobility 2DEG[127–132], and while first principle calculations have been performed for undoped BP[133], very little is known experimentally about its optical properties and their tunability. Bulk BP crystal has a puckered structure, as shown in Fig. 3.1(A), and possesses an anisotropic direct bandgap that is known to dramatically increase from 0.3eV to 2eV as the atomically thin limit (monolayer) is reached[134,135]. In addition, the highly anisotropic band structure and optical properties of BP are extremely susceptible to perturbations in the local dielectric environment[136], temperature[137], electron/hole concentration in the 2DEG in BP[138], electric or magnetic field[139,140], strain[38,39], etc. While monolayer and few-layer BP can exhibit strong light-matter interactions by virtue of excitonic resonances in the visible-near infrared (IR)[23,141], multilayer BP holds more potential in the mid-IR because of its lower bandgap and stronger Drude weight[142]. Quantum well electro-optic effects and its anisotropy near the band-edge have been studied recently in some detail in multilayer BP[143–146]. However, absorption below the optical gap, which should be dominated by free carriers in the 2DEG, is still experimentally poorly understood and has only been investigated theoretically so far[47,133]. The free-carrier response of doped BP films can persist up to mid-infrared frequencies and can be approximated to first order by a Drude model[50,147]. Similar behavior has been observed in graphene[148], but has not been experimentally explored in BP. Knowledge about the charge dynamics can provide us with an understanding of how quasiparticles in BP respond to infrared electromagnetic radiation, and the exact nature of their respective scattering and damping processes. A comprehensive understanding of the polarization-dependent, mid-IR optical properties of BP may facilitate the development of BP-based photonic devices, which hold promise for novel optoelectronic functions in emerging technology applications.

In this work, we report a comprehensive study of the optical conductivity of a 2DEG induced in multilayer BP for different hole and electron densities by performing reflection spectroscopy. Modulation of reflection was observed both above and below the BP band edge. While changes near or above the optical gap can be understood from an interplay of different electro-optic effects in BP (such as Pauli blocking, quantum confined Stark effect, etc.) and modelled using the Kubo formalism, modulation below the band gap is attributed primarily to changes in the intraband optical conductivity which has a Drude like frequency response ($\sigma = \frac{iD}{\pi(\omega+i\Gamma)}$). We measured the Drude weight (D) evolution and thus the change in the optical conductivity as a function of electron/hole concentration in the 2DEG. As predicted by theory, we observed anisotropy of the polarization resolved Drude response due to the difference in the effective mass of carriers along the two principal crystal axes. Changes in the intraband absorption imply a transfer of the spectral weight from the interband transitions, thereby preserving the oscillator f-sum rule for solid-state systems, $\int_0^\infty \Delta\sigma'(\omega)d\omega = 0$. Finally, from the extracted complex polarized dielectric function for BP below the band-edge, we were able to identify an epsilon near zero (ENZ) like regime along the armchair (AC) direction and hence, a transition from dielectric to metallic like response. No such transition was seen for the zigzag (ZZ) direction, confirming that doped multilayer BP is indeed an ideal system to host plasmons with tunable in-plane hyperbolic dispersion in the mid-IR. Furthermore, our results indicate a possible gate tunable optical topological transition for TM polarized light from hyperbolic to elliptical, which suggests interesting opportunities for multilayer BP in mid-IR photonic applications[149].

3.3 OPTICAL AND ELECTRICAL CHARACTERIZATION OF MULTILAYER BP FIELD EFFECT HETEROSTRUCTURE

We employed Fourier-transform infrared micro-spectroscopy to measure reflection spectra of multilayer BP structures. A typical field effect heterostructure, schematically illustrated in side view in Fig. 3.1(B), constructed using van der Waals assembly technique is shown in Fig. 3.1(C), where the BP is 18.7 nm, and the top and bottom h-BN are 36.8 nm and 36.4 nm, respectively. The carrier density in BP was tuned by applying a gate voltage across the bottom hBN and SiO_2 (285nm). Such a geometry allowed independent electrical and optical characterization of the induced 2DEG in BP. Polarized Raman spectroscopy was used to identify the AC and ZZ axes of

BP as indicated in the optical image of the device. All optical and electrical measurements were performed in ambient at room temperature.

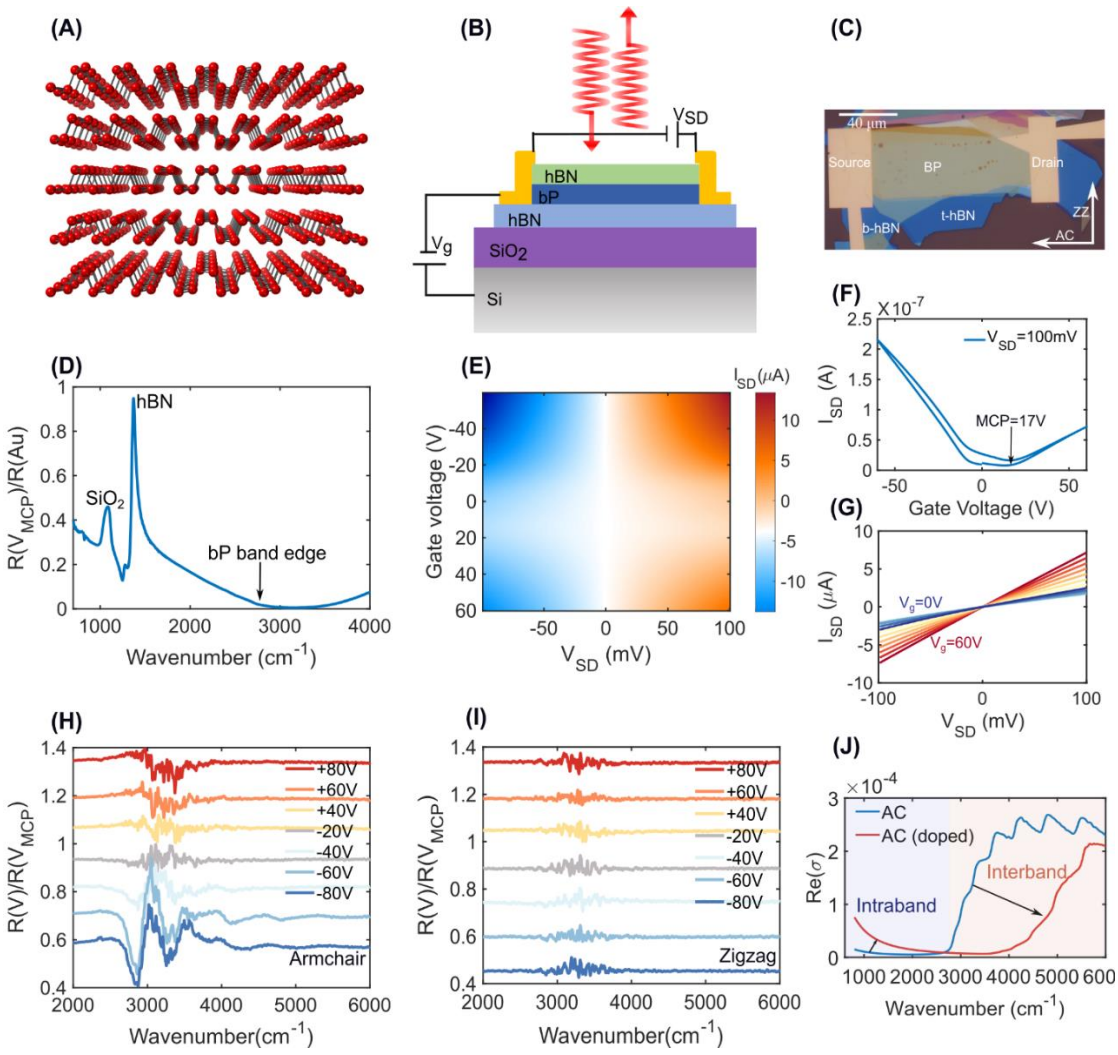

Figure 3.1. Device schematic and electro-optic characterization. (A) Anisotropic puckered crystal structure of BP (P atoms are in sp^3 hybridization). (B) Device schematic and measurement scheme for hBN encapsulated BP devices. (C) Optical microscope image of the device discussed in the main text. (D) Normalized reflection spectrum from the BP device shown in (C). (E) Color-map of source-drain current variation as a function of both gate voltage and source-drain bias. (F) Gate voltage modulated source-drain current at one representative source-drain voltage (100mV). (G) Variation of source-drain current with source-drain voltage showing linear conduction with systematic increase as gate voltage increases on the positive side, the slight dip is due to the fact

that the MCP is not at 0V). (H), (I) Interband optical modulation along the AC and ZZ axis, respectively, showing the anisotropy in the electro-optic effects. (J) Schematic of changes in the AC axis optical conductivity (real part) upon doping.

The reflection spectrum, shown in Fig. 3.1(D), for the same device was measured at the minimal conductance point (MCP), confirmed from two-terminal electrical measurements as shown in Fig. 3.1(E)-(G), with light polarized along the AC direction. This spectrum is normalized to that of optically thick Au (approx. 500 nm) evaporated on the same sample as a reference surface. Three prominent features dominate the spectrum–a narrow hBN phonon around 1370 cm^{-1}, a broad dominant SiO_2 phonon around 1100 cm^{-1} (recent studies[42] show multiple phonon contributions in SiO_2) and the beginning of band edge absorption around 3000 cm^{-1} convoluted with an interference dip coming from the entire stack. Additionally, from our transport measurements, a hole mobility of 1107 $cm^2/V.s$ and an electron mobility of 412 $cm^2/V.s$ were obtained at low doping levels, corresponding to scattering rates on the order of approximately 5-10 meV. As shown in Figs. 3.1(H) and 3.1(I), these reflection spectra can be heavily modified under positive or negative gate voltages.

Modelling the optical conductivity of the BP electron/hole gas allows us to gain an understanding of the quasiparticle dynamics under applied voltage. Our BP flakes are between 10-20 nm thick and described by a sheet conductivity σ since the effective modulation is confined to only 2-3nm from the interface of BP/b-hBN. The thickness of this modulated region was estimated from the results of band bending calculations, using a Thomas-Fermi model[143]. This sheet conductivity has contributions from both interband and intraband processes, given as $\sigma = \sigma_{interband} + \sigma_{intraband} = \sigma_1(\omega) + i\sigma_2(\omega)$. The interband contribution accounts for absorption above the band-edge, including all subbands, while the intraband part accounts for free carrier response. One can explicitly calculate for optical conductivity using the Kubo formalism as follows[50]:

$$\sigma_{interband} = -i\frac{g_s\hbar e^2}{(2\pi)^2}\sum_{ss'jj'}\int dk\ \frac{f(E_{sjk})-f(E_{s'j'k'})}{E_{sjk}-E_{s'j'k'}} * \frac{\langle\phi_{sjk}|\widehat{v_\alpha}|\phi_{s'j'k'}\rangle\langle\phi_{s'j'k'}|\widehat{v_\beta}|\phi_{sjk}\rangle}{E_{sjk}-E_{s'j'k'}+\hbar\omega+i\eta}$$

(3.E1)

$$\sigma_{intraband,j} = \frac{iD_j}{\pi\left(\omega + \frac{i\eta}{\hbar}\right)}, D_j = \pi e^2 \sum_{i=1}^{N} \frac{n_i}{m^*_{i,j}}$$

(3.E2)

Here, $\hat{v}_{\alpha,\beta}$ is the velocity operator defined as $\hbar^{-1}\partial_{k\alpha,\beta}H$, $g_s = 2$ is used to denote the spin degeneracy, f(E) is the Fermi-Dirac distribution function; the indices s(s′) refer to conduction (valence) bands and the indices j(j′) refer to the subbands. H is the low-energy in-plane Hamiltonian around the Γ point, E_{sjk}, ϕ_{sjk} are the eigen-energies and eigenfunctions of H; $m^*_{i,j}$ represents the effective mass of carriers in each subband (i) along a specific crystal orientation j, n_i represents the charge density in each subband and η is a phenomenological damping term.

Electrostatic doping of BP primarily brings about two fundamental changes in the optical response: the emergence of a strong intraband component in the mid to far infrared and a shift of the optical gap (interband transitions), shown schematically in Fig. 3.1(J). A combination of multiple electro-optical effects at the band-edge has been shown to explain the observed modulation, discussed next, also summarized in Fig. 3.2.

1. Pauli blocking/Burstein Moss shift

The fermionic nature of electrons and holes in a semiconductor dictates that optical transitions between occupied states in the valence band and unoccupied states in the conduction band are blocked if the electron states at the same energy and momentum are already filled, leading to reduced absorption. This effect is known as Pauli blocking/Burstein Moss shift. Additionally, since BP has a quantum well electronic band structure, characteristic absorption dips are seen for different subbands as they are filled with increasing doping.

2. Quantum confined Stark effect

When a quantum well is subjected to an external electric field, the electron states shift to lower energies and the hole states to higher energies thereby reducing the effective optical bandgap. Additionally, electrons and holes shift to the opposite sides of the well reducing the overlap integral which reduces the oscillator strength of each transition.

3. Forbidden transitions / 'mixed' transition

In an unperturbed quantum well system, certain transitions have allowed dipole transitions and optical matrix elements which do not vanish. From symmetry arguments those transitions happen to be between subbands of equal principal quantum number index (j=1 VB to j=1 CB, etc.). However, upon the application of an external electric field, modification of the overlap integral between electrons and holes causes the previously vanishing optical transitions to be allowed and they appear as mixed transitions.

4. Band bending

In multilayer systems for a typical field effect heterostructure geometry, a degenerate charge gas is induced at the interface of the active material and the gate dielectric; in our case, the BP/b-hBN interface. However, the charge is not distributed equally in the out of plane direction because the first layer of charge screens the remaining charges. This gives rise to a thickness-dependent charge profile approximated by the Thomas-Fermi screening model. For BP it can be seen from calculations for a charge density of about 5-7x10^{12}/cm^2 the effective channel thickness is about 2.9 nm- meaning the induced electron/hole gas is two-dimensional in nature and not three-dimensional. In all our fitting routines, it is assumed this is the case, and a sheet conductivity for the 2DEG is used (with a static dielectric constant as a background for the whole BP).

To summarize, we explain our observation in Figs. 3.1(H) and (I) as follows. As we dope the system with electrons, we see a suppression of absorption along the AC direction (appearing as a dip) due to Pauli blocking which increases with applied voltage. Higher lying features such as subbands show very weak modulation. Additionally, a mild red shift of the band edge is seen at the highest positive voltages indicative of a Stark shift. However, on the hole side, not only do we see a strong dip at the onset of band-edge transition and at the subband energies we also see a stronger red-shift of the band gap due to a more dominant Stark shift. The band-edge shifts to about 2800 cm^{-1} which is ~30meV below the pristine gap on the hole side, and to about 2900 cm^{-1} which is ~15meV below the optical gap on the electron side. This asymmetry in the Stark shift might be from impurities/residual doping in the system causing an additional field which cancels out in the electron doped case but adds up in the hole doped case. These impurities could also be

causing the reduction of prominent subband oscillations on the electron side. Further nanoscale studies would be needed to elucidate more about the underlying mechanism. The noisy weak modulation for ZZ around 3000 cm^{-1} arises from the fact that the interference dip of the entire stack in our device (which also happens serendipitously to be around the same energy as the band-edge) results in low signal.

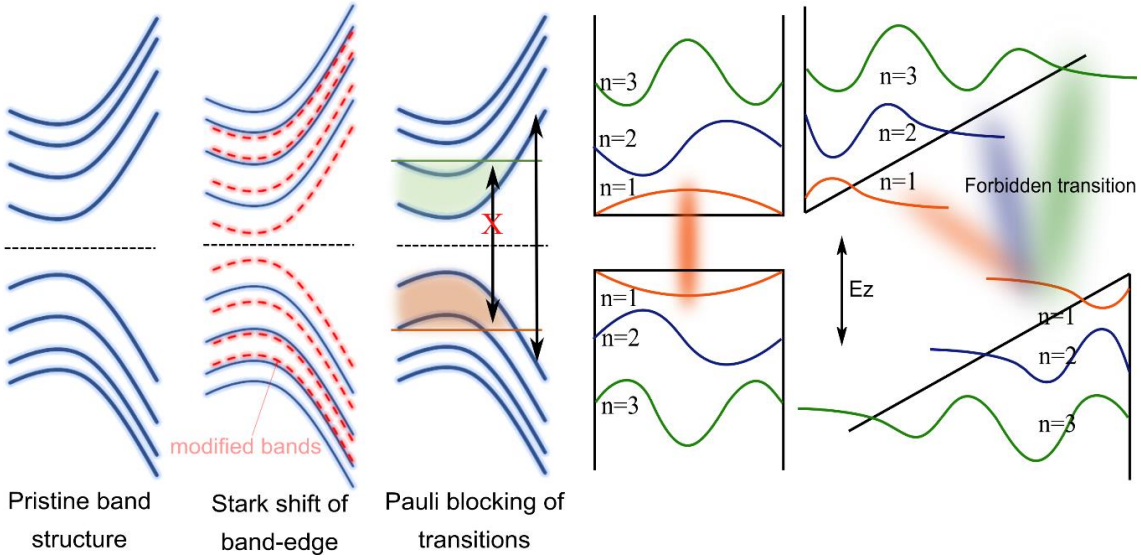

Figure 3.2. Quantum Well electro-optic effects. Schematic of different electro-optic effects occurring at energies near and above the band-edge of a multilayer BP thin film.

All of the observed reflection modulation spectra exhibit strong anisotropy with respect to the BP crystal axes under AC and ZZ polarized illumination. This strong anisotropy is predicted by theory, and results from the puckered honeycomb lattice crystal structure of phosphorene[150]. Our results in Figs. 3.1(H) and 3.1(I) indicate significant optical modulation in the 2DEG and are in excellent agreement with results from previous studies[23,141–143].

3.4 LOW ENERGY DOPING DEPENDENT INTRABAND RESPONSE IN MULTILAYER BP

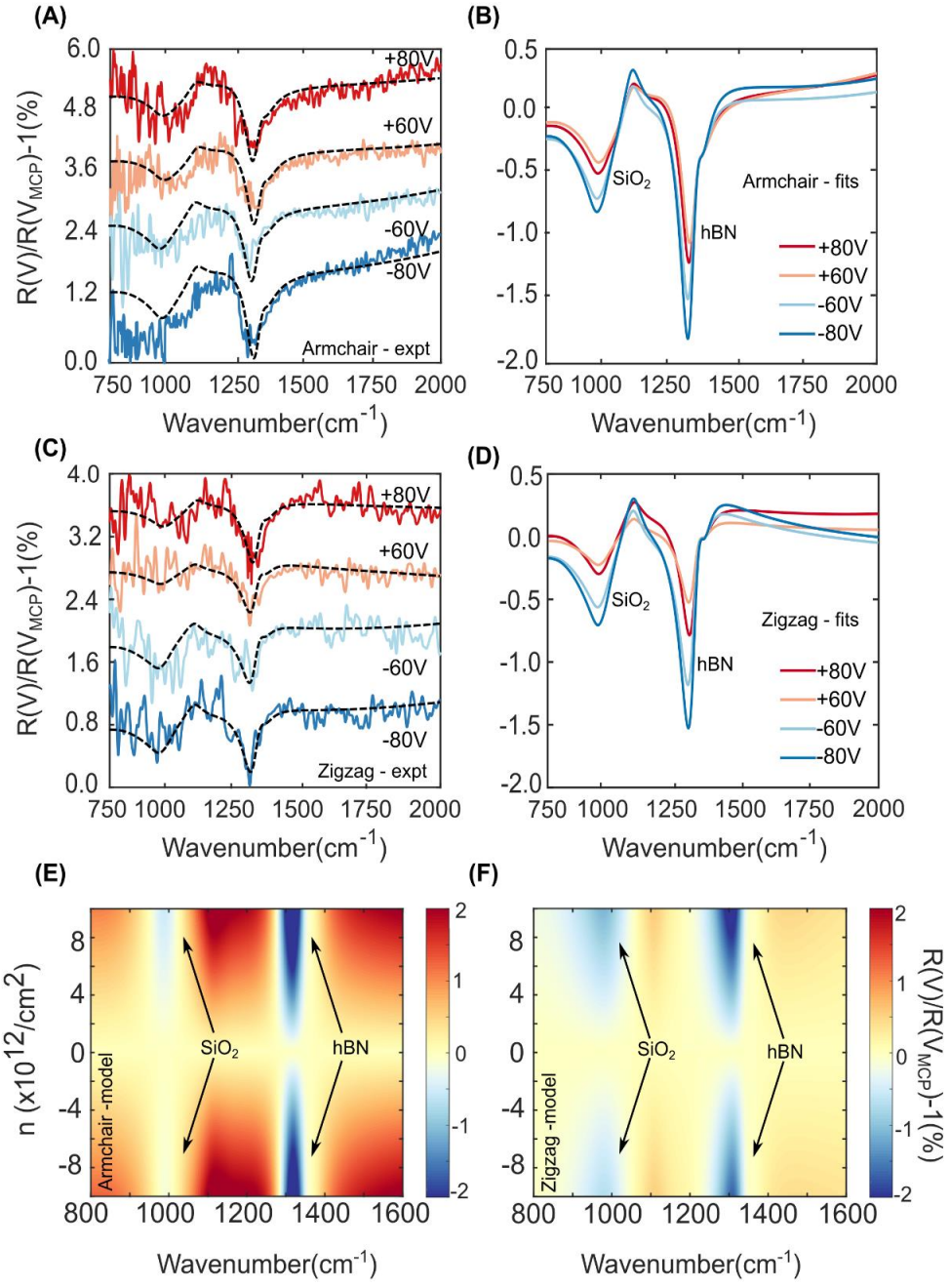

Figure 3.3. Intraband response dominated reflection modulation. (A), (C) Measured (colored lines) and simulated/fit (black lines) intraband response mediated reflection modulation along the AC

and ZZ axis. The fits have been performed between 750-2000 cm^{-1} to eliminate any band-edge effect influence on the optical conductivity so that the Drude model suffices. (B), (D) Fits shown separately, without offset showing a narrowing and strengthening of the Fano-like response near the hBN and SiO_2 phonons with increasing charge density in BP. (E), (F) Modelled false color plot of modulation in reflection spectra (zoomed in between 800 and 1600 cm^{-1}) as a function of doping density for the AC and ZZ direction assuming the following parameters : BP $m_{eff}=0.14m_0$ (AC), $0.71m_0$(ZZ), Si $m_{eff}=0.26m_0$ (electrons), $0.386m_0$ (holes).

We now turn our attention to the low photon energy regime, which is dominated by the intraband conductivity of BP. Fig. 3.3 describes this response, the understanding of which is a central result of this paper. Figs. 3.3(A) and (B) show reflectance spectra (normalized as before) for light polarized along the AC and ZZ axes, respectively. Both electron and hole doping can modify the free carrier response of the 2DEG. As doping increases, a strong spectral feature is observed to appear around the characteristic hBN (~1360 cm^{-1}) and SiO_2 (~1100 cm^{-1}) intrinsic phonon peaks with both electron and hole doping. We propose that this feature results from an increase in the free carrier density, which increases the Drude conductivity and thus modifies the optical properties of BP. This broad intraband modulation interferes with the previously described hBN/SiO_2 phonons, giving rise to an absorption line shape with a Fano-like modulation in the hBN/SiO_2 phonon regime. We hypothesize that this asymmetric Fano-like resonance shape[151,152] indicates optical coupling between the narrow phonon resonances and the weak free carrier absorption continuum. To better understand the nature of the line shape, we performed thin film transfer matrix calculations to fit the spectra and account for multiple reflections and interferences in the heterostructure stack. Our model incorporates a Drude-like function for the intraband optical conductivity of the BP 2DEG, given by equation (3.E2), with which we are able to extract the Drude weight as a function of doping. Assuming a simple parallel plate capacitor model, we can estimate the doping density at each gate voltage. For undoped BP we assume a charge density of $10^{11}/cm^2$ to account for the finite MCP response (coming from any defects or trapped charges). The contribution to the linewidth of the imaginary component of Drude conductivity from dephasing associated with finite scattering times was assumed to be on the order of that obtained from DC transport measurements (approx. 5 meV) which is a valid approximation in the energy

ranges considered here. The possible sources of scattering include electron-phonon coupling, electron-electron repulsion and interaction with defects and impurities. Studies have shown that crystals of layered materials on substrates with strong phonons can also show losses from electron-surface polar phonon coupling[153]. There have also been reports of DC transport mobilities which are not well correlated with optical scattering times, or which even show an anti-correlation[154]. Further fundamental spectroscopic studies at far-IR (THz) frequencies will be required to further elucidate these low energy scattering mechanisms in BP as a function of doping and temperature. Figs. 3.3(C) and (D) summarize the fitted results without any offset to better understand the impact of doping on the lineshape of reflectance modulation. Excellent agreement between experimental data and transfer matrix simulations is visible in Figs. 3.3(A) and (B), which indicates that the intraband (Drude) model suffices to explain the reflectance modulation observed at photon energies well below the band-edge. Figs. 3.3(E) and 3.3(F) also show in false colors the changes in the reflection modulation for AC and ZZ polarization as a function of electron/hole doping density assuming a constant effective mass for BP. Reflection/transmission in highly sub-wavelength BP films is mostly dominated by the losses in the material and thus, it is important to note that we do not incorporate the interband region in our Drude modelling of the sub-bandgap response because we are working much below the (even the Stark shifted) band-gap, where the influence of interband losses is almost negligible to first order. Similar assumptions have been experimentally validated for studies on graphene[148,155]. Also, it should be noted that while the interband anisotropy is primarily governed by the parity of wavefunctions and subsequent selection rules coming from dipole matrix elements in BP, intraband anisotropy stems from the difference in fermionic effective mass along the two crystallographic axes.

3.5 MEASUREMENT OF THE MULTILAYER BP COMPLEX PERMITTIVITY AND TUNABLE EPSILON-NEAR-ZERO AND HYPERBOLICITY

Figures 3.4(A)-(D) illustrate the experimental real and imaginary parts (denoted as ϵ_1 and ϵ_2), of the dielectric function (obtained as $\epsilon_{AC/ZZ}(\omega) = \epsilon_{\infty AC/ZZ} + \frac{i\sigma_{AC/ZZ}(\omega)}{t\epsilon_0\omega}$, where t = thickness of the 2DEG (2.9nm), $\epsilon_{\infty AC/ZZ}$ accounts for oscillators not captured in our "Drude" spectral window) for BP at different doping densities under polarized excitation conditions along

the AC and ZZ directions. At higher energies the dielectric function is dominated by subband transitions whose oscillator strength diminishes upon doping primarily due to Pauli blocking, along with the aforementioned electro-optic effects. The lower energy response is mostly dominated by free carriers.

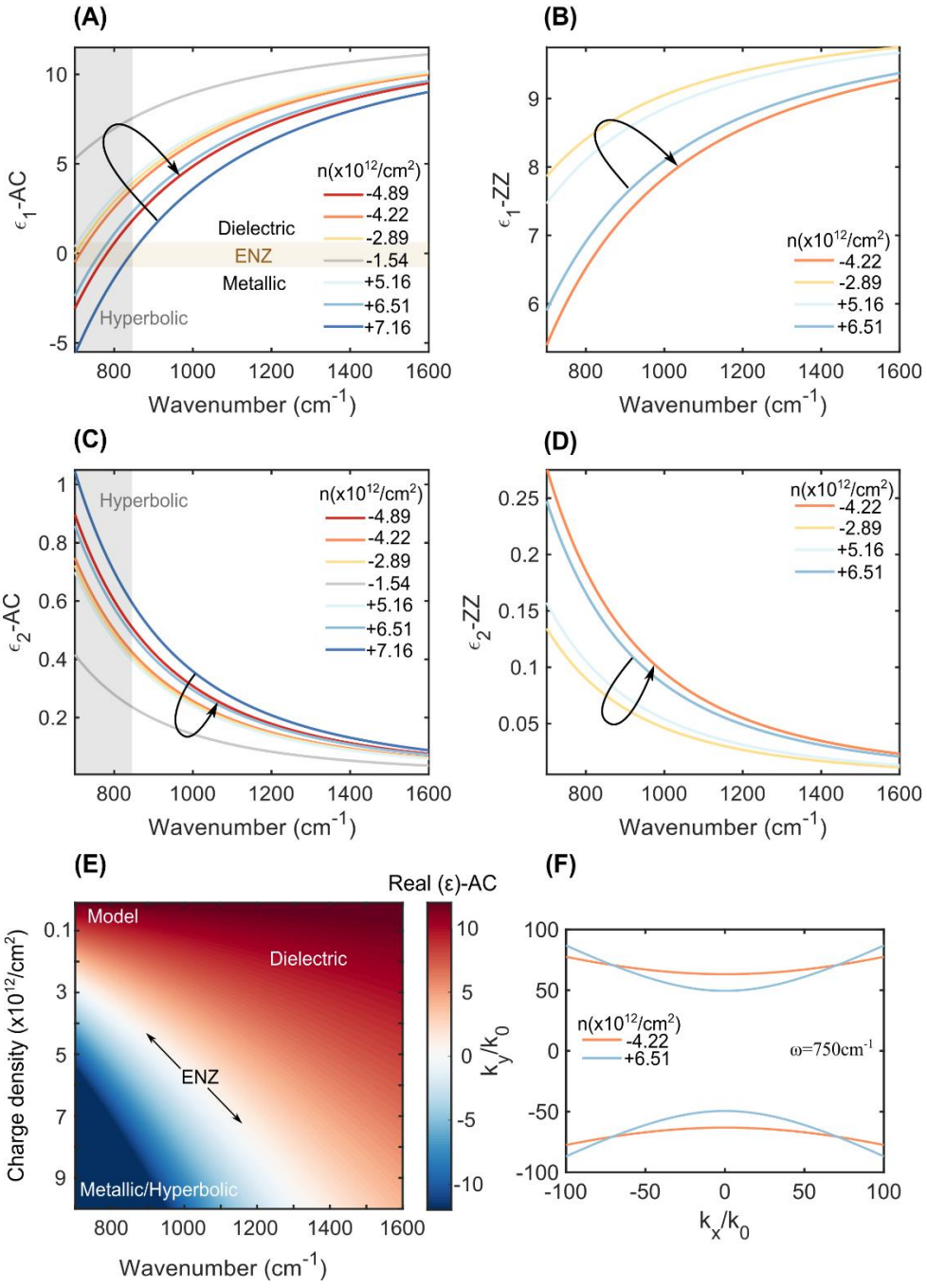

Figure 3.4. Modelled dielectric function and tunable hyperbolicity. (A), (C) Extracted real and imaginary part (denoted as ϵ_1 and ϵ_2) of the dielectric function for BP 2DEG along the Armchair

axis for different doping densities. The orange shaded region shows the ENZ behavior. The region where the real part of the permittivity along the AC axis goes negative while remaining positive for the ZZ direction is the hyperbolic region and extends to frequencies beyond our measurement window. (B), (D) The same for the Zigzag axis. (E) False color plot of the modelled real part of the dielectric permittivity along the AC direction assuming BP $m_{eff}=0.14m_0$ showing the tunability of ENZ. (F) Calculated isofrequency contours for in-plane plasmonic dispersion (TM polarized surface modes) showing the tunability of hyperbolicity.

We observe a strong modulation of the dielectric function below the band gap with doping density, indicating that free carrier response is a significant effect in the mid-IR range. An important finding of our study is the appearance of an epsilon near zero region (ENZ) in BP for higher gate voltages / charge densities along the AC direction, where the real part of the permittivity transitions from positive to negative. A false color plot showing the variation of the modelled real part of the dielectric permittivity with doping density along the AC direction is shown in Fig. 3.4(E). The ENZ region is seen to systematically shift to higher photon energies with increased doping. Here the effective mass of BP is assumed to be $0.14m_0$, independent of doping density, for the sake of simplicity. No such negative permittivity region was identified for the ZZ direction measurements, implying extreme bianisotropy and the possibility to generate surface plasmon modes and in-plane hyperbolic photonic dispersion in BP. We further calculate the isofrequency contours for in-plane plasmons (TM polarized surface modes)[117] for two different doping densities (one on the electron side and one on the hole side) at 750 cm^{-1} to show that the hyperbolic dispersion is electrically tunable. Electrically tunable hyperbolic dispersion, illustrated in Fig. 3.4(F) has intriguing implications, suggesting opportunities for active hyperbolic plasmonics and photonics. We note that the doping density achieved here is modest (~$7x10^{12}$ cm^{-2}), and higher doping densities with larger κ dielectrics may enable the hyperbolic dispersion regime to move to shorter wavelengths. In the frequency regime accessible in our measurements, we do not observe a negative real permittivity along the ZZ direction, and we expect it to occur at much lower frequencies (<500 cm^{-1}), which indicates that any surface plasmon modes at frequencies above 500 cm^{-1} will inherit a hyperbolic dispersion (as shown in Fig. 3.4(F)) whereas those below will inherit an elliptical dispersion thereby undergoing a topological transition in photonic dispersion. It should be possible to electrically tune the transition point, as indicated by our results. Additionally, a Dirac-like dispersion (also known as a Dirac plasmonic point[156]) can be engineered in the system at slightly

lower frequencies than the spectral window accessed in our measurements. Theoretical studies of surface plasmons in BP and their corresponding dispersion relations have been discussed elsewhere[47]; however, our results provide a concrete step in that direction.

In order to account for screening, we model the BP as two parts–1. An actively electronically modulated 2DEG (thickness extracted from Thomas-Fermi screening calculations) and 2. A non-modulated bulk region. It is schematically shown in Fig. 3.5. We also extract refractive index (n,k) data for the modulated 2DEG (with an assumed thickness of 2.9nm) from the obtained σ and plot them in Fig. 3.6 and 3.7, respectively. The static contribution to the anisotropic dielectric function is modelled by using contribution from higher energy oscillators, taken from bulk BP studies, previously shown to be a reasonable approximation for other two-dimensional systems. The results have been extrapolated to much lower photon energies for clarity since the Drude model is expected to suffice. Here, $\sigma_0 = \frac{e^2}{4\hbar}$.

The following relations are employed:

$$\epsilon_{jj}(\omega) = \epsilon_\infty + \frac{i\sigma(\omega)}{t\epsilon_0\omega}, \tilde{n}(\omega) = \sqrt{\epsilon_{jj}(\omega)}, where\ t = thickness\ of\ the\ 2DEG$$

$$\epsilon_\infty(AC/ZZ) = 12/10$$

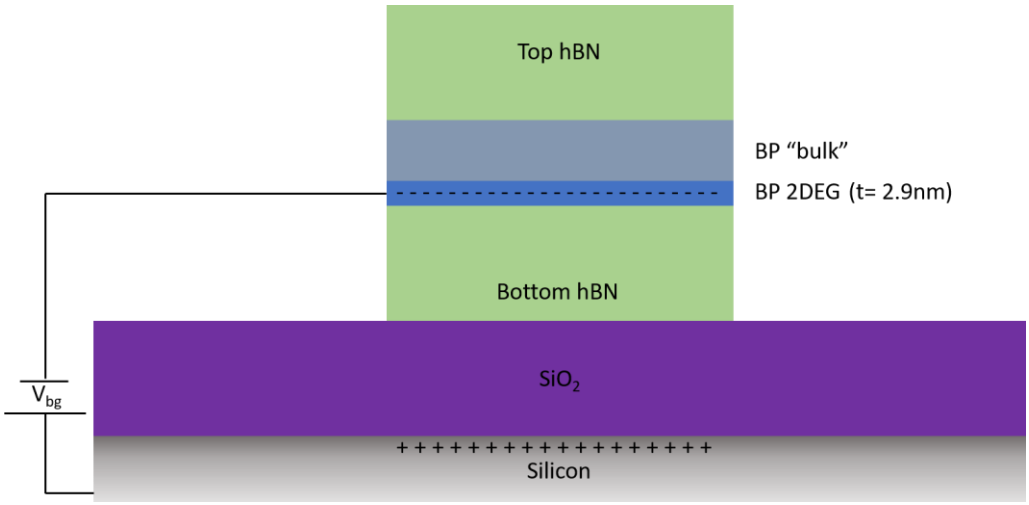

Figure 3.5. Schematic of electrostatic gating in BP device. The formation of an inversion layer is indicated at the interface of SiO_2/Si and bottom hBN/BP (of opposite parity). The BP can be

modelled as two separate parts: 1. Actively electronically modulated labeled as “BP 2DEG” which is ~2.9 nm thick from Thomas-Fermi screening calculations and 2. A non-modulated thick region labeled as “BP bulk” which extends to the remainder of the physical thickness of the BP flake as measured by atomic force microscopy (AFM).

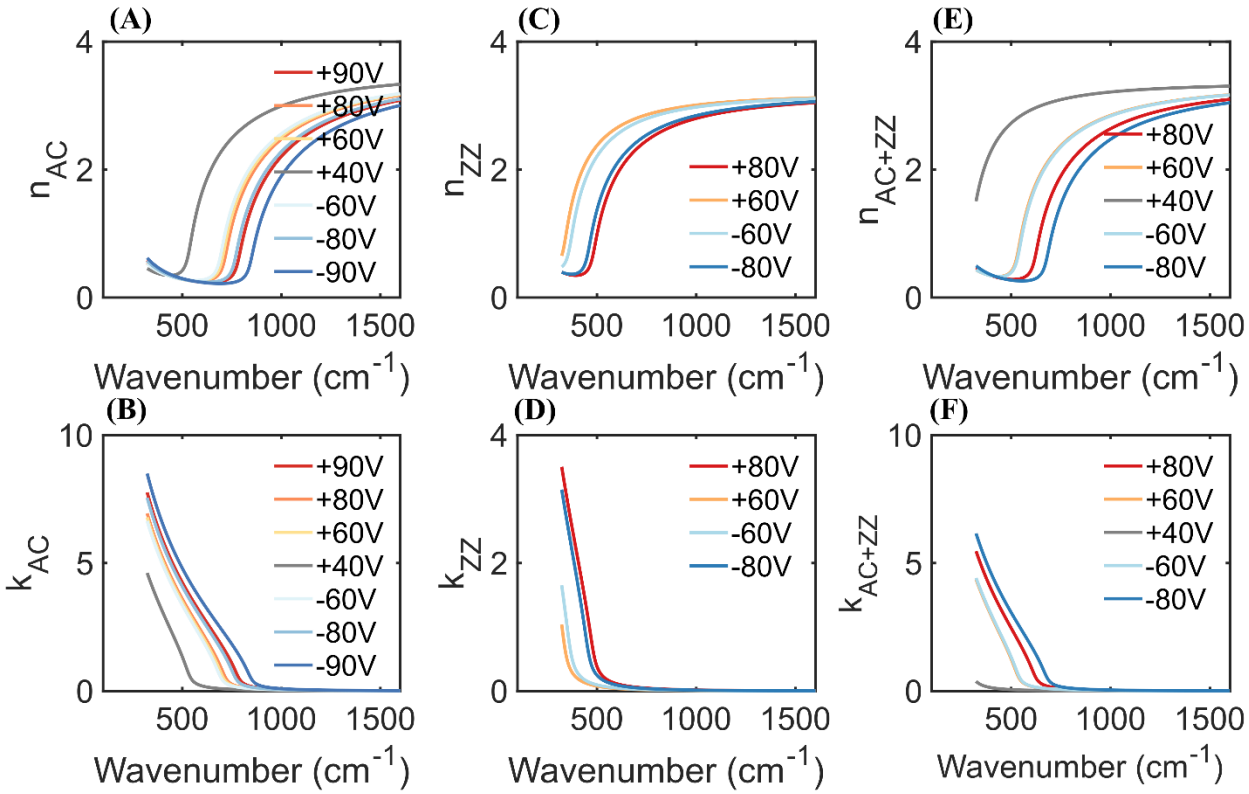

Figure 3.6. Refractive index of doped BP. (A) Extracted real part of refractive index of BP 2DEG as a function of voltage for AC excitation. (B) Extracted imaginary part of refractive index of BP 2DEG as a function of voltage for AC excitation. (C), (D) Same as (A), (B) but for ZZ excitation. (E), (F) Same as (A), (B) but for unpolarized excitation.

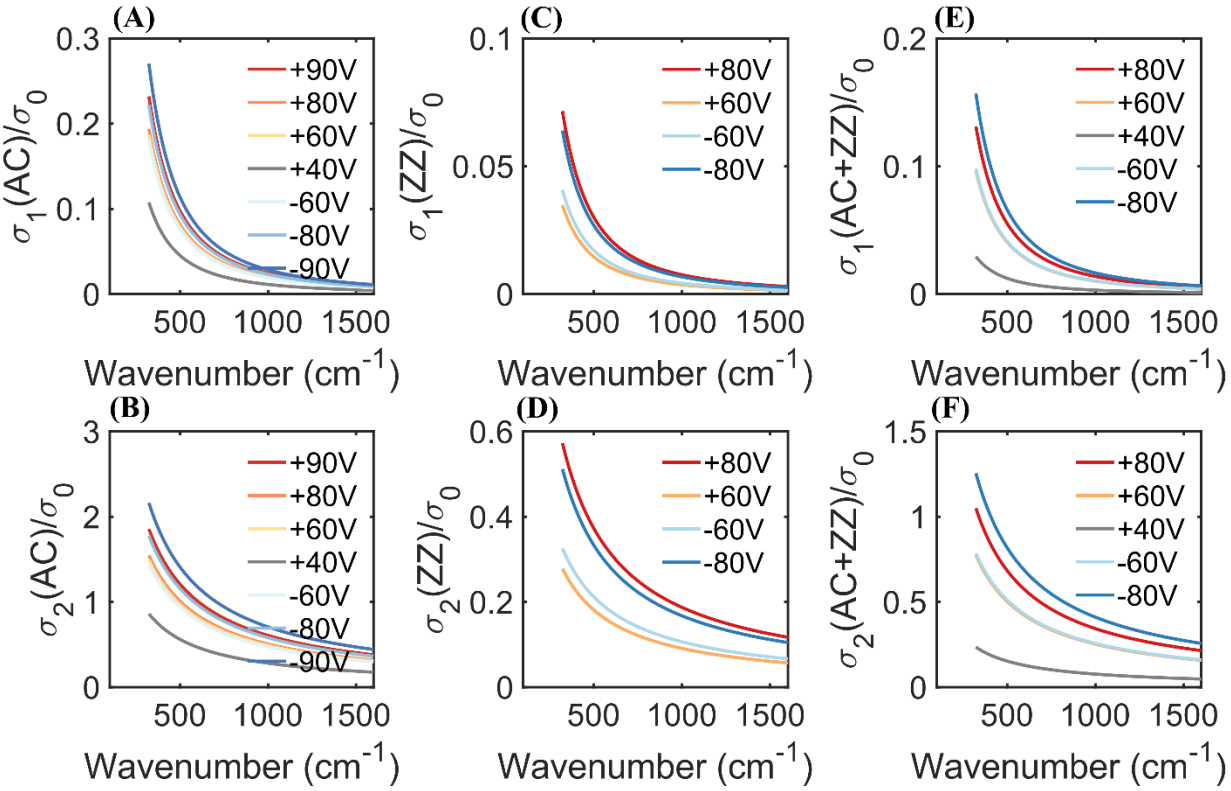

Figure 3.7. Optical conductivity of doped BP. (A) Extracted real part of optical conductivity of BP 2DEG as a function of voltage for AC excitation. (B) Extracted imaginary part of optical conductivity of BP 2DEG as a function of voltage for AC excitation. (C), (D) Same as (A), (B) but for ZZ excitation. (E), (F) Same as (A), (B) but for unpolarized excitation. Here, $\sigma_0 = \frac{e^2}{4\hbar}$.

3.6 DETERMINATION OF CARRIER EFFECTIVE MASSES IN A MULTILAYER BP 2DEG

Finally, we use our experimental results to obtain carrier effective masses that can be compared with results from theory as shown in Fig. 3.8(A) and (B). We see qualitatively good agreement with theory ($m_{eff} \approx 0.14 m_0$) for our results along the AC axis, in fact our extracted fermionic effective mass is slightly heavier than the previously theoretically calculated results. We speculate this could be an interplay of two effects. Firstly, in our BP thin films the 2DEG is highly confined and thus the band dispersion is modified, leading to heavier confined fermions[131]. Additionally, when the Fermi level moves into either the conduction or valence band with gating, we access not

only the minima and maxima of the first subbands in the conduction and valence band, respectively, but also the higher subbands (because of the broad Fermi-Dirac tail at 300K). In BP, for higher lying subbands along the AC axis, the effective mass increases gradually, as given by $m_{AC}^{i} = \frac{\hbar^2}{\frac{2\gamma^2}{\delta^i}+\eta}$, where δ^i is the subband transition energy, γ denotes the effective coupling between the conduction/valence bands and η is related to the in-plane dispersion of the bands[50,147]. It is possible that the carriers participating in the intraband transitions come from a mixture of the different subbands thus leading to an overall lower perceived effective mass. For the ZZ axis ($m_{eff} \approx 0.71 m_0$), we see a slightly larger variation in the extracted effective mass between the electron and hole side. Electronic confinement leads to heavier fermions along the ZZ direction, which is in accordance with our optical measurements for hole conductivity. It is possible that non-parabolic band effects give rise to a slightly lower effective mass for electrons, but further detailed analysis is needed to resolve the observed electron-hole asymmetry. It should be noted that for the ZZ direction the effective mass is not expected to depend on the subband index. As expected from theory, the ZZ carriers are found to be much heavier than carriers associated with transport along the AC direction.

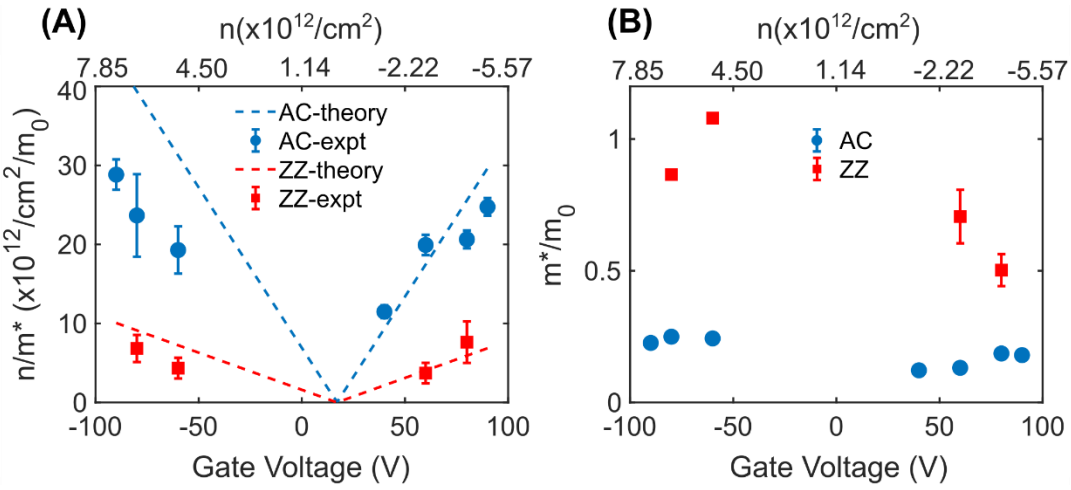

Figure 3.8. Extracted Drude weight and effective mass for BP. (A) Drude weight evolution obtained from fitting reflection data for AC and ZZ axis, plotted with expected Drude weight. (B) Extracted effective mass from the Drude weight fits plotted versus voltage/charge density assuming a parallel plate capacitor model and 100% gating efficiency.

From our experiments we are able to extract Drude weights for both polarization (AC and ZZ) and unpolarized light. In order to explain the trends, we look carefully at how Drude weight should evolve for a quantum well like system - ($D = \pi e^2 \sum_i \frac{n}{m_i^*}, i = subbands$). Our measured value for the effective mass is slightly higher than that expected for few-layer BP. As mentioned in the main text, the origin can be two-fold. One can come from electron confinement. When the doping density is low (near charge neutral), the screening length is ~100nm, which means the whole system is uniformly doped and behaves as bulk. However, as we dope the system the screening length goes down to ~2-5nm (most of the charge resides in the first 2-3 layers) and the system becomes highly confined (2D). Previous quantum transport measurements revealed rather anomalously large average in plane effective masses for BP due to such confinement effects. Another important factor could be the increasing less dispersive nature of the subbands in BP along the AC axis. When we dope the system, i.e., increase/decrease its Fermi level, we fill up not only the first subband, but also higher subbands. From our reflection modulation data in the interband regime, subband oscillations from the first 4-5 states can be seen, which means the Fermi tail is broad enough to have significant occupation in those states. If we calculate the transition energies based on the thickness of our sample, we find that the subbands are closely spaced. When we then proceed to calculate the effective mass for these subbands (given by $m_x^i = \frac{\hbar^2}{\frac{2\gamma^2}{\delta^i}+\eta}, where\ \delta^i\ is\ the\ subband\ energy\ gap$) we see an increase for higher energy states. It is possible that participation of those fermions leads to an overall increase in the measured effective mass. This can be understood as filling up of the different bands in the system. Since our sample is ~18nm thick, the subbands are placed closely (lying within a few k_BT of each other) and as we gate the heterostructure we move the Fermi level from one subband to the next (also evident from our band edge modulation data). For the ZZ direction any increase can come only from confinement since from theory we do not expect a subband dependent effective mass (given by $m_y^i = \frac{\hbar^2}{2v_c}$). For a more quantitative prediction of how the effective mass evolves, a first-principles theoretical framework would be required which accounts for all the electro-optic effects at work, and this is beyond the scope of the present paper. A table summarizing the possible bounds on effective mass is presented here.

Table 3.T1 Bounds on effective masses.

Type of carrier(polarization)	Subband lower bound	Subband higher bound	Confinement lower bound	Confinement higher bound
electron (AC)	0.14m0	0.23m0	0.14m0	0.17m0
electron (ZZ)	-	-	0.71m0	1.16m0
hole (AC)	0.12m0	0.23m0	0.12m0	0.15m0
hole (ZZ)	-	-	0.72m0	1.2m0

The effective masses for electrons and holes in BP can be bounded both due to the screening effect leading to highly confined carriers and also due to different carrier masses coming from higher subbands as the BP is electrostatically gated (i.e., Fermi level is pushed into the conduction or valence subbands). The bounds are presented in this table.

The transition energies are calculated from the equation[141]:

$$\delta_N^n = E_{g0} - 2(\gamma^c - \gamma^v)\cos\left(\frac{n\pi}{N+1}\right)$$

where E_{g0} is the monolayer optical gap, $\gamma^c(\gamma^v)$ is the nearest neighbor coupling between adjacent layers for conduction (valence band), n is the index of transition, N is the number of layers in the system.

For our case E_{g0} = 1.82eV, $\gamma^c - \gamma^v$= 0.73 eV. We plot the transition energies and the corresponding calculated effective mass for the AC direction in Fig. 3.9.

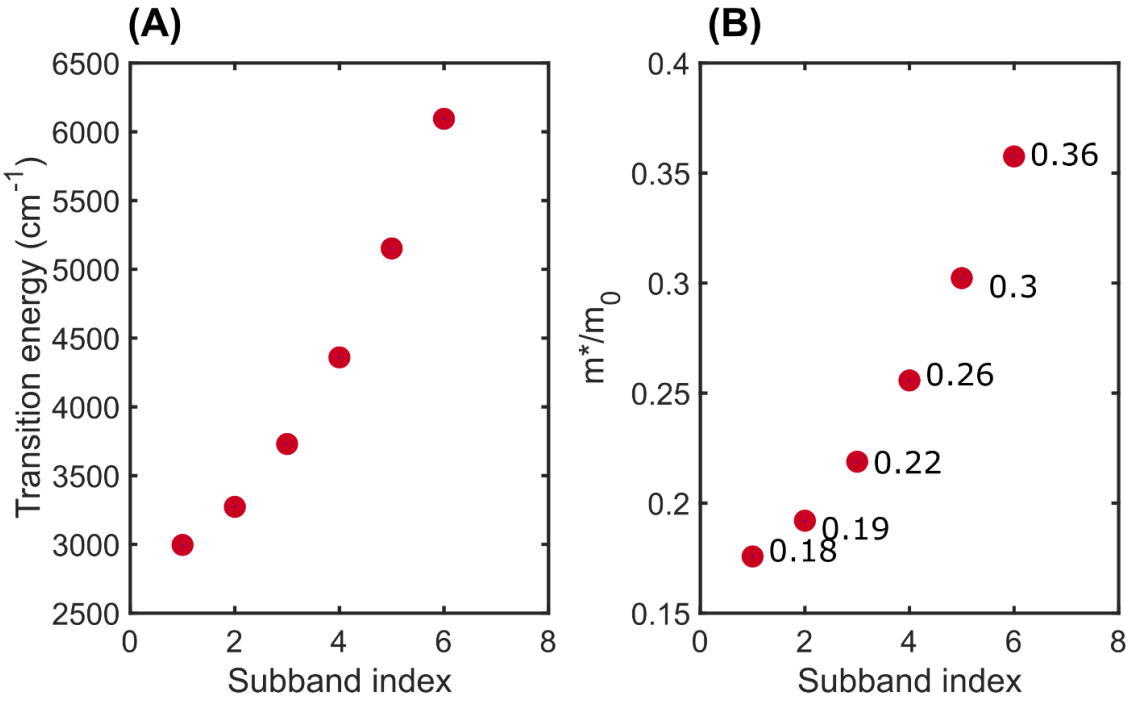

Figure 3.9. Subband effect in BP dispersion. (A) Calculation of transition energies in 18.68nm BP. (B) Corresponding effective mass along the Armchair direction.

In order to verify all of our results, we performed similar measurements with an unpolarized beam on the same sample. We see highly consistent and reproducible interband conductivity modulation effects for light polarized along the AC or ZZ axis. Below the band-edge we see a systematic strengthening of the Fano-like response for both electron and hole doping in the wavelength range near the hBN and SiO_2 phonons. Fits to those data sets are in excellent agreement with our theoretical analysis. Additionally, we find that the effective mass obtained is approximately the average of the in-plane effective masses along the AC and ZZ directions. This indicates that carriers along both the axes participate in the intraband response and is consistent with BP transport measurements. Subtle deviations are expected to occur in the estimation of the effective mass because of the non-symmetric nature of the unpolarized beam in our setup (it is slightly elliptically polarized) and possibly because of complex cross-scattering mechanisms between the two crystallographic directions. Overall, both polarized and unpolarized measurements are in good agreement with theory. We note that it is difficult to eliminate small conductivity changes due to local fluctuations in the charge density arising from charge puddles (bubbles/grain boundaries/defects) in heterostructures since our measurements probe a large area (approx. 2500

μm^2)[157]. Additionally, studies have shown some systems to have an energy dependent quasiparticle scattering rate owing to strong electron-electron and electron-phonon interactions[158,159]. Such interactions can cause additional broadening in both the interband and the intraband absorption features and have not been considered in our data analysis. We also note that in thick BP films (> 5 nm) like those measured here, excitonic effects are negligible and hence have not been considered. We performed measurements on three other BP heterostructures and saw very similar behavior.

3.7 CONCLUSIONS

We have experimentally explored the below bandgap optical response in gated multilayer BP heterostructures and identified the dominant contribution to be a Drude-like optical conductivity due to free carriers in the 2DEG. We find that interband transitions play a negligible role in the low photon energy response for BP, which greatly simplifies modelling of the optical conductivity of BP 2DEGs and subsequent photonic devices. We have measured the anisotropy in the intraband optical conductivity of BP by performing polarized reflection measurements and extracted the effective masses along the two crystallographic axes as a function of charge density. Our intraband optical conductivity results are consistent with any changes in the interband regime and DC transport measurements. Moreover, we demonstrated the existence of a plasmonic regime with electrically tunable hyperbolic dispersion and an ENZ regime. We also identified the wavelength regime for the onset of a topological transition for BP surface plasmons between hyperbolic and elliptical dispersion. Our results provide a foundation for a range of future research directions investigating BP as a strongly bianisotropic (or hyperbolic) mid-IR material for applications such as plasmonics, molecular fingerprinting, sensing, and tailoring thermal emission. They also pose important questions about the different scattering mechanisms in BP amidst a complex phase space of doping, thickness, substrate and temperature, and the nature of the mid-IR to THz response in BP, which motivates future work. Finally, our demonstration of BP as a naturally occurring material with tunable hyperbolic dispersion and bianisotropy suggests applications in novel photonics such as active polarization-sensitive infrared metasurfaces.

Chapter 4. ATOMICALLY THIN ELECTRO-OPTIC POLARIZATION MODULATOR

4.1 ABSTRACT

Active polarization control, highly desirable in photonic systems, has been limited mostly to discrete structures in bulky dielectric media and liquid crystal based variable retarders. Here, we report versatile electrically reconfigurable polarization conversion across the E, S and C telecommunication bands (1410-1575 nm) in van der Waals layered materials, using tri-layer black phosphorus (TLBP) integrated in a Fabry-Pérot cavity. The large electrical tunability of the exciton-dominated near unity birefringence in TLBP enables spectrally broadband polarization control. We show that polarization states can be generated over a large fraction of the Poincaré sphere via spectral tuning, and that electrical tuning enables the state of polarization conversion to span nearly half the Poincaré sphere. Specifically, we observe both linear to circular and cross-polarization conversion with voltage, demonstrating versatility with a high dynamic range.

4.2 INTRODUCTION

Polarization is a fundamental property of light that plays a crucial role in classical and quantum optics. In table-top optical experiments, it is usually tailored using polarizers, wave plates, and phase retarders. Generating arbitrary polarization states on demand is a requirement in a wide range of photonic processes such as circular dichroism sensing of chiral molecules and proteins, polarization-sensitive digital holography, imaging, polarization encoding for photonic qubits and detecting material quasiparticle excitations such as phonons, spins or excitons and their associated anisotropy[160–165]. Active control of polarization demands a platform with two key ingredients–a material whose complex refractive indices can be dynamically tuned[30,166] and in-plane symmetry breaking to generate birefringence, either from an inherent material property[167] or via nanostructured metasurface elements[168,169]. The former can be achieved using different effects, such as the Pockels effect, (magneto-optical) Kerr effect, Pauli blocking, quantum confined Stark effect, free carrier absorption and optical pumping[68,69,166,170–172]. Despite significant advances in the exploration of these phenomena, electrically reconfigurable control of polarization remains

largely elusive and suffers from limited dynamic range of polarization conversion. Furthermore, commercial polarization control devices like variable phase retarders which use liquid crystal or lithium niobate as active media are bulky, difficult to integrate into integrated photonic platforms, restricting the miniaturization of photonic systems.

Two-dimensional (2D), van der Waals, semimetals and semiconductors have yielded new photonic phenomena and directions for realization of chip-based photonics[173,174]. Layered van der Waals semiconductors are known to exhibit strongly bound excitons and are extremely polarizable in the presence of external electric fields, enabling unprecedented electric field-induced doping and refractive index modulation[20,175]. The atomic-scale thickness of van der Waals materials and lack of lattice matching requirement make them attractive candidates for future generation optoelectronics operating in the visible and telecommunications frequency bands for applications such as coherent control of quantum light, free-space and fiber-based communications and light detection and ranging.[31,176] However, most reports on electro-optic modulation in 2D materials, thus far have largely been limited to graphene and transition metal dichalcogenides which are optically isotropic in the layer plane, and hence not suitable for inherent active polarization control. Black phosphorus (BP), a 2D quantum-well like semiconductor exhibits natural birefringence owing to its in-plane anisotropic crystal structure[23,177,178]. Its unique electrically tunable optical dichroism demonstrated at the few-layer limit combined with its thickness tunable bandgap (~750 nm to ~4 μm), opens up possibilities for polarization-sensitive electro-optic conversion at infrared wavelengths in the telecommunication band, with a well-chosen thickness of BP[179–182].

In this work, we show that TLBP manifests a large birefringence in the telecommunication band, between the armchair (AC) and zigzag (ZZ) axis ($\Delta n = n_{AC} - n_{ZZ}$), of ~1.5 because of a strong excitonic feature at 1398 nm. Upon electrostatic doping, this resonance is highly suppressed giving rise to near unity complex refractive index tuning. Furthermore, we demonstrate, that by integrating TLBP into a Fabry–Pérot cavity, the difference in the phase and amplitude of reflected light along AC and ZZ generates polarization states over a large section of the normalized Poincaré sphere (such as linear, elliptical and circular) and over a large spectral range. In addition, we demonstrate active control of the reflected polatization state by electrostatic gating. Specifically, in electrically reconfigurable cavity-based heterostructures, the polarization state was dynamically tuned from linear to circular (like a quarter-wave plate (QWP)) and from nearly *s* to *p*-polarized

(like a half-wave plate (HWP)) by applying voltage at two wavelengths: λ=1442nm and λ=1444nm, near the cavity resonance, respectively. Our results further establish a large anisotropy bandwidth (>160nm) and highlight the potential of TLBP for very broadband active polarization modulation over the telecommunication E, S, and C bands.

A conceptual visualization of polarization conversion is illustrated in Fig. 4.1A. An incoming linearly polarized light illuminates a Fabry-Pérot cavity incorporating TLBP. The polarization state of the reflected light can be electrically tuned to alter its ellipticity (circular to linear polarization) or its azimuthal angle (s- to p-polarization). In this work, the two cavity mirrors are composed of a highly reflecting thick back gold (Au) mirror and a partially transmitting thin top Au mirror. The cavity medium is formed by hBN encapsulated TLBP and PMMA, which acts to adjust the cavity resonance frequency to a critically coupled condition, for maximal polarization conversion.

4.3 OPTICAL CHARACTERIZATION OF ELECTRICALLY TUNABLE EXCITON IN TLBP

To characterize the electrically tunable complex refractive index of TLBP, gate dependent polarized absorption measurements, as shown in Fig. 4.1B, were performed on a sample with the following configuration: hBN/TLBP(with few-layer graphene contacts)/hBN/Au. The charge neutral response (0 Volts) is dominated by a strong excitonic feature at 1398 nm, arising from the optical transition between the lowest (highest) lying conduction (valence) bands, in the quantum well like bandstructure of TLBP[23,182]. For both positive and negative voltages (electron and hole doping, respectively) the peak absorption reduces along with an increase in the linewidth of the excitonic transition. A stronger change is observed in the hole doping response with applied voltage, as compared to electron doping.

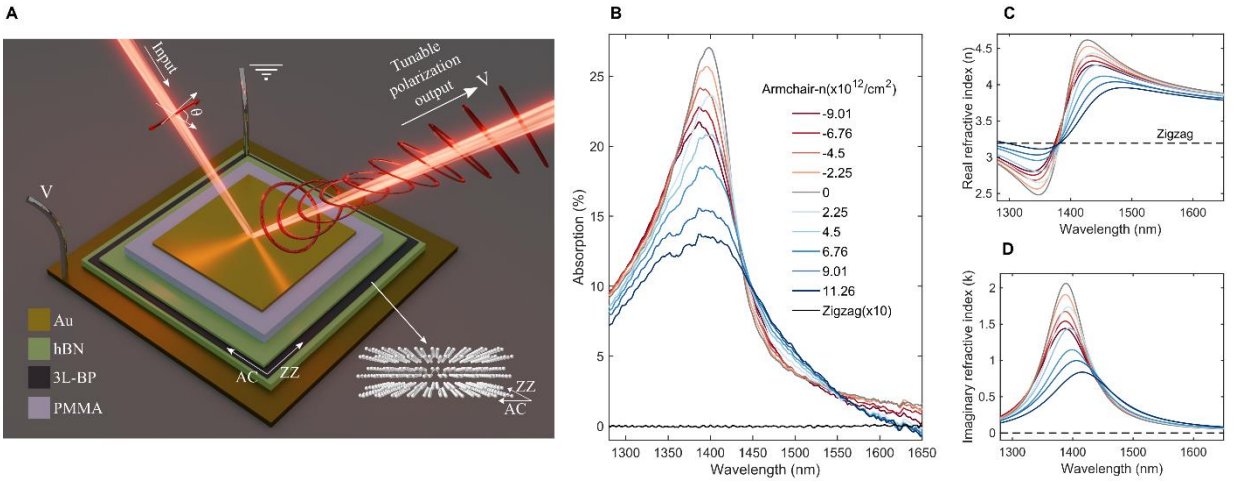

Figure 4.1. Schematic of electrically tunable polarization conversion and TLBP birefringence (A) Schematic of cavity design and polarization conversion. TLBP is incorporated in a dielectric environment between two mirrors (one partially reflective (top) and one highly reflective (bottom)). The incoming beam is linearly polarized, and the output beam can be azimuthally rotated or converted between circular and linear polarization with applied voltage (between the TLBP and the back electrode/mirror), for a fixed wavelength. (B) Experimentally measured polarized absorption from a TLBP device (non-cavity integrated) for different doping densities, along the armchair (AC) direction. The zigzag direction remains featureless for all conditions. (C), (D) Extracted complex refractive index (real and imaginary part, respectively) for TLBP as a function of doping density for the AC and ZZ direction.

Through a Kramers-Kronig consistent transfer matrix analysis of the gate-dependent absorption, the complex refractive indices ($\tilde{n} = n + ik$) of TLBP for different doping densities were estimated, as illustrated in Fig. 4.1C, D. Quite strikingly, near-unity tuning of the complex refractive indices (for both n and k) is observed near the excitonic resonance along the armchair direction. No noticeable feature was seen along the orthogonal direction, zigzag (ZZ), for any voltages, rendering that polarization passive.

A detailed discussion of the possible origins of the strong electro-optic response is provided next.

At the Γ-point of the band-structure in BP, wave functions are either even or odd with respect to reflection across reflection plane σ_h which lies in the x-z plane (where, x is AC, and z is out-of-

plane axis). Wave functions along the x (AC) direction are even with respect to σ_h , whereas those along the y (ZZ) direction are odd. This implies that in a *k.p* approximation, the perturbing Hamiltonian contains vanishing linear terms in the y-direction and close to the Γ-point, the system becomes quasi-one- dimensional. This induces a rather strong anisotropy, especially pronounced at the excitonic resonance/optical band-edge due to the higher optical density of states and the system behaves like an ensemble of one-dimensional exciton chains along the x-direction. In the absence of excitonic features in TLBP, in the near infrared, the dielectric permittivities for the AC and ZZ directions are set by the higher energy oscillators $\left(\epsilon_\infty = 12.5\ (AC), 10.2\ (ZZ)\right)$, which because of differences in the crystal symmetry along those two directions, gives rise to a broadband anisotropy. This anisotropy is exaggerated due to an excitonic feature in the telecom band for TLBP.

4.4 THEORETICAL UNDERSTANDING OF TUNABLE ANISOTROPY IN TLBP

Having established the anisotropy in BP, we move on to explain the strong electrical tunability of the optical properties of BP. When the system (BP) is near charge-neutral/flat-band conditions, the optical susceptibility is strongly dominated by the neutral exciton resonance–which is manifested as a strong peak in absorption along the AC direction. As the gate voltage is tuned to positive/negative values, a two-dimensional electron gas (2DEG) forms at the interface of BP and the bottom hBN. This 2DEG, which effectively increases the Fermi level of BP, results in the following changes:

Coulomb screening of the exciton: This is the predominant mechanism of modulation in our current scheme of electrostatic gating. As the charge density in the 2DEG in TLBP increases, the free carriers effectively screen the field between the bound electron-hole pairs. This reduces the interaction strength of the quasi-one-dimensional dipoles in TLBP (along the AC direction), increases its Bohr radius, and leads to a reduction in the exciton binding energy and thus lowers the oscillator strength. This mechanism is thus also responsible for tuning the anisotropy in the system with gate voltage, as it effectively diminishes the excitonic contribution and the difference of optical response along the AC and ZZ direction are eventually dictated by the higher energy oscillators ($\boldsymbol{\epsilon_\infty}$).

Coulomb scattering of the exciton: This is another important consequence of gating. With more free carriers available, the probability of an exciton to elastically or inelastically scatter off an electron or hole increases. This leads to a reduction in coherence lifetime of the exciton which manifests itself as spectral broadening corresponding to the excitonic transition, seen for both electron and hole doping in our case.

The combined effects are schematically illustrated in Fig. 4.2.

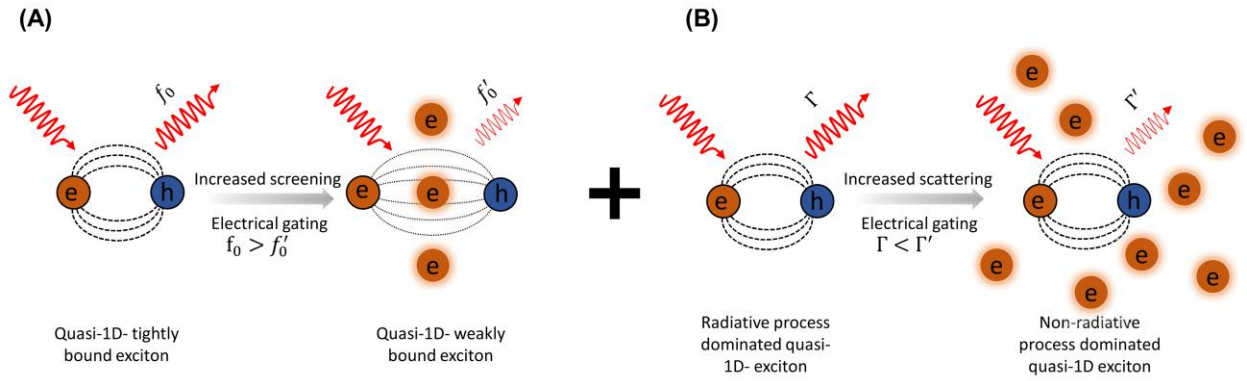

Figure 4.2. Coulomb screening and scattering of quasi-1D excitons (A) Due to electrical gating, free charges increase which reduce the overall attraction between the bound electron-hole pair for the quasi-1D excitons along the AC direction. This screens the electric field lines between them and weakens the exciton, leading to a reduction in binding energy and oscillator strength (f_0). (B) Due to increased charges, excitons now scatter off them much more readily, leading to reduced coherence and broadening of spectral transitions, manifested as larger linewidths (Γ).

We also address some other electro-optic effects seen in typical 2D semiconductors that might be at play:

- Trions–As excess free electrons/holes accumulate in the 2DEG, the probability of an exciton to bind to a free charge to form a trion increases. Compared to the exciton, a trion is lower in energy which manifests as a redshift of the absorption peak. Generally, trions have lower oscillator strength compared to excitons and hence can show up as a reduced absorption peak. This explains the redshift of the excitonic peak upon hole doping (which happens to be more efficient than electron doping for the investigated non-cavity device).
- Band-structure (gap) renormalization–In the presence of excess free carriers, there can be significant band-structure renormalization which leads to energy shifts in the absorption peak.

Typically, band-gap renormalization red shifts the quasiparticle gap. A near exact cancellation of this effect is expected from the reduction in the binding energy of the exciton leaving the spectral position of the exciton nearly unchanged for the doping densities achieved here. This phenomenon is not probed directly through our measurements since the quasi-particle gap is not tracked.

- Pauli blocking–As the Fermi level is increased, the lowest optical transitions below the Fermi level get blocked because of Pauli's exclusion principle, resulting in a blue-shift of the absorption peak. Such features were not seen in our measurements and are expected to occur at much higher charge densities ($>10^{13}/cm^2$).
- Stark shift–The 2DEG induced in BP has its own vertical electric field which can cause a reduction of the bandgap and a red-shift of the absorption peak. We believe this is a very weak (and thus negligible) effect in our current scheme of electrostatics where a pure vertical displacement field (in absence of doping) does not exist, rather the vertical field arises from a thickness dependent doping profile, due to screening. Since the entire thickness of TLBP is below the Thomas-Fermi screening length (see S28), it is justified to consider the entire film to be under uniform doping and have minimal displacement field-dependent energy shifts.

The above-listed 4 effects play a minor role and the most significant effect responsible for large polarization conversion in the cavity-based devices is a change in the oscillator strength of the exciton.

The overall effect of the electrostatic doping on the quasi-1D excitonic absorption spectrum can be schematically represented as follows:

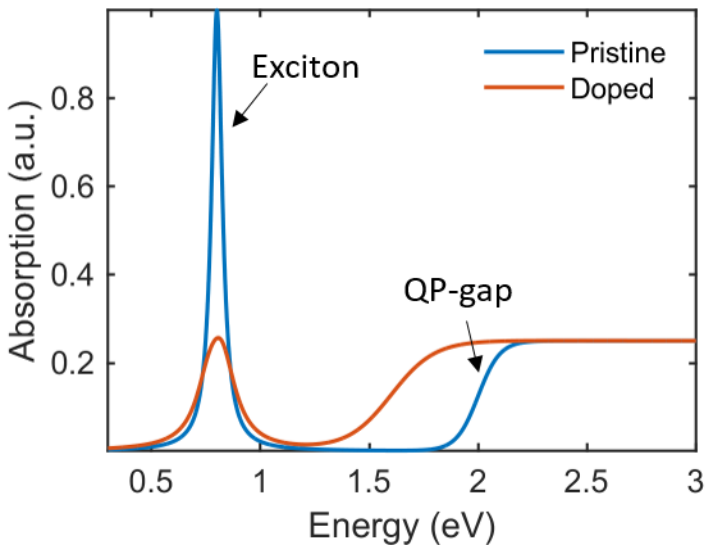

Figure 4.3. Absorption modulation schematic upon doping. Illustrated modulation in absorption reflecting changes in the optical density of states upon doping showing a reduction of exciton oscillator strength and broadening of the transition along with bandgap renormalization and reduction of quasi-particle (QP) band-edge coupled with a reduction in exciton binding energy rendering the exciton resonance nearly unchanged spectrally.

4.5 CAVITY DESIGN AND BROADBAND NATURE OF BIREFRINGENCE IN TLBP

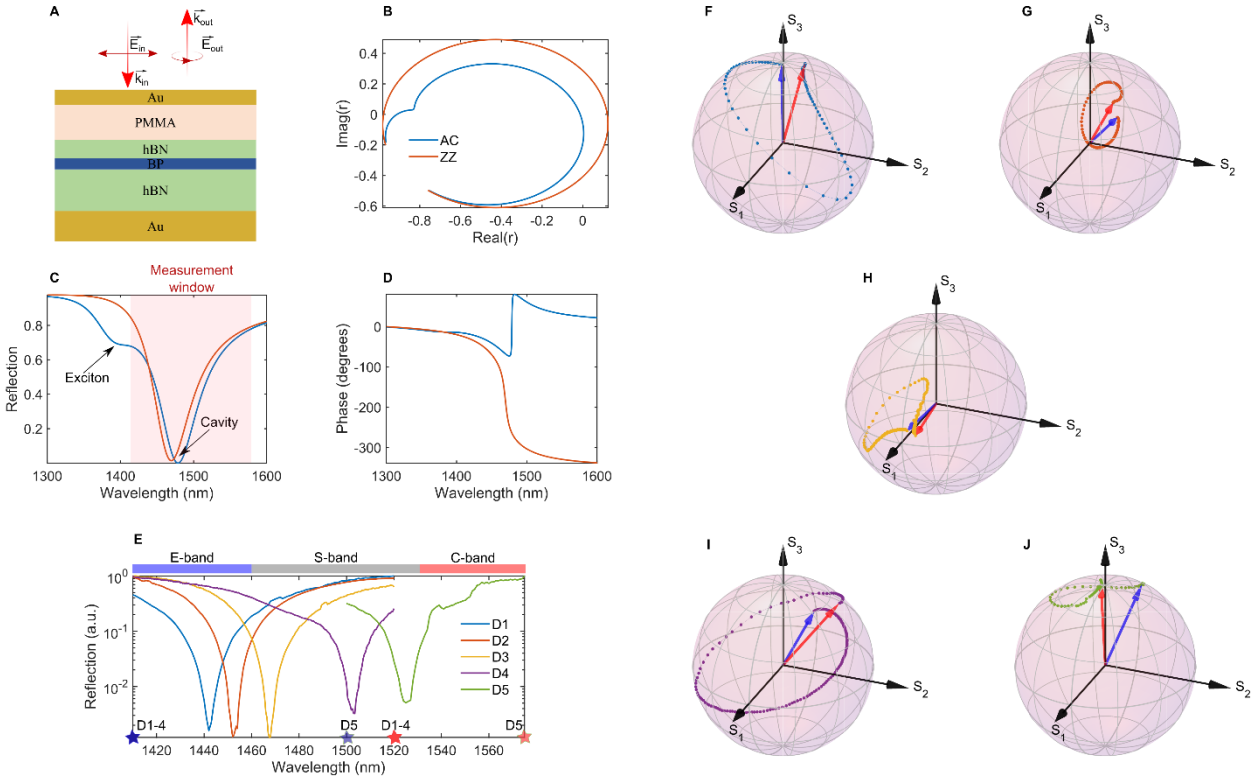

Figure 4.4. Example cavity design for polarization conversion and large anisotropy bandwidth experimental demonstration. (A) Side view of a typical cavity structure adopted in this work. The top and bottom mirrors are formed by thin and thick Au films. The cavity is comprised of hBN encapsulated TLBP and PMMA, which acts as the tunable part of the cavity (in determining the resonance wavelength). (B), (C), (D) Theoretically calculated complex reflection phasor, reflection amplitude and phase spectrum, respectively, for such a typical cavity structure having resonance ~1480 nm, showing difference in both the parameters along AC and ZZ, establishing polarization conversion. (E) Summary of reflection amplitude spectra from 5 representative devices fabricated as part of this study showing tunable cavity resonance. The PMMA thickness was tuned systematically to change the resonance over 90 nm across the telecommunication band (E,S and C). (F)-(J) Experimentally measured spectral trajectories on the normalized Poincaré sphere corresponding to the 5 device resonances plotted in (E). All trajectories show strong spectral

polarization conversion (either in the azimuthal orientation or the ellipticity or both). The difference in the trajectories are intimately related to the critical coupling between the cavity and the incoming polarization. For all the presented trajectories, the azimuthal orientation was aligned nearly 45 degrees to the AC and ZZ direction of the TLBP flake. For each normalized Poincaré sphere, the blue arrows mark the beginning of the spectral scan (1410nm for D1-4, 1500 for D5) and the red arrows mark the end (1520nm for D1-4, 1575 for D5)–also shown as stars in x-axis of (E).

We next designed a heterostructure for polarization conversion by integrating the TLBP in an optically resonant cavity geometry which enhances the degree of polarization conversion. A transfer matrix calculation of a typical Fabry-Pérot cavity design, schematically shown in side view in Fig. 4.4A, yields the complex reflection phasor, amplitude and phase spectra, as illustrated in Fig. 4.4B, C, D respectively. From the phasor diagram in Fig. 4.4B, a prominent and different complex reflectivity feature is seen along the two polarizations. A clear resonance from the cavity is seen at 1479 (1470) nm for the AC (ZZ) direction in the reflection amplitude in Fig. 4.4C, along with a weaker excitonic absorption feature at shorter wavelengths (1398 nm), seen only along the AC direction. Interestingly, the reflected phase along the AC and ZZ, in Fig. 4.4D shows strong differences near the cavity resonance. Taken together, these results indicate the potential for significant polarization conversion of the reflected light. The cavity parameters used in Fig. 4.4B-D are not a unique choice. In fact, the optical anisotropy in TLBP is broadband, enabling operation over the entire wavelength range of the telecommunication E, S and C-bands with appropriate changes in the cavity parameters–primarily via adjustment of the thicknesses of the dielectric medium (hBN or PMMA) and the top Au mirror. Both parameters are important in determining the resonance wavelength and the reflection extinction ratio.

We present numerical results on the effect of the top Au and PMMA thickness on the cavity performance. Here, the thickness of the bottom Au, bottom hBN, TLBP and top hBN were fixed at 100 nm, 120 nm, 1.59 nm, and 52 nm. The refractive indices of Au were adopted from Johnson and Christy, while n=2.17 was used for hBN with no dispersion. For PMMA, n=1.478 was used. AC response of TLBP was modelled with a single exciton with the following parameters–resonance wavelength = 1398.2 nm, oscillator strength = 2.5 meV, broadening/linewidth = 45.1 meV (as extracted from measurements discussed in Fig 2.). ϵ_∞ = 12.5 and 10.2 were used for the

AC and ZZ direction, respectively. The ZZ direction permittivity was assumed to be constant, with no excitonic feature. No thickness dependence was assumed for the complex refractive index for any of the layers. Transfer matrix calculations were run with sweeps of the PMMA thickness and the top Au thickness. Fig. 4.5A shows the evolution of the cavity resonance. As the PMMA thickness is swept, the cavity resonance redshifts due to the overall increase in the optical length of the cavity. As the top Au thickness is increased, the resonance frequency blueshifts because of the change in the reflectivity of the top mirror (higher reflectivity for thicker top Au). Fig 4.5B shows the effect of the top Au and PMMA thickness on the reflection amplitude at the resonance along the AC direction. A trajectory is seen with low reflectivity highlighting the critical coupling condition. This is the physical set of parameters which correspond to the maximal energy transfer to the cavity. Finally, the maximum achieved phase shift difference between the AC and ZZ directions as a function of top Au and PMMA thickness is discussed in Fig. 4.5C. Strong phase difference is seen along the "critical coupling" trajectory. In this work, cavities were fabricated with target critical coupling to the AC direction because that is the electrically tunable polarization direction, while the ZZ remains passive, for all doping conditions.

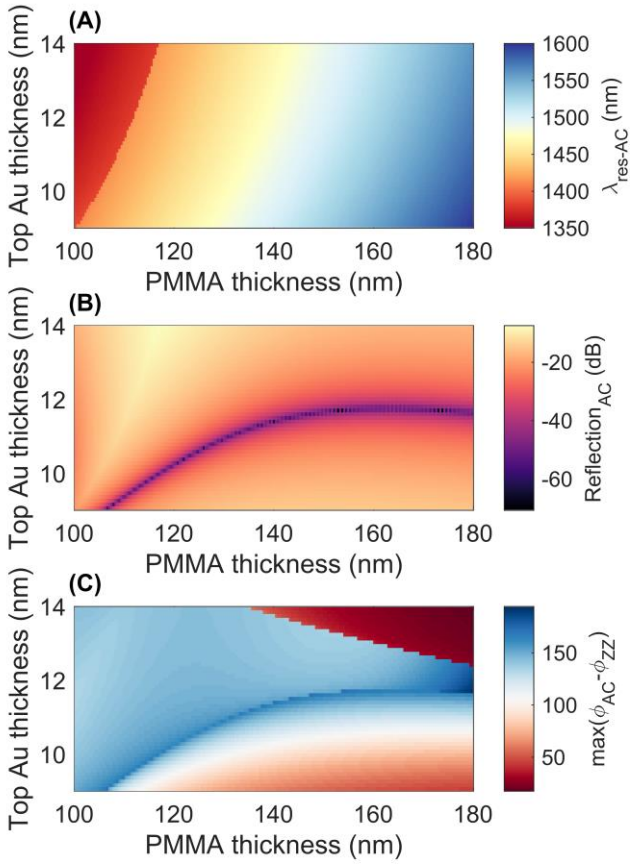

Figure 4.5. Amplitude and phase shift dependence on cavity parameters. Effect of the top Au and PMMA thickness are studied on the cavity performance. (A) Resonance of the cavity (along the AC direction) showing redshifts with increasing PMMA thickness and blueshifts with increasing metal thickness. (B) Reflection amplitude of the cavity (along the AC direction) showing the "critical coupling" trace as a function of top Au and PMMA thickness. (C) Maximum phase shift difference between the AC and ZZ direction plotted as a function of top Au and PMMA thickness. Strong phase shift difference traces follow the reflection amplitude trace, highlighting the importance of critical coupling.

To experimentally demonstrate the broadband nature of the TLBP anisotropy, reflection intensities (S_0) measured from five representative heterostructures are shown in Fig. 4.4E. The PMMA thickness was sequentially tuned to redshift the cavity resonance, spanning approximately 100 nm across the E, S, and C–telecommunication band. For each heterostructure device (D1 to D5), a

corresponding spectral trajectory on the normalized Poincaré sphere is shown in Fig. 4.4F-J, respectively. The blue (red) arrows mark the beginning (end) of the measured spectral trajectory, corresponding to 1410 (1520) nm for D1 to D4 and 1500 (1575) nm for D5. Efficient polarization conversion can be seen for all the devices, confirming the broadband nature of the anisotropy in TLBP coupled with the cavity mode. The differences in the trajectories arise from where the cavity resonance wavelength is with respect to the beginning and ending point of the spectral scans. In addition, the arc length subtended by the trajectories on the normalized Poincaré sphere is intimately related to how well the cavity critically couples to the incoming free-space electromagnetic field and is dominated strongly by the top mirror reflectivity.

4.6 SPATIAL INHOMOGENEITIES IN TLBP-CAVITY SAMPLES

We discuss next the spatial inhomogeneities in typical TLBP-cavity samples. Spatial false colormaps of ellipticity (Fig. 4.6A) and azimuthal angles (Fig. 4.6B), measured for heterostructure device D4, are shown for four different wavelengths near the cavity resonance, illustrating that the polarization conversion has strong spatial variation. The optical image of the sample with appropriately outlined bare cavity (0), 3 and 6-layer BP regions is shown in the inset of Fig. 4.6E. To gain further insight, spectral scans are shown in Fig. 4.6C and D for a select few points (appriopriately labelled) chosen from the aforementioned regions. Strong polarization conversion is seen on the trilayer region. For example, a linearly polarized input (azimuth ~45^{o} to the AC/ZZ axes) is converted to nearly circular (42^{o} ellipticity) at the resonance. An associated feature is seen in the azimuth spectrum as well (with a derivate-like lineshape), peaking at -37^{o} and +42^{o} around the ellipticity resonance. As expected, very weak (no) polarization conversion effects are seen spectrally in the 6-layer (bare cavity) region. The weak effect for the 6-layer region presumably originates from the higher quantum-well subband transitions leading to reduced birefringence.

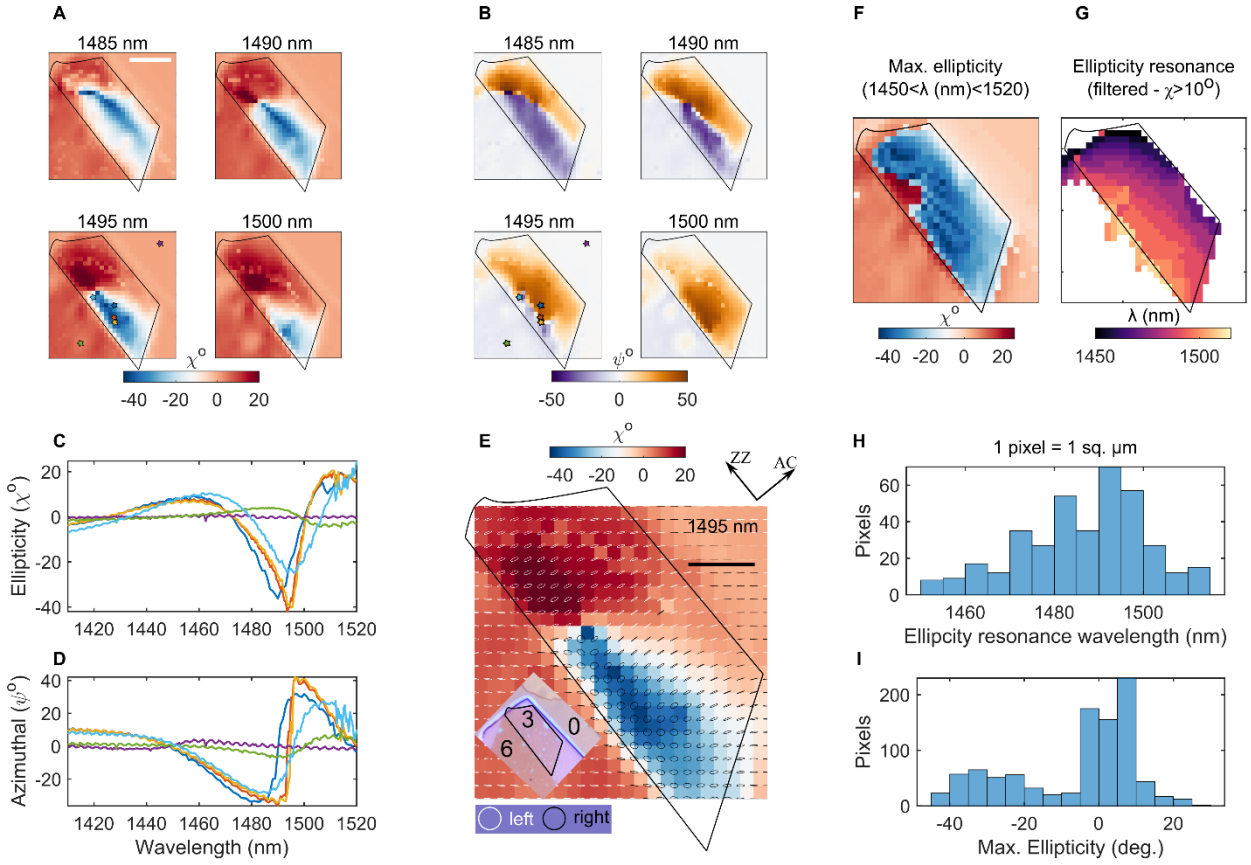

Figure 4.6. Spatial inhomogeneity in optical anisotropy probed by polarization conversion. (A) Spatial maps of ellipticity angle (in degrees) of device D4 for 4 different wavelengths near the resonance (~1490 nm) of the cavity. Black lines indicate the extent of the tri-layer region (Sample optical image shown in inset of (E)). Scale bar (in white) corresponds to 10μm. (B) Same as (A), but for azimuthal angle. (C), (D) Ellipticity and azimuthal angle spectral scans for a few points (marked with appropriately colored stars in (A) and (B)), showing spatial variation of the resonance in the tri-layer region, as well as flat background response from the bare cavity and weak polarization conversion from the 6-layer region. (E) Zoom-in spatial colormap of ellipticity at 1495 nm along with superimposed reflected polarization ellipses at each point, for better visualization of co-variation of azimuthal and ellipticity angles. White lines correspond to right handedness, while black lines correspond to left handedness. Scale bar (in black) corresponds to 5um. Inset. Optical image of the device (D4) outlining the 3-layer (3) region. Also shown is the 6-layer region (6) and the bare cavity (0). (F) Spatial map of maximum ellipticity for each point within a spectral window between 1450 nm and 1520 nm. (G) Spatial map of ellipticity resonance wavelength (filtered for $|\chi|>10^{o}$ to only highlight the 3L region). (H), (I) Histograms of ellipticity

resonance wavelength (filtered for $|\chi|>10^{o}$) and maximum ellipticity (in degrees), where 1 pixel on the map corresponds to 1 sq.μm.

To aid the visualization of co-variation in azimuthal and ellipticity spatially, a false colormap of ellipticity superimposed with measured reflection polarization ellipses, is shown in Fig. 4.6E. The white (black) color corresponds to right (left) handedness. Finally, in Fig. 4.6F and G, spatial maps of the maximum achieved ellipticity over a bandwidth of 70 nm (1450 nm to 1520 nm) and the corresponding resonance wavelength are plotted, respectively. Quite interestingly, the overall achieved maximum ellipticity is relatively homogenous although the spectral distribution is quite broad. The histogram in Fig. 4.6H (filtered for absolute ellipticity values > 10^{o}) confirms a strong centering of the ellipticity response around the resonace wavelength (~1490 nm). Fig. 4.6I shows the distribution of maximum ellipticity achieved for all pixels across the entire map presented in Fig. 4.3F. Two strong peaks are seen near $+10^{o}$ and -35^{o}, corresponding to the peak ellipticity values observed in most of the trilayer region. Our observation of spatially varying complex refractive indices are consistent with dielectric disorder seen in typical 2D heterostructures[157]. We speculate the origin of such behaviour to be two-fold–fabrication induced trapped hydrocarbons and strain between constituent layers in the heterostructure and different stacking orders in TLBP (ABA, AAB and ACA)[38,136,183].

Spatial maps of ellipticity and azimuthal angles are presented for device D2 for different wavelengths in Fig. 4.7 and 4.8. All maps show spatial inhomogeneity attributed to dielectric disorder that originates from strain or trapped bubbles during the heterostructure assembly of the device. Similar trends were observed in all the devices.

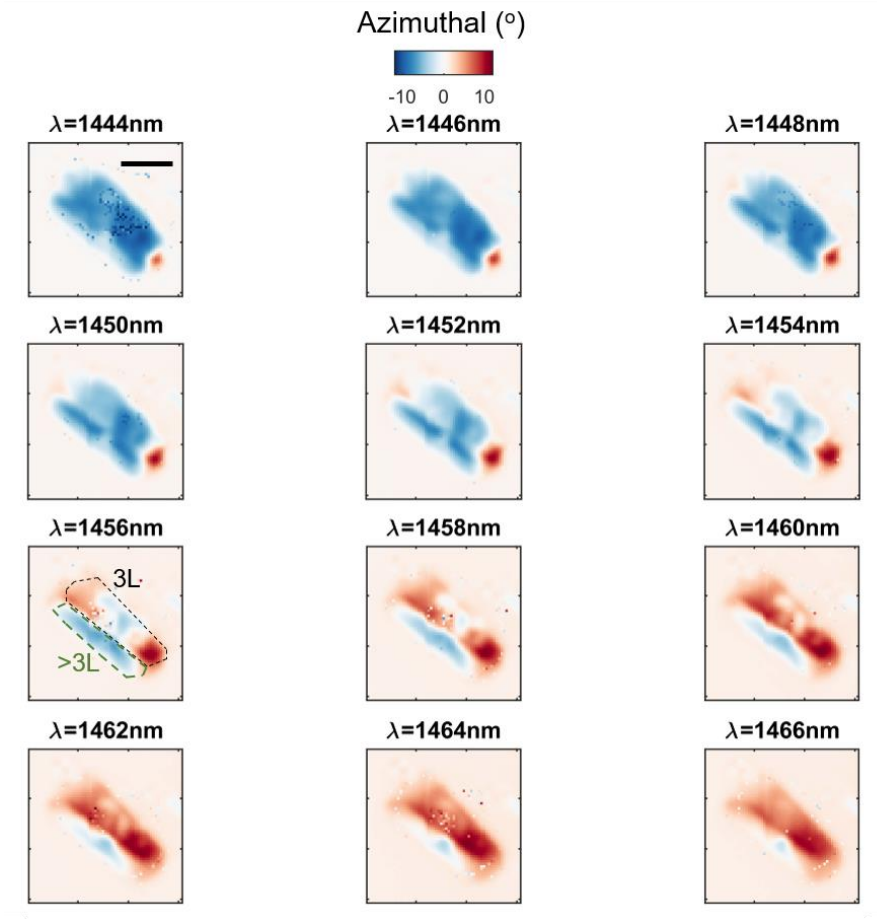

Figure 4.7. Azimuthal spatial colormaps of sample D2 for different wavelengths. Scale bar corresponds to 10 μm. 3L region is outlined in black dashed lines for 1456 nm spatial map, while thicker region is outlined in green.

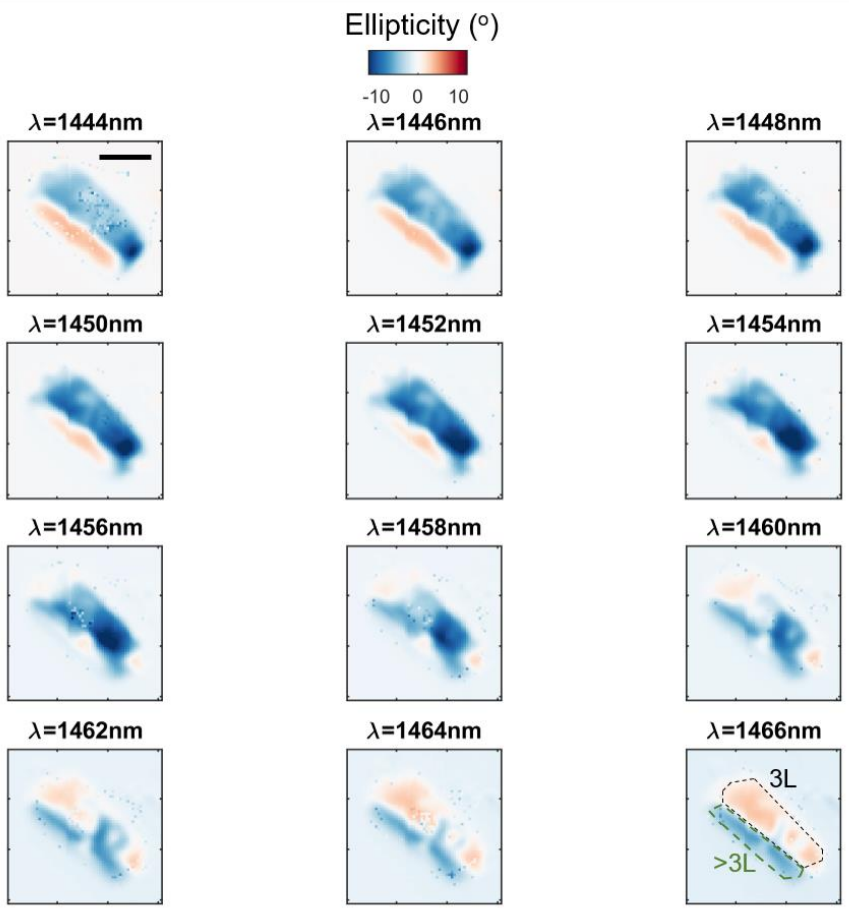

Figure 4.8. Ellipticity spatial colormaps of sample D2 for different wavelengths. Scale bar corresponds to 10 μm. 3L region is outlined in black dashed lines for 1466 nm spatial map, while thicker region is outlined in green.

4.7 ELECTRICALLY TUNABLE POLARIZATION DYNAMICS

We now discuss the electrical tunability of the different polarization parameters, the key result of this work, which is summarized for device D1 in Fig. 4.9. The Stokes (S) parameters (S_0,s_1,s_2,s_3), which completely characterize the polarization conversion induced by the device, are shown as a function of wavelength and gate voltage in the form of false colormaps in Fig. 4.9A-D for hole doping regime. It can be seen that all the three normalized s-parameters tune efficiently around the resonance (~1440 nm) with increased hole doping owing to strong cavity and TLBP interaction.

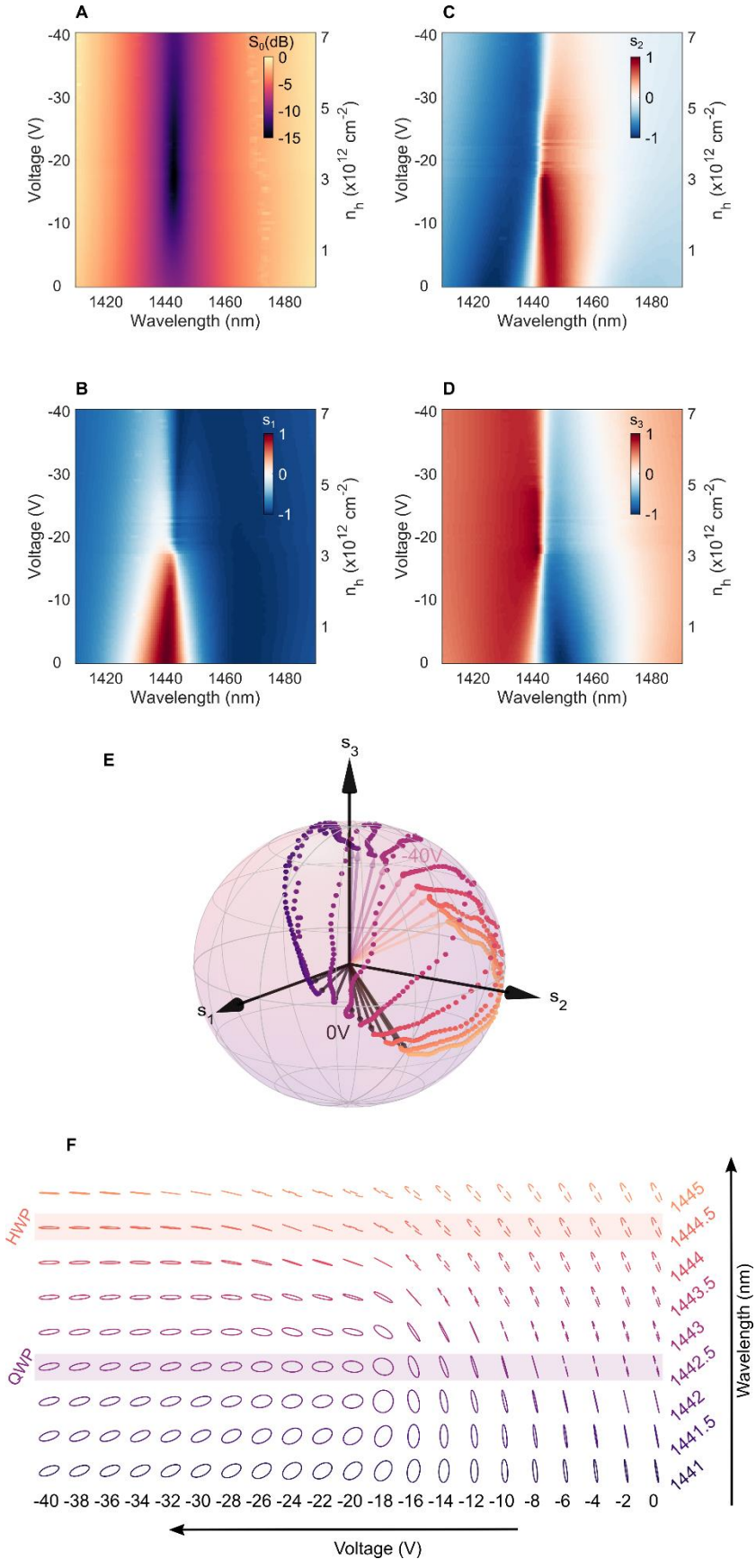
A
B
C
D
E
F
Voltage (V)
Wavelength (nm)
n_h (x10^{12} cm^{-2})
S_0(dB)
s_1
s_2
s_3
-40V
0V
HWP
QWP
Wavelength (nm)
Voltage (V)

Figure 4.9. Electrically tunable polarization dynamics. (A),(B),(C),(D) False colormaps of the evolution of the intensity (S_0) and the three normalized Stokes parameters (s_1,s_2,s_3), determining the polarization state of the reflected light, as a function of wavelength and positive voltages (for electron doping). The results are from device D1. Continuous tuning of all the 4 parameters can be seen around the cavity resonance (~1440nm) for the entire range of doping, illustrating efficient tuning of the polarization state with voltage. (E) Voltage dependent trajectories on the normalized Poincaré sphere for 9 different wavelengths showing large dynamic range in tunability of the reflected polarization state. Each color corresponds to a wavelength (same color code in (F)). The dark arrows mark the beginning of the voltage scan (0V), and the correspondingly colored arrows indicate the end of the voltage scan (-40V)–hole doping. (F) Visualization of the measured reflected polarization ellipse for selected voltages and the same 9 wavelengths as in (E). At 1442 nm a strong change in ellipticity is seen where the state becomes almost circular at -18V and the ellipticity decreases for higher voltages–acting like a QWP. The change in ellipticity is associated with a change in the azimuthal orientation of the beam. At 1444 nm however, minimal change in ellipticity is seen with a strong change in the azimuthal orientation–effectively behaving like a HWP. The solid (dashed) lines correspond to right (left) handedness.

A competition between the excitonic absorption and the cavity resonance governs the overall optical response of the system, due to the close proximity of the two features.

Hence, maximising the polarization conversion requires carefully adjusting the incident polarization to balance the losses along the two principle axes of TLBP for a fixed orientation of the device. To quantify the degree of polarization conversion, traces on the normalized Poincaré sphere were measured for different input ellipticity and azimuth. The longest arc was found for nearly linearly polarized input at an angle of ~27° with the AC axes of TLBP, corresponding to a vertical polarization in the lab frame. Our observations of the electrically-driven changes in the S-parameters are consistent with the measured complex refractive indices of TLBP, including a stronger hole-doped response compared to electron-doping. For example, in all the three S-parameters a suppression of the overall magnitude of the resonance is seen which is caused by the reduction in excitonic anisotropy. In addition, the linewidth of the aforementioned features reduce with increasing voltage due to a suppression of the losses along the AC direction. We note that the

polarization rotation at the resonance wavelength is primarily enabled by the higher absorption along the armchair axis than the zigzag axis (Fig. 4.1D), further enhanced by the cavity.

To visualize the changes in the reflected polarization states better, traces on the normalized Poincaré sphere for different wavelengths around the resonance are plotted as functions of gate voltage. Fig. 4.9E shows such traces on the normalized Poincaré sphere for 9 different wavelengths. The dynamic range corresponds to nearly half the normalized Poincaré sphere in terms of solid angle subtended by the voltage-driven arcs. Quite intriguingly, two very interesting traces can be identified. The first one is at 1442 nm, where the ellipticity changes between 0.3° to 43.7° to 16.8° between 0, -18 and -40 V, showing tunable quarter-wave plate operation. In contrast, at 1444 nm, the azimuthal angle is tuned from 24.6° to 89.4° between 0 and -40V with suppressed ellipticity changes, demonstrating tunable half-wave plate operation. At other wavelengths it is possible to demonstrate a wide variety of elliptically polarized states. A two-dimensional map of different polarization ellipses measured as a function of 9 different wavelengths (same wavelengths and color code as Fig. 4.9E) is shown in Fig. 4.9F for voltages between 0 and -40V (hole doping), where the strongest changes are noted. This map better illustrates the quarter-wave plate and half-wave plate like operation, as well as other intermediate polarization conversion configurations. A similarly high dynamic range for polarization conversion is also seen for electron doping (Fig. 4.10). A general trend noted in these voltage dependent polarization conversion measurements is that upon doping the TLBP, the spectral trajectory on the normalized Poincaré sphere can be collapsed to a point–a manifestation of electrically tunable anisotropy suppression. Thus, the larger the trajectory at nearly charge neutral doping conditions, the higher the capability to access a wide range of polarization states by applying a voltage.

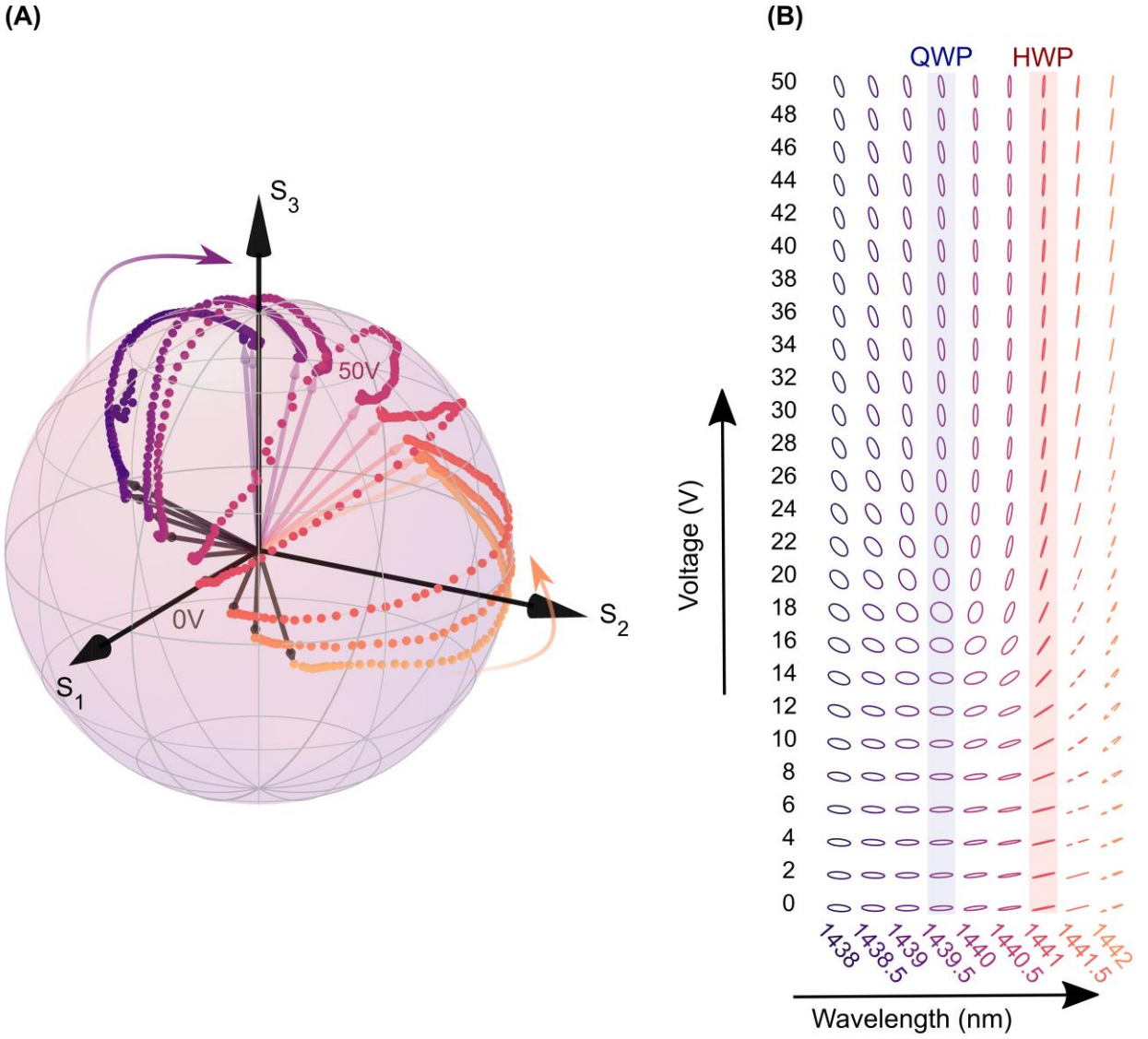

Figure 4.10. Normalized Poincaré sphere dynamics and polarization conversion for electron doping. (A) Voltage dependent trajectories for 9 different wavelengths from 0V to +50V (electron doping) showing highly versatile polarization generation. Colors correspond to the same 9 wavelengths shown in (B). (B) Two-dimensional map of generated polarization states as a function of wavelength and voltage for 9 wavelengths and select few voltages. Half-wave plate (HWP) like operation is seen for 1441 nm, whereas quarter-wave plate (QWP) like operation is seen for 1439.5 nm.

4.8 CONCLUSIONS

In conclusion, our results shed light on the versatility of BP as an active medium for electronically reconfigurable broadband polarization conversion. The Γ-point nature of the direct-band minima enables BP to have pronounced band-edge optical anisotropy spanning from visible (750 nm) to the mid-infrared (4 μm)[23,182], while free carrier modulation provides access to mid to far-infrared wavelengths (>5 μm)[181]. Three-layer black phosphorus is of particular interest for polarization conversion at telecommunications wavelengths, owing to its near unity birefringence close to the excitonic resonance. These findings, which are unique to TLBP, combined with a resonant optical cavity enabled voltage-controlled polarization conversion at the atomically thin limit–represent a new direction for active control of optical polarization at the nanoscale. The demonstrated high dynamic range of polarization conversion may open an avenue for realization of densely integrated arrays of nanoscale BP electro-optic polarization converters, as a fundamental step beyond discrete dielectric polarization converters in lithium niobate or arrays based on micron-scale liquid crystals spatial light modulator. Previous reports on high-speed BP electro-photoresponse[184] and recent advances in cm-scale layer-controlled growth of BP thin-films[185] suggest that unparalleled possibilities may emerge for large-area, broadband polarization selective sensing, photodetection, and active electro-optic modulation.

Chapter 5. RYDBERG EXCITONS AND TRIONS IN MONOLAYER $MoTe_2$

5.1 ABSTRACT

Monolayer transition metal dichalcogenide (TMDC) semiconductors exhibit strong excitonic optical resonances which serve as a microscopic, non-invasive probe into their fundamental properties. Like the hydrogen atom, such excitons can exhibit an entire Rydberg series of resonances. Excitons have been extensively studied in most TMDCs (MoS_2, $MoSe_2$, WS_2 and WSe_2), but detailed exploration of excitonic phenomena has been lacking in the important TMDC material molybdenum ditelluride ($MoTe_2$). Here, we report an experimental investigation of excitonic luminescence properties of monolayer $MoTe_2$ to understand the excitonic Rydberg series, up to 3s. We report significant modification of emission energies with temperature (4K to 300K), quantifying the exciton-phonon coupling. Furthermore, we observe a strongly gate-tunable exciton-trion interplay for all the Rydberg states governed mainly by free-carrier screening, Pauli blocking, and band-gap renormalization in agreement with the results of first-principles GW plus Bethe-Salpeter equation approach calculations. Our results help bring monolayer $MoTe_2$ closer to its potential applications in near-infrared optoelectronics and photonic devices.

5.2 INTRODUCTION

Excitons[14], excitations which consist of bound electron-hole pairs, in monolayer transition-metal dichalcogenide (TMDC) semiconductors are a suitable platform to investigate a rich variety of condensed-matter phenomena–such as Mott insulators[186,187], Wigner crystals[188], and light-induced magnetic phases[189]–via optical spectroscopy due to their high binding energy and large oscillator strength[15,190–193]. The pronounced optical resonances due to excitons in TMDCs lie below the electronic gap and arise from their atomically thin, two-dimensional nature, which features pronounced quantum confinement and weak dielectric screening[14,15,191,193,194]. In monolayer TMDCs, a valley degree of freedom[195–197] emerges from the crystal structure with C_3 and broken inversion symmetries, which give rise to lowest-energy excitonic states with two-fold degeneracy and displaying opposite chiral selection rules. Beyond the lowest-energy optical excitations, excitons can also exist in hydrogenic internal excited states[19,198,199], known as Rydberg excitons,

which by virtue of their relatively larger wavefunction[191,200] offer a sensitive probe of exciton-electron, exciton-exciton, and other quasiparticle interactions, making them attractive candidates for optical quantum sensing[201–203]. Additionally, Rydberg excitons offer a way to realize giant light-matter interactions (similar to Rydberg atoms) and can be studied in cavity quantum electrodynamics and nonlinear optical measurements[204,205]. While typically observed in resonant reflection measurements[28,194], a number of recent studies on extremely high-quality TMDC samples have reported signatures of Rydberg excitons in photoluminescence (PL)[19,27,29,206,207]. Although such states have been extensively characterized in monolayer MoS_2, $MoSe_2$, WS_2 and WSe_2, [19,27–29,198,206–209] they have not been well explored in monolayer $MoTe_2$ [209].

The 2H phase of monolayer $MoTe_2$ is semiconducting, with the smallest bandgap (in the near infrared) among the Mo-based TMDC materials[17,210–216]. Several studies have reported a phase transition to the metallic-1T' phase, under high carrier doping conditions, which may be useful in phase change photonics[217,218]. The optical properties of $MoTe_2$ change dramatically under the extreme conditions of carrier doping, but even at lower carrier doping ($\sim 10^{11}$ cm^{-2}), the excitonic properties are significantly altered and yield information about quasiparticle and exciton interactions and define exciton-electron dynamics[27,206,207,219]. Because of the presence of heavy tellurium atoms, the spin-orbit coupling effects (~230 meV for valence band and ~43 meV for conduction band) [Champagne et al., submitted] and bright-dark A-exciton splitting (~25 meV)[213] in $MoTe_2$ are much more significant compared to the other Mo-based TMDCs. Additionally, $MoTe_2$ is one of the few van der Waals materials to emit near the silicon band-edge and hence, an accurate understanding of the photo-physics of the entire Rydberg series under different conditions of excitation density, temperature and doping can guide future development of near-infrared optoelectronic and photovoltaic components–such as detectors, modulators, and light emitting diodes.

In this work, we report results of the experimental characterization of the optical properties of electrostatically gated monolayer $MoTe_2$, probed via photoluminescence measurements. Combining high-quality heterostructures and a resonant back-reflector geometry, we identify different optical transitions corresponding to the excitonic Rydberg series. The evolution of emission as a function of temperature reveals a semiconductor-like behavior with quantitative estimation of zero-temperature energies and Rydberg exciton-phonon coupling strengths. By

controlling the charge density in the monolayer $MoTe_2$ from charge neutrality up to electron/hole densities of ~10^{12} cm^{-2} we find strong modulation of optical transitions and continuous tuning of the ground and excited state excitonic manifold–which is computed and illustrated in Fig. 5.1(a). We also perform first-principles calculations based on many-body perturbation theory (MBPT) to obtain the excited-state properties of monolayer $MoTe_2$ including many-electron interactions. First principles GW plus Bethe Salpeter equation (GW-BSE) calculations with a new plasmon pole model developed [Champagne et al., submitted] to account for the dynamical screening of carriers show that the strong tunability is attributed to enhanced screening of the excitonic states from the increased electron density as well as phase space filling which leads to Pauli blocking of optical transitions. Our *ab initio* calculations also capture well the trion binding energy close to charge neutrality. Additionally, a linear linewidth broadening is observed which is attributed to enhanced exciton-electron scattering with increasing carrier density, in qualitative agreement with explicit calculations that consider the scattering of excitons to the degenerate Fermi sea.

5.3 OPTICAL CHARACTERIZATION

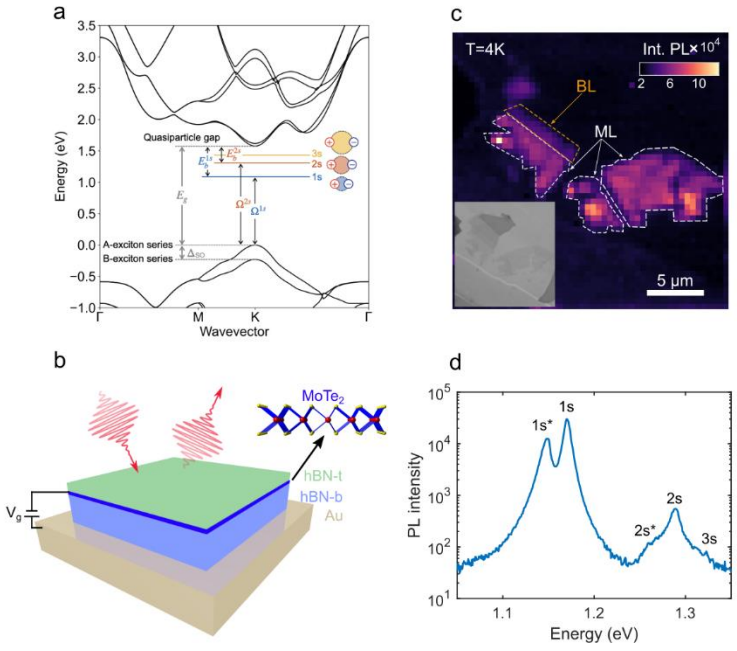

Figure 5.1. Electro-optic investigation of Rydberg excitons in monolayer $MoTe_2$. (a) Excitonic energy landscape of Rydberg series in monolayer $MoTe_2$ with the quasiparticle band structure, exciton state energies Ω^S, and exciton binding energies E_b^S obtained using GW-BSE calculations. (b) Investigated device geometry consisting of hBN encapsulated monolayer $MoTe_2$ on Au

substrate with applied gate voltage. (c) Integrated PL intensity map of investigated sample at 4K. Bright spots indicate monolayer. Inset–optical micrograph of sample. (d) Example PL spectra with assigned Rydberg states.

To efficiently probe the optical properties of monolayer $MoTe_2$ samples, we adopt a Salisbury-screen[57] geometry, shown schematically in Fig. 5.1(b). The $MoTe_2$ is placed approximately a quarter wavelength away from a back-reflector of optically thick gold which also acts as the bottom electrode, to cause a destructive interference of the electromagnetic field at the monolayer, thereby enhancing light-matter interaction. This configuration results in a mild Purcell enhancement of the emission[220] ($F_p \sim 2$, where F_p is the Purcell factor) and allows efficient tuning of the Fermi level in $MoTe_2$ with the application of a gate voltage across the bottom hBN.

Measurements of the spatial dependence of PL at $T = 4K$ yield bright, uniform emission from the monolayer regions of the device. Fig. 5.1(c) shows integrated PL counts, $I_{PL} = \int_{\lambda=800nm}^{1150nm} I(\lambda)d\lambda$, over a bandwidth from 800nm (~1.55eV) to 1150nm (~1.07eV). The bilayer regions exhibit lower emission and a broader peak, while very faint emission is seen from the multilayer regions. There have been reports investigating whether bilayer can become direct gap semiconductor at lower temperatures using emission spectroscopy because of the similar photoluminescence quantum yield[214], $PLQY = \frac{\gamma_r}{\gamma_r + \gamma_{nr}}$, where γ_r, γ_{nr} are the radiative and non-radiative rates, respectively. From our measurements, we find the ratio of the PLQY of the monolayer to bilayer to be three, indicating that the indirect to direct gap transition might happen when $MoTe_2$ is thinned to a bilayer. A representative PL spectrum (Fig. 5.1(d)) from one of the brightest monolayer spots shows sharp emission around 1.172 eV and 1.149 eV with linewidths of 7.13 and 8.77 meV, respectively, which we attribute to the A1s exciton and trion, as reported previously[17,212–216]. Some of the cleanest regions of the sample show extremely narrow linewidths, the narrowest obtained being ~4.48 meV, indicating high sample quality, as shown in Fig. 5.2.

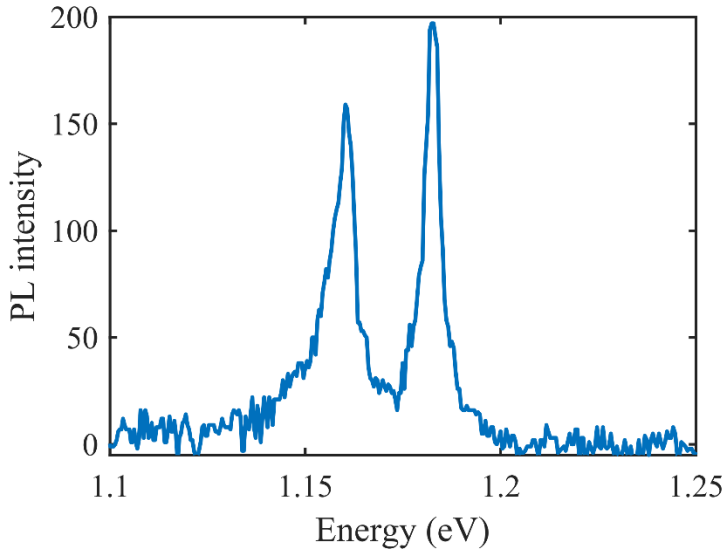

Figure 5.2. Narrowest emission line obtained for the A1s neutral exciton transition.

Ab initio GW-BSE calculations using a modified plasmon pole model to account for dynamical screening associated with free carriers [Champagne et al., submitted] support our understanding of the experimental spectra and enable prediction of important optical properties such as the quasiparticle band gap, optical resonance energies, and exciton binding energies. Within this formalism, one- and two-particle excitations can be calculated using state-of-the-art GW and GW-BSE approach, respectively. Computational details are reported in S4.13 and elsewhere [Champagne et al., submitted]. In monolayer $MoTe_2$, the lowest interband excitonic transition is bright and occurs at the degenerate K and K' points in the Brillouin zone (Fig. 5.1(a)). Due to spin-orbit coupling effects, a splitting of both the valence band maximum and conduction band minimum occurs, resulting in two distinct series of excitons, typically labeled as A and B excitons. The optical gap computed with the first-principles GW-BSE approach, and which corresponds to the lowest-energy A1s exciton energy, is found at $E_{opt} = 1.09$ eV, in good agreement with the experimentally measured gap. The computed GW quasiparticle gap is $E_g = 1.58$ eV, (S4.15). Thus, we predict an exciton binding energy of $E_b = E_g - E_{opt} = 490$ meV for the lowest energy optically-bright excited state. Because of strong Coulomb interactions in low dimensions, charged excitons (trions) are expected to form in monolayer $MoTe_2$. We calculate the binding energy of the negatively charged exciton from first principles by solving the corresponding equation of

motion for three-quasiparticle correlated bound states (S4.16) and obtain 20.6 meV (S4.16), in agreement with former reports[17] and measured values of ~23 meV.

Additional luminescence peaks are seen at higher energies at 1.269 eV, 1.29 eV and 1.315 eV, and have been identified as the A2s trion, A2s exciton and A3s exciton, respectively, in accordance with previous reports on $MoTe_2$[209] and other TMDCs. The assignment of these excitonic and trionic peaks is in accordance with nomenclature which reflects how the exciton wavefunction transforms under the crystal symmetry in analogy with the hydrogen atom[221]. Our ab-initio GW-BSE calculations (S4.15) predict higher excited state excitons at 1.31 eV, 1.35 eV, and 1.43 eV, corresponding to the A2s, B1s, and A3s excitons, respectively. The slight discrepancy in the peak energies and re-ordering of the B1s and A3s exciton is likely related to the enhanced screening of $MoTe_2$ by the hBN dielectric, which is not considered in the calculations. The observation of Rydberg states up to 3s enables investigation of stronger Rydberg interactions, as well as photon-matter coupling, in $MoTe_2$. The linewidths observed for these excited states are exceptionally narrow, ~10 meV and ~25 meV for the 2s and 3s exciton, respectively. Additionally, the brightness of the 2s state is ~10% of the 1s state which is comparable to or higher than that for other TMDCs.

5.4 POWER AND TEMPERATURE DEPENDENT DYNAMICS

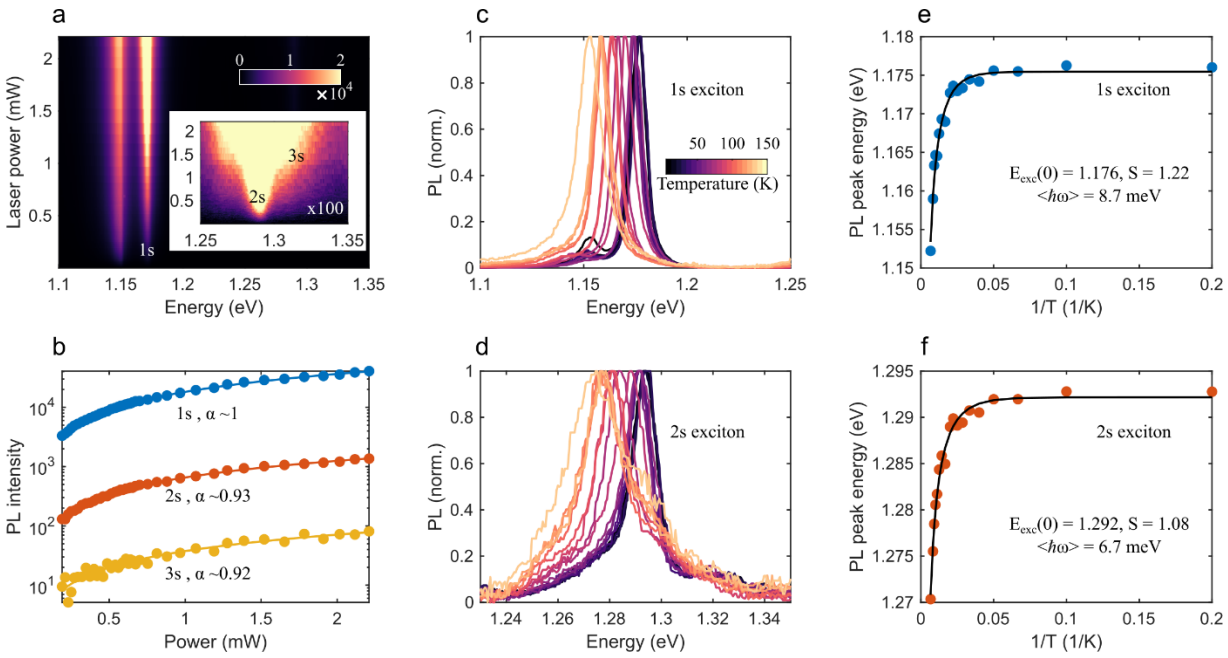

Figure 5.3. Pump power and temperature dependence of Rydberg excitons. (a) PL intensity variation with increasing pump power for the 1s exciton. Inset–PL(x100) for the 2s and 3s exciton. (b) Semi-log scale plot of intensity dependence of PL with pump power and corresponding fits to a power-law showing excitonic emission ($I_{PL} = I_0\, P^{\alpha}$). (c), (d) Temperature variation of normalized PL spectrum for the 1s and 2s exciton regions, respectively. (e), (f) Fits to a temperature model estimating different parameters for the 1s exciton and 2s exciton.

To verify that the emission is excitonic in nature, we performed pump-power dependent photoluminescence measurements. We scanned the incident pump fluence over 2 decades in intensity and observed an increase in the emission intensity (Fig. 5.3(a)). A mild spectral broadening is associated with increasing pump density, originating from enhanced exciton-exciton interactions. We analyze the peaks by fitting to a Lorentzian lineshape profile, $I_{PL} = \sum_{i=Rydberg\ states} \frac{\frac{A_i \Gamma_i}{2}}{(\omega-\omega_i)^2+\left(\frac{\Gamma_i}{2}\right)^2}$ -- $(5.E1)$, where A_i is the oscillator strength, Γ_i is the broadening (full-width at half maximum) and ω_i is the resonance frequency of each resonance, respectively.

We can extract the integrated PL intensity, $\int I_{PL,i}(P)\, d\omega = C_{0,i}P^{\alpha_i}$, where P_i is the incident power and α_i is the exponent for each resonance, $I_{PL,i}$ is given by equation 5.E1 and $C_{0,i}$ is a dimensionless constant as a function of pump power. Near linear scaling is seen for all the excitonic states as shown in Fig. 5.3(b), plotted in semi-log scale, with exponents as $\alpha = 1, 0.93, 0.92$ for 1s, 2s and 3s states, respectively. This excludes any defect related emission as no saturation or non-linearity is observed over 2 orders of magnitude of incident pump power.

Rydberg excitons in $MoTe_2$ also show strong temperature dependence, consistent with previous observations in other TMDCs. While the lowest energy state has been investigated for $MoTe_2$, there is lack of knowledge about the excited state dynamics with temperature. Our measurements, in Fig 5.3(c) and (d) for the 1s and 2s exciton, respectively, show a redshift for excitonic states with increasing temperature which can be modeled with a semi-empirical semiconductor bandgap dependence of the form $E_{exc}(T) = E_{exc}(0) - S\langle\hbar\omega\rangle\left[\coth\left(\frac{\langle\hbar\omega\rangle}{k_BT}\right) - 1\right]$, where $E_{exc}(0)$ is the resonance energy at zero temperature limit, S is a dimensionless constant, k_B is the Boltzmann constant and $\langle\hbar\omega\rangle$ is the average phonon energy[212]. From the fits, we extract the parameters summarized in Table 5.T1, also shown in Fig. 5.3(e), (f). Furthermore, the PLQY drops with increasing temperature, which is attributed to an increase in accessible non-radiative decay channels from the phonon contributions (evident from the linewidth broadening with increasing temperature, shown in Fig. 5.4), while the radiative contribution remains constant. The zero-limit exciton energy indicates the Rydberg state energy levels, in close agreement with ab initio GW-BSE computed energy levels (A1s: 1.09 eV and A2s: 1.31 eV), which correspond to $T = 0K$. Interestingly, the relative intensity of the 2s exciton state with respect to the 1s state grows with increasing temperature (see Fig 5.4), possibly stemming from weaker coupling with the phonons.

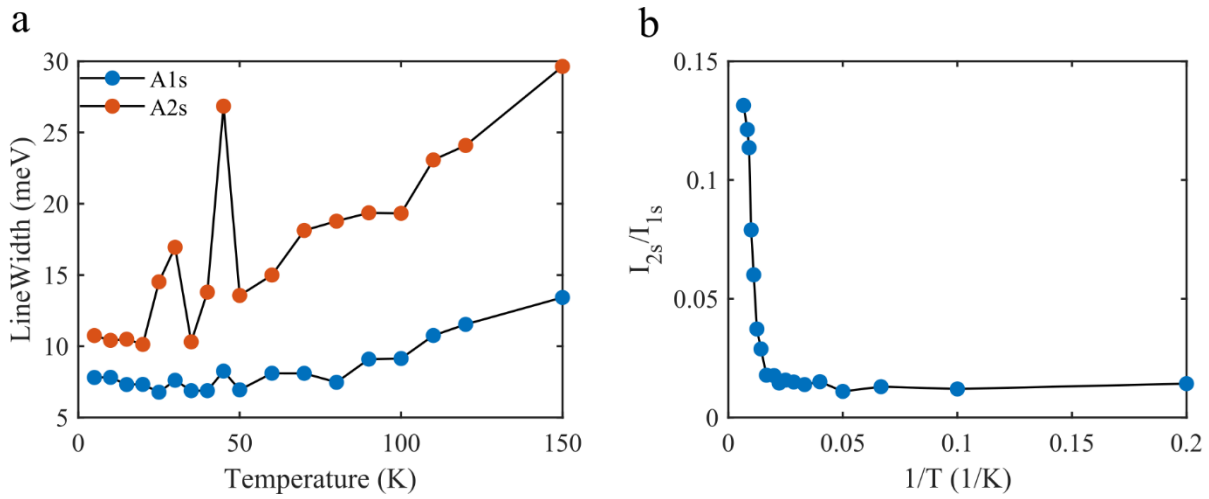

Figure 5.4. Temperature dependent emission properties. (a) Temperature dependent linewidth broadening of the A1s and A2s excitonic state. (b) Intensity ratio of the 2s/1s excitonic state with temperature (1/T).

Table 5.T1. Experimentally measured zero-temperature exciton energy and exciton-phonon coupling parameters for the Rydberg states.

State index	Energy $(E_{exc}(0))$ (eV)	S	$\langle\hbar\omega\rangle$ (meV)
1s	1.176 ± 0.019	1.22 ± 0.434	8.7 ± 7.009
2s	1.292 ± 0.018	1.08 ± 0.304	6.7 ± 5.825

5.5 ELECTRICALLY TUNABLE RYDBERG EXCITON EMISSION

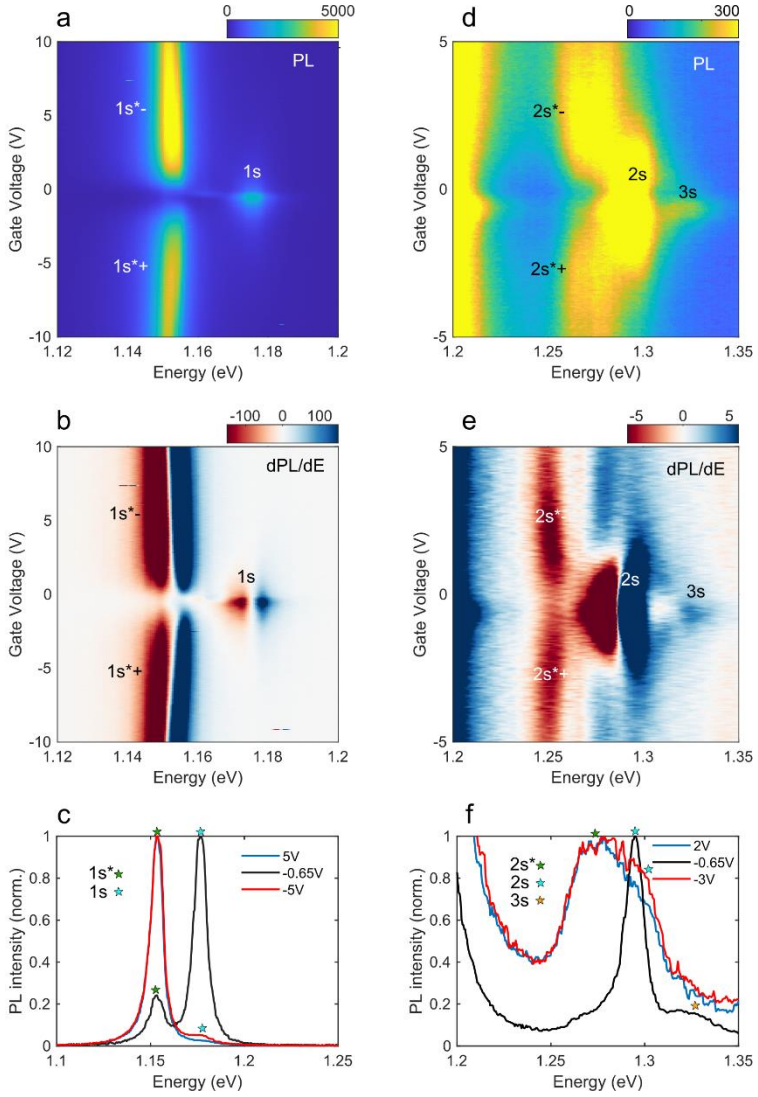

Figure 5.5. Gate dependent PL spectrum of Rydberg excitons. (a), (d) PL intensity of different neutral exciton species and their corresponding trion features as a function of gate voltage near the 1s and 2s/3s resonance, respectively. (b), (e) Derivative of the PL spectra, $\frac{dPL}{dE}$, shown in (a), (d). (c), (f) Line cuts of the PL spectrum at different voltages showing the different exciton and trion resonances.

Reduced dielectric screening and strong electron-hole Coulomb interactions in two dimensional semiconductors make their electronic and optical properties highly sensitive to their dielectric environments[22,193,194,199,219,222,223]. In particular, the presence of free carriers can significantly affect the electronic landscape of a TMD monolayer[17,27,206–208,219]. A key finding of our study, summarized in Fig. 5.5, is the carrier dependence of the exciton-electron interaction, as quantified by the gate voltage dependence of the exciton and trion emission properties. We first focus near the 1s exciton resonance illustrated in Fig. 5.5(a)-(c). A false color map shows the evolution of the 1s exciton and trion peaks as a function of applied gate voltages ($V_g = -10V$ to $10V$). At very low voltages the neutral exciton peak dominates in emission, but with a very small change in the carrier density the trion peak rapidly emerges as a dominant feature on either side of $V_g \sim -0.65V$ (which is identified as the charge neutral condition from the peak in neutral 1s exciton emission intensity). At higher voltages the emission from the neutral exciton is completely suppressed. While trion emission grows in intensity for higher voltages, it eventually saturates and shows a slight reduction at even higher voltages. Such changes are better visualized in the derivative of PL with respect to energy ($\frac{dPL}{dE}$), shown in Fig. 5.5(b) and (e) for different regions of the gate voltage. The resonances corresponding to the 2s and 3s excitonic states show a qualitatively similar doping dependence (Fig. 5.5(d)-(f)). Line-cuts corresponding to near charge neutral condition and finite doping showing strong exciton and trion emission spectrum are plotted in Fig. 5.5(c) and (f) for the 1s and 2s, 3s states, respectively.

5.6 DOPING DEPENDENT EXCITON EMISSION PROPERTIES

To quantitatively understand the doping induced changes in the emission dynamics, the spectrum is fitted to a sum of multiple Lorentzian features, as given by (5.E1), corresponding to the different exciton and trion states.

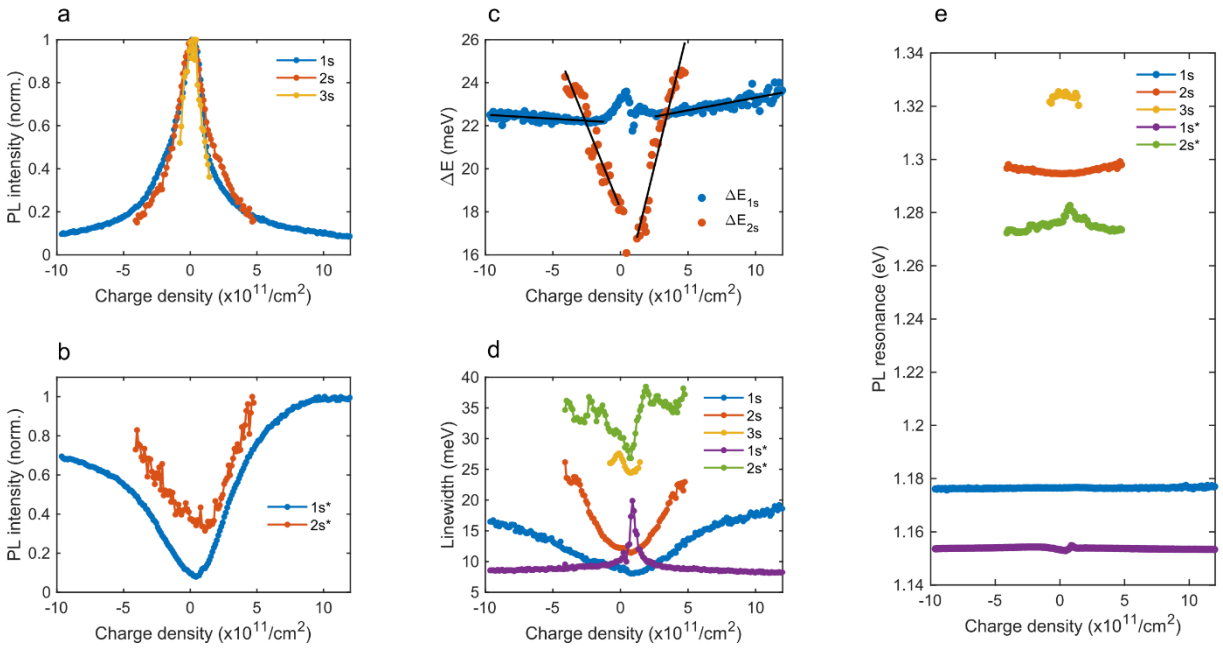

Figure 5.6. Gate tunable PL properties of Rydberg excitons. (a), (b) PL intensity (normalized) of different neutral exciton, trion species, respectively, as a function of charge density. (c) Energy shifts between the neutral exciton and the trion for 1s and 2s states as a function of charge density. (d) Evolution of the linewidth and (e) resonance energy of various exciton and trion states as a function of charge density.

The evolution of the peak intensity, linewidth and energy are then extracted as a function of carrier density, with the results presented in Fig. 5.6. Fig. 5.6(a) and (b) quantify the changes in the PL intensity of the different exciton and trion states, as discussed previously. A crossover-density (N_c) is defined where the exciton and trion intensities overlap and is identified to be $V_g = 0.296V$ and $V_g = -1.36V$ on the electron and hole side, respectively, for the 1s state. This corresponds to charge densities of $N_c^- = 2.08x10^{11}\ cm^{-2}$ and $N_c^+ = 1.54x10^{11} cm^{-2}$, respectively. Additionally, as seen in Fig. 5.6(e), the exciton slightly blue shifts (2s much more than 1s) with increasing charge density, while the trion redshifts. A qualitatively similar trend is seen for the features corresponding to the 2s exciton state and a crossover-density of $V_g = 1.24V$ and $V_g = -2.42V$, corresponding to $N_c^- = 4.19x10^{11}\ cm^{-2}$ and $N_c^+ = 3.95x10^{11}\ cm^{-2}$ is identified on the electron and hole side, respectively. The emission strength from the 3s trion state, which

appears red-shifted to the 3s excitonic state, is not high enough to perform further quantitative analysis. However, from the derivative of PL measurements in Fig. 5.6(e) and (f), it is clear that a similar qualitative picture also holds true for the 3s state. Further studies with magnetic fields are required to study quantitative dynamics of the even higher states, so that the visibility is improved. Our observations are consistent with previous reports of gate-tunable exciton and trion intensities in other TMDCs[27,206,207].

The energy differences ($\Delta E = E_{exciton} - E_{trion}$) between the exciton and trion exhibit an unusual gate dependence and show striking difference between the 1s and 2s states (Fig 5.6(c)). An overall slight blue shift of the energy difference ΔE_{1s}~1 meV, over a doping density of n~$1x10^{12}$ cm^{-2} is seen. A linear fit for ΔE_{1s} reveals a rate of change in the exciton energy of $0.103\ \frac{meV}{10^{11}\ cm^{-2}}$ ($0.118\ \frac{meV}{10^{11}\ cm^{-2}}$) for the electron (hole) doping. A zero-density limit of the energy shift provides the trion binding energy which is 21.94 meV (22.14 meV) for the negative (positive) trion. The energy shift is highly exaggerated for the 2s state, where a much larger shift of ΔE_{2s}~10 meV is seen over a smaller doping density of n~$5x10^{11}$ cm^{-2}. A similar analysis yields $1.57\frac{meV}{10^{11}\ cm^{-2}}$ $\left(2.56\ \frac{meV}{10^{11}\ cm^{-2}}\right)$ for the electron (hole) doped case. The trion binding energies are estimated to 18.14 meV (13.76 meV) for the negative (positive) side. The lower binding energy of the 2s trion compared to the 1s state follows from the lower binding energy of the corresponding neutral state. This unusually larger energy shift is understood as stemming from the larger wavefunction of the 2s state and thus, higher susceptibility to the electronic landscape which also is evident from the stronger dependence of the oscillator strength with doping density of the 2s state as compared to the 1s state. These results are illustrated in Fig. 5.6(c) and summarized in Table 5.T2. In general, we expect the sensitivity of self-doping to increase dramatically with even higher lying Rydberg states.

Table 5.T2. Experimentally measured binding energy and energy shifts for Rydberg trions.

State index	$E_{b,trion^+}$(meV)	$E_{b,trion^-}$ (meV)	$\frac{\Delta E}{\Delta n^+}$(meV/$10^{11}$ cm^{-2})	$\frac{\Delta E}{\Delta n^-}$(meV/$10^{11}$ cm^{-2})
1s	22.14 ± 0.20	21.94 ± 0.10	0.118 ± 0.03	0.103 ± 0.02
2s	13.67 ± 0.12	18.14 ± 0.09	2.56 ± 0.16	1.57 ± 0.19

We also measure the linewidth evolution (Fig. 5.6(d)) and observe that neutral exciton states exhibit linewidth broadening as a function of doping density. Additionally, while the 2s trion broadens, the 1s trion remains nearly unchanged with increasing carrier concentration.

5.7 DISCUSSION

To better understand doping induced changes in the optical properties we use first-principles GW and GW-BSE calculations with a modified plasmon pole model [Champagne et al., submitted] to compute the exciton spectrum under different carrier densities. For optical excitations close to the band edge, we find two main effects to support our experimental observation: (i) a doping-independent ground exciton energy (Fig.5.7(b)) and (ii) a suppression of the exciton oscillator strength (Fig.5.7(c)). Numerical results are reported in Table 5.T3.

Table 5.T3. Computed Rydberg exciton binding energy and relative dipole moment as a function of doping density.

Doping density (cm^{-2})	A1s		A2s		A3s	
	ΔE_b (meV)	Rel. Dipole Moment	ΔE_b (meV)	Rel. Dipole Moment	ΔE_b (meV)	Rel. Dipole Moment
0	0	1	0	0.25	0	0.09
2.3×10^{11}	-116	0.58	-78	0.08	-90	0.03
1.6×10^{12}	-246	0.28	-173	0.03	-192	0.02
3.0×10^{12}	-301	0.10	Not detectable			
4.5×10^{12}	-353	0.05				
5.9×10^{12}	-366	0.02				
8.7×10^{12}	-368	0.01				

The evolution of the exciton energy with increasing doping density arises from an interplay of various effects[224–226]. In the low-doping regime, the doping-independent exciton energy results from a compensation between the band gap renormalization and exciton binding energy reduction (Fig.5.7(a) and (b)), expected from the reduced electron-hole Coulomb interaction.

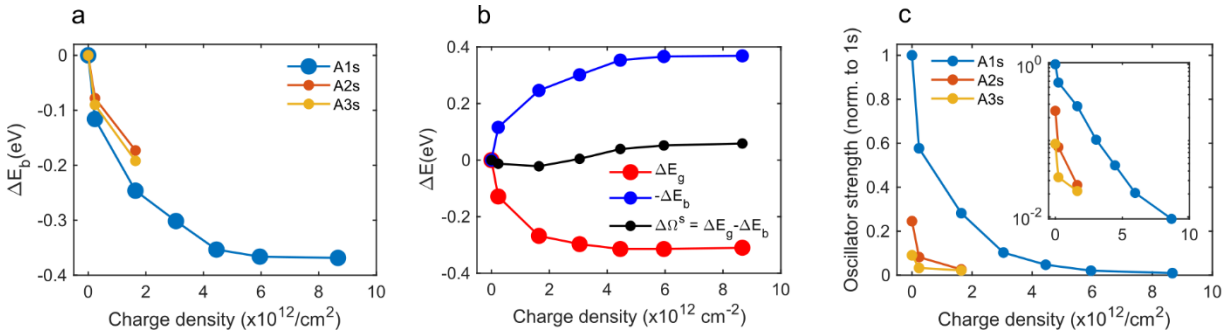

Figure 5.7. Doping dependent theoretical results. Doping dependence of (a) the variation in exciton binding energy, ΔE_b, for the ground A1s exciton, and the excited A2s and A3s states, (b) the variation in exciton energy $\Delta\Omega^s$ (black curve), the exciton binding energy ΔE_b (blue curve), and the renormalization of the QP band gap ΔE_g (red curve) for the ground A1s exciton, (c) the oscillator strength for the A1s, A2s and A3s states. (inset) Same as (c) plotted in semi-log scale on the y-axis.

At higher doping concentration, the ground exciton peak is expected to blueshift slightly, as the exciton binding energy saturates, while the quasiparticle gap slightly increases due to an increase of the energy continuum with the free carrier concentration[225]. In addition, as the doping density increases, the exciton delocalizes in real space (exciton wave function reported in Fig. 5.8), and Pauli blocking prevents transitions around the K valley, which is eventually reflected in a decrease of the oscillator strength of the exciton peak, as shown in Fig.5(c). This argument can be related to the intrinsically lower oscillator strength (and by reciprocity, lower PLQY) of the higher order Rydberg states–also due to a more delocalized wave-function in real space. Similarly, the exciton binding energy and oscillator strength of the A2s and A3s excited states decrease rapidly, and the corresponding peaks quickly vanish above a doping density of $2\text{x}10^{12}$ cm^{-2}.

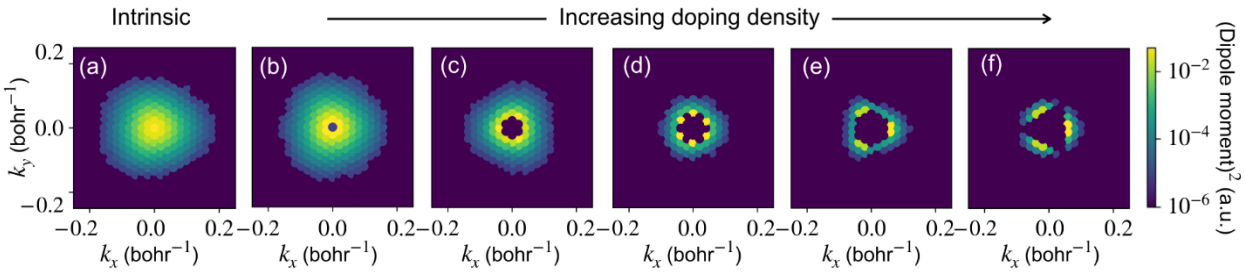

Figure 5.8. Wave-function evolution with doping density. (a)-(f) Evolution of the exciton (A1s) wavefunction as a function of doping density showing Pauli blocking. (b) 2.3 x10^{11} cm^{-2} (c) 1.6 x10^{12} cm^{-2} (d) 3.0 x10^{12} cm^{-2} (e) 4.5 x10^{12} cm^{-2} (f) 5.9x10^{12} cm^{-2}.

The average lifetime, τ, of an unstable particle is related to the decay rate γ, as $\tau = \frac{1}{\gamma}$. The PL linewidth L, obtained as $L = \frac{\hbar}{\tau} = \hbar\gamma$, provides information about intrinsic contributions from radiative exciton lifetime and dephasing from exciton-phonon scattering, as well as extrinsic inhomogeneous broadening effects (e.g., doping, defects, substrate-induced disorder). In $MoTe_2$ monolayer, the bright exciton state is energetically below the dark states, which, at low temperature, prevents scattering towards intervalley exciton states that would require the absorption of a phonon. Therefore, at low temperature, the intrinsic contributions to the linewidth are dominated by radiative exciton decay[227]. Using Fermi's golden rule[228], we compute a radiative exciton lifetime of 0.3 ps, corresponding to a radiative linewidth of 2.2 meV for the ground exciton. The discrepancy with the experimental zero-doping linewidth of 7.13 meV comes from inhomogeneous broadening effects, such as the presence of defects or substrate effects. Furthermore, due to the presence of a back reflector which gives rise to a slight Purcell enhancement in emission, it is expected that the enhanced radiative rate is higher than the computed one in vacuum (by approximately ~2). With increasing doping density, charged excited states, known as trions, emerge and couple to the excitons. Using the microscopic many-body theory developed in previous studies[226], we expect an approximately linear exciton linewidth broadening with doping density (~8.7 meVcm^{-2}, in our measurements) due to enhanced exciton-electron scattering.

5.8 CONCLUSIONS

In summary, we report on the optical luminescence features of a monolayer $MoTe_2$, including Rydberg excitons up to 3s states, by combining results of experimental photoluminescence measurements and first principles calculations. We observe a linear dependence of the exciton peak energy with incident pump fluence and a red shift with increasing temperature, following a semi-empirical semiconductor relationship. The optical response can further be modulated with gate voltage, with an efficient exciton to trion conversion. With increasing doping density, we predict (i) a reduction in the exciton oscillator strength and (ii) a near-constant (mild blueshift) exciton energy, supporting our experimental measurements. Our understanding of $MoTe_2$ photo-physics creates a foundation for understanding and design of future optoelectronic devices in the near infrared.

Chapter 6. SIGNATURES OF EDGE-CONFINED EXCITONS IN MONOLAYER BLACK PHOSPHORUS

6.1 ABSTRACT

Quantum confining two-dimensional excitons in van der Waals materials via electrostatic trapping[229,230], lithographic patterning[231–234], Moiré potentials[235–238], and chemical implantation[239,240] has enabled controlled tailoring of light emission. While such approaches rely on complex preparation of materials, natural edges provide an omnipresent, yet rich playground for investigating quantum-confined excitons. Here, we observe that certain edge sites of monolayer black phosphorus (BP) strongly localize the intrinsic quasi-1D excitons, yielding discrete spectral lines in photoluminescence, with nearly an order of magnitude linewidth reduction. We find, through a combination of detailed structural characterization using transmission electron microscopy of BP edges and rigorous GW+BSE calculations of BP nanoribbons, that certain atomic reconstructions in conjunction with strain and enhanced sensitivity to the electrostatic environment can give rise to such distinct emission features. We observe linearly-polarized emission from edge reconstructions that preserve parent mirror symmetry, which agree well with our calculations. Furthermore, we demonstrate strong electrical switching of the edge-excitons, similar to an excitonic transistor. Our results motivate investigation of BP nanoribbons and quantum dots for tunable quantum light generation, metasurfaces and implementation into solid-state photonic circuits for quantum information processing as well as for the study of exotic phases that may reside in such edge-based structures.

6.2 INTRODUCTION

The quest to generate tunable light for classical and quantum-optics based applications has rendered two-dimensional (2D) semiconductors hosting strongly bound excitonic quasiparticles[13,241] as emerging candidates. A combination of strong oscillator strengths due to reduced screening[200], presence of Rydberg excited states[15,242] and polarization-selective properties[197,243] make excitons desirable in many frontiers. For example, a strong confinement of excitons in real space to discretize their center of mass motion results in a smaller Bohr radius and

a longer lifetime–which facilitates dipole-dipole interactions enabling exploration of quantum non-linear effects[244]. Owing to the strong susceptibility of excitons to external manipulation, schemes such as gate-defined electrostatic traps[229,230], strain engineered landscapes[231–234,237], Moiré potentials in twisted bilayer systems[235–238] and ion-irradiated point defects[239,240] have been explored to achieve exciton control and confinement. One strategy that has been overlooked, thus far, is the edges of two-dimensional crystals–where the symmetry breaking of the crystalline structure as well as an effective reduction in dimensionality at the edges directly results in a locally modified electronic structure. Such modifications can have important implications in building electronic, optical, thermoelectric, and catalytic devices. Moreover, edges have been known to host exotic transport properties including the observation of metallic and topological states[245–248] as well as display novel optical effects[249–251], but little is known about its impact on excitonic properties.

Not only are edges ubiquitous to every material, but they can also exhibit strong gradients and inhomogeneities in the dielectric environment and strain landscape–which could, with judicious schemes, be harnessed to confine excitons. An extremely large deformation potential[252–255] and high sensitivity to environmental screening[222] puts monolayer black phosphorus (BP) in a unique position to have strongly modified excitons at the edges. Furthermore, unlike the well-investigated transition metal dichalcogenides (i.e., MX_2, where M = Mo, W and X = S, Se, Te) that have its band-edge at the K point[14], BP exhibits highly anisotropic optical transitions at the Γ point, which results in a larger sensitivity to layer thickness and subsequent quantum confinement effects[177,256,257]. In fact, several theoretical reports on BP nanoribbons and quantum dots have predicted the emergence of quantum-confined edge states with distinct opto-electronic properties[258–261]. BP edges exhibit vastly different properties depending upon the fracture plane - armchair (1,0), zigzag (0,1) or a mixed (such as 1,3) configuration[250,262–266]. Additionally, edges undergo atomic reconstruction to minimize their free energy in a non-periodic environment, some of which perturb lattice symmetries and modify optical selection rules, causing a rotation of the exciton dipole[250,262,265,267]. However, despite such predictions for novel electronic states at the edges of monolayer BP, they have remained elusive likely due to the air-sensitive nature of BP, which is exasperated in the monolayer limit[268].

In this work, we report on novel optical properties observed at certain edge sites of high quality exfoliated monolayer BP heterostructures encapsulated in an inert environment with hexagonal boron nitride (hBN). We use low-temperature confocal photoluminescence measurements and find striking differences in the optical spectrum at such edge sites compared to the interior of the sample. For brevity, we address optical transitions seen at the edges of samples as "edge excitons" and the transitions from the interior as "interior excitons", for the remainder of the text. Transmission electron microscopy on bare and graphene-encapsulated monolayer BP flakes indicate atomically rough morphology at the edges, along with signatures of edge reconstruction and strain inhomogeneity. Through rigorous GW+BSE calculations of reconstructed edges in phosphorene nanoribbons we find the emergence of additional states in the optical absorption, whose wave functions are strongly confined to the edges. Our results are best explained through an interplay of emergence of edge reconstruction-driven optical transitions and sensitivity of the edges to strain and screening effects. Finally, we demonstrate that the edge excitons can be modulated (switched on and off) with an electrostatic gate through a combination of an in-plane dc Stark effect and doping-induced screening.

6.3 OPTICAL SPECTROSCOPY OF EDGE EXCITONS

A typical sample in this study is conceptually illustrated in Fig. 6.1(a), where a heterostructure consisting of a monolayer BP flake, encapsulated in hBN dielectric layers (right schematic) exhibits distinct emission features at the edges compared to the interior of the crystal (left schematic). We present spectroscopic data from a total of four devices–two containing electrostatic gates–showing similar behavior. Confocal, spatially-resolved photoluminescence spectra were acquired with a continuous-wave 532 nm (2.33 eV) excitation laser (see appendix for details of the measurement configuration). The false colormap of integrated photoluminescence intensity in Fig. 6.1(b) shows bright uniform emission from the monolayer regions of sample #gateD1. Quite strikingly, in contrast to previous reports on monolayer BP excitons[22,256,269], we notice significantly different spectral features at the edges of the flake–plotted in Fig. 6.1(c). Each spectrum has been normalized to unity, with the color scheme matching that of the spatial location labels (stars) in Fig. 6.1(b). A series of narrow, sharp emission lines emerge, that appear on top of a relatively broad background envelope which resembles emission from a typical monolayer exciton in the interior of the BP flake. For a better comparison, normalized spectra from the interior and one

edge-site are plotted together, in Fig. 6.1(d). Clearly, the spectral features corresponding to the edge and interior display significant differences and merit further investigation. Since the emission background envelope at the edges qualitatively resembles that of the interior in its lineshape, it implies that the optical cross section (~500 nm) overlaps with the interior and is larger than the spatial extent of the edges in these measurements. The spectrally narrow lines emerging at the edges are quite sensitive to the spatial location in the heterostructure and are, generally, not energetically even in spacing. The edge emission peaks exhibit typical linewidths between ~3-10 meV, while the interior exciton has a linewidth of ~>30-50 meV–varying slightly across different heterostructures and spatial locations due to fabrication-induced sample inhomogeneities[157]. An approximate order of magnitude reduction in linewidth likely arises from stronger quantum confinement and decoupling of the excitons from the lattice, resulting in reduced scattering of the excitonic quasiparticles.

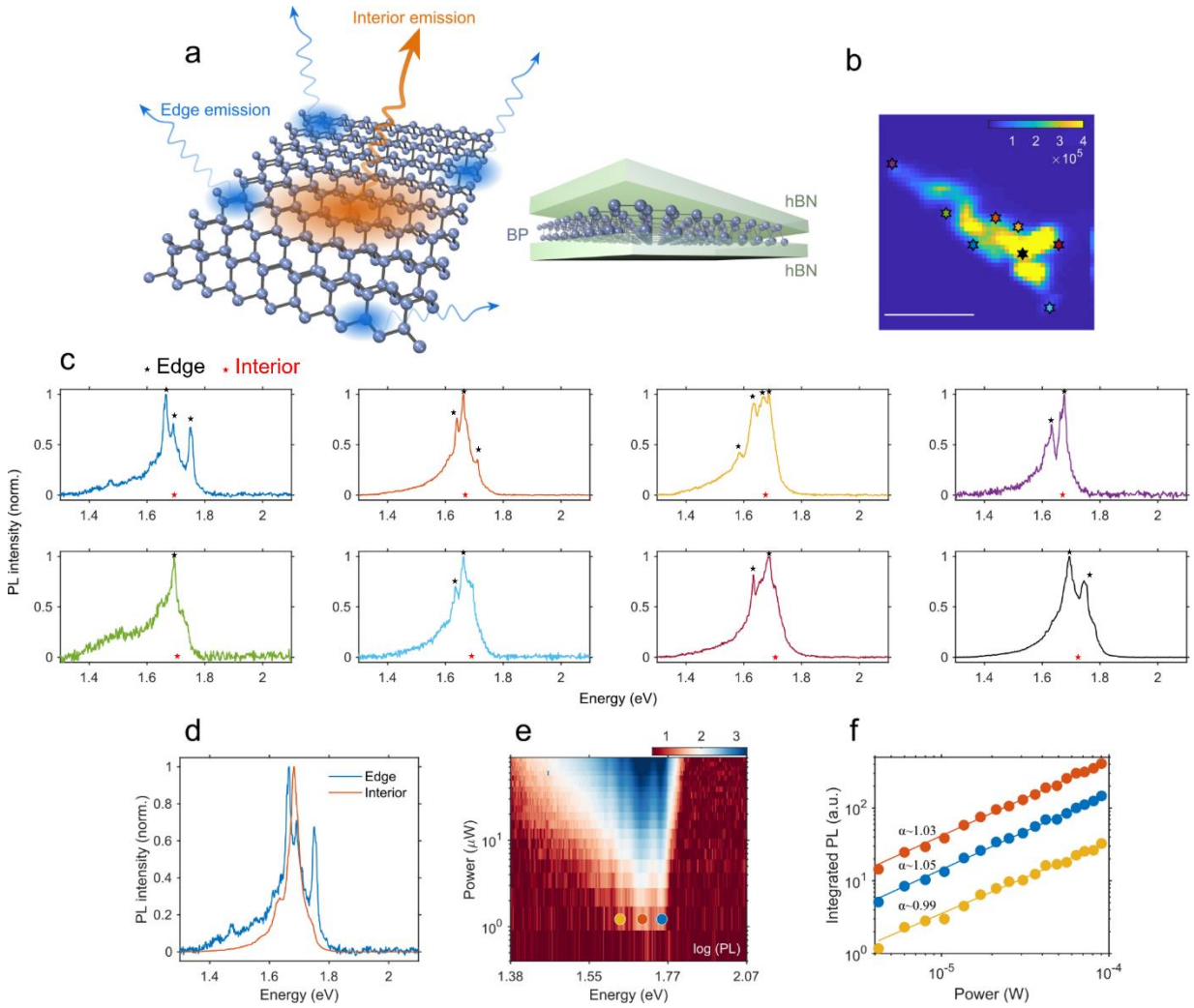

Figure 6.1. Emergence of edge excitons in monolayer BP. (a) Schematic of two different emission mechanisms originating from interior (orange) excitons and edge (blue) excitons and typical heterostructure schematic studied in this work. (b) Integrated PL intensity map of a MLBP sample (#gateD1) with spatial points marked along certain edges showing bright and distinct peaks (scale bar is 5 μm). (c) Normalized PL spectrum from points marked in (b). (d) Normalized PL spectra from an edge and the interior of the sample shown in (b) to highlight the spectral feature differences. (e) Variation of PL spectrum (log scale color) with incident laser power (y-scale log) for an edge spot containing three distinct peaks. (f) Power law fit to the integrated PL intensity for the corresponding three peaks in (e) showing linear excitonic behavior (α~1), plotted in log-log scale.

Most of the edge emission features showed power scaling analogous to the interior confirming the observed emission to be excitonic in nature. Emission from one such spot (from sample #D6) has been shown in Fig. 6.1(e) as a false colormap (in log scale) of photoluminescence spectrum versus incident power. The three peaks at 1.75, 1.69 and 1.63 eV display near-unity exponent ($\alpha = 1.05, 1.03$, and 0.99, respectively) evolution, as shown in Fig. 6.1(f). This establishes that the discrete features are excitonic in nature and do not show saturation in emission up to ~100μW of incident power (~1.21 GW/m^2)–ruling out point defects or multi-excitonic species. Furthermore, a similar analysis across twenty-four measured spots on one sample revealed a small variation in the exponent (α) between 0.9 and 1.1 (appendix), indicating that the intensity linearity should be a generic feature to all edge excitons.

Interestingly, the power dependence for edge excitons does not show non-linearity or saturation behavior–meaning they are still in a quasi-1D regime, but an order of magnitude lower linewidth (higher temporal coherence and longer lifetime) establishes a strong decoupling from the lattice. We find edge excitons to occur between 1.61 and 1.72 eV, over a bandwidth of 110 meV and generally red shifted with respect to the interior exciton; occasionally we find blue-shifted features like in Fig. 6.1(d). Furthermore, the interior emission is best described by a sum of two Lorentzian oscillators–one corresponding to the excitonic transition and one shoulder peak which is likely from native defects in the crystal (shown in Fig. 6.2). Further studies on higher quality crystals may enable even narrower linewidths of both the interior and edge excitons, resulting in complete spectral separation of the two types of excitons. It is worth noting that not all edges exhibit such peaks and is likely related to the diversity of edge terminations possible, as discussed later.

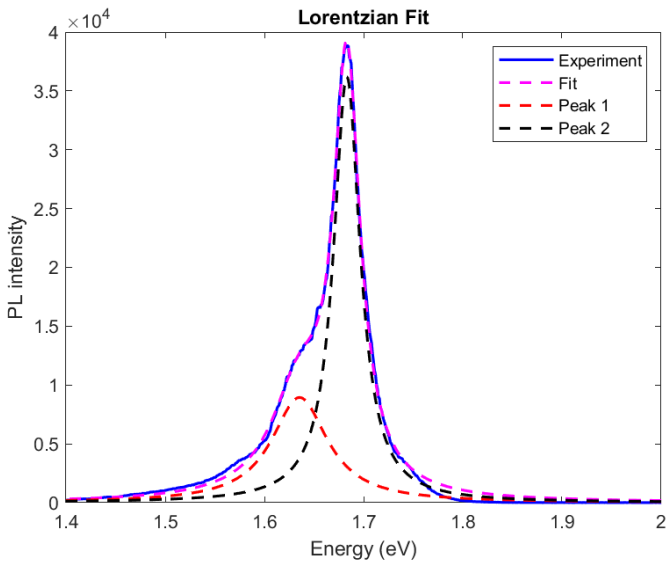

Figure 6.2. Lorentzian fit to monolayer BP emission. 2-peaks fit to an interior exciton emission from the interior of device #gateD1. The peak at ~1.7 eV is the interior exciton while the lower energy shoulder peak is likely from defects in the native crystal.

6.4 POLARIZATION AND TIME-DEPENDENT PHOTOLUMINESCENCE

BP is known to have strong linear dichroism in its emission properties due to its unique crystal structure and optical selection rules–motivating investigation of the polarization dynamics of the edge excitons. Fig. 6.3(a) displays a false colormap of photoluminescence spectra as a function of polarization angle for a spatial location in sample #D6. The individual peak intensity variation with emission azimuthal angle, associated with the emission colormap shown in Fig. 6.3(a), pointed with arrows, were fit to a polar equation of the following form $I = I_0 \cos^2(\theta - \theta_0) + c$, where, θ_0 is the azimuthal orientation of the emission and I_0, c are constants which denote the peak, polarized and unpolarized, background component of the total emission, respectively. The results of the fits, summarized in Fig. 6.3(b), clearly show that all of the emission patterns fit well to a linear dipole model, establishing that emission observed from these states are linearly polarized.

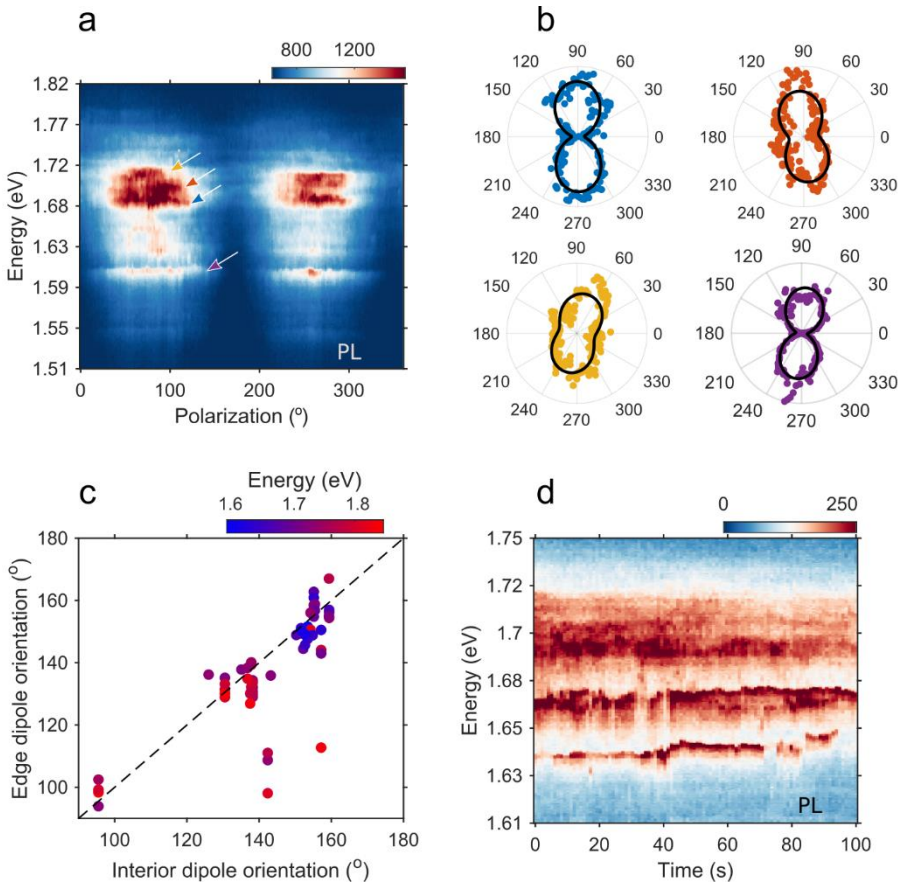

Figure 6.3. Polarization and time-dependent emission dynamics. (a) PL spectrum from one edge site as a function of polarization (measured by rotating the analyzer on the emission side). The emission is nearly aligned with each other and the interior background with small azimuthal mismatch between the peaks. (b) Polar plots, along with dipolar fits, to determine the azimuthal orientation of different peaks corresponding to emission profiles in (a). (c) Comparison of the interior exciton orientation versus the edge states (as determined by fitting the peaks to Lorentzian shaped discrete edge states and an interior contribution). The color of the spots is determined by the emission energy, as shown in the color bar (in eV). (d) Spectral wandering and blinking seen in emission as a function of time for one representative edge site.

Quite interestingly, for Fig. 6.3(a), the polar plots show nearly similar dipole alignment with small angular mismatch in the azimuthal orientation. To investigate this in more details, we studied multiple spatial spots across all four devices and the aggregated azimuthal variation between the local interior exciton (which corresponds to the local armchair direction and is extracted from the

background envelope of the emission profile), and the edge excitons is plotted in Fig. 6.3(c), along with a guide to the eye line (with a slope of 1). The color for each spot denotes the emission energy, as indicated by the color scale bar. Under the absence of a mechanism responsible for breaking mirror symmetry and modifying the optical selection rules, the interior and edge excitons are expected to be nearly aligned in their orientation. A large cluster of states are indeed found to be lying close to the dashed line–establishing that the edge exciton emission is intimately linked to the intrinsic anisotropy of BP.

We monitored temporal spectral variation from many such edge sites (appendix), revealing jitter and blinking behavior, out of which emission from one such site is shown in Fig. 6.3(d), indicating that the emission is arising from confined states that are more sensitive to local charge fluctuations. The sensitivity to local charge fluctuations is likely due a combination of charge hopping at the dangling bonds on the edges, hopping between nearly degenerate edge-reconstruction states, and a reduced density of states. This is in stark contrast to the interior emission which is stable under continuous pumping on similar time scales (appendix).

To estimate the binding energy of these states, we performed temperature dependent emission measurements. Since the absolute PL intensity is dependent not only on the binding energy (radiative efficiency) of a state but also on geometric factors, we found it unreliable to study the intensity trends quantitively as a function of temperature–given that the measurement system drifts at least a spot size over large temperature ranges, making quantitative comparison challenging. However, most of these edge excitonic states disappear between 40 and 70K or broaden significantly to merge into the interior exciton envelope as seen in temperature dependent measurements (shown in Fig. 6.4). We can thus put an upper bound of 3-6 meV as the dissociation energy of these states.

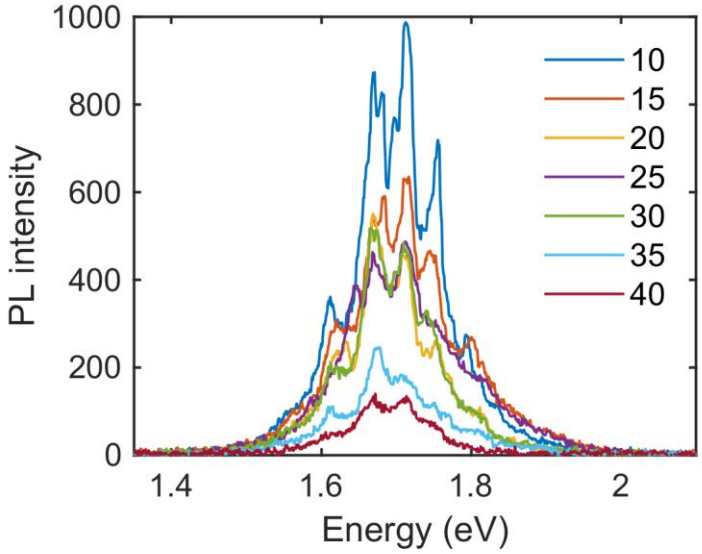

Figure 6.4. Temperature dependent emission spectrum from one spot showing diminishing emission strength as well as linewidth broadening as temperature is increased (measured on sample #D6).

6.5 ELECTRON MICROSCOPY IMAGING OF EDGES AND THEORETICAL CALCULATIONS

To understand the structural origin of the distinct emission peaks, we employ aberration-corrected transmission electron microscopy (TEM) to analyze the atomic registry of monolayer BP within the interior region and at the edge. A typical high-resolution TEM (HRTEM) image of the bare monolayer BP (Fig. 6.5(a)) shows an interface that separates the crystalline and amorphous regions. The crystalline region matches well with the simulated phase contrast of monolayer BP (space group 64: *Cmca*) imaged with an under-focused electron beam about -5.5 nm from the Scherzer defocus (Fig. 6.5(a) inset within the orange borderlines). Two P atoms, which are located at different sub-planes, form a pair that display the dark-contrast atomic column along the [010] zone axis (Fig. 6.5(a)). Positions of the P-atom pairs can be identified and labeled with false-colored dots by a custom-built algorithm based on the phase contrast variance, allowing for the measurement of projected spacings. Each of the atomic positions is color-coded based on the mean value of the projected spacings with the nearest neighboring pairs (Fig. 6.5(b)). The histogram of

the projected spacings (Fig. 6.5(c)) can be fitted with two Gaussian profiles, suggesting a bimodal distribution associated with the interior (0.295 nm ± 0.008 nm) and edge (0.321 nm ± 0.008 nm) spacings. The interior spacing predominated by the "white" dots in the crystalline region (Fig. 6.5(b)) agrees well with the theoretical value of 0.2975 nm in the monolayer BP structure. Bulk defects, such as vacancies and atomic dislocations cause local expansion ("red" dots) and compression ("blue" dots) in spacings. In one case, the condensation of vacancies causes part of an atomic layer to go missing. In contrast, the edge consists of the "red" dots that distribute along the zigzag direction which is perpendicular to the P-atom pairs. The increase in the projected spacing along the zigzag edge with respect to that of the bulk is about 9% in all free-standing monolayer BP samples we examined using TEM, indicating a tensile strain at the edge. The lattice expansion appears to arise from the reconstruction of P atoms near the edge surviving the microscopic fracture and amorphization caused by mechanical exfoliation and transfer. Taken together, the observations suggest that atomic-scale roughness and reconstruction, and inhomogeneous strain distributions may be the origin of the distinct optical emission features at BP edges.

Motivated by these findings, we theoretically investigated a number of BP nanoribbons with different edge reconstructions, focusing on structures that were previously predicted to display small formation energy and have a bandgap[267]. At the density functional theory (DFT) level we find, out of the twenty-four previously computed edge structures with armchair and zigzag fracture orientations, five promising structures that accord well with our observed results, highlighted in Fig. 6.5(d).

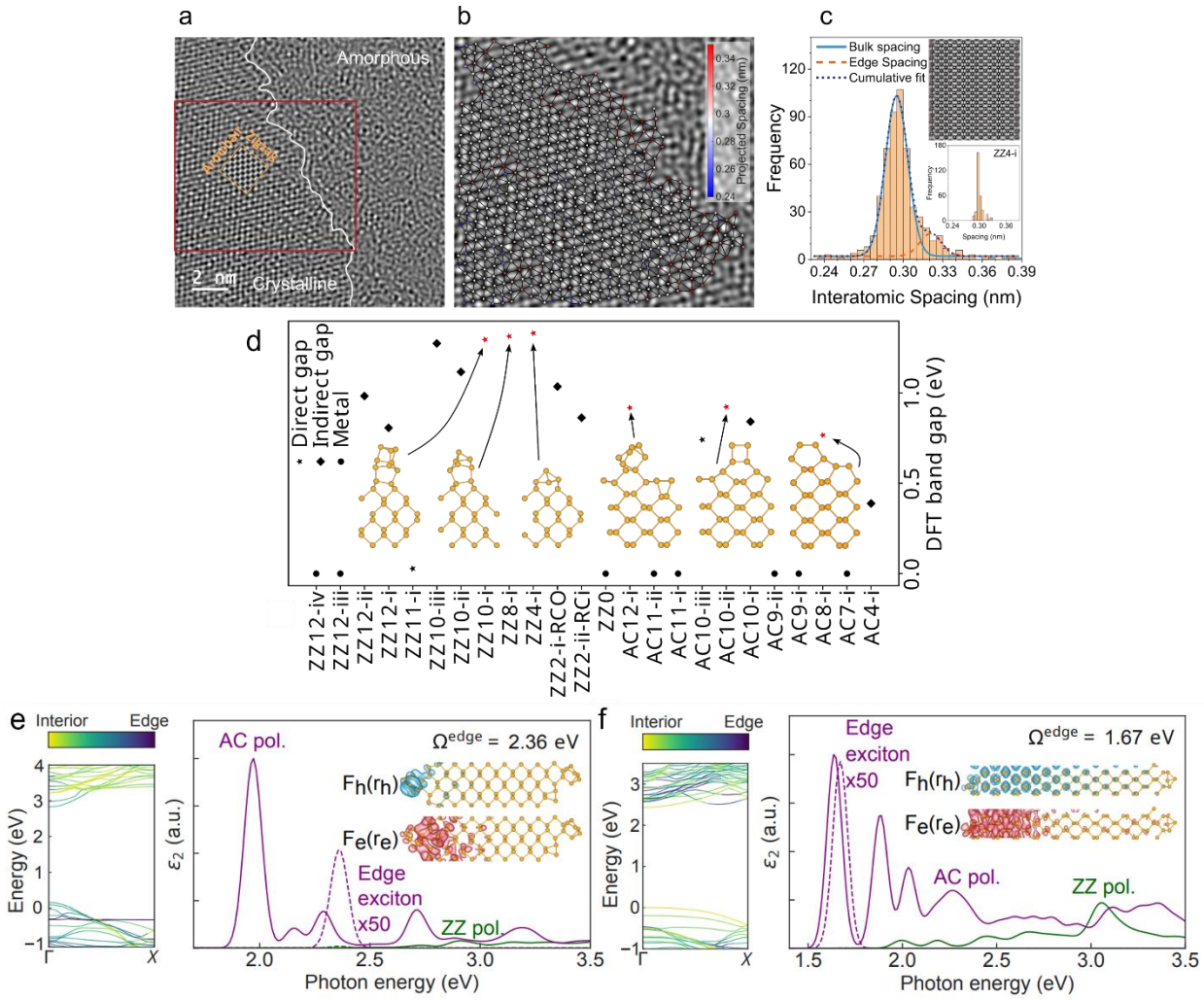

Figure 6.5. Structural and theoretical characterization of BP edges. (a) High-resolution TEM image of free-standing monolayer BP with minimum exposure to air showing an interface (magenta) between the crystalline (left) and the amorphous (right) region. The crystalline image matches well with a phase contrast image (inset with orange borderlines) simulated using a multi-slice algorithm (QSTEM) with a defocus about -5.5 nm away from the Scherzer defocus. (b) Positions of the two neighboring P atoms (dark contrast) identified and labeled with color-coded dots within the indicated area (red borderlines) in (a), based on the phase contrast variance, allow for the measurement of projected spacings. (c) Histogram of the projected spacings fitted with two Gaussian profiles: Peak 1 (turquoise, solid) and Peak 2 (red, dashed), suggesting a bimodal distribution of the interior (0.295 nm ± 0.008 nm) and edge (0.321 nm ± 0.008 nm) spacings in the monolayer BP. Inset shows simulated ZZ4-i nanoribbon edge. (d) DFT level computation of band

structure of 25 favorable edge reconstructions in BP. (e), (f) Quasiparticle band structure for the AC12-i and ZZ4-i edge-terminated structures computed at the GW level of theory and projected over the edge and (2D) interior states. Optical absorption spectrum computed from first-principles GW-BSE calculations for the ZZ4-i and AC12-i structures. Dash lines indicate the position of the edge exciton energy, with an inset showing the electron and hole contribution of the edge exciton. The oscillator strength of both edge excitons is on the order of 10^{-2} times smaller than the lowest-energy peak. Iso-contour shows the exciton wavefunction squared with the electron (F_e) and hole (F_h) coordinates integrated out.

Optical absorption, which is directly related to the imaginary part of the dielectric function, for both armchair and zigzag edges, shows distinct peaks in agreement with experimental observations originating likely due to quantum confinement effects. Upon projection of the optical absorption to interior and edge contributions (appendix), we find two likely structures that exhibit edge excitons maintaining the same dipole orientation as the 2D interior states, one in structure AC12-i and another in ZZ4-i as shown in Fig. 6.5(e) and (f), respectively. These edge excitons have nearly the same polarization direction as the interior exciton as they preserve the inherent mirror symmetry, but are dimmer than the brightest, lowest energy exciton with the oscillator strength being lower by two orders of magnitude–further supported by lack of features from such states in absorption spectroscopy. Their energies are spectrally quite close to the lowest energy exciton (~0.39 eV and ~0.01 eV above the lowest energy for AC12-i and ZZ4-i, respectively). Further, we expect a stronger sensitivity of the edge excitons to dielectric screening compared with interior excitons due to stronger confinement and smaller Bohr radius at the edges[194,222]. This increased sensitivity of dielectric screening can also result in a redshift between the edge and interior excitons, although this is likely a higher-order effect[194]. Therefore, we hypothesize that the origin of the narrow excitonic edge emission is a combination of atomic reconstruction at the edges, along with strain inhomogeneity and increased sensitivity to electrostatic screening effects. It is unclear whether the linewidth probed over a diffraction limited spot (~500 nm radius) is due to multiple sites of slightly different reconstruction having nearly degenerate energies or sites with similar reconstruction experiencing strain gradients. Further, since the electrostatic screening of the hBN encapsulation likely broadens the intrinsic linewidth of the edge excitons, substantially narrower linewidths may be achievable with the appropriate dielectric environment.

6.6 ELECTRICAL TUNING OF EDGE AND INTERIOR EMISSION

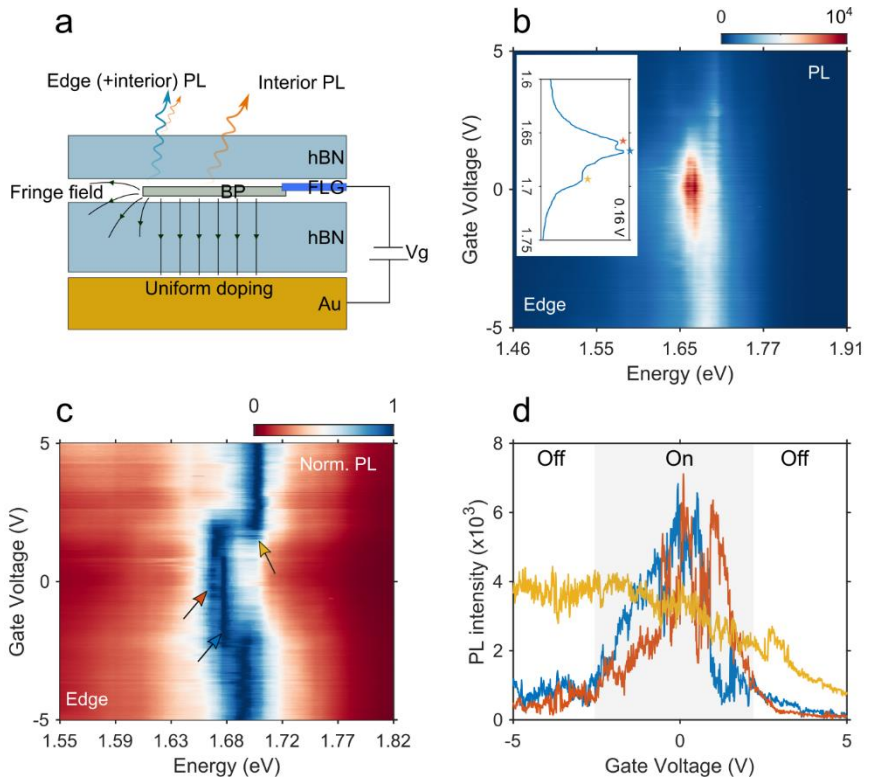

Figure 6.6. Gate tunable edge emission. (a) Schematic of gate-tunable heterostructure geometry showing uniform doping region in the interior and fringe-field effects at the edge. (b) PL spectrum from an edge site (from #gateD1) as a function of gate voltage between -5V and 5V, taken in steps of 10mV. Inset shows a PL spectrum at 0.16V revealing two additional red-shifted peaks corresponding to the edge exciton along with the interior exciton emission. (c) Same as (b) but normalized for each voltage to the maximum emission feature to highlight the dominant spectral features in each band. (d) PL intensity variation for the three features marked in (c) and (d) in yellow (interior contribution) and orange and blue (edge contribution), as obtained from Lorentzian fits to each spectrum at a given voltage. Marked in shaded grey is the "on" voltage window of the edge excitons.

Finally, we demonstrate how the edge excitons can be strongly manipulated using electrostatic gates; a schematic of the device is shown in Fig. 6.6(a). In short, monolayer BP is encapsulated in

hBN and voltage is applied across a back electrode of gold and top electrode of few layer graphene. Fig. 6.6(b) shows false colormap of the variation of the PL intensity measured on an edge-site, as the gate voltage is scanned from -5V to 5V. Three clear spectral features emerge which are also shown in spectrum in the inset of Fig. 6.6(b). Two, spectrally narrow, features of emission (marked with blue and orange arrows) coming from the edge excitons dominate at very small voltages. At larger positive or negative voltages, the interior emission feature takes over. To better illustrate the transfer of spectral weights between the different features, Fig. 6.6(c) shows the normalized PL spectrum at each voltage as a false colormap. Analyzing the peak intensities extracted from fitting spectrum at each gate voltage to a sum of Lorentzian features, we find that while the interior exciton monotonically decreases for increasing electron doping, the two edge exciton states show a near symmetric behavior with strong turn on at approximately -2.5V and turn off at approximately +1(2)V, for peak 1 (in blue) and 2 (in orange), respectively, as shown in Fig. 6.6(d). The monotonically varying gate-dependent background emission originates from the interior exciton which is further confirmed by measuring a similar dependence at a spatial spot in the interior of the device (shown in Fig. 6.7).

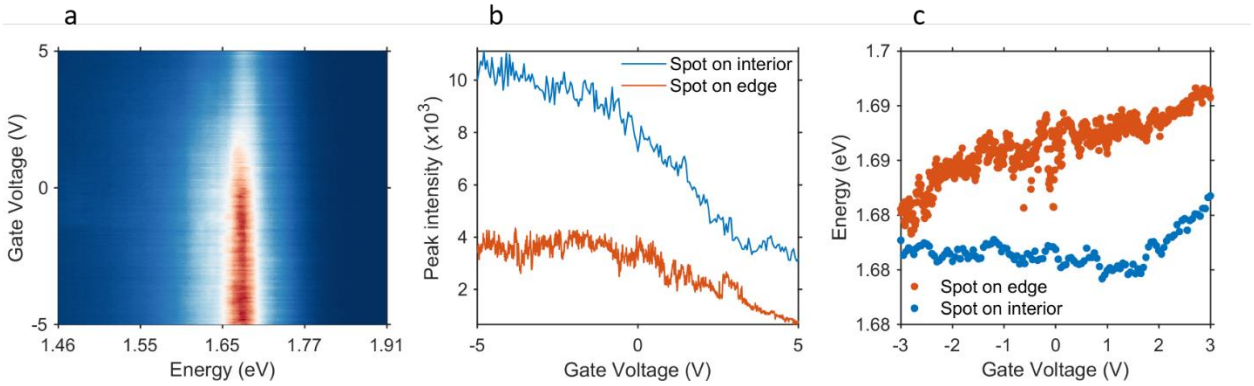

Figure 6.7. Comparing interior emission between interior and edge. (a) PL spectra as a function of gate voltage for a spot in the interior of device #gateD1 showing reduction of excitonic emission as the voltage is increased. (b) Gate dependent peak intensity of interior exciton emission when the laser spot is excited on the interior of the sample and the edge. Both show monotonic dependence with differences only in the absolute intensity of emission. (c) Shifts in peak energy for the interior exciton as a function of gate voltage to compare the differences between having the spot on the interior and on the edge. A stronger shift is seen at the edge implying that the in-plane

Stark effect also plays a role in determining the interior exciton dynamics at the edge along with doping induced screening effects.

The anomalous gate-dependent emission from the interior and edge excitons reveals significant differences in the dominant electro-optic effects at play. The monolayer BP (in the interior) is n-doped at zero bias and shows strong quenching of PL as more electrons are added (positive gate voltages) due to enhanced screening effects[270]. However, the edge of the sample experiences band bending effects likely due to redistribution of electronic charges arising from atomic reconstruction. Our gate-dependent PL measurements indicate an upward band bending, which aligns the Fermi level of the edge close to intrinsic, leading to bright emission from the edge under no bias. In addition, strong fringing effects at the edges invalidate a parallel plate capacitor approximation and lead to emergent in-plane electric fields causing a linear dc Stark effect. Through finite element simulations of the electric field distribution at the edge of BP for the same heterostructure, we find an in-plane field strength $F_x \sim 1 - 50 \frac{V}{\mu m}$ near the edge at $V_g = 2V$. We also expect doping induced screening effects to play a role in a similar manner for the edge, as it does for the interior, albeit more strongly due to the localized nature of the edge exciton (see Fig. 6.8). Collectively they lead to 1. reduction of PL intensity and 2. linear energy shift of the resonance with field strength.

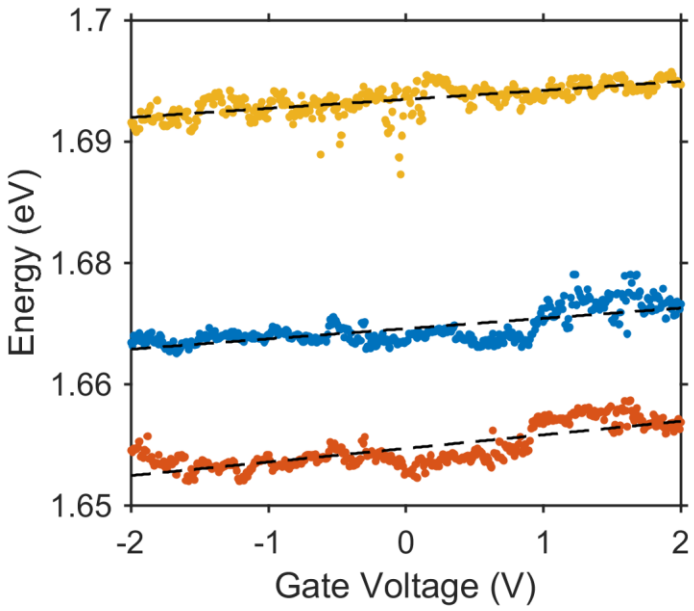

Figure 6.8. Linear fits to resonance energies corresponding to the two edge exciton peaks (blue and orange) and interior exciton peak (yellow), as illustrated in Fig. 6.7.

The linear slopes are 0.76 and 0.95 for the blue and orange curves, respectively. The resonance energies have been extracted by fitting PL spectrum at each voltage to a sum of Lorentzian curves.

From gate dependent PL measurements (Fig. 6.6), we can, to first order, get an estimate of the in-plane projection of the dipole, as follows. The linear stark effect can be represented with the following equation:

$$\Delta E_x = -\frac{(e.d\ cos\theta\ V_x)}{d_x} \quad (6.E1)$$

where ΔE_x is the change in resonance energy, $e.d$ is the dipole moment, θ is the angle the dipole subtends with the x-y plane, V_x is the applied in-plane voltage and d_x is the distance across which this voltage is applied. From this relation, we obtain:

$$\Delta E_x = -e.d\ cos\theta F_x \quad (6.E2)$$

where F_x is the in-plane field. We first fit PL spectrum at each voltage to a sum of Lorentzian features corresponding to the interior and edge excitons (for data presented in Fig. 6.6(c)) and obtain the evolution of resonance energies for each exciton peak–which we further approximate by linear fits in a voltage window where emission signal is high from the edge excitons to decouple doping effects as much as possible. The resonance energies are fit to the following linear equation:

$$E_{res}(V) = E_0 + \alpha V \quad (6.E3)$$

where $E_{res}(V)$ is the voltage-dependent resonance energy, E_0 is the resonance energy under no voltage and α is the slope of the fit. We can thus rewrite E2 as follows:

$$\alpha\ (10^{-3})\ eV = -(e.d\ cos\theta\ F_x). \quad (6.E4)$$

$$\alpha\ (10^{-3})V = -(d\ cos\theta) * \frac{[1-50]}{\mu m} V \quad (6.E5)$$

$$d\ cos\theta = \frac{\alpha}{[1-50]}\ nm \quad (6.E6).$$

The estimate for the in-plane field $F_x \sim \frac{[1-50]V}{\mu m}$ is obtained from electrostatic simulations as detailed before. For the edge exciton at ~1.67 eV ($\alpha = 0.76$), this yields $dcos\theta \sim \frac{0.76}{[1-50]} = [0.02 - 0.76]\ nm$ and $\sim \frac{0.95}{[1-50]} = [0.02 - 0.95]\ nm$ for the exciton at ~1.66 eV ($\alpha = 0.95$), which is the range of dipole projection in the x-y plane.

6.7 CONCLUSION AND DISCUSSION

In summary, we observed signatures of localized exciton emission from certain edges of monolayer BP using low-temperature photoluminescence spectroscopy. These excitons are distinct from their conventional 2D (quasi-1D in the case of BP) counterparts because of higher temporal coherence due to reduced scattering and stronger confinement, resulting in the narrowest

linewidths reported thus far for any BP-based system. By further tailoring the edges of BP and maximizing its optical cross section (such as in bottom-up synthesis of BP nanoribbons or quantum dot nanostructures)[271], a variety of novel optical devices are possible that takes advantage of the narrow polarized optical linewidths and high gate tunability. Resonant optical coupling of edge excitons would also enable spectral separation and isolation of individual edge states, enabling quantum optical applications. By creating extremely small nanostructures, it may also be possible to increase nonlinear interactions between edge excitons, resulting in hybridized excitonic states. We envisage that the discovery of these edge excitons will enable a wide variety of novel, BP-based, photonic applications.

Chapter 7. OUTLOOK AND FUTURE DIRECTIONS

In this thesis, we have demonstrated that van der Waals materials are attractive for various photonic and opto-electronic applications[31,64,171,173,174,184,272]. They provide ideal testbeds for optical spectroscopy to investigate fundamental physics[14,45,120,155,235,236,273,274], as well as are promising candidates for coupling with nanophotonic structures and metasurfaces to achieve superior control of light[30,124,125,173]. Such a unique intersection enables realization of next generation photonic devices such as optical modulators, light emitting diodes, lasers for optical computing, information processing, augmented and virtual reality and holography. It also inspires discovery of new van der Waals materials and heterostructures with exotic properties that can enable multi-functional control of light[10,275–279].

Next, we briefly propose some possible future research directions for each of the projects undertaken and described in this thesis, to elucidate what opportunities lie next.

7.1 INTERBAND AND INTRABAND EXCITATIONS IN FEW LAYER BLACK PHOSPHORUS

Few layer BP hosts interband (from conduction band to valence band) and intersubband transitions in the 1-4 μm range. These transitions can be strongly tuned via multiple electro-optic effects like Pauli blocking/Burstein-Moss shift, quantum-confined Stark effect, and modification of symmetry-induced selection rules–enabling a medium whose complex refractive indices can be altered. When combined with judicious photonic designs, optical modulators, and detectors with high efficiency/detectivity or responsivity can be constructed in the mid-infrared. For example, proposals[184,280] on a waveguide-integrated BP photodetector with intrinsic responsivity of ~135 mAW^{-1} and orders of magnitude reduction in dark current compared to its graphene-counterpart are quite interesting. Similarly, Chang[281] demonstrated mid-infrared LED operation by combining few layer BP with silicon photonic waveguides. Even higher efficiency light emission can be achieved by using photonic crystal cavities with adiabatic out-coupling–which is a common strategy used routinely in photonics research (see - https://www.zurich.ibm.com/st/photonics/adiabatic.html).

In the mid to far-infrared range (beyond 5 μm) BPs hosts intraband or Drude optical transitions–that primarily arise due to collective charge oscillations of the free electrons or holes. As noted earlier, such transitions are also strongly polarization dependent (due to the differences in the effective mass and the scattering rates) and enable dielectric to metallic transition along one crystal axis (armchair) via charge-injection. Transition to optically metallic is possible for the zigzag direction as well but under much heavier doping. This opens up the field of plasmonics in BP, more specifically, hyperbolic plasmonics[46,109,111,112,114,115,118,148,149]. A structured surface such as a grating is typically used to excite surface plasmons from free space to account for the momentum mismatch of the two modes. As previously explored in graphene plasmonics[43,44,97], BP can be patterned into nanoribbons which act as dipole resonators. Varying the ribbon width will modify the surface plasmon resonance condition, roughly according to the following relation–$\omega_p \sim \frac{1}{\sqrt{W}}$, where ω_p is the plasmon resonance frequency and W is the width of the nano-ribbon. 100 nm ribbons are relatively straightforward in terms of fabrication and are expected to yield plasmon resonances at a wavelength of order 20-50 μm. Not many bright sources and detectors exist in this range, and to circumvent that issue, we adopt

a Salisbury screen-like device with a back reflector - which enhances the light-matter coupling in the BP nanoribbons. Through the use of higher order Fabry-Perot modes which correspond to optical path lengths of $L = \frac{m\lambda}{4n}$ (with m = 5,7,9), we can generate a larger spectral density of resonances. A schematic of this plasmonic device and FDTD simulation results that predict its resonant optical response are presented in Figure 7.1.

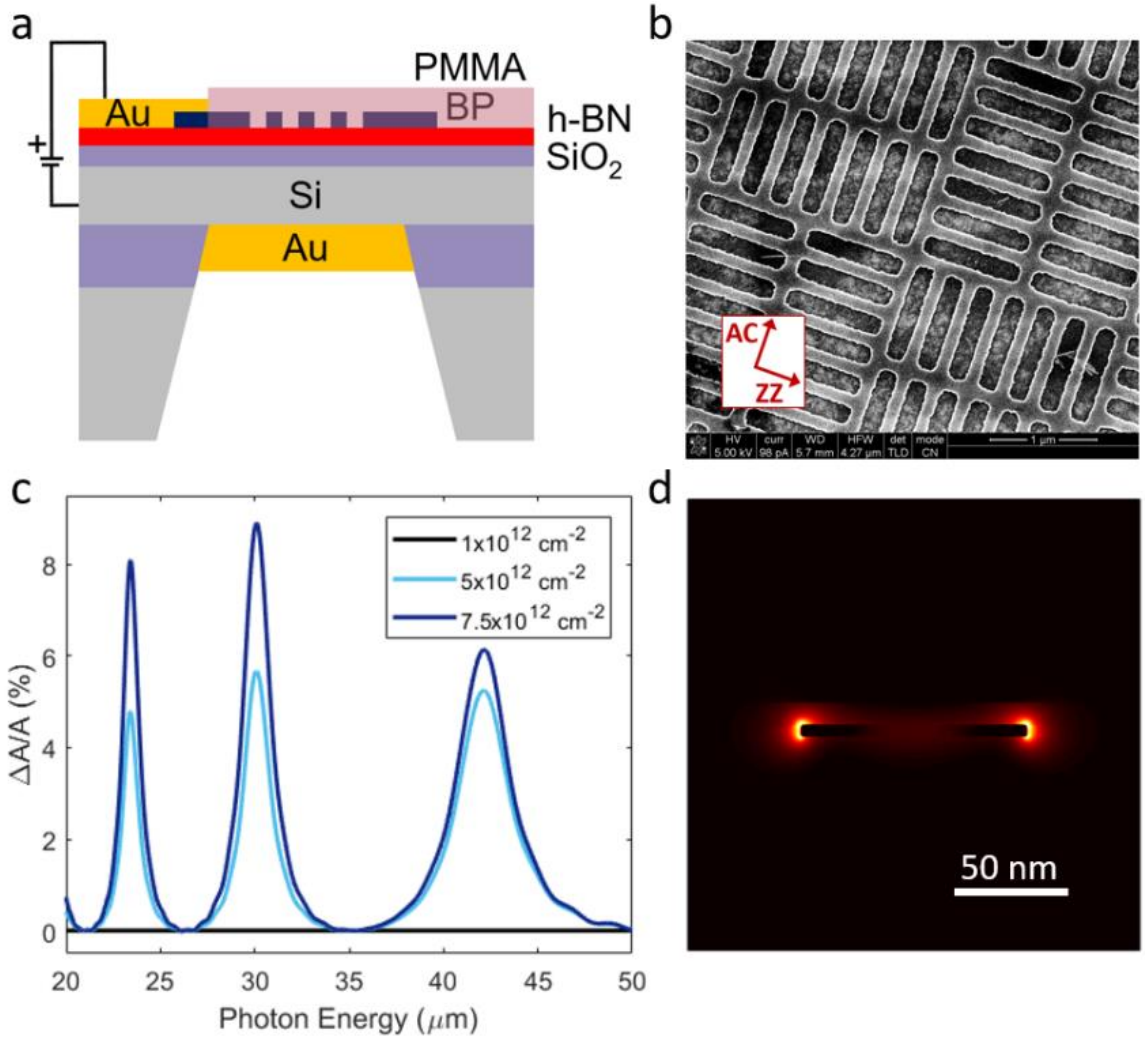

Figure 7.1. Black phosphorus hyperbolic plasmons device. (a) Schematic of gate-tunable black phosphorus plasmonic resonator device, including a silicon dielectric spacer and gold back reflector. (b) Scanning electron microscope image of nanoribbons fabricated in few-layer black phosphorus, aligned to its crystal axes. (c) Simulated absorption modulation for 100 nm black phosphorus ribbons in the device geometry illustrated in (a), normalized to the $1x10^{12}$ cm^{-2} doping

case. The observed resonances are a convolution of spectrally narrow Fabry-Pérot modes due to the dielectric spacer and a single broad surface plasmon mode. (d) Electric field intensity profile surrounding an individual nanoribbon at 30 microns for $7.5x10^{12}$ cm^{-2} doping.

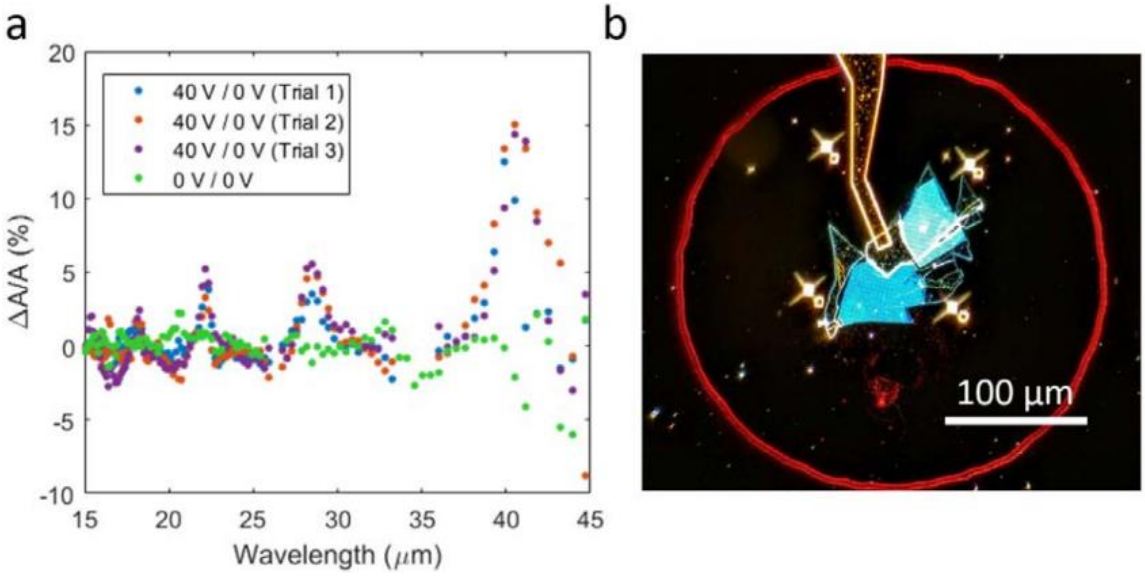

Figure 7.2. Infrared optical results on BP nanoribbons. (a) Armchair axis absorption modulation measured in 100 nm black phosphorus nanoribbons on a Salisbury screen device, as described in Figure 6.2. Three separate trials indicate nearly identical absorption modulation with doping, while the (green) baseline without doping shows zero modulation. (b) A dark field optical microscope image of a completed nanoribbon Salisbury screen device. The large red circle is the rim of the silicon membrane, the yellow finger extending down from the top is a gold contact, and the bright blue regions are the nano-patterned portion of the black phosphorus flakes.

Fabrication details:

The fabrication begins with a silicon membrane device, on silicon on insulator chips with a commercially grown, 50 nm top silicon oxide gate dielectric. Using dry transfer process, a layer of ~5-10 nm thick hexagonal boron nitride is stamped on top of the silicon oxide. This is mainly to increase the mobility of black phosphorus devices which is otherwise dominated by interfacial trap states. Using the same process, a black phosphorus flake, exfoliated onto PDMS, is stamped, and transferred to the membrane. This is followed by standard fabrication techniques like electron-beam lithography, reactive ion etching and electron-beam evaporation for metal deposition to complete the device. Encapsulation with PMMA or h-BN is then used to prevent degradation of black phosphorus. Using Helium focused ion beam (FIB) irradiation, we have also made nanoribbons in BP that are about ~10 nm in width but the time required to pattern multiple of these structures very quickly grows and becomes intractable. The initial experimental characterization for infrared absorption modulation in the mid to far infrared was performed at the Advanced Light Source (ALS), Berkeley. We used an FTIR spectrometer (Nicolet is-50) coupled to an infrared microscope. To boost detectivity we used a helium-cooled, silicon bolometer detector that can measure up to 50 μm. Some of the initial results are shown in Figure 7.2. While repeatable absorption modulation is seen with electrostatic doping for armchair axis polarization–the origin may derive from black phosphorus plasmons as well as resonantly enhanced silicon free carrier absorption, or black phosphorus free carrier absorption. While these results are encouraging, more measurements are needed to confirm the signatures of plasmons.

Once measured, this may enable in-plane beam steering. By modifying the degree of anisotropy of the BP through electrostatic gating, the propagation of a surface plasmon polariton could be redirected, essentially creating a switch to guide plasmon ‘traffic’ in plane. Another way to overcome fabrication of black phosphorus nanoribbons and still observe plasmons would be to use the strategy of acoustic plasmons, as proposed in Ref. [48]

One more interesting problem to study in BP, is the transition arising from bands within the conduction or valence band, as demonstrated in other systems[282]. BP offers a highly anisotropic environment with regards to these transitions due to the selection rules. Since these transitions are quite low in energy, BP will emerge as a promising system for anisotropic mid to far-IR photovoltaics and opto-electronics once these transitions are found experimentally. The only challenge to observing these transitions lie in the mismatch of optical field oscillations and the symmetry of these transitions but those can be overcome by using near-field coupling techniques or photonic modes that allow efficient conversion between free-space and the required symmetries for electromagnetic oscillations.

7.2 ATOMICALLY THIN ELECTRO-OPTIC POLARIZATION MODULATOR

As demonstrated previously, trilayer BP, when integrated with optical resonators or nanophotonic structures can enable realization of diverse polarization states across the Poincare sphere via electrical tuning. This is enabled by the large refractive index change around the exciton resonance due to strong screening of the Coulomb field due to electrons/holes. This work can be further extended to develop compelling technologies at telecom wavelengths. One immediate follow up of this work (as also numerically illustrated in the supplemental material of broadband electro-optic polarization conversion in atomically thin black phosphorus) is to replace the lossy metallic mirrors in the Fabry-Perot cavity and sandwich BP between high quality distributed Bragg reflectors (DBRs). Numerically, such structures show working efficiencies of >90% and phase shift of 2π which is promising for full polarization control. Introducing two unit-cells of orthogonally aligned BP layers would enable traversal of the full Poincare sphere with voltage controls only, with much higher efficiencies. One such work is underway currently, where two trilayer unit-cells of BP are being combined in a nanophotonic cavity to traverse the full normalized Poincare sphere at a fixed wavelength by tuning the voltage only. An initial design of such a structure, along with some preliminary fabricated devices and results of full-wave simulations of the different Stokes parameter (as a function of BP excitonic oscillator strength controlled with doping) is illustrated in Figure 7.3.

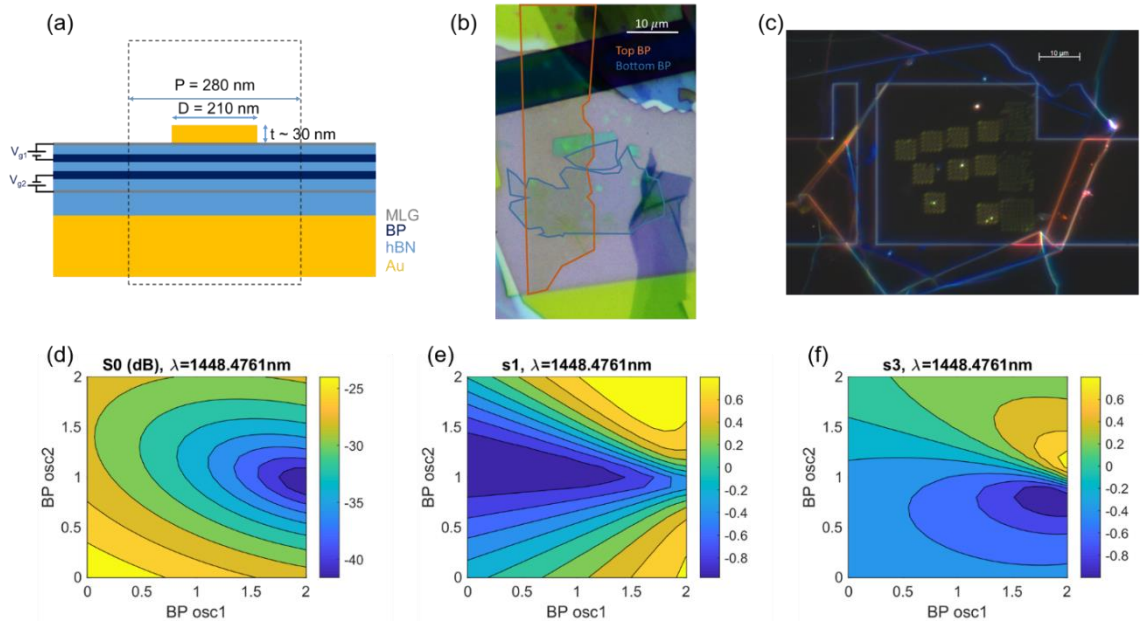

Figure 7.3. Dual trilayer BP-based metasurfaces. (a) Proposed schematic of twisted BP metasurface. (b) Optical microscope image of a fabricated heterostructure containing two trilayers of BP twisted at ~90 degrees. (c) Dark field microscope image of patches of resonators of varying radii fabricated in a heterostructure containing hBN-BP-hBN-Au. (d)-(f) S0, s1, s3–Stokes parameter calculated for structure (a) optimized for critical coupling as a function of top and bottom gate voltage (represented as BP oscillator strength in meV) at a wavelength of 1448.48 nm.

Another attractive direction is to pursue generation of vortex beams with certain topological charge. By creating optical resonators where gate control is independently controllable in each "pizza pie" sector and incorporating BP as the active element it may be possible to switch between vortex beams of different topological charge[283]. It is now an active area of research in the Atwater group, following directly from the BP polarization control results.

BP can also be incorporated into photonic structures to achieve polarization-dependent high absorption at room and low temperatures. Simple Salisbury screen structures can allow trapping of ~>60% of incoming light by placing the BP layer at a quarter wavelength away from a back-reflector.

One challenge with most active materials is the covariation of amplitude and phase (polarization) due to simultaneous tuning of the real and imaginary part of the refractive index as constrained by Kramers-Kronig relations. The polarization control results can be improved and made more technologically compelling by adding a third lossy material which is isotropic and whose complex refractive properties can be independently tuned. This would allow three independent gate-controlled parameters which is sufficient to tune the three Stokes parameters without any compromise. A great choice for such a system is monolayer or few layer graphene. Judicious designs with three gates would be needed to realize such structures.

7.3 RYDBERG EXCITONS AND TRIONS IN $MoTe_2$

In $MoTe_2$, we studied the role of Rydberg excitons in photoluminescence and how charge injection effects the same. An immediate next step of this work is to perform the measurements under high magnetic field which increases the visibility of even higher order excitons (n>3). In other TMDCs such as WSe_2 and WS_2, states up to n~12 have been observed through a variety of measurements such as absorption, emission, and photocurrent spectroscopy[284]. As the quantum number of the Rydberg states increases, the wave function also grows due to an increase in the Bohr radius which makes it attractive for many applications such as sensing and non-linear optics.

As seen in our measurements, Rydberg excitons with larger quantum number show higher energy shifts upon doping–thereby acting as precise self-doping sensors[206,207,219]. Due to their larger wavefunction they can also acts as dielectric environment sensors as already demonstrated in previous reports. This technique can be useful in non-invasive probing of fundamental properties of many systems such as long-range order, phase transition, etc.

When coupled with optical cavities, Rydberg excitons can enable non-linear properties via exciton-exciton interactions[204]. Since the wavefunctions are large, at a certain exciton density, when the Bohr radius exceeds the inter-exciton distance, strong dipolar repulsive interactions dominate. Such interactions can shift the exciton energy by more than a linewidth of the emission. When a cavity is strongly coupled to such excitonic state, this shift manifests as modified transmission or absorption. This forms the basis of non-linear optical absorption whereby increasing the pump density the transmission or absorption can be changed in a non-linear fashion[204,205]. $MoTe_2$ is a promising candidate as it exhibits strong photoluminescence from higher order Rydberg excitons in the near-infrared (silicon) wavelength.

7.4 $MoTe_2$–SCOPE AND OUTLOOK FOR PHASE TRANSITION

One of the primary reasons why $MoTe_2$ gained attention even after similarly behaved TMDCs had been well explored was because of the variety of phases it exists in–1T', T_d, and 2H and possible alloys with W ($Mo_{1-x}W_xTe_2$). A handful of theoretical studies and later, a few experimental reports, proposed that by doping 2H phase of $MoTe_2$ with electrons, an instability can be generated which causes the system to phase transition into the 1T' phase[217,285]. This is attractive for phase-change photonics since charge injection can be much faster than thermally or mechanically induced phase transitions. Furthermore, for a monolayer system, at the exciton resonance a phase transition can induce a complex refractive index change of order ~1 or more– which is compelling for optical modulation with high depth. However, the methods used previously involve ionic liquid or laser ablation, making them less attractive for high-speed and low energy operations. In addition, the characterization methods used to identify the different phases have not been very rigorous and the origin of new Raman modes could also be attributed to tellurium formation, rather than the 1T' phase. Thus, the system merits further investigation on whether this phase transition occurs through a metastable phase and if so, can it be achieved on solid-state systems.

We have attempted two experiments in that direction with some promising evidence, described as follows.

- Solid-state ionic substrates (Raman spectroscopy)

Two substrates–lanthanum fluoride (LaF3) and lithium conductive glass ceramic (LiCGC) were used.

Lanthanum Fluoride (LaF_3) is a solid superionic conductor which has been used extensively in solid state EDL transistors. LaF_3 conducts fluorine ions, and the application of an external electric field leads to F^- ion migration towards or away from the interface. This results in two EDLs, based on F^- accumulation and depletion at opposite sides of the electrolyte, thus forming nanoscale capacitors with large electric fields at the interfaces. The highest carrier density given in literature for LaF_3 EDL gating is 5 x 10^{13} cm^{-2}, as measured by in gating $MoSe_2$[286]. When using LaF_3 as a back gate, the electrochemical window ranges from -2.0 V to 2.0 V.

Lithium Conductive Glass Ceramic (Li CGC) is an ion-conductive glass ceramic in which Li^+ ions are can migrate within a solid oxide material framework. This substrate has a similar operating principle to the LaF_3 substrate, where the application of a gate voltage leads to ionic movement giving regions with excess and depleted Li^+ concentrations at the interfaces. Flat surfaces are necessary to increase the geometric capacitance of the EDL, and Li CGCs is one of the few commercially available substrates with a polished surface, achieving average surface roughness of 1.1 nm. The highest reported carrier density for Li GCGs is 1×10^{14} cm^{-2} in gating single-layer graphene[287]. When using the Li CGCs as a back gate, the electrochemical window is in the range from -2.0 V to 3.5 V.

Multiple devices were studied in a field-effect transistor architecture, shown in Figure 7.4, with different alloys of $Mo_{1-x}W_xTe_2$ using both substrates. While gating was seen in both cases, phase transition was not seen clearly except one device on LaF_3 substrate–which might be due to electrostatic and electrochemical effects. Future studies can help clarify further the underlying cause of such modulation seen in Raman spectroscopy.

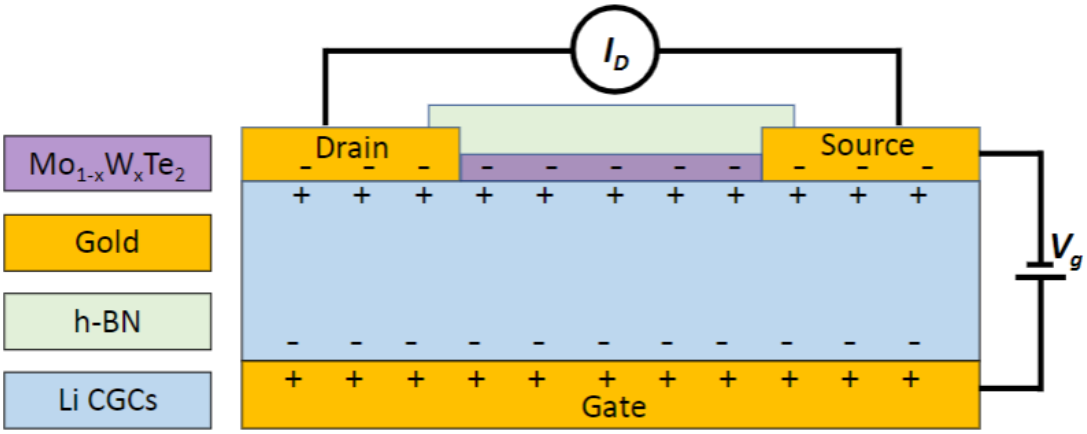

Figure 7.4. Schematic of FET-like devices studied for Mo1-xWxTe2 Raman spectroscopy. Two contacts, source and drain were pre-patterned on the ionic substrates and a back contact was evaporated using electron-beam evaporation. Exfoliated flakes were then transferred using the dry-transfer method.

Potassium ion dosing (ARPES)

We used potassium ion dosing on multilayer flakes with the idea that the top-most layer(s) would be doped by the neighboring K-ions and show signs of structural phase transition. To do so, a technique called angle resolved photo-emission spectroscopy was used at the Lawrence Berkeley National Lab, Advanced Light Source–beamline 7. In short, this technique is widely used to measure the band structure of materials with its sensitivity being highest at the surface. While signatures of doping were seen in the band structure of multilayer 2H $MoTe_2$ as strong renormalization effects, before we could reach doping densities required for phase transition, a large coverage of K-monolayer began forming on the surface. This reduced the visibility of bands from the $MoTe_2$ and enhanced the appearance of quantum well like states formed at the interface of K and $MoTe_2$.

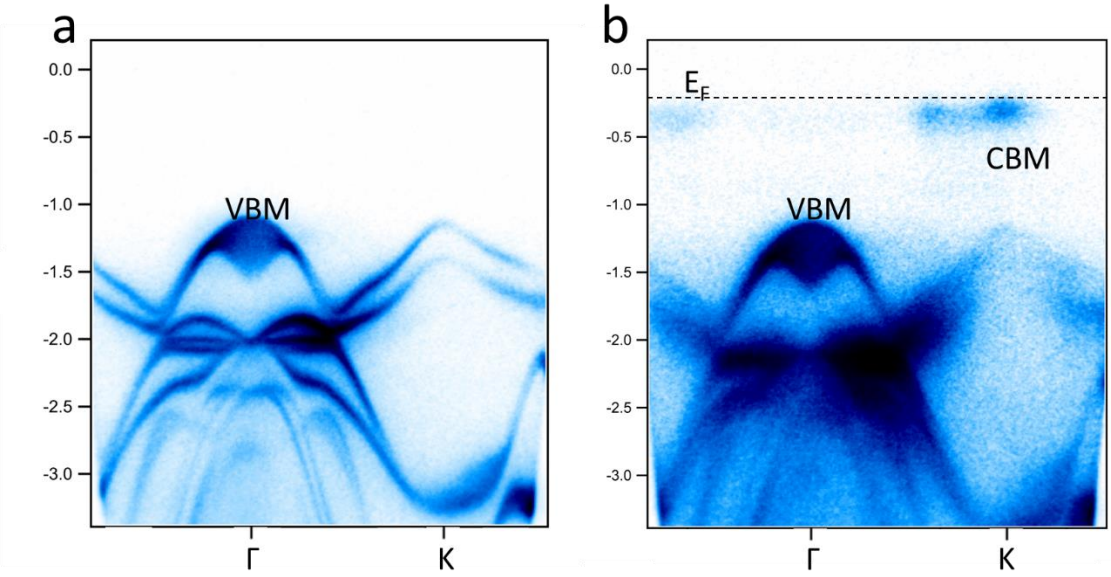

Figure 7.5. ARPES measurements of $MoTe_2$. (a) Pristine band structure of 2H phase of $MoTe_2$ bulk crystal. (b) Band structure of K-dosed crystal showing bandgap renormalization and appearance of conduction band minimum. VBM–valence band maximum, CBM–conduction band minimum.

7.5 OUTLOOK FROM QUANTUM-CONFINED EXCITONS IN MONOLAYER BLACK PHOSPHORUS EDGES WORK

As our experiments point out, edges of monolayer BP can act as sites for exciton trapping, leading to higher quantum confinement. Such effects are manifested in the photoluminescence spectrum as narrow, additional peaks on top of the quasi-1D exciton. This concept can be further extended to develop a multitude of technologies.

First, since the emission is polarized, one can envision developing even narrower linewidth states (effectively single emitter states) with well-defined polarization. In naturally exfoliated flakes it is often tricky to control the orientation of the tear/edge of a flake. However, with controlled growth techniques of phosphorene edges[271], polarization and emission energy can be precisely tuned to

match the desired metric which is attractive for tunable emission applications in the near-infrared/visible spectrum (displays).

Second, if single emitter states can be reliably generated, this system can be used to develop qubits. By incorporating gates, such states can be populated with electrons/holes and turned off–thereby creating a real-time qubit switch. Single photon sources are well established in other TMDCs and known to originate from vacancies or strain induced lattice deformations[232–234,239,240,288]. No such report exists in BP, but our work is the first in that direction.

Third, coupling these emitters with plasmonic or photonic structures can enable strong enhancement of the light emission via Purcell effect. In fact, near-field polarization tuning of such dipole antennas could be used to alter the intrinsic polarization of emission. Polarization conversion structures made of BP (previously demonstrated in three layers but extendable to monolayer) could be cascaded to electrically tune the polarization of the emission. Taken together, the polarization and the quantum yield could be electrically controlled.

Finally, our work explores a single edge but when two such edges are brought in close proximity coupling between them emerges which is interesting to investigate. This can be achieved by either fabricating nanoribbons of BP, previously done in transmission electron microscopy, along different orientations or by controlled growth of BP nanoribbons, like previous reports in graphene. It is possible such a system can host exotic physics like extended edge states with topological properties and spin-polarization.

7.6 CONCLUDING REMARKS ON BP'S POTENTIAL IN COMMERCIAL TECHNOLOGY

BP is an extremely promising material for opto-electronic technology as demonstrated in this thesis and other reports. However, a big challenge which prevents adoption of BP for commercial application is its air-sensitive nature. BP can easily oxidize in a matter of minutes when thinned down to a few layers and requires immediate encapsulation. A variety of passivation techniques have been tested in our lab from atomic layer deposition of aluminum oxide to electron-beam evaporation of silicon dioxide. The best encapsulant was found to be hexagonal boron nitride (hBN)–another van der Waals insulator–which can be exfoliated and used to cap BP on both sides. One important point worth noting is that unless the hBN completely covers the BP, oxidation can still originate from the exposed parts. In-plane oxidation is much faster than out-of-plane oxidation and thus, multilayer flakes are much more stable than monolayers.

Another challenge in adopting BP for commercial technology lies in reliably growing large area, uniform, and controlled thickness of BP. Unlike TMDCs, where significant progress has been made in high-quality growth of monolayer films, the only report on reliably growing BP films has been using pulsed laser deposition. Further research needs to be done on improving the quality of such films. Eventually, if BP can be grown or transferred on to high-quality hBN films, large area opto-electronic can be commercialized in the near, mid, and far-infrared wavelengths.

*I wish for a **'bright'** future for black phosphorus.*

Chapter S1. Supplementary Information for Electrical Control of Linear Dichroism in Black Phosphorus from the Visible to Mid-Infrared

S1.1 Identification of Crystal Axes

To identify the principal crystal axes of the BP flakes, cross-polarization microscopy was used. Incident light passes through a linear polarizer, then the sample, and finally through a second, orthogonal linear polarizer. This technique has been previously described in this thesis. By rotating the sample, the fast and slow optical axes (and hence crystal axes) are identified.

S1.2 AFM Characterization of Flake Thickness

To characterize the thickness of the BP flakes, AFM measurements are made of the entire device stack. Cross-cuts of AFM images of the flakes are shown in Figure S1.1. We note that, as previously described, AFM measures a thickness 2–3 nm larger than the true value, due to the presence of thin phosphorus oxide layers at each interface. Moreover, we note that the presence of the top oxide and nickel coatings prevent perfectly accurate determination of thickness, and therefore we additionally determine thickness based on the energy levels of the band gap and intersubband transitions.

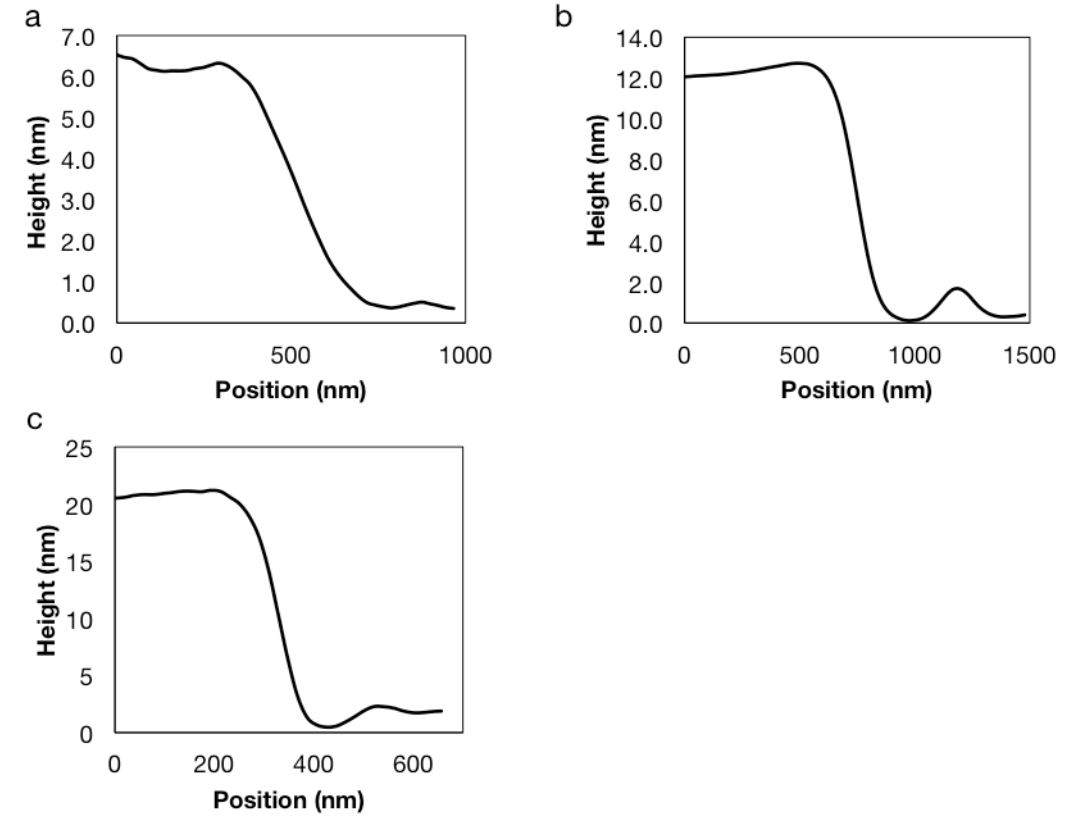

Figure S1.1. AFM Characterization of Flake Thickness. (a) AFM crosscut of '3.5 nm' thick flake, showing measured thickness of 6.5 nm. (b) AFM crosscut of '8.5 nm' thick flake, showing measured thickness of 11.5 nm. (c) AFM crosscut of '20 nm' thick flake, showing measured thickness of 20 nm. Thicknesses have some uncertainty due to Ni/Al_2O_3 top layers.

S1.3 Tunability for 8.5 nm Flake along Zigzag Axis

Fourier transform infrared spectroscopy is used to measure electrical tunability of extinction for light polarized along the zig-zag crystal axis of the 8.5 nm flake, as with the 3.5 nm flake. The corresponding spectra for tunability of the floating device under an applied field and contacted device under direct gating are shown in Fig. S1.2a and S1.2b, respectively. No tunability is seen for this polarization, as with the 3.5 nm flake.

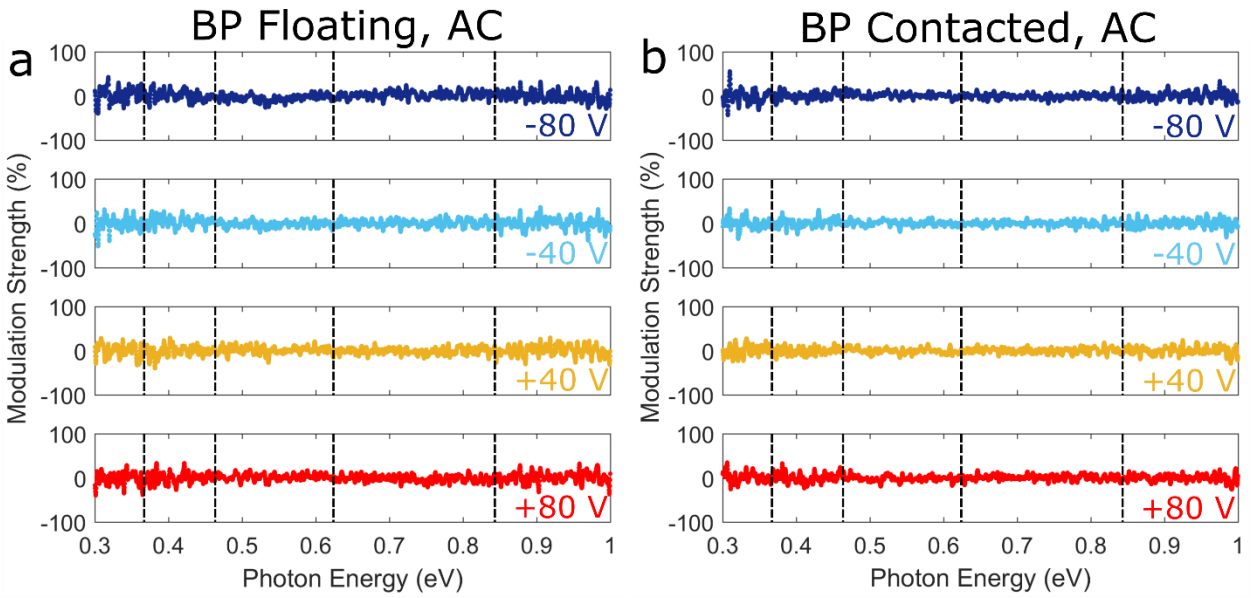

Figure S1.2. Tunability for 8.5 nm Flake along Zigzag Axis. (a) Tunability of BP oscillator strength with field applied to floating device, for light polarized along the ZZ axis. (b) Tunability of BP oscillator strength with gating of contacted device, for light polarized along the ZZ axis.

S1.4 Tunability for 8.5 nm Flake at Lower Energies

To better understand the behavior of the QCSE at the band edge of the 8.5 nm flake, a second measurement was made of electrical tunability of extinction for light polarized along the armchair crystal axis of the 8.5 nm flake using a KBr beam splitter instead of CaF_2. With better resolution at lower photon energies, clear QCSE red shifting of intersubband transitions can be seen at the lowest transition energies. The tunability strength is plotted in arbitrary units since the extinction tunability is still normalized to the CaF_2 extinction / oscillator strength maximum.

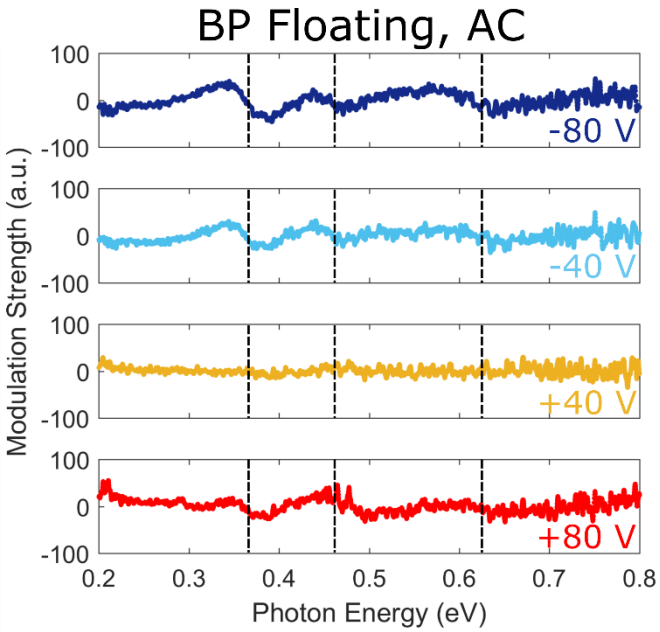

Figure S1.3. Tunability for 8.5 nm Flake at Lower Energies. Tunability of BP oscillator strength with field applied to floating device, for light polarized along the ZZ axis, measured at lower photon energies.

S1.5 Optical Response of Top Contact Material

In order to verify that no interference effects or spurious absorption features are present in the fabricated device for visible measurements, we performed full wave Finite Difference Time Domain (FDTD) simulations using the Lumerical software package. We verify that the transmittance through 5 nm Ni/90 nm Al_2O_3/5 nm Ni/0.5 mm $SrTiO_3$ is featureless, and therefore we can be confident that all tunability is due to the BP. For this reason, we select Ni as the semi-transparent top and bottom-contact and 45 nm thick top and bottom gate dielectrics of Al_2O_3.

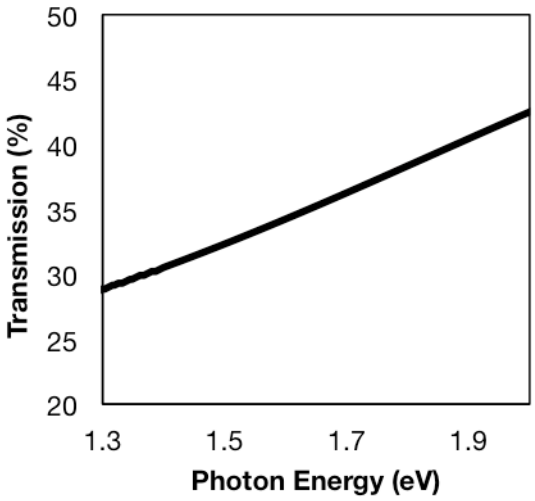

Figure S1.4. Optical Response of Top Contact Material. FDTD simulation results of transmittance through Ni/Al_2O_3/Ni/$SrTiO_3$ superstrate/substrate for visible BP measurements. No features are observed.

S1.6 High reflectance modulation of 6 nm BP flake

In order to demonstrate that thin BP films can generate technologically compelling absolute modulation depths, we present armchair-axis FTIR reflectance data for a 6 nm flake. This data, for which reflectance at 100 V is normalized to reflectance at zero bias, is presented in Figure S5. The device structure consists of 6 nm BP on 285 nm SiO_2 on Si, with a 10 nm Al_2O_3 cap. Further, the observed modulation depth can be dramatically enhanced by integrating the BP into a resonant optical cavity.

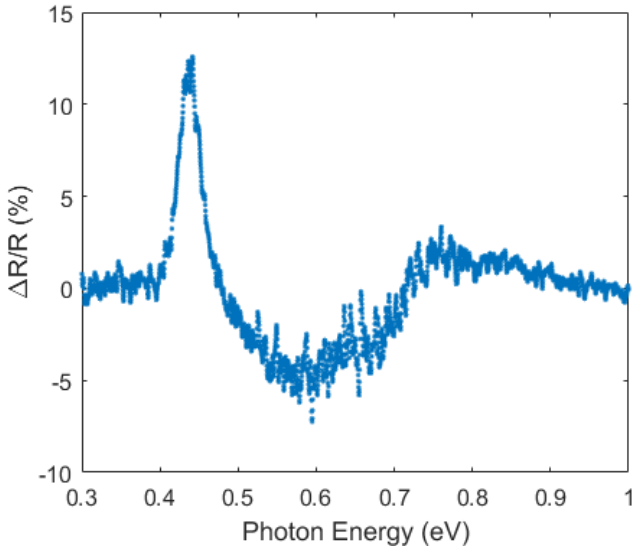

Figure S1.5. High reflectance modulation of 6 nm BP flake. Armchair-axis FTIR reflectance is shown for 100 V bias, normalized to the zero-bias reflectance. Data taken at room temperature under ambient conditions.

Chapter S2. Supplementary Material for Intraband Excitations in Multilayer Black Phosphorus

S2.1 Unpolarized measurements

We also repeated measurements on our device without a polarizer and were able to see consistent modulation data both in the interband and the intraband regime. From the fits to the Drude weight, effective masses that are close to the average of the effective masses of the AC and ZZ axis were obtained, as shown in Fig. S2.1.

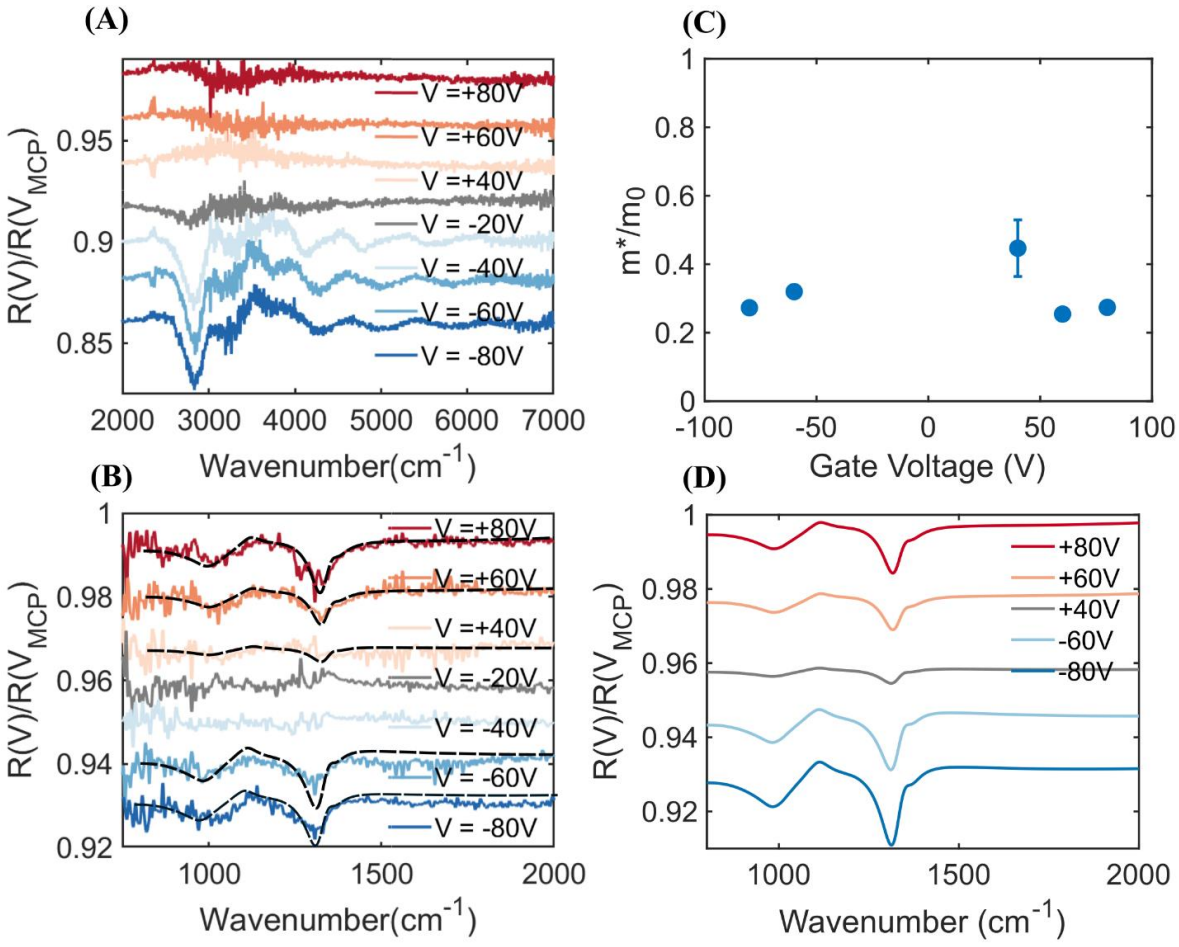

Figure S2.1. Unpolarized response from BP device. (A) Unpolarized reflection modulation at the band-edge for different electron and hole densities. (B) Same for below the band-edge region along

with fits (dotted black lines). (C) Assuming a parallel plate capacitor model, extracted effective mass of free carriers (D) Fits to the experimental data (some curves at very low voltages [close to MCP] do not fit well due to extremely low signal and have been avoided).

S2.2 Transfer matrix model

We employed a transfer matrix model to account for the multiple reflections in our device. It is formulated as follows:

For a stack consisting of N layers, we have

$$\begin{pmatrix} t \\ 0 \end{pmatrix} = J_{N_{total}} \begin{pmatrix} 1 \\ r \end{pmatrix}, \text{where } J_{N_{total}} = \prod_{i=1}^{N} J_i$$

$$J_i = \frac{1}{2} \begin{pmatrix} e^{i(k_i - k_{i+1})z_i}\left(1 + \frac{k_i - \omega\mu_0\sigma}{k_{i+1}}\right) & e^{-i(k_i + k_{i+1})z_i}\left(1 - \frac{k_i + \omega\mu_0\sigma}{k_{i+1}}\right) \\ e^{i(k_i + k_{i+1})z_i}\left(1 - \frac{k_i - \omega\mu_0\sigma}{k_{i+1}}\right) & e^{-i(k_i - k_{i+1})z_i}\left(1 + \frac{k_i + \omega\mu_0\sigma}{k_{i+1}}\right) \end{pmatrix},$$

$$k = \text{wavevector}, z = \text{thickness}, i = \text{layer index}.$$

The term $\omega\mu_0\sigma$ is invoked only at interfaces containing the 2DEG, else excluded.

Reflection and transmission are given by:

$$T = \frac{\widetilde{n_N}}{\widetilde{n_1}}|t|^2, \qquad R = |r|^2, \qquad \text{where } \widetilde{n_m} = \text{complex refractive index of layer} - m.$$

The complex permittivity of SiO2 is adopted from Kischkat et al. shown in Fig. S2.2, and that of Si is adopted from Salzberg et al. The permittivity of hBN is modelled using a single Lorentzian oscillator (we only probe the in-plane phonon since the incident E-field is perpendicular to the c-axis), extracted by fitting the reflection data near the hBN phonon.

$$\epsilon_{hBN} = \frac{\epsilon_\infty\left(1 + {\omega_{pl}}^2\right)}{{\omega_{tl}}^2 - \omega^2 - i\gamma\omega}$$

$$\epsilon_{hBN} = 4.95, \omega_{pl} = 841.25\ cm^{-1}, \omega_{tl} = 1368.4\ cm^{-1}, \gamma = 9.42\ cm^{-1} \quad \text{(top hBN)}$$

$$\epsilon_{hBN} = 4.95, \omega_{pl} = 850.12\ cm^{-1}, \omega_{tl} = 1364.1\ cm^{-1}, \gamma = 9.31\ cm^{-1}$$ (bottom hBN)

The 2DEG formed simultaneously of opposite charge in the Si is modelled as : $\sigma = \frac{n_{Si} e^2 m_{eff}^{-1}}{\omega + i\Gamma}$, where n_{Si} is equal to n_{BP}, m_{eff} = 0.26m0 (for electrons), 0.386m0 (for holes), Γ=130cm^{-1}.

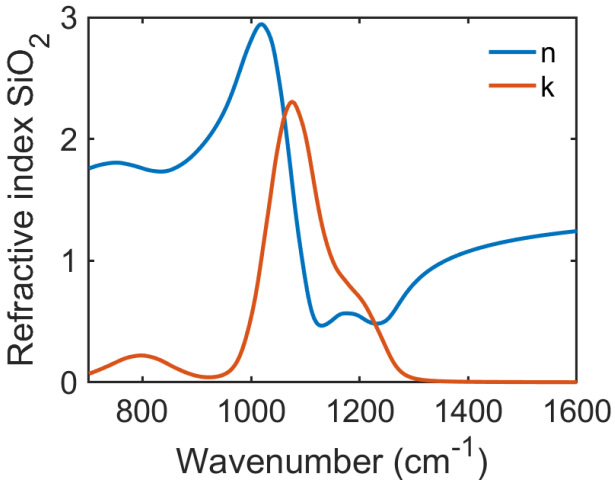

Figure S2.2. SiO_2 refractive index. n,k data adopted for SiO_2 (dominated by phonons).

S2.3 Modulation line shape

The observed modulation line shapes below the band edge are reminiscent of Fano-like resonances in our measurements. A Fano resonance occurs when there is an optical coupling between a sharp resonance like a narrow linewidth phonon and a broad continuum like the intraband Drude absorption in BP. We neglect the effect of Si 2DEG to simplify our analysis (it behaves similar to the BP 2DEG except the anisotropy). We examine the Fano lineshape in the presence of each phonon system (namely, hBN and SiO_2) with BP in Fig. S2.3. For hBN a sharp phonon dominates the Fano resonance; however, for SiO_2 several phonons contribute to the Fano resonance. Overall, we see a superposition of these resonances in the experimental data since both materials are present in our heterostructures. For clarity, the charge density in BP was assumed to be 10^{13}/cm^2 with the polarization along the AC direction.

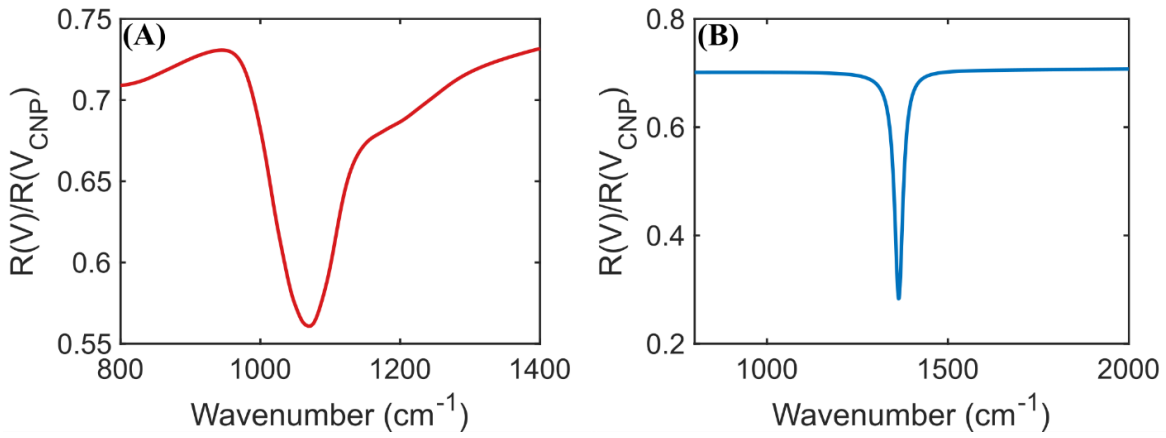

Figure S2.3. Fano response in the system. (A) Fano like response for BP/SiO_2 system. (B) Same for BP/hBN system.

S2.4 AFM data

AFM scans to measure the thickness of BP, and top and bottom hBN flakes are shown in Fig. S2.4

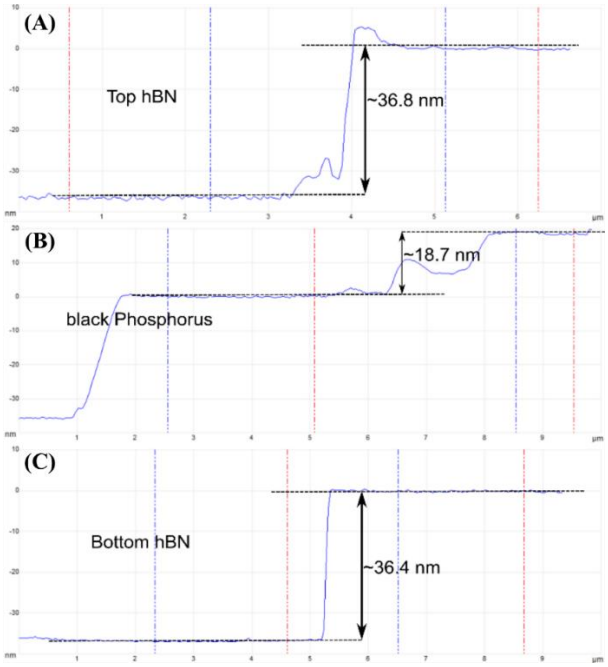

Figure S2.4. AFM data. (A) AFM line scan for top hBN. (B) AFM line scan for BP flake. (C) AFM line scan for bottom hBN.

S2.5 Parallel plate capacitor model

The electrostatics of our device is modelled as follows–the voltage applied between BP and the Si causes the hBN and SiO_2 to act as a dielectric between two parallel plates (BP and Si). The capacitance is calculated as

$$C_i = \frac{\epsilon_0 \epsilon_{r,i} A}{d}, \; i - \text{denotes the material (hBN and } SiO_2).$$

hBN and SiO_2 are in series, so the capacitance adds up as $C_{eff} = \frac{C_1 C_2}{C_1 + C_2}$. Assuming ϵ=3.9 for both hBN and SiO_2, we obtain $C_{eff} = \frac{10.7\text{nF}}{\text{cm}^2}$. Plugging this into $q = C * (V - V_{MCP})$, we get the charge density in the induced gas in BP ($V_{MCP} = 17\text{V}$), as plotted in Fig. S2.5. At the highest voltages on the electron side, we induce up to $4.9 \times 10^{12}/\text{cm}^2$, and on the hole side we induce up to $7.2 \times 10^{12}/\text{cm}^2$. Even higher charge density may be had by going to higher voltages, however, to be able to reliably repeat measurements on the same device without any breakdown, such regimes were avoided.

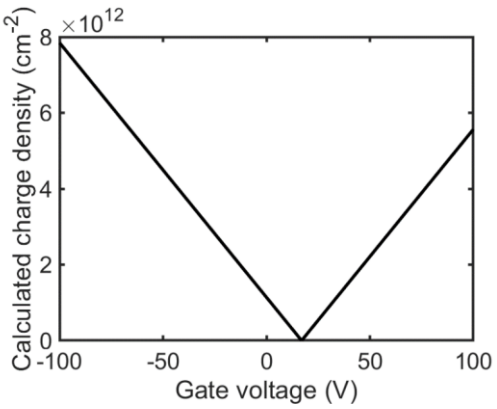

Figure S2.5. Capacitor model for BP. Charge density induced in BP as calculated from parallel plate capacitor model.

S2.6 Thomas Fermi screening model

The charge induced in BP is not uniformly spread over the entire thickness, rather concentrated in the first 2-3 layers and then decaying exponentially. A Thomas-Fermi screening model is employed to understand the charge distribution in BP, shown in Fig. S2.6. A length scale of ~2.9

nm for a charge density of about 5-7x10^{12}/cm^2 is obtained for the effective thickness of the 2DEG, which is then used to calculate the dielectric constant and the refractive index.

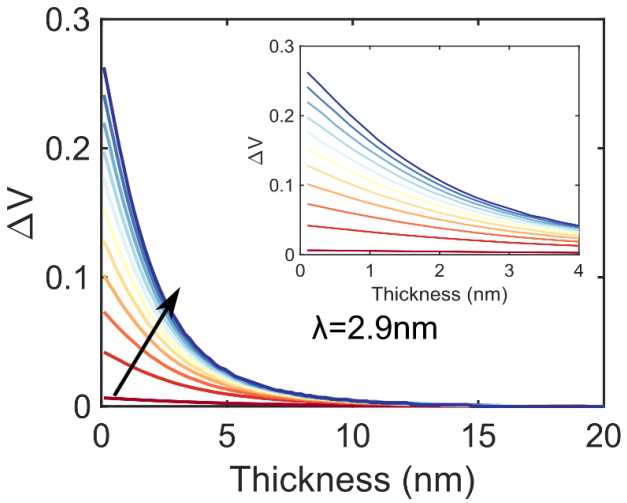

Figure S2.6. Band bending in BP. Thomas Fermi screening calculation in BP as the charge density varies from 10^{11}/cm^2 to 10^{13}/cm^2. Inset–zoomed in up to 4 nm.

S2.7 Dirac-plasmonic point

We note that for the carrier densities obtained in the measurements, there exists a Dirac-plasmonic point (DPP) where the isofrequency contour dispersion almost becomes linear. However, this happens at frequencies slightly below the cutoff of our measurements. The DPP is quite sensitive to the doping and also the frequency as summarized in Fig. S2.7.

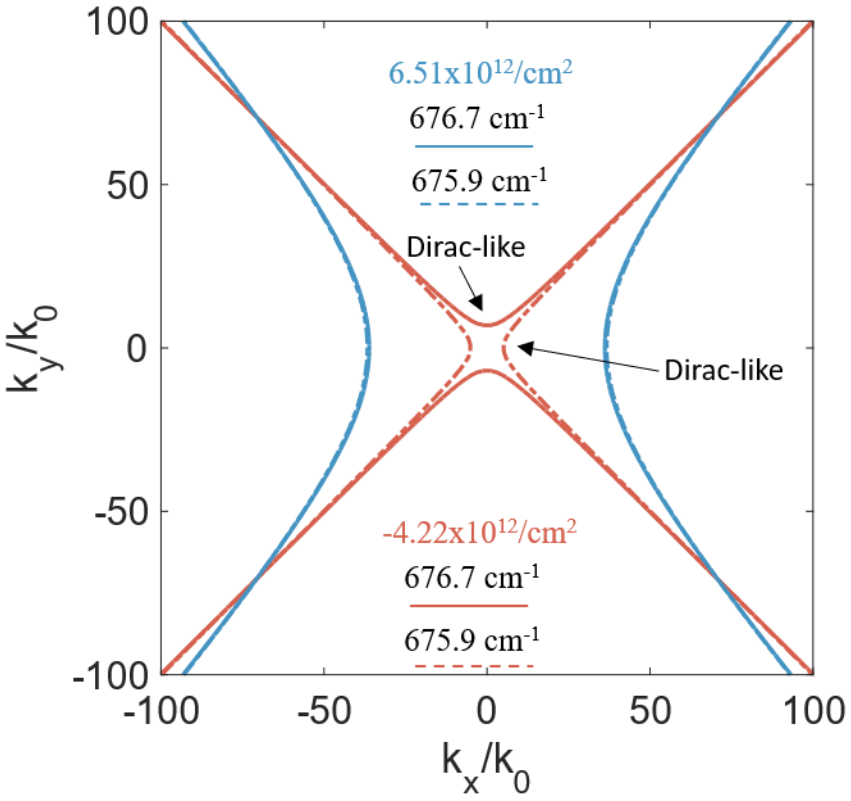

Figure S2.7. Isofrequency contours (IFC) around Dirac-plasmonic point. IFCs are calculated for in-plane propagating plasmon (TM) modes at two frequencies:676.7 cm^{-1} and 659.9 cm^{-1} and two carrier densities:4.22x10^{12}/cm^2 (electron) and 6.51x10^{12}/cm^2 (hole). For higher doping densities, the IFCs are less sensitive to small changes in the frequency, however for lower doping densities, the IFCs are quite sensitive to small changes in the frequency and flip the sign of the hyperbolic dispersion. They also become almost linear adopting a Dirac-like nature.

Chapter S3. Supplementary Information for Atomically Thin Electro-Optic Polarization Modulator

S3.1 Fabrication process

Mechanically exfoliated tri-layers of BP (exfoliated using Scotch-tape) were identified on PDMS substrates with the aid of optical contrast. Mild heating of the tapes (~50-70ºC) during the exfoliation process yields large area BP thin flakes. We found ~7% contrast in the grey channel per monolayer, meaning tri-layers showed around 21% contrast. This was also verified with optical absorption measurements for 1-5 layers of BP, where the bandgap changes dramatically with thickness. hBN and few-layer graphene (FLG) flakes were exfoliated (using Scotch-tape) on pre-cleaned SiO_2/Si chips (sonicated for 30 minutes in Acetone and Isopropanol (IPA), followed by oxygen plasma : 70 W, 90 mTorr for 5 minutes). Clean flakes of desired thickness ranges were identified with a combination of optical microscopy and atomic force measurements (AFM). A dome-shaped (polycarbonate/polydimethylsiloxane) PC/PDMS stamp was used to pick-up the individual layers in a top-down approach (hBN-BP-FLG-hBN), at temperatures between 70-110ºC. Pre-patterned electrodes with back reflectors were prepared using electron-beam lithography (100 keV, 5nA) and electron-beam evaporation of Ti(3nm)/Au(100nm). Assembled heterostructures were dropped on the electrodes at 200ºC. Subsequently, the PC film was washed by rinsing the sample overnight in chloroform and finally in IPA. For devices without the top mirror, this was followed by wire-bonding to chip carriers. For passive cavity samples, PMMA of desired thickness (adopted from calibration curve by Kayakuam) was spin-coated on the entire device, followed by baking at 180ºC for 3 minutes. This was followed by electron-beam evaporation of the top metal (Au) of the desired thickness at 1**Å**/s at base pressures of ~3×10^{-8} Torr. For active devices, this was followed by opening windows to the electrical contacts and wire-bonding to chip carriers.

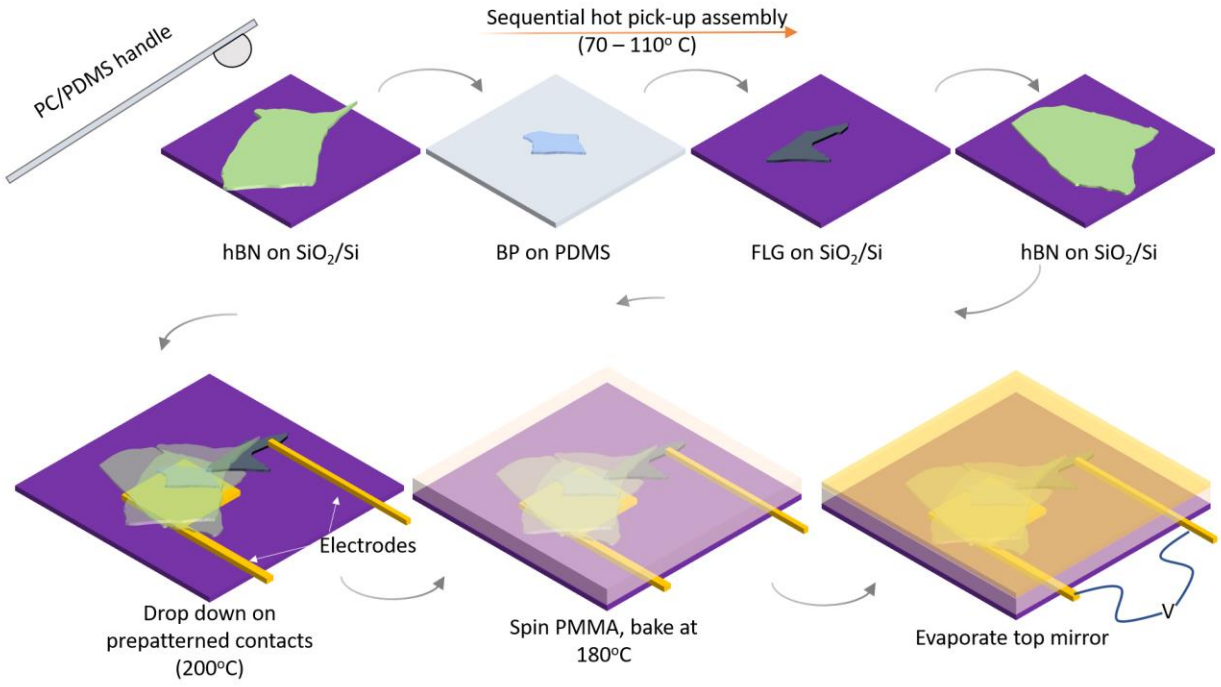

Figure S3.1. Schematic of the fabrication process illustrating the pickup process.

S3.2 Example of a typical BP staircase flake

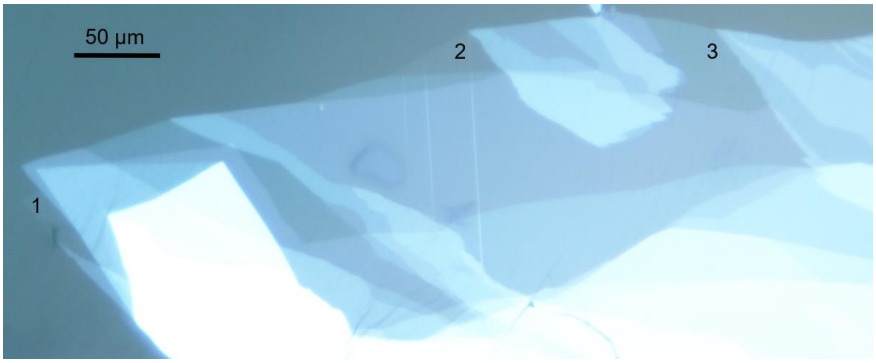

Figure S3.2. Optical image of a BP flake. A typical exfoliated BP staircase flake on PDMS. 1, 2 and 3 layers are marked–confirmed with optical contrast. Other thicknesses can also be seen. Scale bar corresponds to 50 µm.

S3.3 Optical images of devices studied for this study

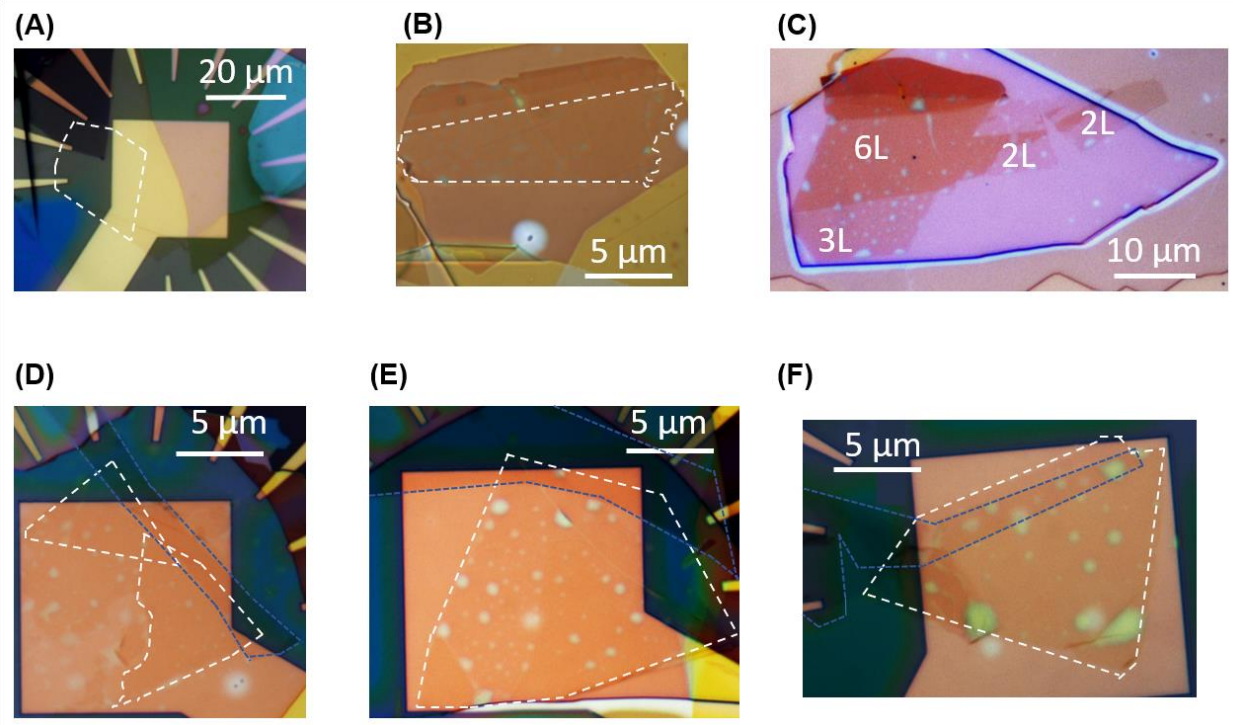

Figure S3.3. Optical images of representative devices investigated for this study. (A)–Non-cavity device for extracting electrically tunable complex refractive index of TLBP (shown in Fig. 2). (B), (C)–Passive cavity integrated devices. (D), (E), (F)–Active cavity integrated devices. The white outlines denote BP, while the blue outlines denote the contacting few layers graphene flake.

S3.4 Raman spectroscopy to identify BP crystal axes

Typical Raman spectra are shown as a function of the incident polarization (linear) of the excitation laser. The strongest response in the A^2_g peak is seen for the armchair (AC) orientation, whereas for the zigzag (ZZ) orientation the same response is the weakest. This combined with linearly polarized absorption measurements enable robust determination of the BP crystal axes. A 514 nm laser was used for the excitation.

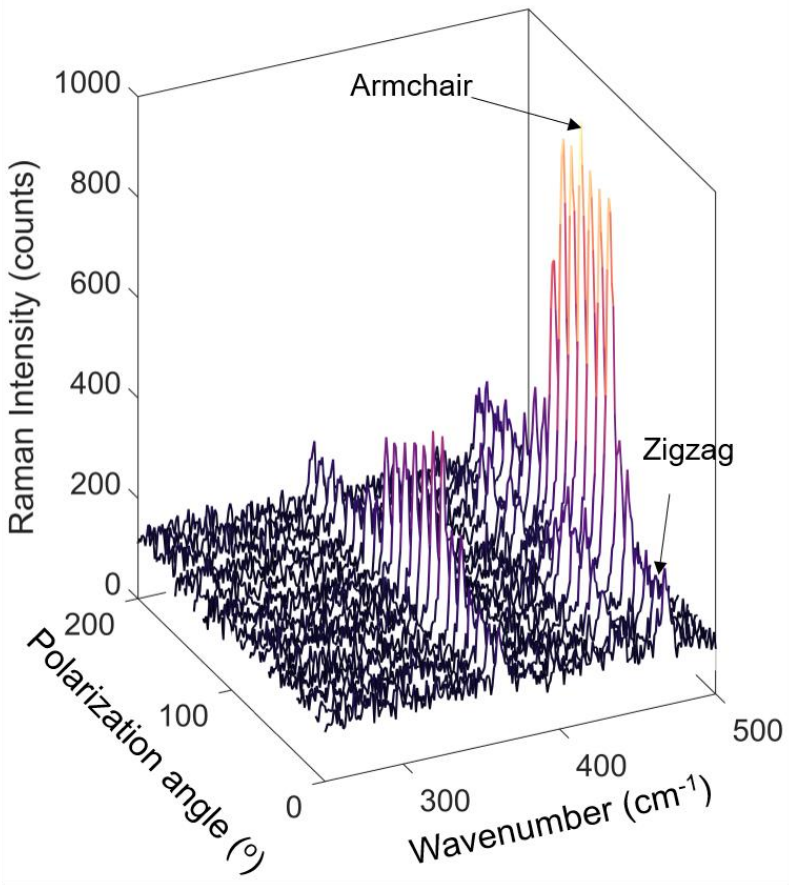

Figure S3.4. Polarized Raman spectroscopy for BP axis identification. Raman spectrum for TLBP as a function of incident linear polarization excitation. A^1_g, B_{2g} and A^2_g modes are seen clearly. Strongest response from the A^2_g mode is seen along the armchair (AC) orientation, whereas along the zigzag (ZZ) direction it is the weakest.

S3.5 Charge density calculator

In the devices investigated in this work, the voltage was applied between the back-electrode\back-Au mirror and the TLBP (grounded). The charge accumulated in the TLBP was estimated using a parallel-plate capacitor model. Since the thickness of the TLBP samples studied (~1.6 nm) are below the Thomas-Fermi screening length (~3nm) for charge densities accessed in this work ($<10^{13}/cm^2$), the entire TLBP can be assumed to be equipotential. The bottom hBN is the dielectric capacitor, which enables the formation of a two-dimensional electron gas at the TLBP. Hence, the capacitance is calculated as follows :

$$C = \frac{\epsilon_0 \epsilon_r A}{d}$$

where, C = capacitance, ϵ_0 = vacuum permittivity, ϵ_r = relative dielectric permittivity of hBN (ϵ_r = 3.9), A = area of the capacitor, d = thickness of the hBN flake.

The charge density is subsequently calculated as:

$$n = \frac{C}{A}(V - V_{CNP})$$

where, n = induced charge density (cm^{-2}), V = applied voltage, V_{CNP} = voltage at charge neutral point. The CNP is estimated from reflectivity measurements, where the highest excitonic absorption is seen. An example gate voltage to charge density (for device D1) conversion is shown.

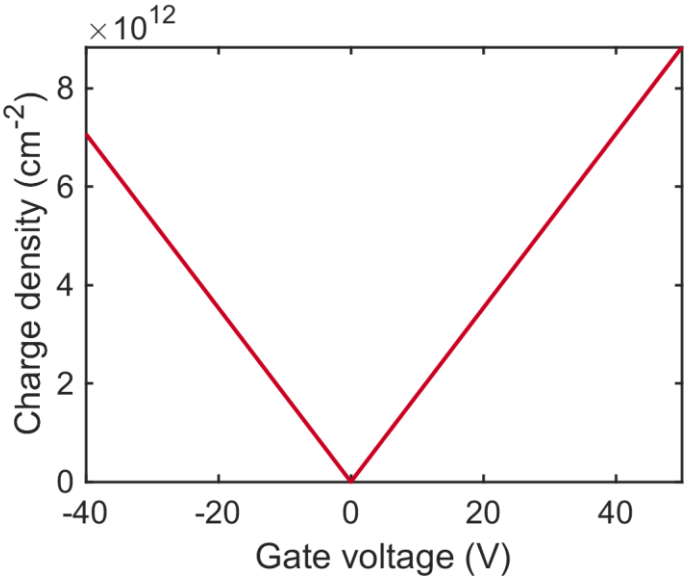

Figure S3.5. Parallel-plate capacitor model. Estimated charge density versus applied gate voltage for Device D1, using the parallel plate capacitor model.

S3.6 Schematic of the experimental setups used for optical characterization

The differential reflectivity measurements were done with the aid of a chopped (mechanical chopper ~419 Hz) supercontinuum white light source (Fianium Super-K FIU 15) and Ge photodetector. Input light was polarized with a wire-grid linear polarizer. Lock-in amplifiers were

used to improve the overall signal quality, locked to the chopper frequency. Voltage was applied using Keithley 2400. In all measurements, the BP was grounded while voltage was applied to the back-electrode. A flat Au surface was used to normalize the reflectivity data. Newport motion controllers (ESP 301) were used to generate spatial maps.

For the polarization conversion measurements, a tunable laser in the near-infrared (Santec TSL-210 covering 1410 to 1520 nm and Newport Velocity 6400 covering 1500 to 1575 nm) was used as the source. A polarimeter (PAX1000IR2) was used to measure the polarization state of the reflected light. Motion controllers (MT3-Z8) were used to perform spatial mapping. Keithley 2400 was used to apply voltage. The input polarization state was controlled using a linear polarizer and a half-wave plate. Labview and python scripts were written to automate data acquisition.

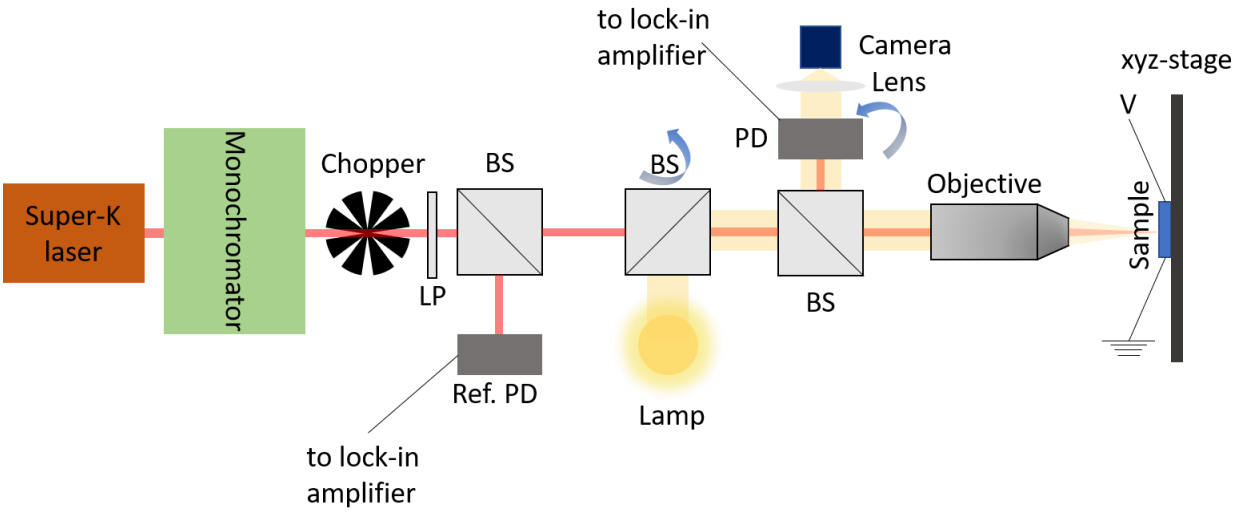

Figure S3.6. Broadband reflectivity characterization setup. Schematic of the optical setup used to characterize the complex refractive index of TLBP as a function of doping density. LP–linear polarizer (wire-grid), PD–photodetector (Ge), Ref. PD–Reference photodetector (Ge), BS–Beam splitter. Blue arrows denote optics on flip mounts.

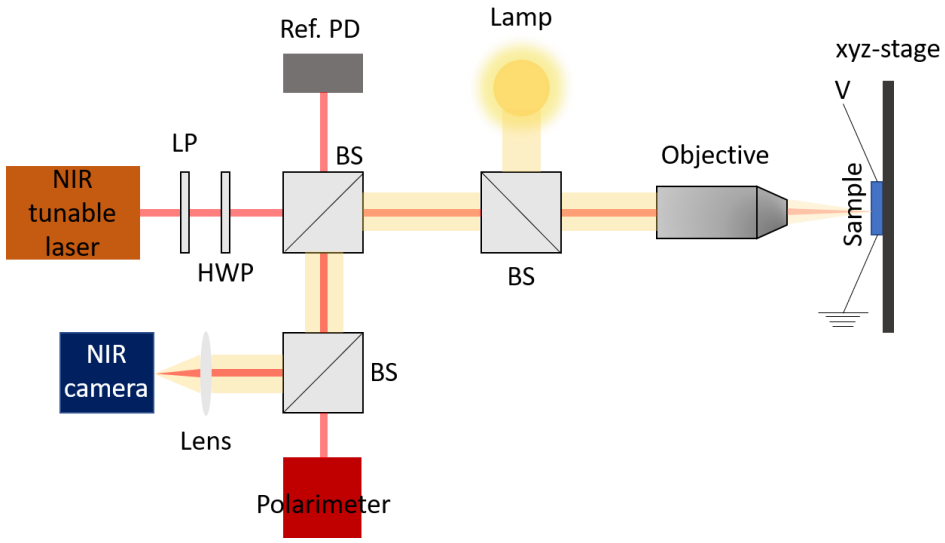

Figure S3.7. Polarization conversion measurement setup. Schematic of the optical setup used to characterize the polarization conversion. LP–linear polarizer, HWP–halfwave plate, Ref. PD–Reference photodetector (InGaAs), BS–Beam splitter.

S3.7 Phenomenological tight-binding model for TLBP bandgap

We begin our discussion of the optical properties of TLBP with a simple phenomenological tight-binding model. TLBP is a direct bandgap semiconductor with its band minima at the Γ-point. In the low energy approximation, coupling among only nearest-neighbours needs to be considered. For monolayer BP, the Schrödinger equation reads:

$$\mathrm{H_{1k}}\psi_{1k} = \mathrm{E_{1k}}\psi_{1k}$$

$\mathrm{H_{1k}}$ is the Hamitonian at the Γ-point for monolayer BP. For N-layers, considering nearest layer coupling as γ_k, the Hamiltonian can be constructed as:

$$H_{Nk} = \begin{pmatrix} H_{1k} & \gamma_k & 0 & \cdots & 0 \\ \gamma_k & H_{1k} & \gamma_k & \cdots & 0 \\ 0 & \gamma_k & H_{1k} & \cdots & 0 \\ \vdots & \vdots & \vdots & \ddots & \vdots \\ 0 & 0 & 0 & \cdots & H_{1k} \end{pmatrix}$$

Solving the N-layer Hamiltonian produces eigenvalues of the following form:

$E_{Nk} = E_{1k} - 2\gamma_k \cos\left(\frac{n\pi}{N+1}\right)$, where n=1, 2, 3…N.

The optical transition energies are given by : $E_{ij}^{N} = E_{CB} - E_{VB} = E_{g0} - 2(\gamma_{CB} - \gamma_{VB}) \cos\left(\frac{n\pi}{N+1}\right)$, where $E_{g0} = E_{CB1} - E_{VB1}$ is the bandgap of monolayer BP. For $3-$layers, using $E_{g0} = 1.9$ eV, $\gamma_{CB} - \gamma_{VB} = 0.73$ eV, (known from previous studies ([23,182])) we achieve $E_{11}^{3} = 0.868$ eV $= 1429$ nm, which is in close agreement with the measured optical bandgap of 1398 nm. Thus, the tight binding model works as a good approximation to estimate the lowest energy optical transition for TLBP.

S3.8 Discussion about the excitonic framework in TLBP and doping dependence

While the 1-D tight binding model works as a good approximation to estimate the optical bandgap (and higher order transitions) of TLBP, it is not sufficient to capture the screening effects which dictate the optical susceptibility of the system at finite-doping levels, since it does not capture the electron-hole correlations. A more accurate way to model the susceptibility of TLBP is to consider excitons in the Wannier-Mott framework, where they obey the following equation:

$$\left(-\frac{\delta}{\mu_x^* \delta x^2} - \frac{\delta}{\mu_y^* \delta y^2} + V_{eh}(r)\right)\psi_i(x,y) = E_i \psi_i(x,y)$$

where, $\mu_{\substack{x \\ y}} = \left(\frac{1}{m^*_{e_{\substack{x \\ y}}}} + \frac{1}{m^*_{h_{\substack{x \\ y}}}}\right)^{-1}$ is the reduced excitonic mass of TLBP in the AC (x) and ZZ (y) direction, and m_e^* and m_h^* represent the conduction and valence band effective masses. It is noteworthy that the optical transitions in the ZZ direction remain disallowed due to symmetry arguments. Taking into account the polarizability of the 2D-sheet and nonlocal screening from the enviroment, the e-h interaction potential can be simplified into the Rytova-Keldysh potential as follows:

$$V_{eh}(r) = -\frac{2\pi e^2}{(\epsilon_a + \epsilon_b) r_0}\left[H_0\left(\frac{r}{r_0}\right) - Y_0\left(\frac{r}{r_0}\right)\right]$$

where, $r = \sqrt{x^2 + y^2}$ is the e-h distance, H_0 and Y_0 are the Struve and Neumann functions, respectively. ϵ_a and ϵ_b are the dielectric function of the environment (in our case, hBN, $\epsilon_{hBN} = 3.9$) and $r_0 = \frac{d\epsilon_{TLBP}}{\epsilon_a + \epsilon_b}$ is the screening length, with d = thickness of TLBP (1.59 nm) and ϵ_{TLBP} is the dielectric function of TLBP. The screening length (all other parameters kept constant) primarily depends on the dielectric function (ϵ_{TLBP}) or the polarizability of the TLBP. Under static conditions (no doping), the aforementioned set of equations can be solved numerically to obtain the binding energies of the entire Rydberg series of excitons along the AC direction. It is noteworthy, that within our window of optical measurements, only the ground state of the Rydberg series is experimentally probed. Under finite doping, the polarizability or the dielectric function of TLBP is heavily modified since the excitonic contribution is suppressed due to a decrease of the screening length (r_0)–realized from Thomas-Fermi screening calculations. Assuming $m_{eff} = 0.16m_0$, we numerically solve for the binding energy of the ground state exciton as a function of the screening length (r_0). The range of screening lengths is extracted from Thomas-Fermi calculations of band-bending, which for the range of doping densities accessed in these measurements ($n = \frac{10^{12}}{cm^2}$ to $\frac{7x10^{12}}{cm^2}$) turns out to be approximately between 2 and 10 nm, decreasing with increasing charge density. It can be clearly seen that the binding energy drops with the reduction in screening length, in line with our measurements. Note that the Hamiltonian is only solved along the AC direction.

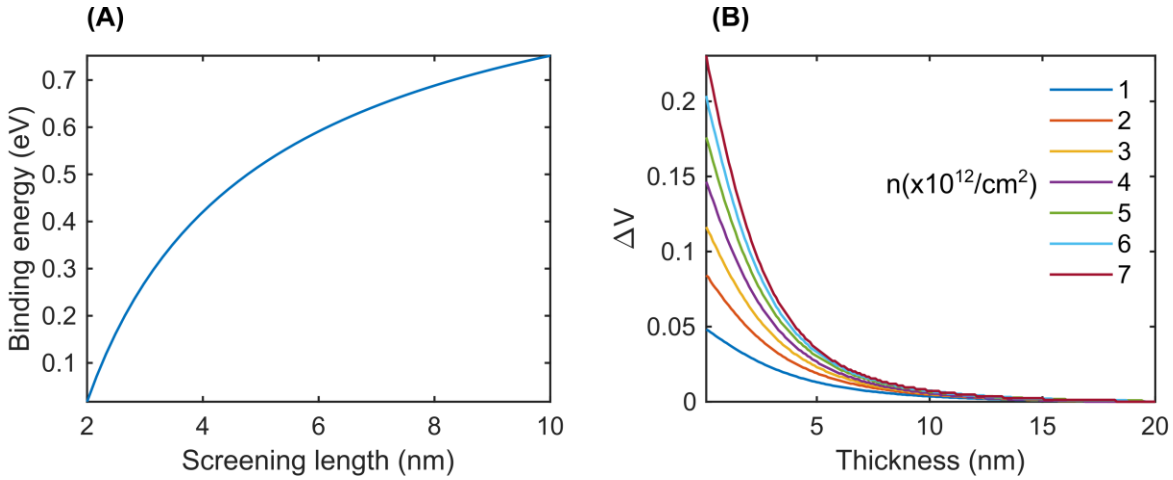

Figure S3.8. Binding energy change with screening length and doping. (A) Calculated binding energy of the ground state exciton as a function of screening length using the Rytova-Keldysh potential. (B) Band-bending (screening profile) as a function of doping density in BP.

Furthermore, the oscillator strength of the excitonic absorption varies inversely with the Bohr-radius of the exciton, $|\phi_{ex}(n)|^2 \propto \frac{1}{a_B^2(n)}$. In the presence of finite doping with a reduction in the binding energy, the Bohr-radius increases, leading to a drop in the oscillator strength.

S3.9 Extracted exciton parameters for TLBP as a function of gate voltage/doping density

Having discussed a theoretical framework for the modulation mechanism, we present here the results of the different exciton parameters (modelled as a Lorentzian) as a function of doping density, which enables us to quantify the doping dependence. The optical sheet conductivity of TLBP is modelled as follows :

$$\tilde{\sigma}(\omega) = \frac{4i\sigma_0 f_0 \omega}{\omega - \omega_0 + \frac{i\Gamma}{2}}$$

where, σ_0 is the universal conductivity, ω_0 = exciton frequency/resonance wavelength, f_0 = oscillator strength and Γ = broadening/linewidth of the resonance.

The optical conductivity can be converted to complex refractive index via the following relations:

$$\tilde{\epsilon} = \epsilon_{\infty} + \frac{i\tilde{\sigma}(\omega)}{d_{BP}\epsilon_0\omega}$$

$$\tilde{n} = n + ik = \sqrt{\tilde{\epsilon}}$$

where, ϵ_{∞} accounts for the contribution of higher (than the exciton) energy resonances, d_{BP} = thickness of the BP layer and $\tilde{\epsilon}$ and $\tilde{n}$ are the complex dielectric function and refractive index.

By fitting the gate dependent differential reflectivity measurements using transfer matrix calculations, we extracted the exciton parameters at each voltage. Fig. S3.9A tracks the changes in the resonance wavelength corresponding to the excitonic transition. A strong redshift is seen for negative gate voltages (hole doping), whereas very mild blueshift is seen for positive gate voltages (electron doping). An inset shows the relationship between the applied gate voltage and estimated charge density using the capacitor model. On either sides of charge neutral condition (0V), a reduction of the oscillator strength is seen (more dramatic on the hole side) with a broadening of the resonances, summarized in Fig. S3.9B and S3.9C, respectively. These observations are in line with the expected electro-optic effects–the strong Coulomb screening from the excess induced carriers reduces the binding energy of the exciton and lowers its oscillator strength. Increased scattering of the excitons with free charges increases the effective linewidth of the transition. The asymmetry between the electron and hole doping is likely related to the efficiency of contacts to BP and the presence of defect states that pin the Fermi energy on the electron side, thus limiting the modulation depth. This also explains why for hole doping a redshift is seen–due to higher gating efficiency the optical response is dominated by trions which are at lower energies than excitons, whereas for the electron side the contribution is comparatively less. We note that at room temperature, optical features are quite broad in BP and since no explicit trion peak was observed, the absorption was modelled with a single Lorentzian feature corresponding to the exciton.

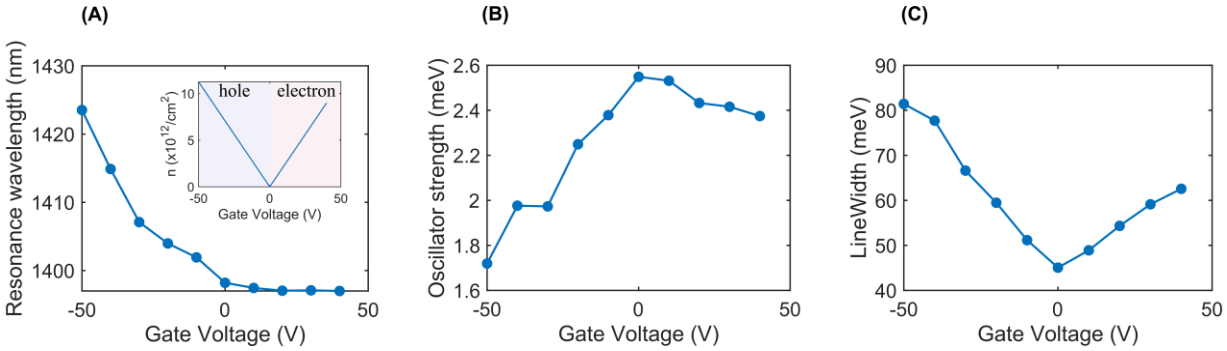

Figure S3.9. Exciton parameter modulation with gate voltage for TLBP. Tuning of the exciton resonance parameters as a function of applied gate voltage. (A), (B) and (C) show changes in the resonance wavelength, oscillator strength and the linewidth of the excitonic resonance as a function of gate voltage, respectively. An inset in (A) shows the relation between the applied gate voltage and the estimated charge density in the BP 2DEG.

S3.10 Variation of the integrated optical conductivity (loss function) with doping

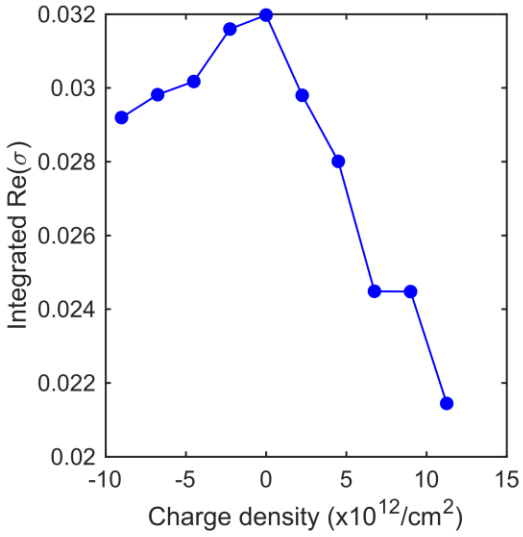

Figure S3.10. Integrated real optical conductivity variation with doping. The real part of optical conductivity is proportional to the loss function ($\propto Im(\epsilon)$) which dictates the overall optical response for such thin films. As doping is increased on either side, a drop in the loss function indicates reduced absorption due to screening of the excitons via free charges leading to a reduction

in binding energy and oscillator strength. The integration (over optical measurements bandwidth) assumes a single excitonic feature and no other oscillators.

S3.11 Transfer matrix formalism for theoretical design of cavity-based devices

We employed a transfer matrix model to account for the multiple reflections in our cavity-based devices. It is formulated as follows:

For a stack consisting of N layers, we have

$$\begin{pmatrix} t \\ 0 \end{pmatrix} = M_{N_{total}} \begin{pmatrix} 1 \\ r \end{pmatrix}, \text{where } M_{N_{total}} = \prod_{i=1}^{N} M_i(\omega)$$

$$M_i(\omega) = \frac{1}{2} \begin{pmatrix} e^{i(k_i - k_{i+1})z_i}\left(1 + \frac{k_i - \omega\mu_0\sigma}{k_{i+1}}\right) & e^{-i(k_i + k_{i+1})z_i}\left(1 - \frac{k_i + \omega\mu_0\sigma}{k_{i+1}}\right) \\ e^{i(k_i + k_{i+1})z_i}\left(1 - \frac{k_i - \omega\mu_0\sigma}{k_{i+1}}\right) & e^{-i(k_i - k_{i+1})z_i}\left(1 + \frac{k_i + \omega\mu_0\sigma}{k_{i+1}}\right) \end{pmatrix},$$

$$k = \text{wavevector}, z = \text{thickness}, i = \text{layer index}.$$

The term $\omega\mu_0\sigma$, where σ is the sheet conductivity, may be invoked only at interfaces containing 2D-thin films (for example, TLBP) where optical conductivity is used, else excluded if refractive index is used. Both approaches produced consistent results for non-cavity devices. However, for cavity-based devices a refractive index approach was used due to its accuracy over the sheet conductivity model due to multiple round trips of light within the cavity (leading to increased "optical thickness" of thin 2D sheets).

Reflection and transmission are given by:

$$T(\omega) = \frac{\widetilde{n_N}}{\widetilde{n_1}}|t|^2, \qquad R(\omega) = |r|^2, \qquad \text{where } \widetilde{n_m} = \text{complex refractive index of layer} - m.$$

S3.12 Jones matrix for TLBP birefringence and calculation of Stokes parameters

The polarization state of the reflected light from a device with TLBP can be calculated using the Jones vector method as follows. First, the reflected light amplitude and phase are calculated using the transfer matrix method assuming illumination along only the AC or the ZZ direction. Then, the cavity can be treated as a retarder plate (for both amplitude and phase) and its Jones matrix is given as:

$$J_{cavity} = \begin{pmatrix} r_{AC}e^{i\phi_{AC}} & 0 \\ 0 & r_{ZZ}e^{i\phi_{ZZ}} \end{pmatrix}$$

For a given rotation (θ) between the input optical beam and the TLBP axis, the effective Jones matrix is:

$$J_{out} = R(\theta)\begin{pmatrix} r_{AC}e^{i\phi_{AC}} & 0 \\ 0 & r_{ZZ}e^{i\phi_{ZZ}} \end{pmatrix}R(-\theta)$$

$$R(\theta) = \begin{pmatrix} \cos(\theta) & -\sin(\theta) \\ \sin(\theta) & \cos(\theta) \end{pmatrix}$$

$$J_{out} = \begin{pmatrix} \cos(\theta) & -\sin(\theta) \\ \sin(\theta) & \cos(\theta) \end{pmatrix} * \begin{pmatrix} r_{AC}e^{i\phi_{AC}} & 0 \\ 0 & r_{ZZ}e^{i\phi_{ZZ}} \end{pmatrix} * \begin{pmatrix} \cos(\theta) & \sin(\theta) \\ -\sin(\theta) & \cos(\theta) \end{pmatrix}$$

$$J_{out} = \begin{pmatrix} r_{AC}e^{i\phi_{AC}}\cos^2(\theta) + r_{ZZ}e^{i\phi_{ZZ}}\sin^2(\theta) & \cos(\theta)\sin(\theta)\left(r_{AC}e^{i\phi_{AC}} - r_{ZZ}e^{i\phi_{ZZ}}\right) \\ \cos(\theta)\sin(\theta)\left(r_{AC}e^{i\phi_{AC}} - r_{ZZ}e^{i\phi_{ZZ}}\right) & r_{AC}e^{i\phi_{AC}}\sin^2(\theta) + r_{ZZ}e^{i\phi_{ZZ}}\cos^2(\theta) \end{pmatrix}$$

Let $E_x = r_x e^{i\phi_x}$ and $E_y = r_y e^{i\phi_y}$, then, the Stokes parameters are given as:

$$S_0 = |E_x|^2 + |E_y|^2, S_1 = |E_x|^2 - |E_y|^2, S_2 = 2\mathrm{Re}(E_x E_y^*), S_3 = -2\mathrm{Im}(E_x E_y^*)$$

For clarity, the Stokes parameters can be normalized as:

$$s_1 = \frac{S_1}{S_0}, s_2 = \frac{S_2}{S_0}, s_3 = \frac{S_3}{S_0}$$

The azimuthal and ellipticity can then be calculated as:

$$\psi\ (\mathrm{azi.}) = \arctan\left(\frac{s_2}{s_1}\right), \chi\ (\mathrm{ell.}) = \arctan\left(\frac{s_3}{\sqrt{s_1^2 + s_2^2}}\right)$$

S3.13 Broadband polarization conversion

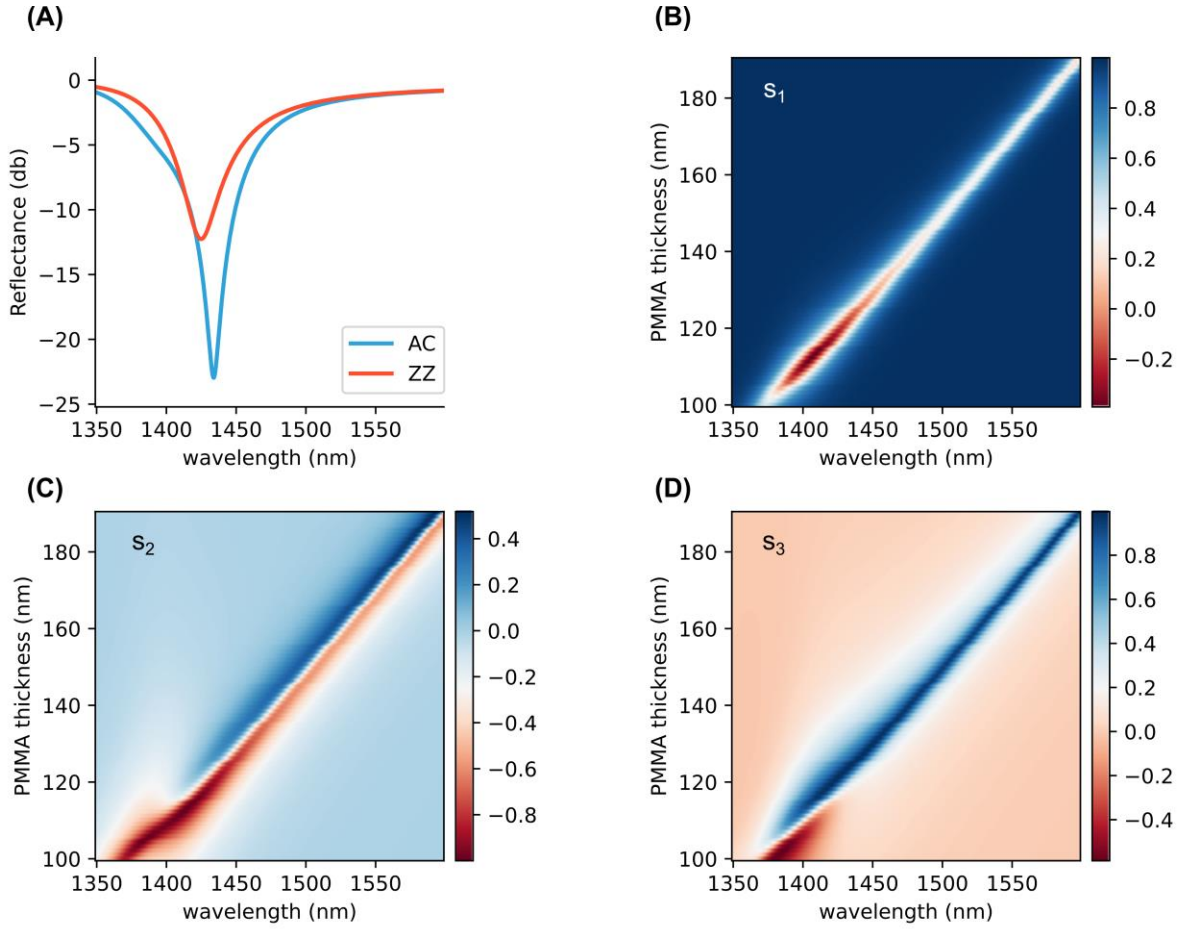

Figure S3.11. Broadband polarization conversion simulations. (A) Reflectance along the AC and ZZ direction for a cavity with parameters matching D1. (B), (C), (D) Normalized Stokes parameters (s_1, s_2, s_3) as a function of cavity length obtained by tuning the PMMA thickness showing efficient broadband polarization conversion.

S3.14 Spatial variation of refractive index in a non-cavity sample in TLBP

Results from a non-cavity device containing TLBP flake encapsulated in hBN on Au are presented here. Spatial variation of the complex refractive index is seen across the flake. The TLBP studied here was broader in linewidth.

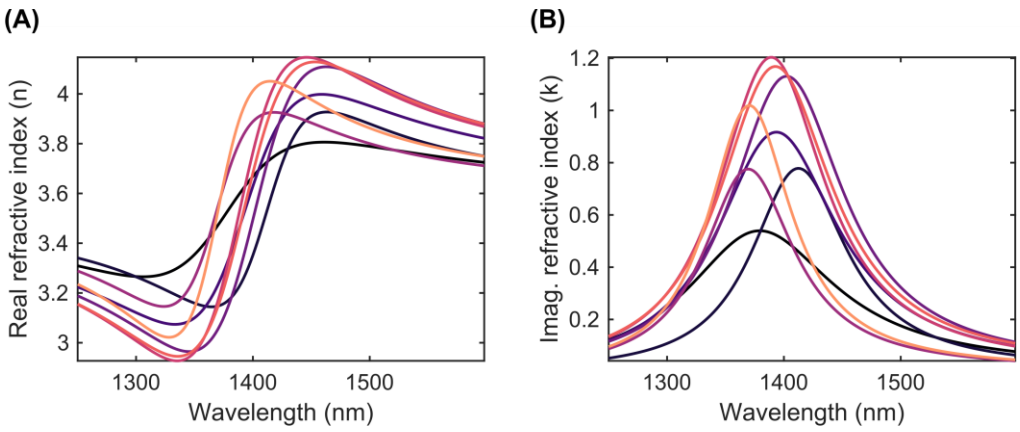

Figure S3.12. Spatial optical inhomogeneity in TLBP samples. Spatial variation of real (A) and imaginary (B) part of complex refractive index in a TLBP flake.

S3.15 Effect of different thickness on the cavity resonance and polarization conversion

A staircase sample was fabricated to study the effect of different thicknesses of BP on the cavity resonance. A systematic red shift is seen as a function of BP thickness, as expected. Adding more layers increases the effective optical path length inside the cavity which explains the redshift of resonance. However, very weak polarization conversion was seen from thicknesses other than 3-layers. This reiterates the importance of choosing tri-layer flakes for working in the telecommunications band, since the anisotropy is very high near the excitonic resonance. In Figure S3.13A, B, C reflection spatial colormaps can be seen at three different wavelengths (1460 nm, 1510 nm, and 1560 nm) showing changes in contrast for different thicknesses. Figure S3.13D illustrates the systematic redshift of the cavity resonance as a function of thickness. Figure S3.13E, F illustrates the strongest polarization conversion in the 3L region as quantified by the ellipticity and azimuthal angle.

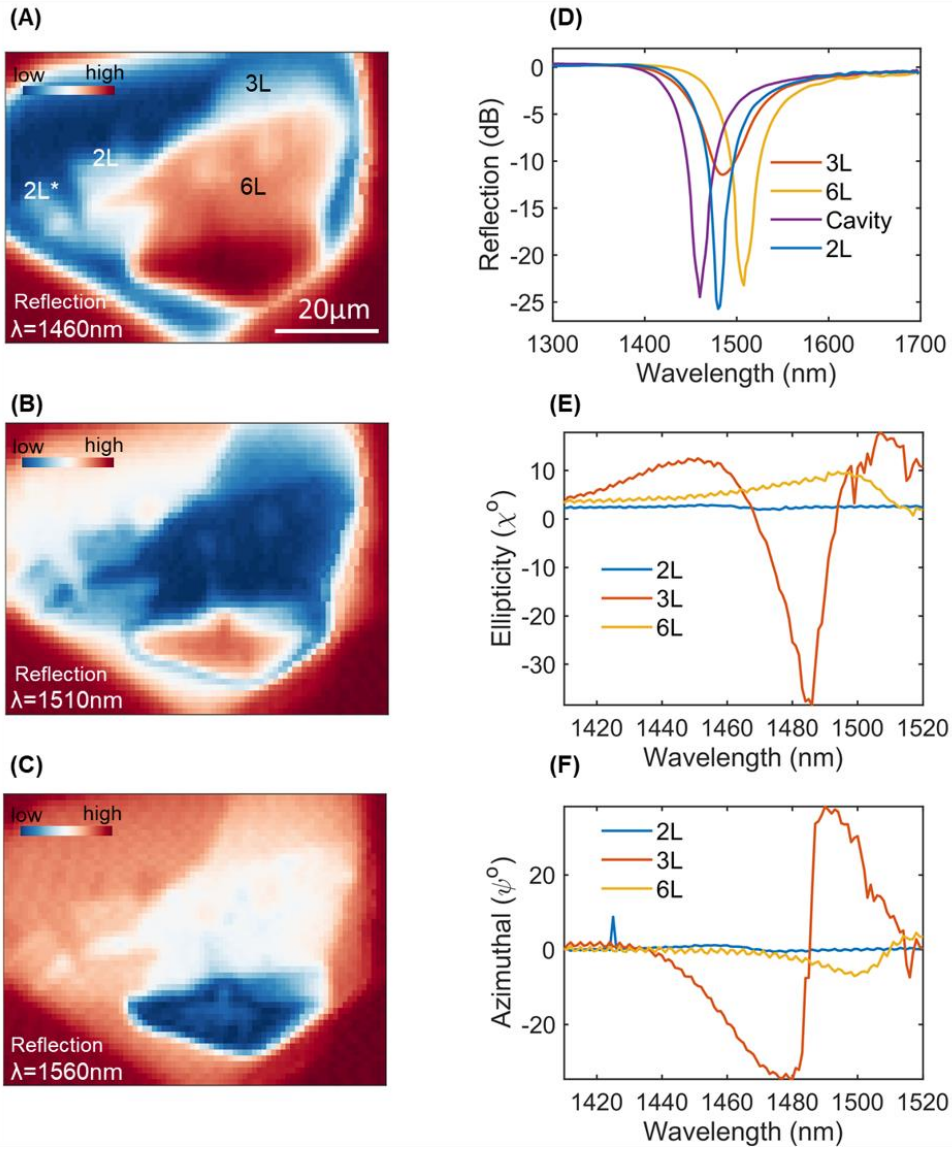

Figure S3.13. Effect of thickness on the cavity resonance and polarization conversion. (A), (B), (C) Reflection spatial maps at 3 different wavelengths (1460 nm, 1510 nm, and 1560 nm) for device D4 showing difference in contrast for different thicknesses of BP. (D) Reflection amplitude spectrum for different thicknesses of BP (2,3 and 6 layers) and bare cavity–illustrating redshift of cavity resonance with increasing thickness of BP. (E) Ellipticity and (F) Azimuthal angle spectrum for 3 different thicknesses of BP, showing highest polarization conversion in TLBP (3-layers).

S3.16 Effect of the incident polarization state on the polarization conversion

We investigate here, numerically, the effect of incident polarization on the spectral trajectory traversed on the normalized Poincaré sphere. To illustrate conditions close to the experimental measurements, two sets of simulations are presented–the first one with the cavity resonance along the AC direction at 1440 nm and the second one at 1495 nm, corresponding to conditions in Device D1 and D4, respectively. The difference in spectral trajectories arise from the competition between the excitonic absorption along the AC direction and the cavity resonance and represents a tuning knob to access different polarization states.

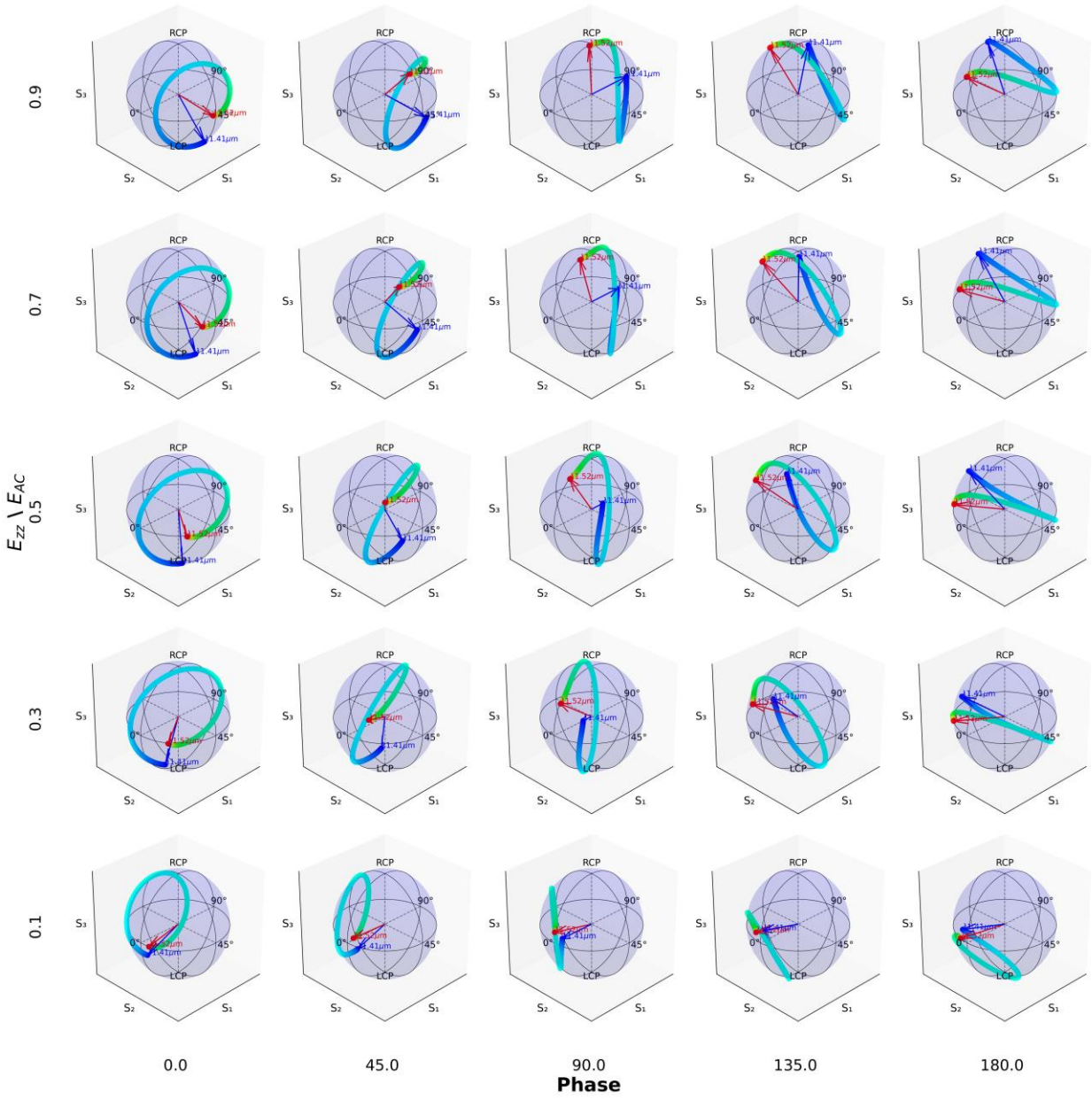

Figure S3.14. Polarization conversion dependence on incident polarization. Effect of the input polarization condition on the evolution of spectral trajectories on the normalized Poincaré sphere is shown. As the phase delay and the relative amplitudes are tuned between the AC and ZZ component of the incident light, different trajectories are undertaken. The cavity resonance along the AC direction is at 1440 nm. The blue (red) arrow denotes the polarization state at 1410 (1520) nm.

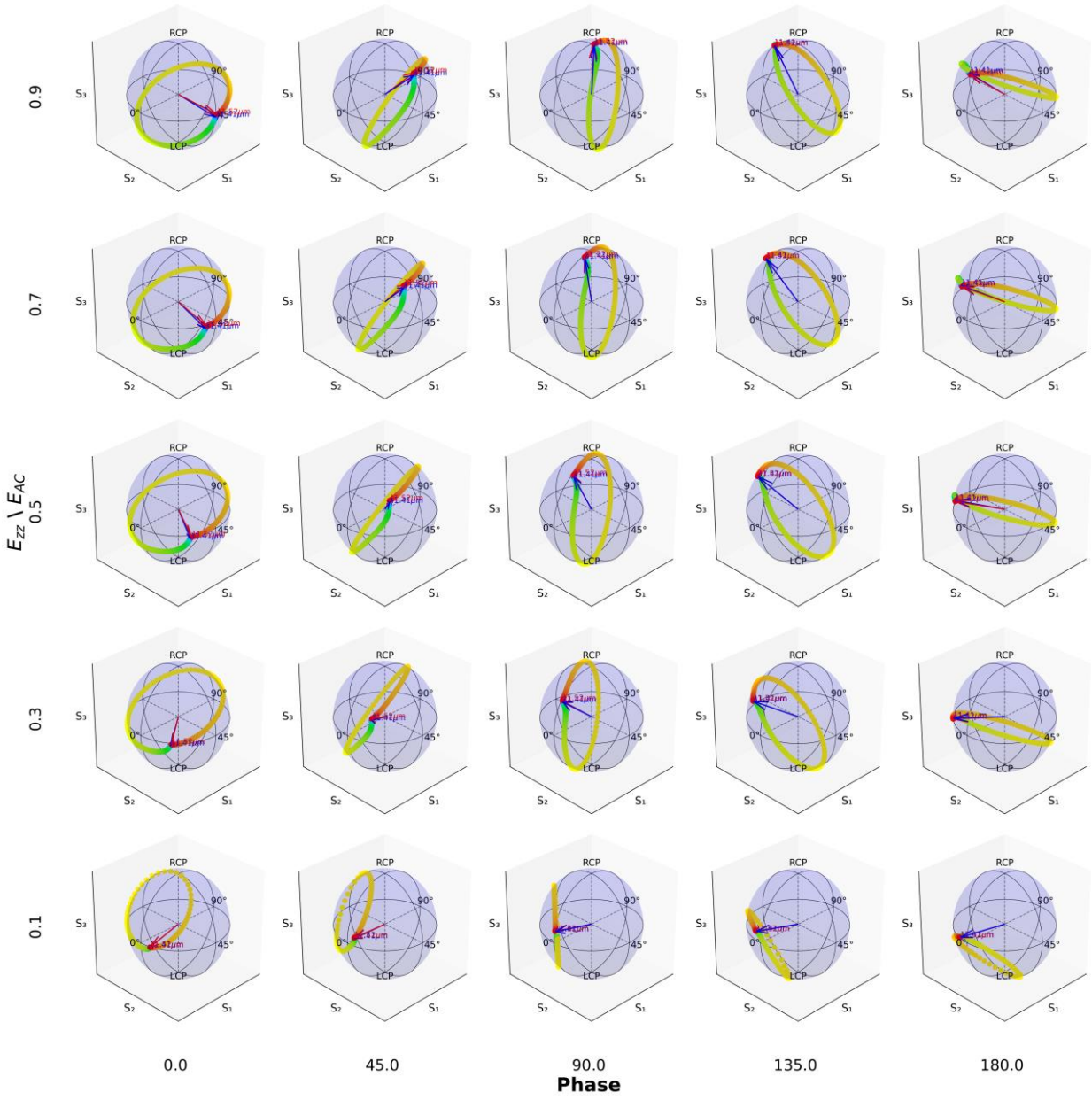

Figure S3.15. Polarization conversion dependence on incident polarization. Effect of the input polarization condition on the evolution of spectral trajectories on the normalized Poincaré sphere is shown. As the phase delay and the relative amplitudes are tuned between the AC and ZZ component of the incident light, different trajectories are undertaken. The cavity resonance along the AC direction is at 1495 nm. The blue (red) arrow denotes the polarization state at 1410 (1520) nm, overlapping.

S3.17 Numerical modelling of cavity-enabled polarization conversion

We discuss here, through numerical modelling, the effect of the different exciton parameters on the polarization conversion performance of a typical cavity. Fig S3.16 summarizes our findings by showing the azimuthal and ellipticity dependence on the exciton broadening, oscillator strength and the exciton resonance wavelength. The most striking impact on the polarization conversion is seen from the oscillator strength, which dictates how strong the exciton, hence the anisotropy, is. Impact of the broadening or the resonance frequency is relatively weak on the azimuthal angle. Similarly, for ellipticity also, a strong dependence is seen on the oscillator strength. Quite interestingly, while the overall magnitude of the ellipticity resonance is reduced with decreased oscillator strength, for wavelengths slightly below 1440 nm, a non-monotonic dependence is seen. This wavelength range can be used to tune ellipticity from a low value to a high vale and back to low again, making it attractive for tunable quarter-wave plate like operation. This non-monotonicity stems from the co-variation of amplitude and phase as a function of exciton parameters, which are both captured in ellipticity. With increasing doping, while the refractive anisotropy is reduced which causes the overall ellipticity change to decrease, the losses are quenched too, which increases the Q-factor of the cavity resulting in the lineshape modification and higher ellipticity for certain wavelength ranges. A small impact of broadening is seen on ellipticity, whereas a monotonic but sizeable effect is observed with resonance frequency of the exciton on the same. Cavity parameters used were: top Au = 10.5 nm, PMMA = 140 nm, top hBN = 53 nm, BP = 1.59 nm, bottom hBN = 119 nm.

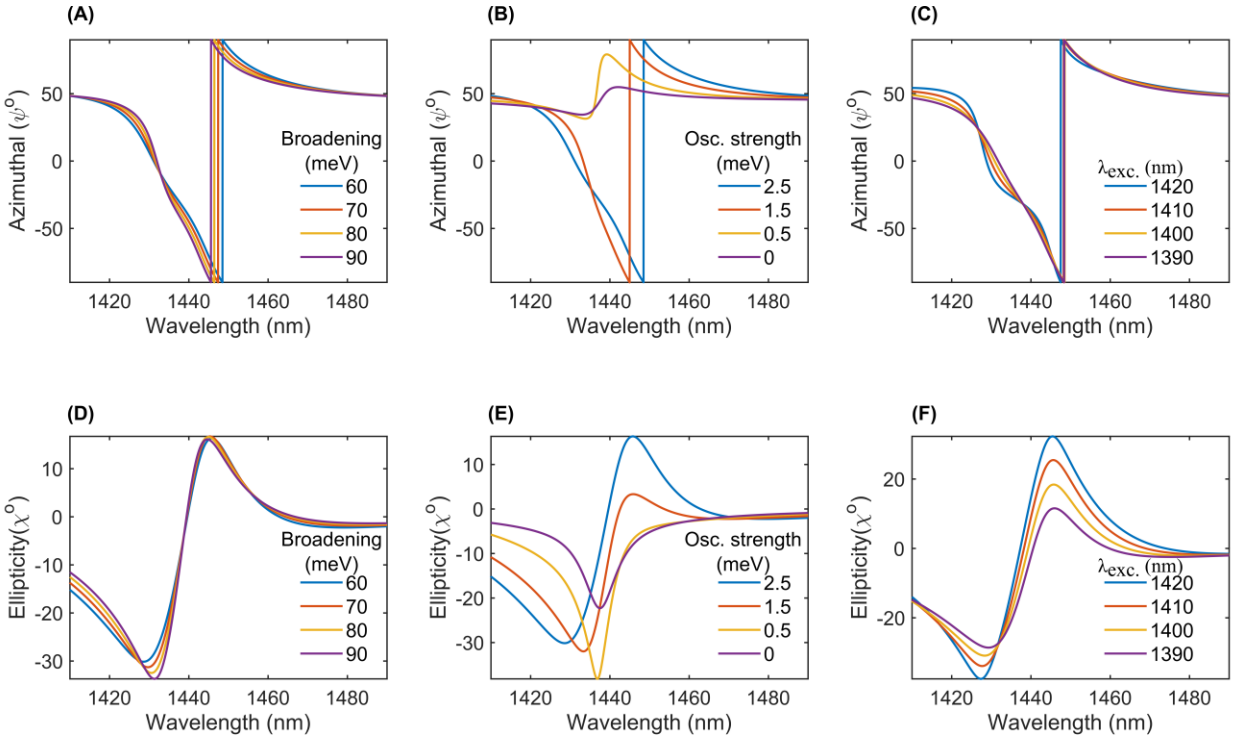

Figure S3.16. Polarization conversion dependence on exciton parameters in TLBP. Effect of different exciton parameters on the azimuthal and ellipticity of a typical cavity-based device. (A), (B), (C) Effect on azimuthal angle for different exciton broadening, oscillator strength and resonance wavelength, respectively. (D), (E), (F) Same as (A)-(C), but for ellipticity.

Since the polarization dynamics is most strongly tuned with the strength of the oscillator, we can numerically estimate the cavity spectral variation with doping. We plot the Stokes parameters (S_0, s_1, s_2, s_3) as a function of the oscillator strength. An excellent agreement with experimental measurements is seen, confirming that screening of the exciton due to free carriers is the major driving mechanism for polarization conversion.

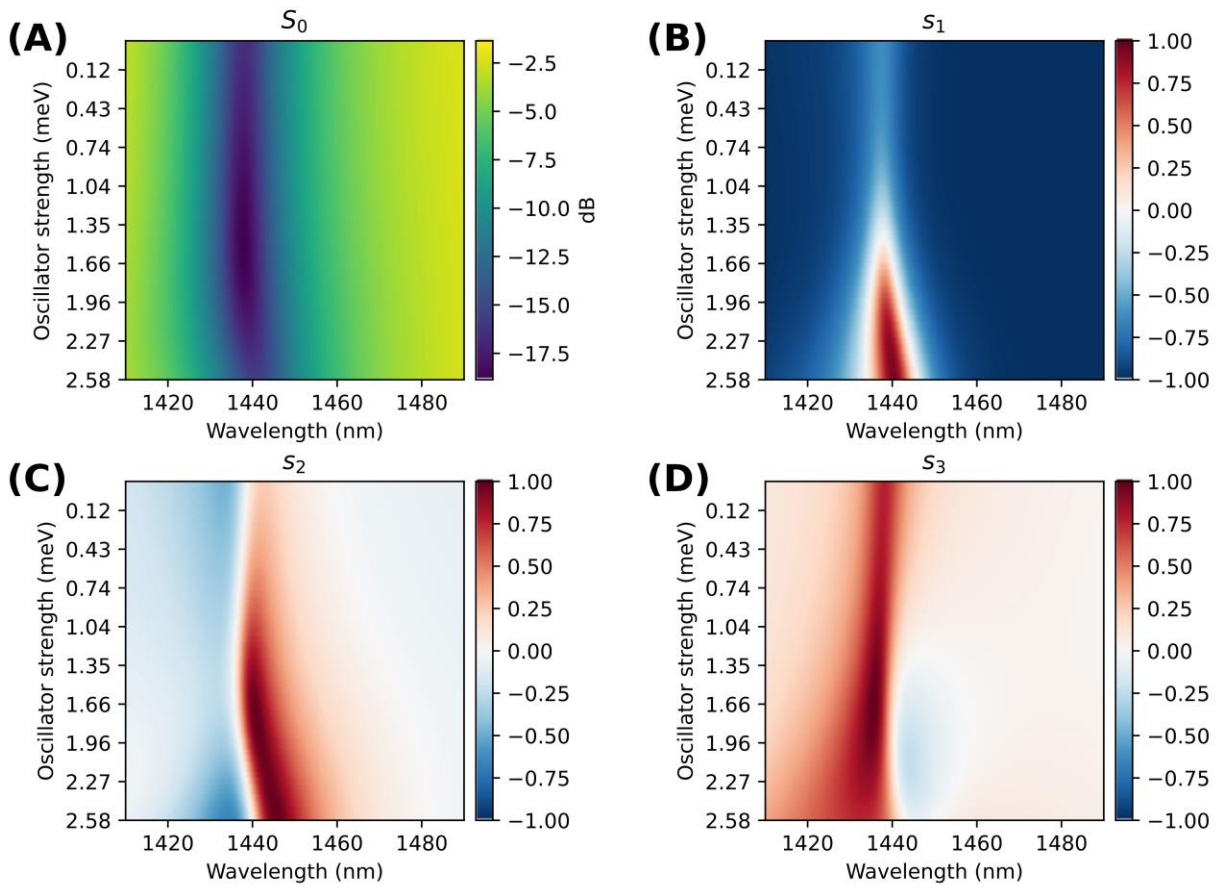

Figure S3.17. Numerical modelling of cavity enabled polarization conversion. (A) Intensity (S0) variation with oscillator strength of the exciton in TLBP. The cavity parameters correspond to device D1. (B), (C), (D) s1, s2, s3 showing the same. This agrees with our experimental observation of the electrically tunable polarization conversion results.

S3.18 Additional gating results from other spots on D1

Here, we discuss the gating results from other spatial positions on device D1. The general trend of the spectral trajectory collapsing in arc length is observed for all points. However, the exact trajectories traced out on the normalized Poincaré sphere are determined by the local complex refractive index of the TLBP and its gate tunability.

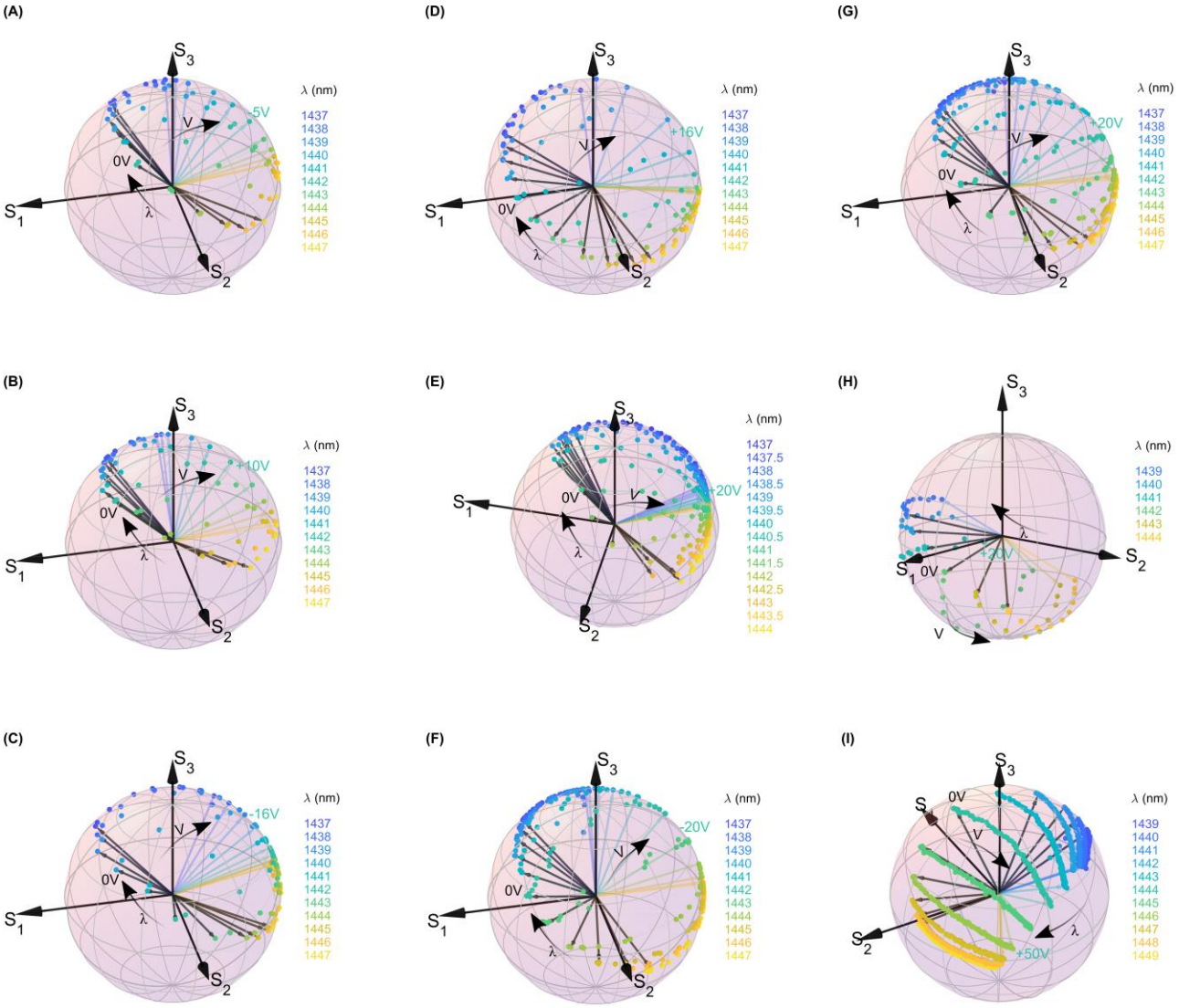

Figure S3.18. Normalized Poincaré sphere dynamics from additional spatial points in device D1. (A)-(I) Normalized Poincaré sphere trajectories for different wavelengths for different voltages for different spots in device D1. Each color corresponds to a different wavelength. For each color, the voltage trajectory direction is marked. Beginning and end voltage values are marked for each

measurement. The dark arrows point the 0V condition for each wavelength and the light (color coded for each wavelength) arrows denote the highest voltage point.

S3.19 Full spectral dynamics on the normalized Poincaré sphere

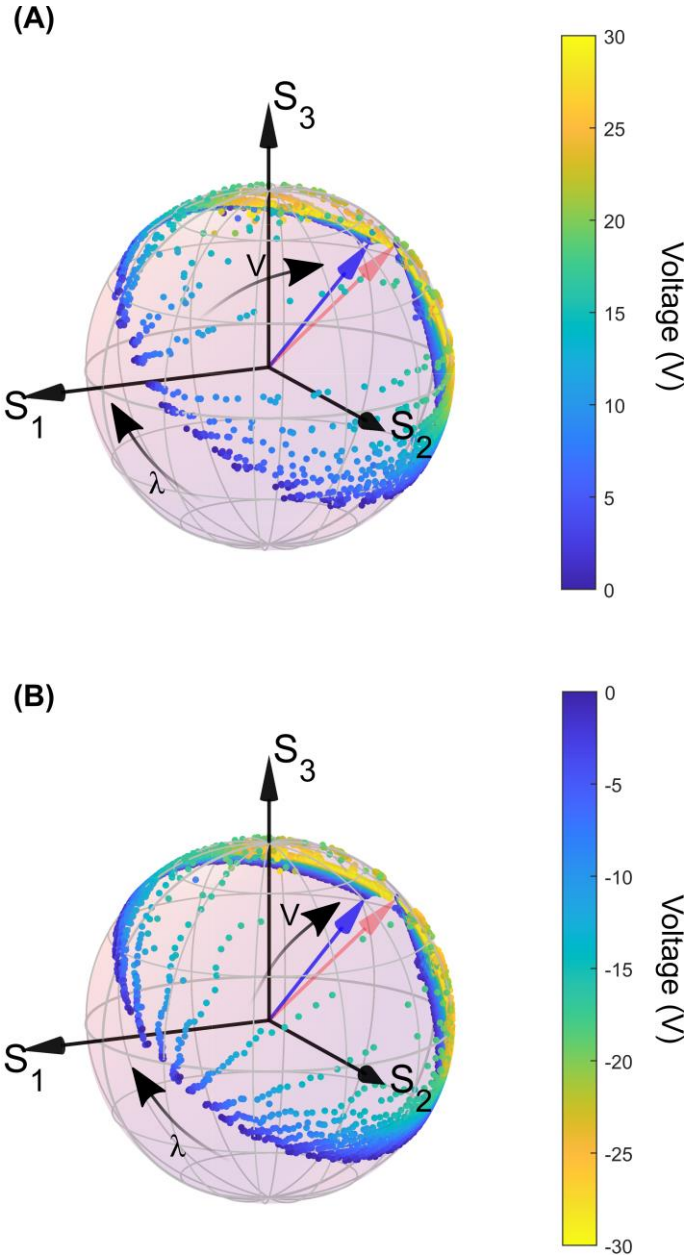

Figure S3.19. Spectral and voltage tuning of normalized Poincaré sphere trajectories for Device D1. (A) Evolution of polarization conversion for positive voltages (electron doping) and (B) negative voltages (hole doping). The same color represents a spectral scan (from 1410 nm to 1520

nm in steps of 0.5nm), while a color variation shows changes of the spectral trajectory with voltage from 0 to 30V for (A) and 0 to -30V for (B), in steps of 0.5V. Blue arrows represent polarization state at 1410 nm for 0V while red arrows represent the same at 1520 nm.

S3.20 Normalized Stokes parameter tuning on electron and hole doping

A competition between the excitonic absorption and the cavity resonance governs the overall optical response of the system, due to the close proximity of the two features. Hence, maximising the polarization conversion requires carefully adjusting the incident polarization to balance the losses along the two principle axes of TLBP for a fixed orientation of the device. To quantify the degree of polarization conversion, traces on the normalized Poincaré sphere were measured for different input ellipticity and azimuth. The longest arc was found for nearly linearly polarized input at an angle of ~27° with the AC axes of TLBP, corresponding to a vertical polarization in the lab frame.

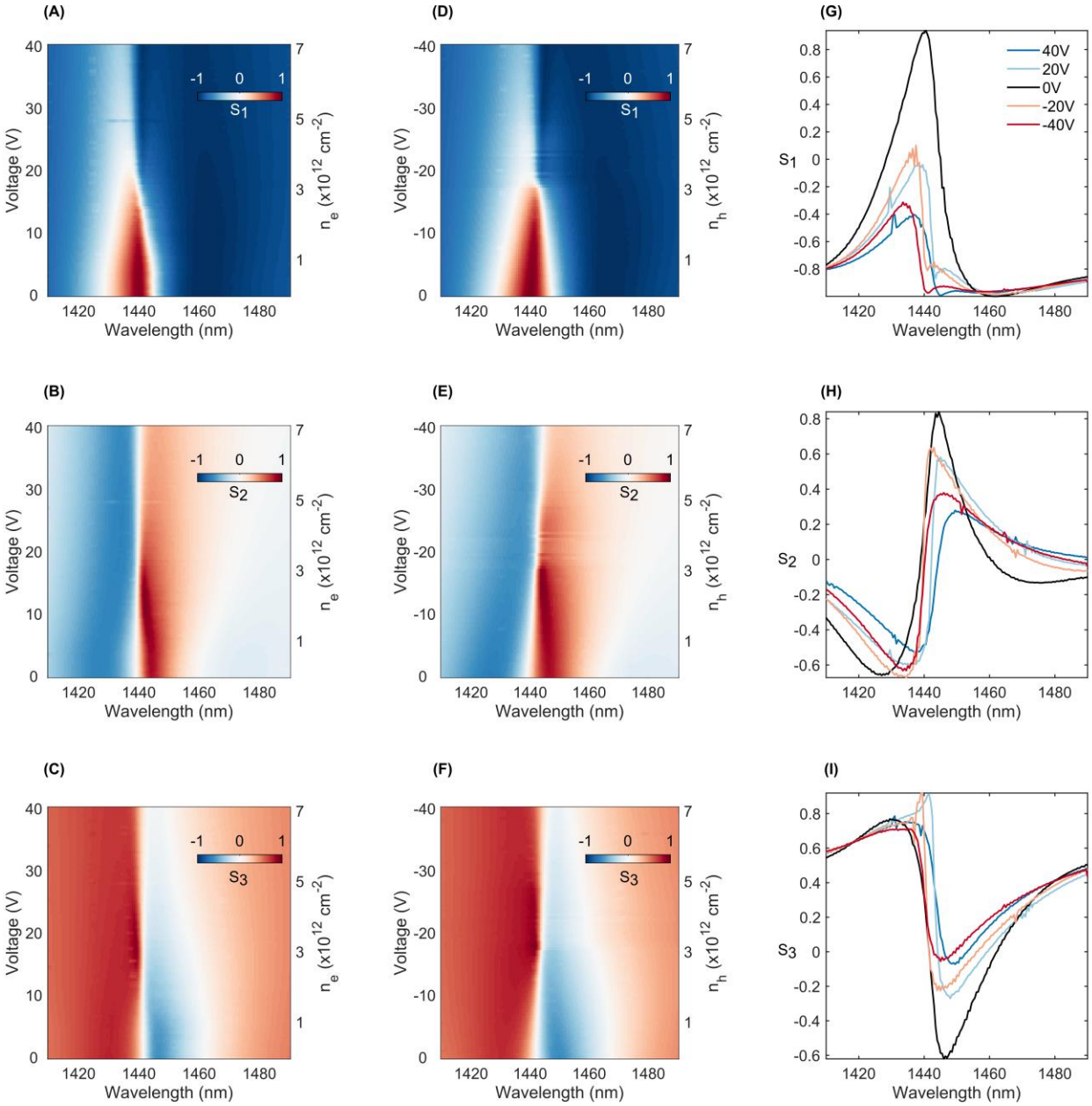

Figure S3.20. Normalized Stokes parameters with electron and hole doping. (A), (B), (C) False colormaps of the evolution of the three normalized Stokes parameters (s_1,s_2,s_3), determining the polarization state of the reflected light, as a function of wavelength and positive voltages (for electron doping). The results are from device D1. Continuous tuning of all the 3 parameters can be seen around the cavity resonance (~1440nm) for the entire range of doping, illustrating efficient tuning of the polarization state with voltage. (D), (E), (F) Same as (A), (B), (C) but for negative voltages (for hole doping), showing similar changes as the electron doped side. The nearly symmetric nature of the doping dependence shows that at 0V, the device is at charge neutral

conditions. (G), (H), (I) Line cuts taken from the false colormaps for the three normalized Stokes parameters (s_1, s_2, s_3 respectively) for 5 different voltages (0V, 20V, 40V, -20V, -40V) to visualize the changes with higher clarity.

S3.21 Reflectance changes on electron and hole doping

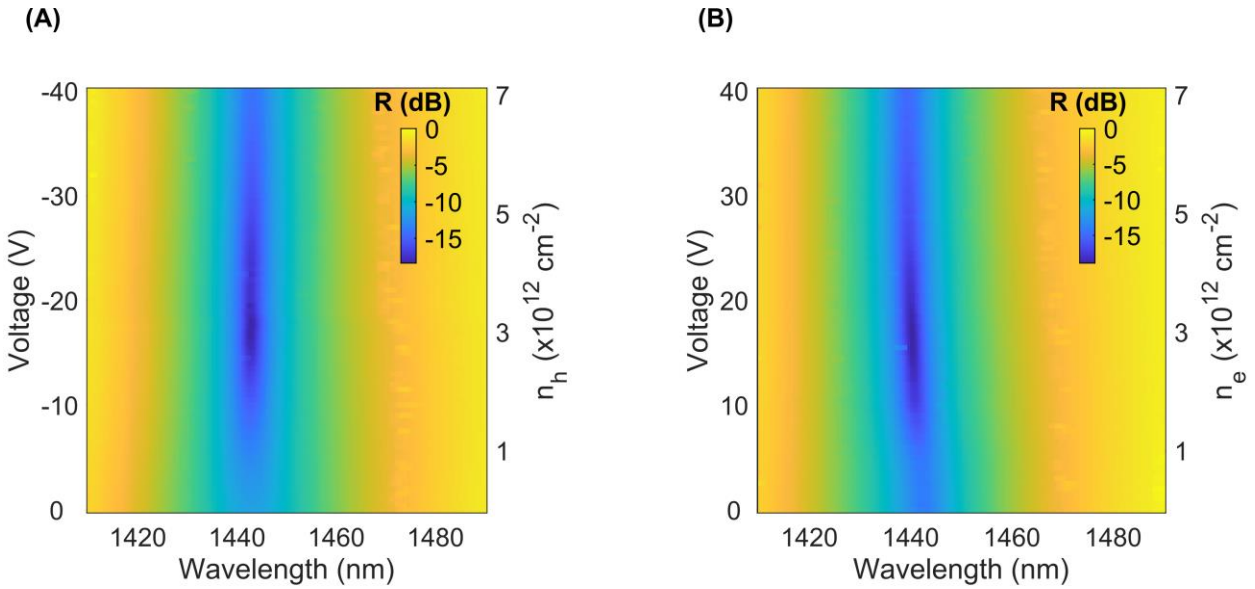

Figure S3.21. Reflectance change (S0) of the cavity upon electron and hole doping. (A), (B) show the change in the reflectance (Stokes intensity S_0) of the device D1 as a function of wavelength for different applied voltages on the hole doping and electron doping side, respectively. The colormaps are plotted in dB for better clarity.

S3.22 Azimuthal and ellipticity changes on electron and hole doping

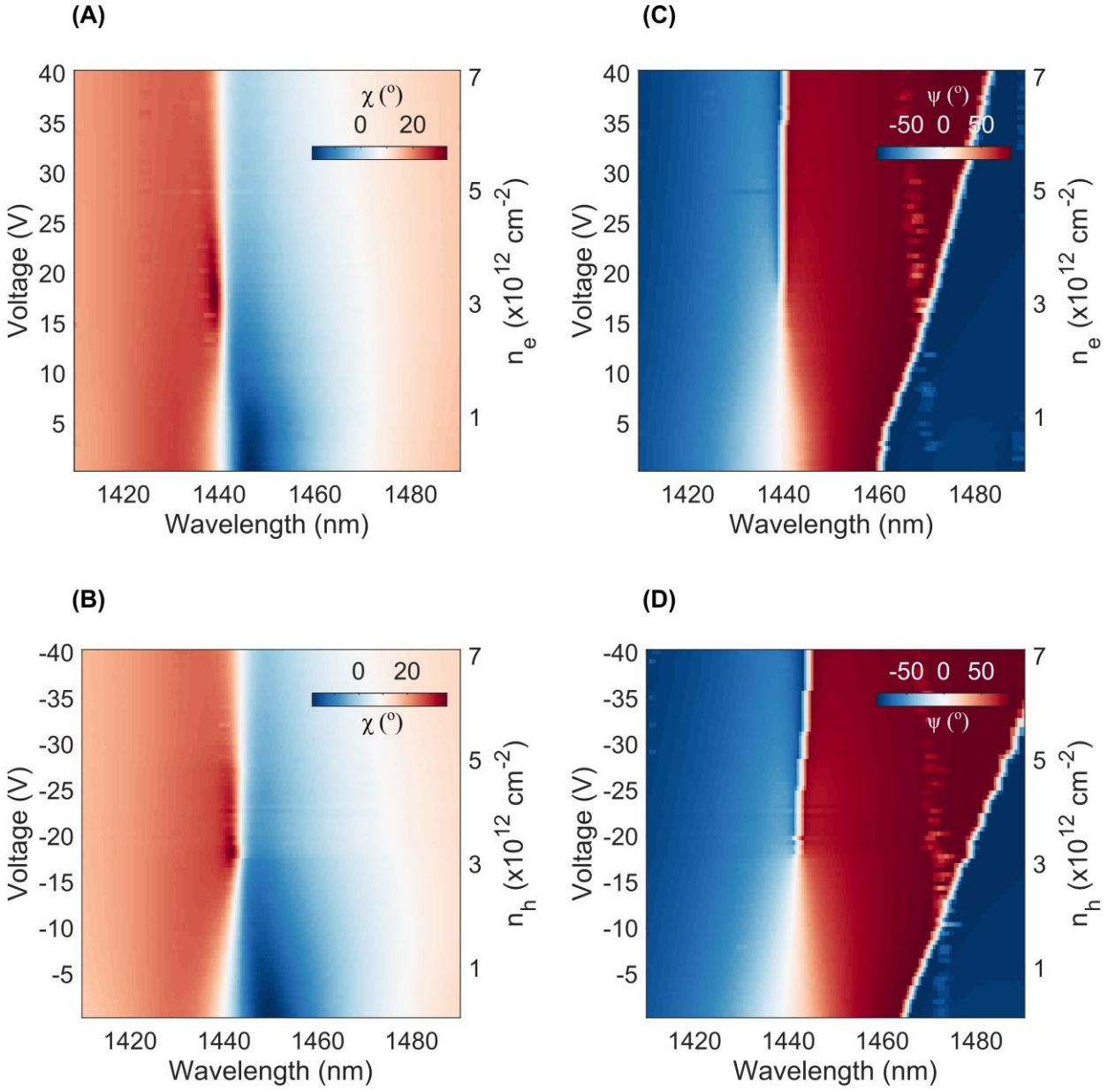

Figure S3.22. Azimuthal and ellipticity angle change upon electron and hole doping. (A), (B) show the changes in the ellipticity angle (χ), in degrees, of the device D1 as a function of wavelength for different applied voltages on the electron doping and hole doping side, respectively. (C), (D) show the same as (A) and (B), but for the azimuthal angle (ψ), in degrees. The abrupt jump in the azimuthal angle is a numerical artifact arising from the indistinguishability between +90° and -90°.

S3.23 Additional gating results from a 5-layer BP device

We present here electrically tunable reflection contrast measurements performed on a 5-layer BP sample. The device geometry is the same as the one adopted for 3-layer devices (hBN-BP/FLG-hBN/Au). Fig. S3.23A shows the reflection contrast along armchair (AC) and zigzag (ZZ) directions. A strong excitonic feature at 2 μm is seen along the AC direction, while a featureless spectrum is seen along the ZZ direction. Upon application of gate voltage, strong modulation of the reflectivity is seen. Fig. S3.23B summarizes the results demonstrating the same. The changes are visualized better when normalized to the reflectivity at 0 V. The strongest modulation is seen at 2 μm, which confirms that the origin of this electro-optic response originates from the exciton dynamics. These measurements were performed using a Fourier transform infrared (FTIR) white light source coupled with an infrared microscope in ambient conditions. These measurements demonstrate that efficient polarization conversion can also be achieved at much longer wavelengths (~2 μm) due to the large excitonic tunability. In fact, the thickness of BP can be tuned, and the operation wavelength can span the entire visible (750 nm) to mid and far-IR range (~3-20 μm).

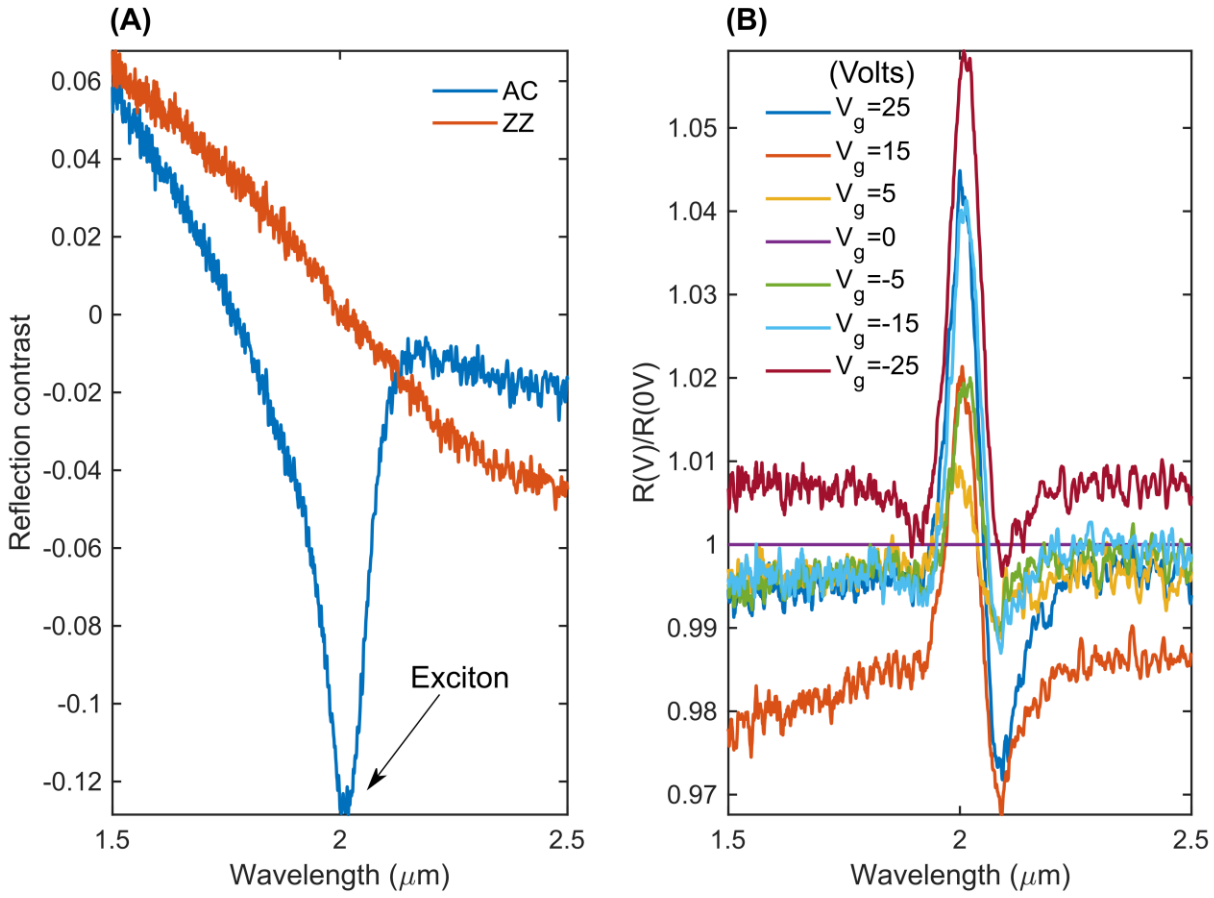

Figure S3.23. Gate-dependent reflectivity modulation in 5-layer BP device. (A) Reflection contrast showing excitonic feature along the AC direction and a featureless spectrum along the ZZ direction. (B) Relative reflection (w.r.t. 0V) shows strong modulation under different applied biases, with the strongest tuning near the excitonic resonance.

S3.24 Choice of three-layer BP (TLBP)

We motivate here why TLBP was used in the study over other thicknesses of BP. The choice of three-layers is primarily driven by the compelling technological advantages of constructing electro-optic modulators in the telecom band such as for optical fiber communication (typical losses are ~0.2 dB/km at 1.5 μm as compared to 8 dB/km at 640 nm), quantum networks and photonic integrated circuits (based on Silicon). Previous reports on layer-dependent bandgap in BP support the fact that BP is well suited for operation from visible to mid-IR. Furthermore, these

studies clearly show the evolution of the optical bandgap (excitonic resonance) in BP as a function of layer thickness. While the optical bandgap is in the visible (~750 nm) for monolayer BP, it saturates at ~4 μm for >20nm thin films. Three layers hits the sweet spot with an excitonic resonance ~1400 nm, particularly suited for the window of telecom operation.

Furthermore, the electrical tunability of such optical transitions is expected from similar studies in monolayer TMDCs and few-layer BP. The key physics driving the polarization conversion tunability (or in general terms, tuning the exciton polarizability) is the suppression of excitons due to screening by induced free charges. These effects are most prominent for monolayer TMDCs owing to their direct bandgap and strong excitons, while for bilayer or multilayer TMDCs, the bandgap becomes indirect, and the magnitude of electrically driven changes reduce. However, for BP, because of the band minima being at the Γ-point (arising out of D_{2h}^{18} point group crystal symmetry), the direct nature of the bandgap is always maintained and thus the excitonic effects and its tunability remain quite significant at the few-layer limit, as shown in our work, for both TLBP and 5-layers BP. The modulation fraction decreases as the thickness of BP is increased, which stems from the finite Thomas-Fermi screening length that governs the amount of effective modulation depth in the vertical direction in a semiconductor channel. Such length scales are typically of order ~2-3 nm for the charge densities accessed here for BP; anything thicker is effectively not modulated beyond the Thomas-Fermi screening length. The Thomas-Fermi screening length can be visualized in the following plot:

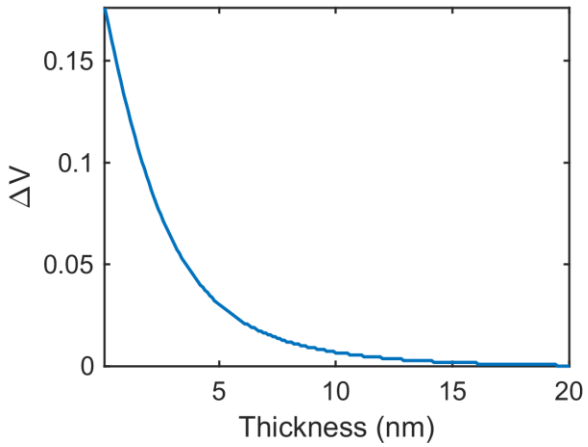

Figure S3.24. Thomas-Fermi screening effect in BP. Band-bending in multilayer BP as a function of thickness for a charge density of $5 \times 10^{12}/cm^2$. A Thomas-Fermi screening length (λ_{TF}) of 2.9 nm is obtained.

To summarize, both the bandgap being conveniently in the telecom band along with the high electrical tunability of the exciton drives our choice of three-layers BP (TLBP). The same effect can however be shown in monolayer BP in the visible/NIR (600-900 nm), bilayer BP in the NIR (900-1200 nm), and so on and so forth. Finally, the degree of polarization conversion will ultimately depend on the coupling between the cavity and free space and hence the cavity would need to be designed for the right working wavelength.

S3.25 Comparison of polarization conversion mechanism with liquid crystals

The distinction between bulk materials and excitonic 2D semiconductors, particularly TLBP in this case, is quite important. While the electro-optic operation hinges on the physical re-orientation of the dipoles for bulky materials like liquid crystals, such is not the case for 2D excitons. The physical mechanism of the operation of our device is the screening effect of the excitons by the excess induced charges in TLBP which eventually effect the dipole oscillator strength. The vertical electric field that is generated in the capacitor (hBN in our devices) alters the charge density in the TLBP–which acts as the other plate of the parallel plate capacitor (the back Au is the first plate). This causes the quasi-1-D dipoles which are in-plane to be affected by the out of plane electric field from the capacitor. Thus, when a normally incident light interacts with the heterostructure,

the in-plane dipoles influence the in-plane electromagnetic fields. Previous measurements of tuning the dipole strength in TMDCs have also leveraged this strong vertical-field induced doping to tune the interaction with an in-plane optical field. However, due to lack of crystal symmetry breaking in the in-plane direction, such efforts have failed to control polarization.

It is also important to note, that thus far, no evidence points to actual reorientation of the dipoles (initially along x-direction) with gating, but rather a reduction in the oscillator strength and enhanced scattering.

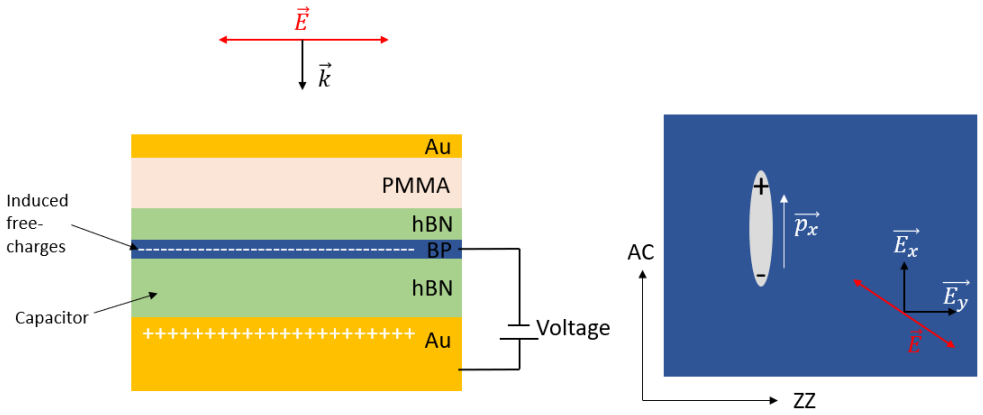

Figure S3.25. Dipole interaction with optical field in TLBP. Side view of capacitor geometry of working BP device. The two plates of the parallel-plate capacitor are the BP and the back Au electrode/reflector. Free carriers are induced in the BP with applied voltage. Incident optical field (polarized in the in-plane direction, perpendicular to the vertical capacitor field) is shown, along with the Poynting vector. A top view of the BP flake along with the dipole orientation is shown, with the Armchair (AC) and Zigzag (ZZ) axes marked. Incident field (in-plane) can be decomposed along the AC and ZZ direction, marked as x and y, respectively. The x-component is strongly influenced by the exciton-enhanced cavity interaction (which is also electrically tuned), whereas the y-component is only influenced by the cavity and not the exciton and thus is not tuned.

S3.26 Cyclic measurements for electrically tunable devices

Multiple cyclic measurements were done on all gate tunable devices, and the results are highly consistent. No noticeable hysteresis was observed when the voltages were swept in a cyclic fashion. The cyclic scheme adopted in this work is as follows: 0V to +20V, back to 0V, to -20V

and then back to 0V. The normalized Stokes parameters (s_1, s_2, s_3) and the voltage sequence for one such device (D1) is shown in Fig. S3.26.

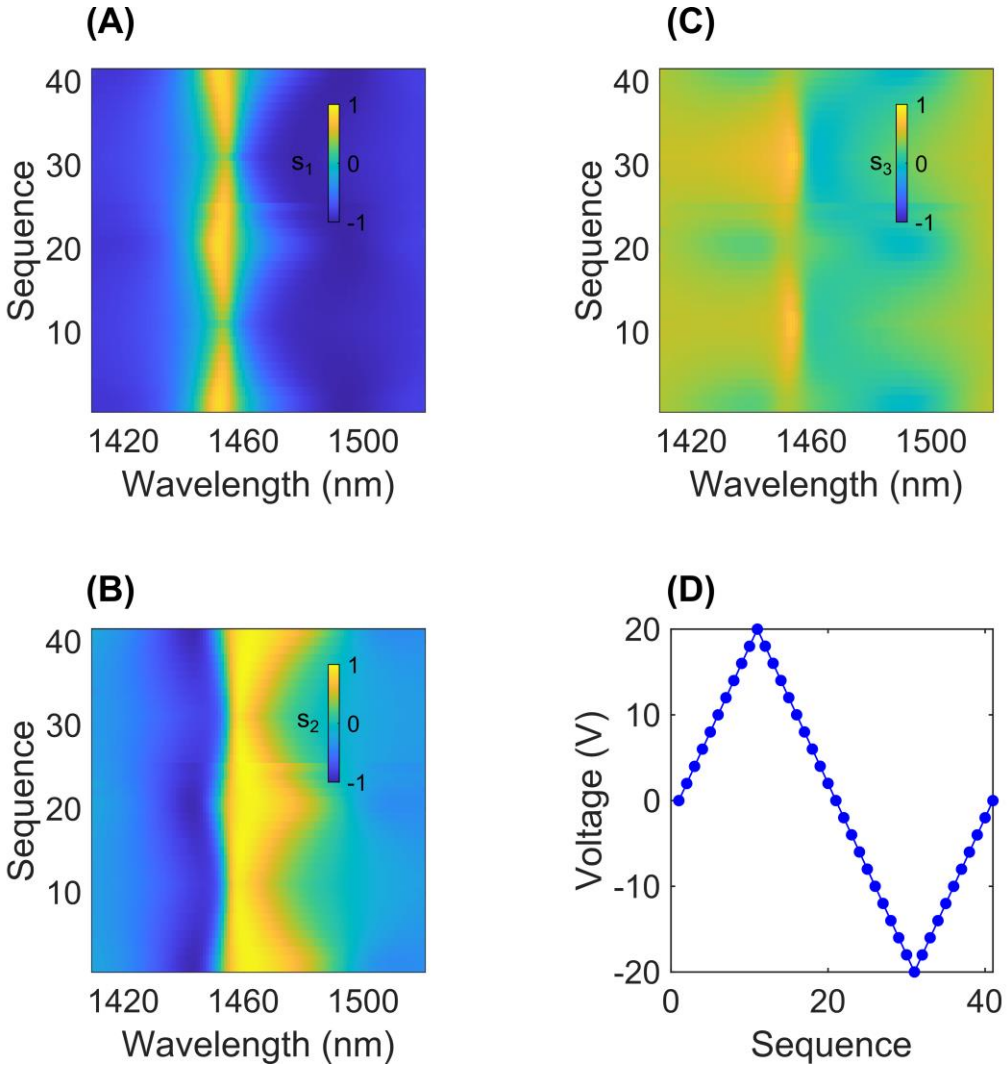

Figure S3.26. Cyclic Stokes measurements. (A), (B), (C) Normalized Stokes parameters (s_1, s_2, s_3) spectra measured as a function of voltage in a cyclic fashion. (D) The applied voltage as a function of the sequence number.

S3.27 Discussion about edge effects in spatial mapping of polarization conversion

"Edge effects" may result from the convolution of an atomically sharp edge encountered at the end of a BP flake and a gaussian beam, in the spatial maps presented. In the current measurement configuration, we are limited by the optical diffraction limit, and it is not possible to resolve an

atomically sharp edge. Thus, a true edge is not measured, rather it is convolved with the nearest pixel. So, near the edges, the ellipticity appears reduced because the finite size (~1.5-2 μm) gaussian beam samples both the BP flake + cavity and the no-BP cavity only region. Furthermore, the blueshift in the resonance compared to the interior of the BP flake can be understood from the fact that the beam is sampling less material or reduced cavity length (as it scans half a TLBP and half a missing BP region, for example) and thus the cavity resonance blueshifts. To prevent a convolution of the edge effect and true polarization dynamics, all the gate tunable and passive device measurements shown in the paper have been done in the interior of the samples and not at the edges. Further higher resolution measurements, such as tip-based near field microscopy, would be required to address if there are any true edge effects, such as edge lattice reconstruction and how that influences the polarization conversion. An illustration of the finite size of the beam and the sampling effect is shown for further clarity in Fig. S3.27.

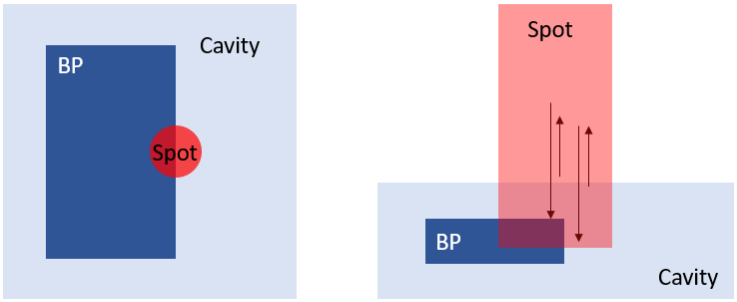

Figure S3.27. Edge effects in spatial mapping. Top view and side view illustration of cavity and BP, along with the gaussian (diffraction limited) beam at the edge showing sampling from both the regions leading to different polarization conversion at the edge compared to the interior of the sample (spot size is exaggerated for clarity).

S3.28 Outlook towards high efficiency polarization modulators based on BP

Our current work illustrates the versatility of using BP, especially TLBP (for telecom band), as an active material for polarization conversion. In the current scheme of operation in a modest quality factor cavity and sufficiently close to the excitonic feature, the overall reflectivity of the devices is low. Several ways may be adopted to boost this efficiency to a higher value. Firstly, to increase

the overall reflectivity, high-Q cavities (such as photonic crystal cavities, DBR-based Fabry-Pérot cavities, etc.) can be combined with BP at sufficiently detuned wavelengths (detuned from excitonic resonance) to reduce the losses in the system. This obviously requires a judicious choice of thickness for BP depending upon the working wavelength. For example, at 1550 nm, we expect bilayer (or even monolayer) BP to be a good candidate. Furthermore, to increase the doping concentration and thus the modulation depth, higher dielectric permittivity materials such as HfO_2 can be used. This has been shown to be an effective strategy for low-loss electro-optic modulation recently for TMDCs. Better growth of higher quality BP crystals showing prominent excitonic behavior on different substrates is needed however to make this a viable strategy. Here, we show numerically how such a design would work using experimentally measured complex refractive indices for TLBP and integrated with an ultra-low loss dielectric mirror based Fabry-Pérot cavity, operating at a sufficiently detuned wavelength. The structure considered here consists of a top DBR of 20 pairs of SiO_2/SiN_x (n=1.45/1.87), TLBP, 10-nm gate dielectric Al_2O_3 (n=1.73), a buffer layer of SiN_x (n=1.87) to adjust the cavity resonance, a bottom DBR of 40 pairs of $AlAs/Al_{0.1}Ga_{0.9}As$ (n=3.5/3.05) and a GaAs substrate (n=3.55). The refractive indices for AC BP and AC-doped BP were taken from measurements done at 0V and 50V (hole doping). As can be seen for a working wavelength of 2986.6 nm a phase shift of ~2π can be obtained between undoped and doped conditions, whereas the reflectance stays extremely high (>95%) for the same wavelength. Similarly, the top and bottom pairs can be appropriately designed to maintain high reflection all throughout the spectral window, with a slight compromise in the achieved phase shift. Here, we show the performance of the same design with 17 top pairs (instead of 20), which gives us a maximal phase shift of ~1.55π with over 90% reflection at the working wavelength, but also maintaining >65% for the entire spectral range which is already an extremely high reflection efficiency.

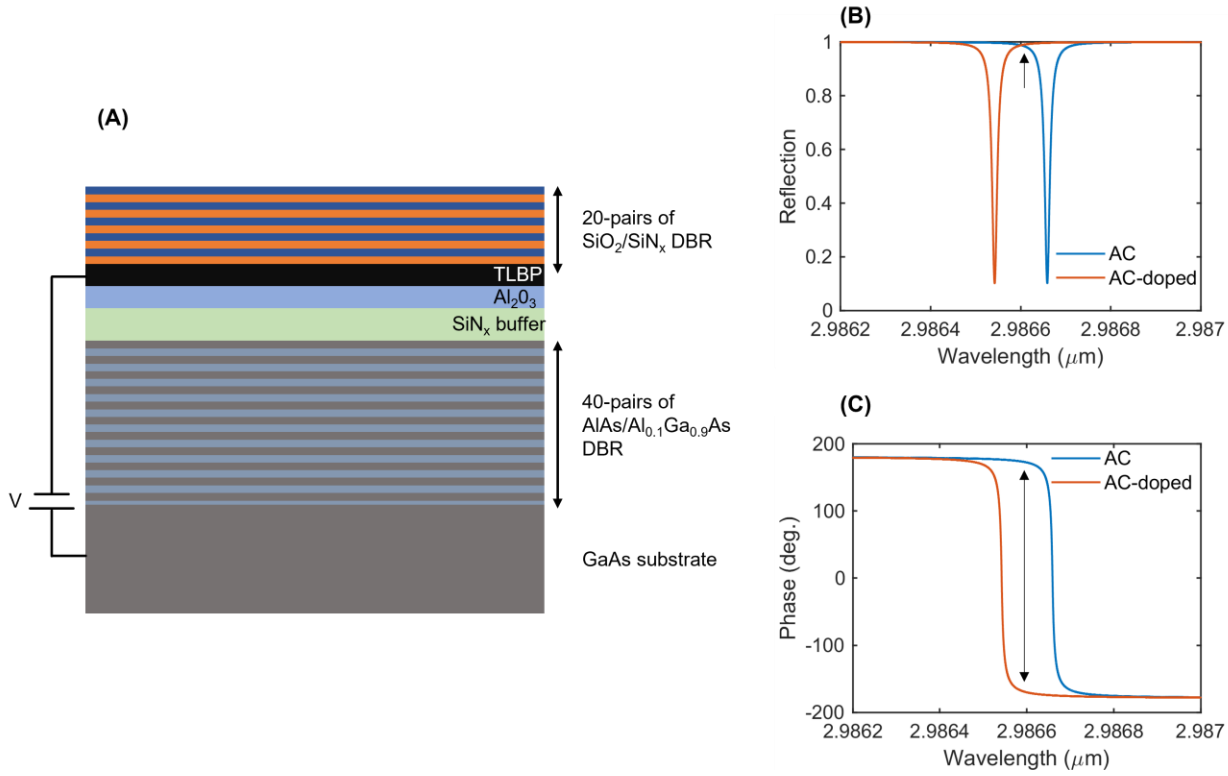

Figure S3.28. High efficiency numerical design for polarization conversion. (A) Double DBR based Fabry-Perot cavity design incorporating BP. (B) Reflection and (C) phase from the corresponding cavity structure for pristine and doped armchair (AC) direction.

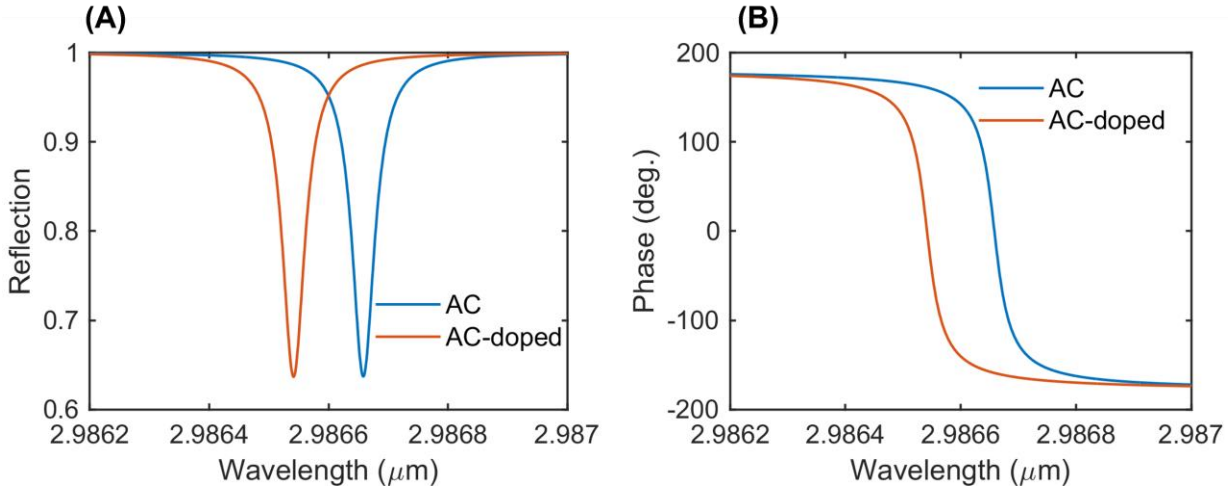

Figure S3.29. High efficiency numerical design for polarization conversion. (A) Reflection and (B) phase from the proposed cavity structure in Fig. S3.28 for pristine and doped armchair (AC) direction for 17-top pairs instead of 20.

Furthermore, for two-state polarization switching devices (applications requiring switching between two-states of polarization such as linear to circular polarization), the design can be tuned to have no amplitude modulation and only polarization modulation. An illustration of this can be already seen in our current working devices. For example, if we analyze the intensity, ellipticity and azimuthal for hole doping in Fig. S36, around 1450 nm, minimal change in intensity (<0.3 dB) and azimuthal angle is seen with significantly large change in ellipticity (~21^0) between 0V, -20V and -40V. Such designs may be further optimized by tuning the cavity resonance for wavelength of interest.

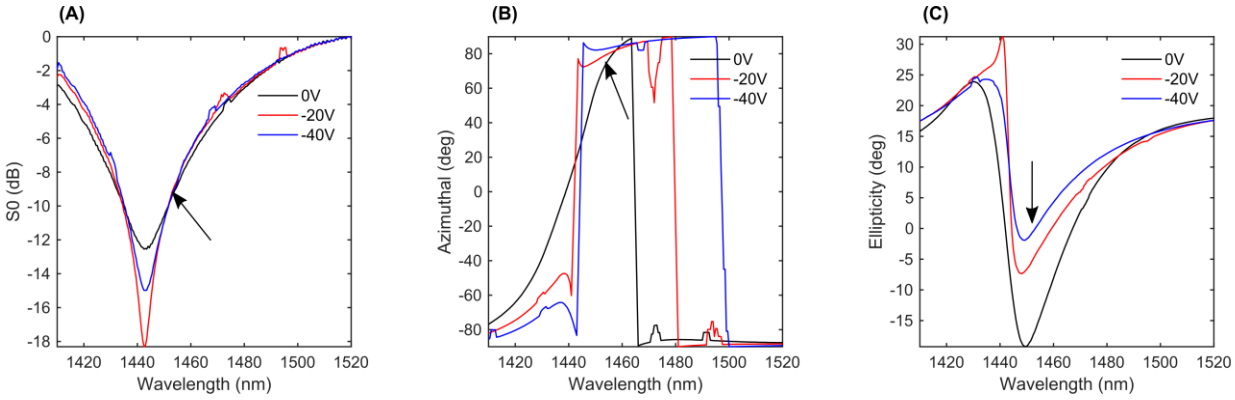

Figure S3.30. Amplitude, azimuthal and ellipticity line cuts for hole doping. (A) Amplitude spectrum for three distinct voltages (0V, -20V, -40V) corresponding to hole doping, showing variation in the intensity at the resonance. (B), (C) Same as (A) but for azimuthal and ellipticity angle. A region around 1450 nm can be identified to have nearly constant amplitude modulation, minimal azimuthal change but large ellipticity modulation.

Finally, we comment on the possibility of complete independent control of both amplitude and phase which requires multiple degrees of freedom (at least 2). We believe judicious dual gate designs, multiple cascaded BP unit-cells and hetero structuring with a broadband lossy material, like graphene, to balance the losses in the two system to keep the amplitude constant, might pave the way towards such control.

Chapter S4. Supplementary Information for Rydberg Excitons and Trions in Monolayer $MoTe_2$

S4.1 Crystal growth, device fabrication, and experimental methods.

SiO_2 (285 nm)/Si chips were cleaned with ultrasonication in acetone and isopropanol for 30 min. each, followed by oxygen plasma treatment at 70 W, 300 mTorr for 5 min. Monolayer $MoTe_2$, few layer hBN and graphene flakes were directly exfoliated using Scotch-tape at 100 ºC to increase the yield of monolayer flakes. Monolayer thickness was initially identified using optical contrast (~7 % contrast per layer) and later verified with atomic force microscopy. hBN thickness was confirmed with atomic force microscopy. Flakes were assembled with a polycarbonate/polydimethylsiloxane (PC/PDMS) stamp with pick-up at temperatures between 80 ºC -110 ºC. The entire heterostructure stack was dropped on prefabricated gates at 180 ºC. The polymer was washed off in chloroform overnight, followed by isopropanol for 10 min. Given the air-sensitive nature of $MoTe_2$ monolayers, exfoliation, identification of $MoTe_2$ flakes and stacking of the entire heterostructures were done in a nitrogen purged glovebox with oxygen and moisture levels below 0.5 ppm. Gates were fabricated on SiO_2 (285 nm)/Si chips with electron beam lithography (PMMA 950 A4 spun at 3500 rpm for 1 min. and baked at 180 ºC, 10 nA beam current and dosage of 1350 $\mu C/cm^2$ at 100 kV), developing in methyl isobutyl ketone: isopropanol (1:3) for 1 min., followed by isopropanol for 30 s and electron beam evaporating 5 nm Ti/95 nm Au at 0.5 $\frac{Å}{s}$ deposition rate. Liftoff was done in warm acetone (60º C) for 10 min., followed by rinse in isopropanol for 5 min. The gates were precleaned before drop-down of heterostructure by annealing in high vacuum ($2x10^{-7}$ Torr) at 300 ºC for 6 h. The chip was then wire-bonded with Aluminum wires on to a custom home-made printed circuit board.

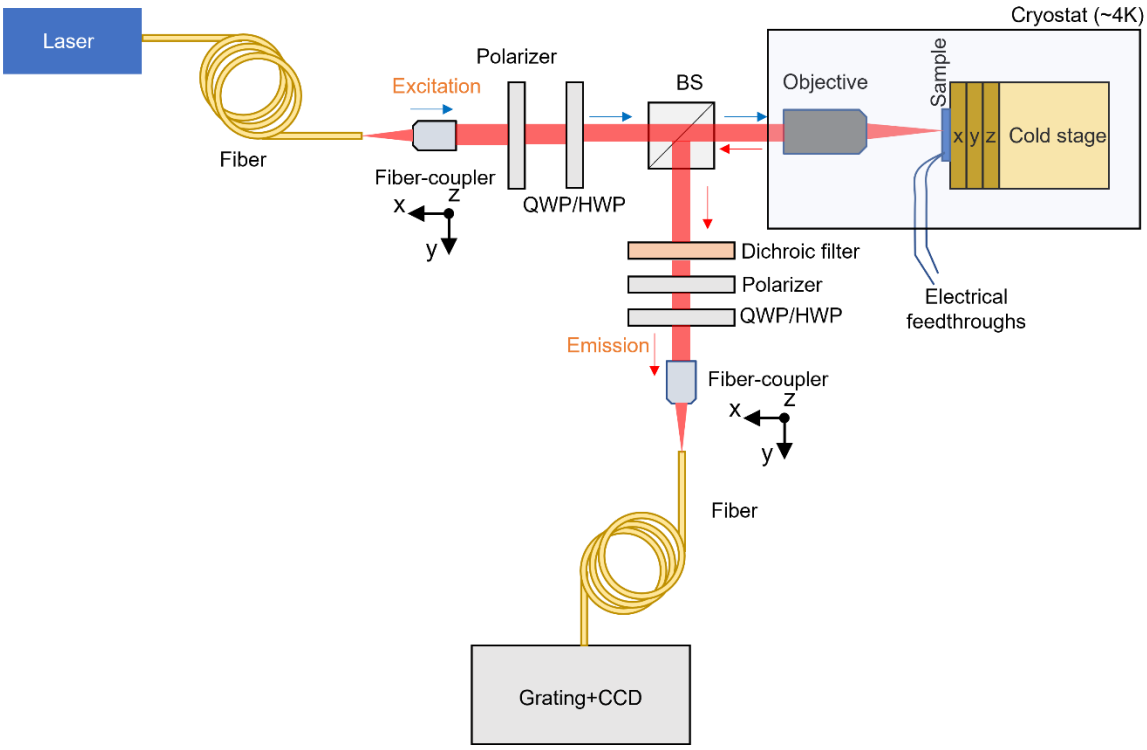

Figure S4.1. Schematic of the low-temperature confocal optical PL setup used. BS–Beam Splitter, QWP/HWP–Quarter/Half Wave Plate.

Low temperature confocal photoluminescence measurements were performed in an attoDRY800 closed-cycle cryostat at base pressures of $<2\text{x}10^{-5}$ mbar. Sample was mounted on a thermally conducting stage with Apiezon glue and stage was cooled using a closed-cycle circulating liquid helium loop. Temperature was varied between ~4K and 300K. A 532 nm (Cobolt) continuous wave laser was used as the excitation source with power ranging between 10 nW and 1 mW, focused to a diffraction limited spot. Emission was collected in a confocal fashion with a cryogenic compatible apochromatic objective with an NA of 0.82 (for the visible and NIR range, LT APO VISIR) and dispersed onto a grating-based spectrometer (with 150 grooves per mm with a Silicon CCD)–Princeton Instruments HRS 300. Voltage was applied using a Keithley 2400. Data was acquired with home-written MATLAB codes.

$MoTe_2$ single-crystals were grown by the chlorine-assisted chemical vapor transport (CVT) method. A vacuum-sealed quartz ampoule with polycrystalline $MoTe_2$ powder and a small amount

of $TeCl_4$ transport agent (4 mg per cm^3 of ampoules' volume) was placed in a furnace containing a temperature gradient so that the $MoTe_2$ charge was kept at 825 °C, and the temperature at the opposite end of the ampoule was about 710 °C. The ampoule was slowly cooled after 6 days of growth. The 2H phase of the obtained $MoTe_2$ flakes was confirmed by powder X-ray diffraction and transmission electron microscopy studies. Flakes obtained from the aforementioned source as well as commercially available $MoTe_2$ (2D Semiconductors) were investigated with similar results.

Atomic Force Microscopy was performed using Bruker Dimension Icon in tapping mode. Data analysis was performed in MATLAB.

S4.2 Choice of optical geometry

The optical geometry adopted here is a Salisbury screen resonant near the A1s exciton transition. Such an optical cavity is illustrated in Figure S4.2. An optical spacer (dielectric) is placed atop a back reflector (metal or dielectric mirror) and an absorbing layer is placed on the spacer. The thickness of the spacer is chosen to be quarter wavelength $\left(\frac{\lambda}{4n}\right)$ such that after one round trip in the cavity the light has travelled a total distance of $\frac{\lambda}{2n}$ which introduces a π phase shift between the incoming and outgoing electromagnetic wave. This enables near perfect light absorption at the resonance wavelength enabling strong light-matter interaction. In our structures, since we have a top hBN the Salisbury screen condition was estimated from a transfer matrix approach to find the right hBN thicknesses which was used as a guide to select suitable hBN top and bottom flakes. The modelling assumed the following parameters:

1. hBN dielectric/optical spacer ($n = 2.2, k = 0$)
2. $MoTe_2$ monolayer absorbing sheet (optical conductivity model) $\sigma(\omega) = \frac{4i\sigma_0 p_0 \omega}{(\omega-\omega_0)+\frac{i\Gamma}{2}}$, where $\sigma_0 = \frac{e^2}{4\hbar}$, $p_0 = \frac{\gamma_r}{4\pi\omega_0\alpha}$ γ_r $(2\ meV)$ is the oscillator strength, ω_0 $(1.17\ eV)$is the resonance frequency and Γ $(7\ meV)$ is the broadening associated with the optical transition.
3. Refractive index of Au (back reflector) was adopted from Johnson and Christy .
4. A top layer of hBN (5 nm) was added.

Calculations were done using a standard 1D transfer matrix model (with stackrt function in Lumerical as well as home-written MATLAB code). Furthermore, our choice of a back-reflector of gold suppresses any photoluminescence coming from the silicon substrate, which would be emitted in a similar wavelength/energy range λ_{Si}~$1150nm$, E_{Si}~$1.07\ eV$ at low temperatures.

In a false color map of absorption spectrum variation with bottom hBN thickness shows high absorption at the excitonic resonance for thicknesses around 100 nm. Motivated by these calculations, the bottom hBN for the device was chosen to be 97.3 nm (confirmed by AFM measurements)–limited by the occurrence of naturally exfoliated thicknesses.

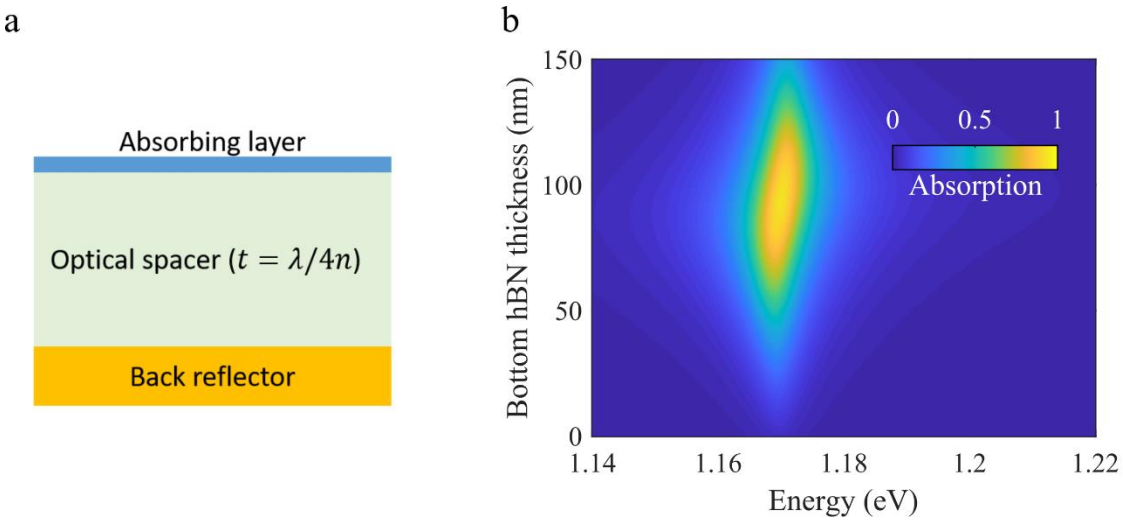

Figure S4.2. Schematic and calculation of optical geometry. (a) Schematic of a quarter wavelength Salisbury screen geometry. (b) Absorption spectrum as a function of bottom hBN thickness showing the cavity-enhancement.

S4.3 Estimation of Purcell enhancement

Simulation set-up details:

Initially, the transfer matrix (1D) model was used to optimize the structure for a resonant Salisbury screen design. The obtained parameters were then fed into Lumerical FDTD (schematic in Figure S4.3a) as follows:

- hBN dielectric/optical spacer ($n = 2.2, k = 0$), total thickness of 102.3 nm.

- Refractive index of Au (back reflector) was adopted from Johnson and Christy, assumed to be optically thick (~150 nm).
- A uniform mesh of 2nm was used in all directions around the dipole and the total simulation span was taken to be $5\mu m$, to eliminate any artifacts.

An x-polarized dipole (in-plane of the simulation) was used to mimic the emission from $MoTe_2$. Since the physical thickness of a monolayer ($t \sim 0.7\ nm$) is much smaller than the wavelengths of interest ($\lambda \sim 1\mu m$) it is justified to assume the dipole is completely in plane with no out-of-plane component. Perfectly matched layers (PML) boundary conditions were used on all sides and the dipole wavelength was chosen to match the A1s exciton emission ($\lambda = 1.172\ eV$ or $1058\ nm$). Field profile (power) monitors were placed around the dipole in XZ and YZ configuration and the total field (real) intensity recorded as shown in Figure S4.3b and c, respectively. From the dipole analysis (in built) in Lumerical FDTD, we estimated a Purcell factor–$F_p = 2.012$.

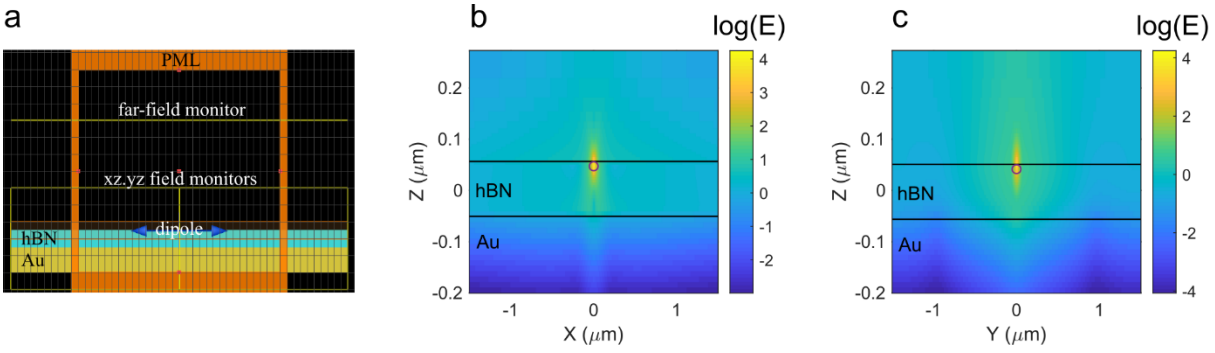

Figure S4.3. Details of lumerical simulation. (a) Simulation setup XZ view in Lumerical FDTD. (b), (c) XZ, YZ monitor for $\log(Re(E))$ profile, respectively.

S4.4 Comparison of monolayer and bilayer PL spectra

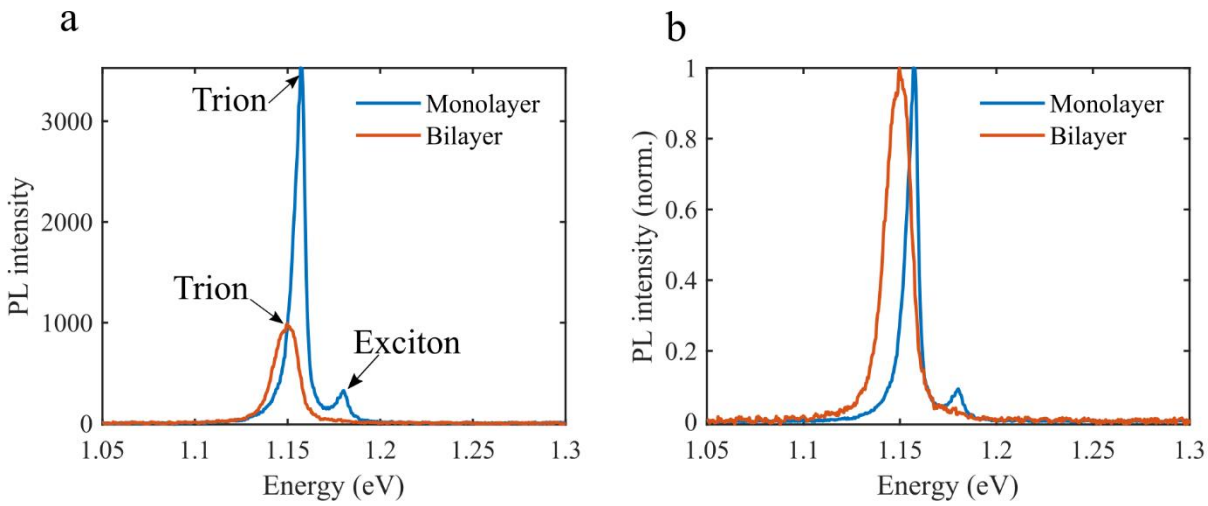

Figure S4.4. Comparison of monolayer and bilayer $MoTe_2$ emission. (a) PL spectrum from monolayer and bilayer regions of the same device. (b) Same as (a), but normalized.

The trion peak dominates for both the monolayer (1.157 eV) and bilayer (1.149 eV) spectrum under no applied bias. The exciton peak for the monolayer occurs at ~1.181 eV. The sample is lightly n-doped as confirmed by gate dependent measurements. The trion peak for the bilayer is 8 meV lower in energy than the monolayer and about 3.5 times less bright. Since the doping density is the same for the monolayer and the bilayer as they are part of the same flake, the intensities are linked to the quantum yield differences.

S4.5 Optical image of $MoTe_2$ monolayers

The following two monolayer (ML) region containing flakes were used in the device fabrication (both show ~7% contrast). A bilayer (BL) region is also seen in the first flake. Scale bar–2.5μm.

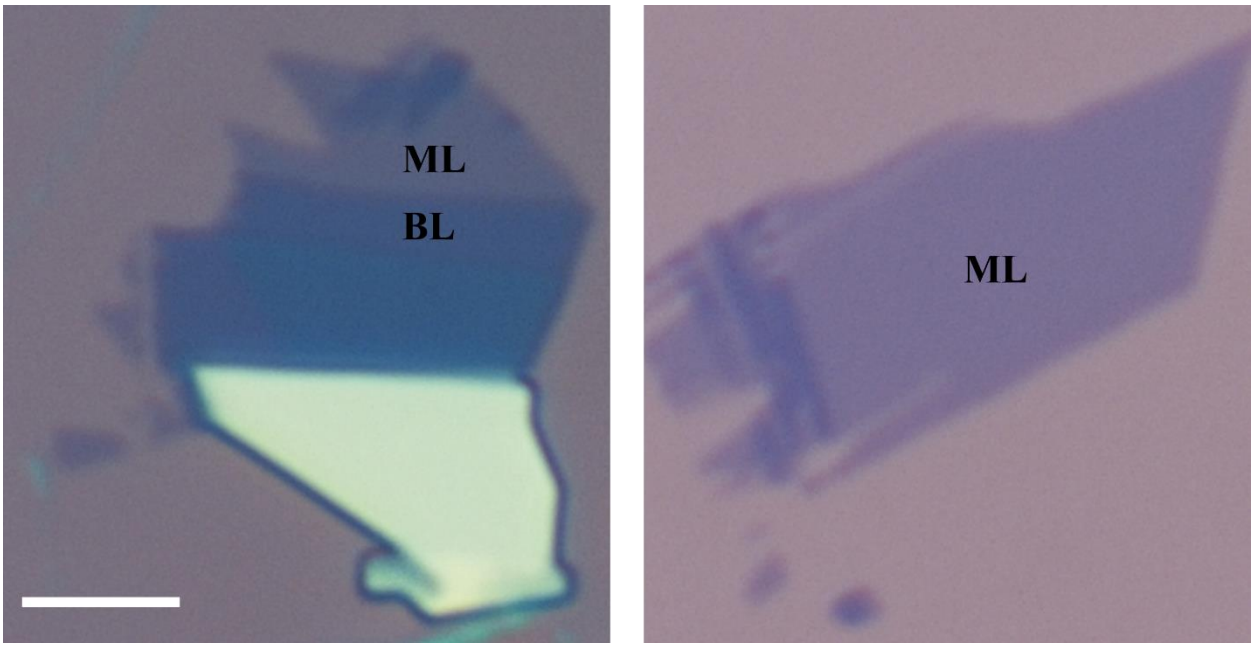

Figure S4.5. Optical microscope image of flakes used for the device fabrication.

S4.6 Charge density calculations

We assume a parallel-plate capacitor model where the two plates of the capacitor are the back reflector/electrode (gold) and the monolayer $MoTe_2$. This assumption is justified in the dc limit since the MoTe2 is semiconducting. This yields the following relation:

$\frac{C}{A} = \frac{\epsilon_0 \epsilon_{r,hBN}}{d_{hBN}}$, where $\epsilon_{r,hBN} = 3.9$ and $d_{hBN} = 97.3\, nm$.

$n = C(V - V_{CNP}) = \frac{\epsilon_0 \epsilon_{r,hBN}(V - V_{CNP})}{d_{hBN}}$, where $V_{CNP} = -0.65V$ (as estimated from PL measurements).

The relation between applied gate voltage and sheet charge density in $MoTe_2$ is depicted in Figure S4.6.

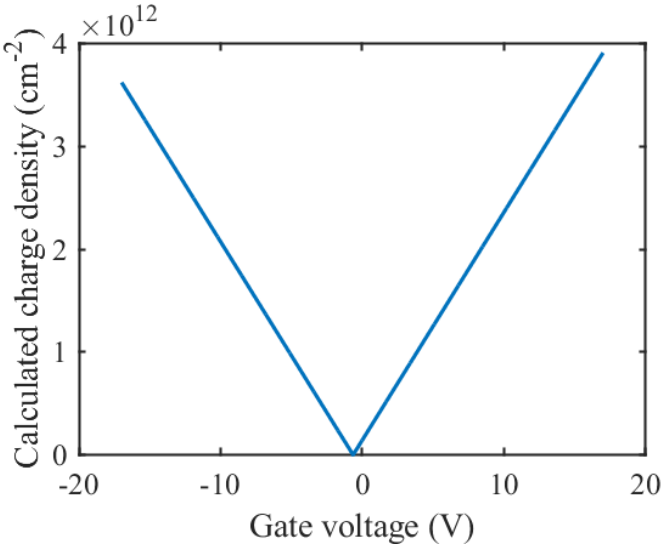

Figure S4.6. Applied gate voltage to sheet charge density conversion assuming parallel plate capacitor model in the dc limit.

S4.7 Power dependent emission spectrum

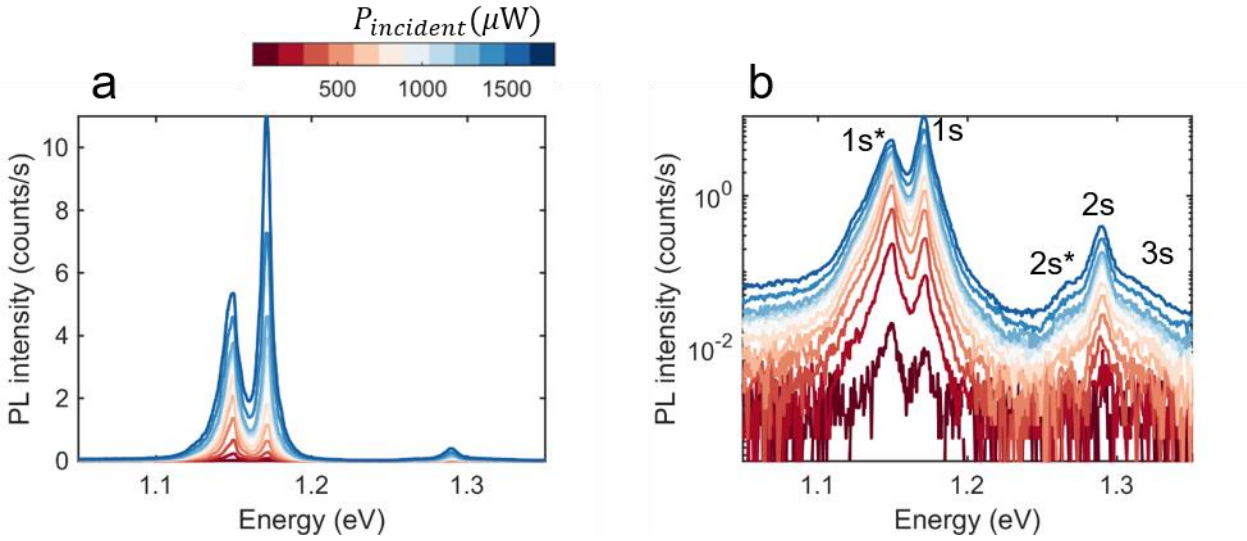

Figure S4.7. Power dependent photoluminescence spectrum over 3 decades of pump intensity. (a) is in linear and (b) is in log scale. The resonances are labelled in (b).

S4.8 Gate dependent PL fits

Fits to the PL spectrum data are shown in Figure S4.8 and S4.9 showing good match between the two.

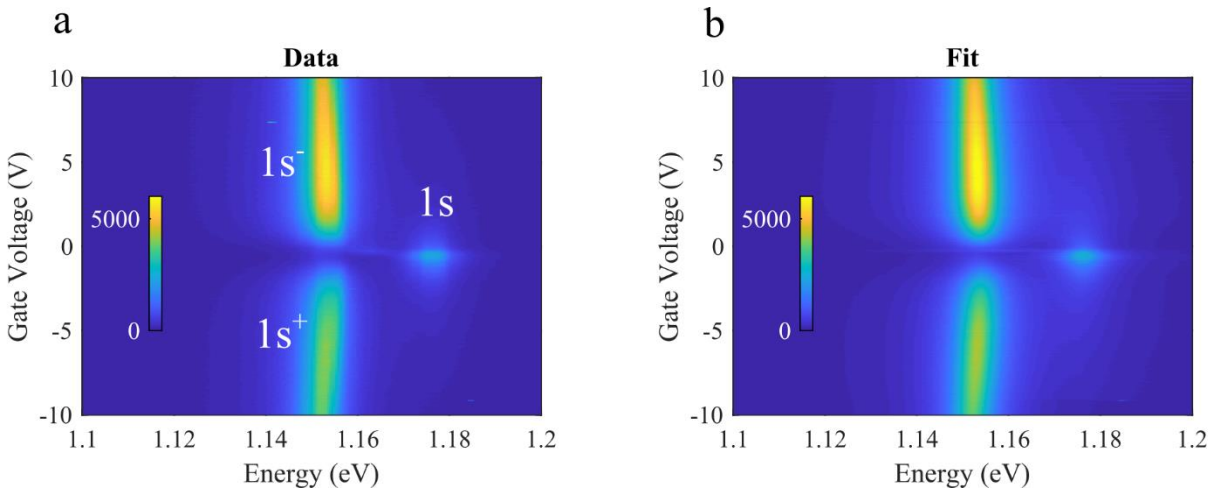

Figure S4.8. Fit to gate dependent experimental data around 1s region. (a) Experimental PL data around the A1s resonance region showing the neutral exciton and the charged trion resonances. (b) Multi-Lorentzian fit to the PL data shown in (a).

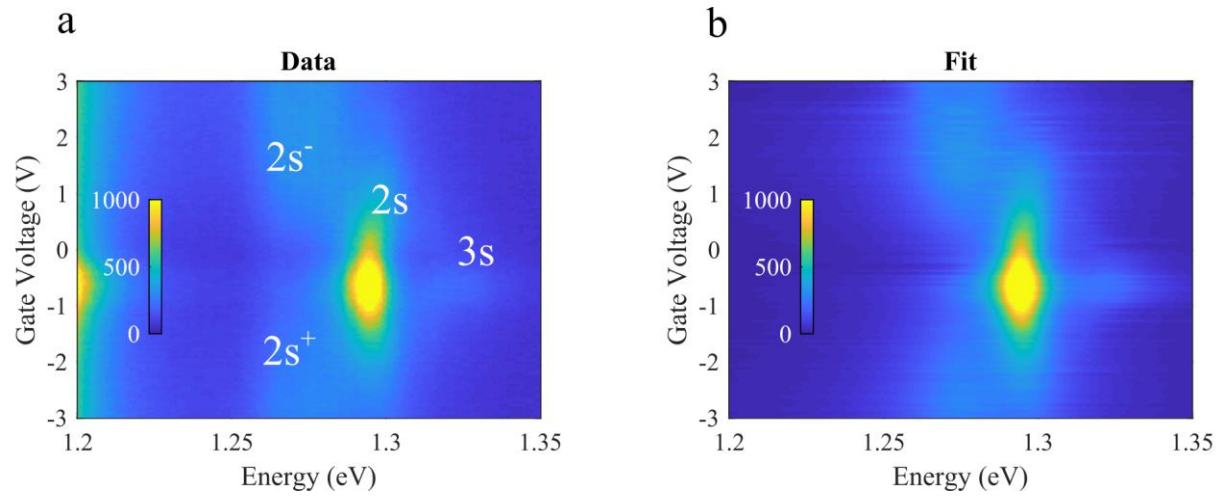

Figure S4.9. Fit to gate dependent experimental data around 2s region. (a) Experimental PL data around the A2s/3s resonance region showing the neutral exciton and the charged trion resonances. (b) Multi-Lorentzian fit to the PL data shown in (a).

S4.9 Gate dependence of additional spot

We have measured across 30 spots in the two devices presented and cycled the same spot through more than 10 sequences of gating between -17V and 17V and also repeated the measurement on a third device and all of them have yielded similar results. The only observable that varied across the spots and samples is the photoluminescence quantum yield which is well-known in the van der Waals community to be inhomogeneous across samples due to imperfections in fabrication techniques resulting in strain and bubble formation in-between layers in heterostructures. Results from another spot are summarized in Figure S4.10.

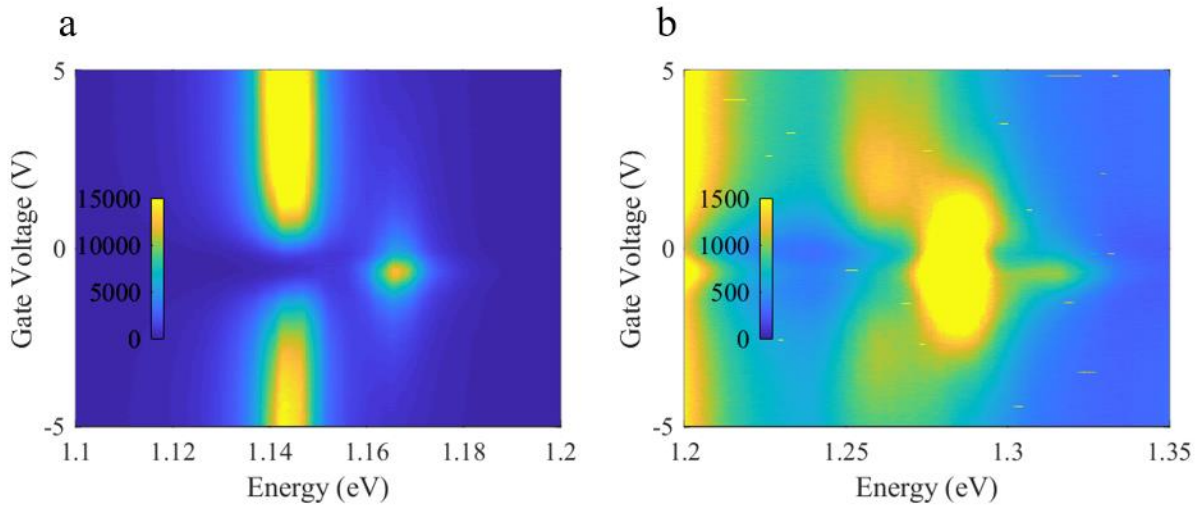

Figure S4.10. Gate-dependent data from additional spot. (a) Experimental PL data around the A1s resonance region showing the neutral exciton and the charged trion resonances. (b) Same as (a) but for 2s/3s resonances.

S4.10 Absolute intensity of exciton and trion emission modulation

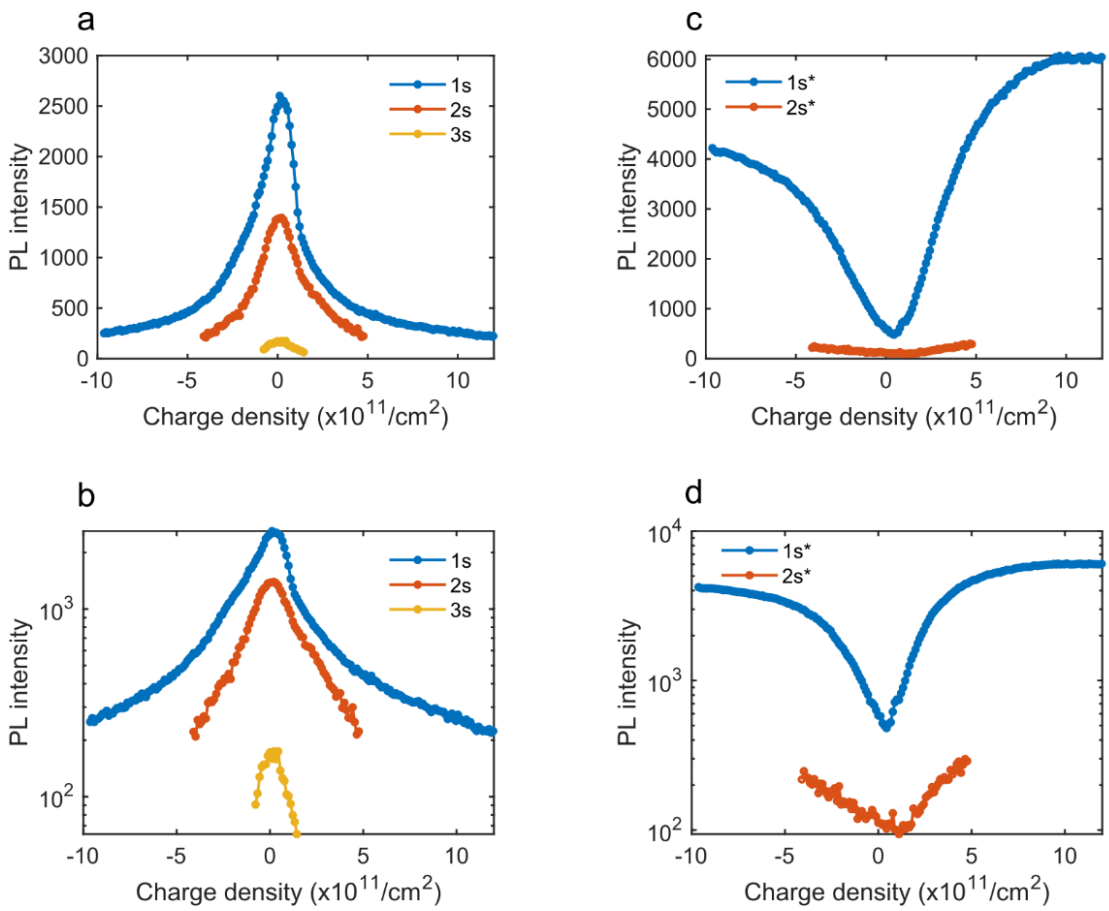

Figure S4.11. Gate dependent emission fit parameters (intensity). (a) Absolute photoluminescence intensity of Rydberg excitons as a function of charge density in linear scale. (b) Same as (a) in semi-log scale. (c) Absolute photoluminescence intensity of trions associated with Rydberg excitons as a function of charge density in linear scale. (d) Same as (c) in semi-log scale.

S4.11 Energy shift of exciton and trion emission

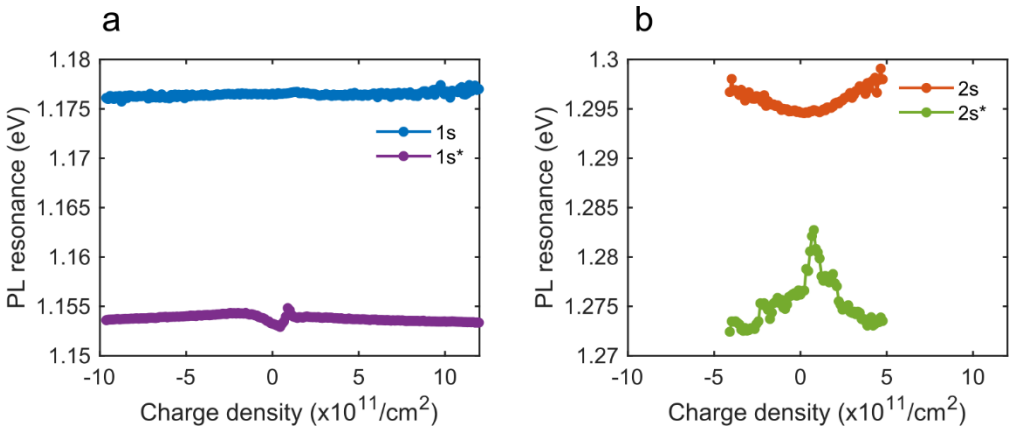

Figure S4.12. Gate dependent emission fit parameters (energy). (a) Energy shifts of the A1s exciton and trion as a function of doping density. (b) Energy shifts of the A2s exciton and trion as a function of doping density.

S4.12 Comparison of $MoTe_2$ with MoS_2, $MoSe_2$, WS_2, and WSe_2

Table S4.T1. Binding energy (meV) of Rydberg excitons of all TMDCs.

Material	A1s	A1s+	A1s-	A2s	A2s+	A2s-	A3s	A3s+	A3s-
MoS_2	440(±80)[289], 261[18], 221[290], 222[291]	-	27[18], 18(±1.5)[73]	91[18], 48[291]	-	-	53[18], 20[291]	-	-
$MoSe_2$	231[290], 208[292]	24.3(±0.1)[293], 23.7(±0.1)[293], 27[292]	26.1(±0.1)[293], 23.1(±0.2)[293]	56[292]	22.7(±0.4)[293], 22.6(±1.0)[293], 27[292]	24.6(±0.2)[293], 16.4(±0.7)[293]		13.1(±0.3)[293]	13(±0.5)[293]
WS_2	320(±50)[289], 180[290]	-	-	-	-	-	-	-	-
WSe_2	172[294], 167[290], 170[242], 169[284], 370[13]	20.5(±0.1)[293], 17.5(0.1)[293]	29(±0.1)[293], 27.1(±0.1)[293]	41[294], 39[242], 40[284]	18.4(±0.3)[293], 9.2(±0.7)[293], 14.1[295]	17.8(±0.4)[293], 18.6[295]	20[294], 13[242], 17[284]	-	-
$MoTe_2$	177[290], 156[296], 580(±80)[297], 404(±19), *490*	24[298], 24[297], 22.14(±0.2)	24[298], 27[297], 21.94(±0.1)	288(±18), *270*	13.67(±0.12)	18.14(±0.09)	*150*	-	-

Not cited numbers are from this work combing experiments and theory, *theory only ($MoTe_2$).*

Table S4.T2. Gate dependence of energy shift of charged Rydberg excitons of all TMDCs.

Material	A1s+	A1s-	A2s+	A2s-	A3s+	A3s-
MoS_2	-	-	-	-	-	-
$MoSe_2$	-0.75 ± 0.05[293], -1.91 ± 0.06[293], 0.9[292], 0.4[299]	1.10 ± 0.07[293], 2.9 ± 0.1[293], 1.2[299]	-7.9 ± 0.6[293], -2.9 ± 1.6[293], 3.9[292], 1.8[299]	11.1 ± 0.6[293], 7.0 ± 1.0[293], 4[299]	-23.8 ± 1.6[293]	13.7 ± 2.3[293]
WS_2	-	-	-	-	-	-
WSe_2[293]	-0.18 ± 0.02, -1.74 ± 0.03	1.2 ± 0.1, 2.3 ± 0.1	-5.5 ± 0.4, -1.8 ± 0.1	4.7 ± 0.3	-	-
$MoTe_2$	-0.40±0.10	0.28±0.05	-8.59±0.54	4.23±0.51	-	-

Noted quantity is $\frac{d\Delta E}{dE_F}$, where $E_F = \frac{n\pi\hbar^2}{m^*}$ (n is the sheet charge density and m^* is the effective mass).

This work ($m_e^* = 0.647m_0, m_h^* = 0.805m_0$). Effective mass obtained from GW+BSE calculations ($MoTe_2$).

S4.13 Computational details

We first perform density functional theory (DFT) calculations with the Perdew-Burke-Ernzerhof (PBE) generalized gradient approximation[300] with the Quantum Espresso package[301,302], which uses a plane-wave basis set, and norm-conserving pseudopotentials[303,304]. We use a cut-off energy of 125 Ry and include a vacuum of along the out of plane direction, to avoid spurious interactions with repeated unit cells. Both in-plane lattice parameters and atomic coordinates are optimized within the unit cell. A uniform 24x24x1 k-grid is used in the self consistent density calculation, whereas the wave function is generated on a 12x12x1 k-grid. Spin orbit coupling (SOC) is considered. The GW calculations[305–307] are performed with the Berkeley GW code[308,309] using a generalized plasmon pole (GPP) model[307] for the undoped system. Calculations are done with a dielectric cut-off energy of 35 Ry, on a 12x12x1 q-grid with the nonuniform neck subsampling

(NNS) scheme[310], with 6,000 states in the summation over unoccupied states, and using a truncated Coulomb interaction[311]. The BSE matrix elements are computed on a uniform 24x24x1 coarse k-grid, then interpolated onto a 288x288x1 fine k-grid, with two valence and four conduction bands. For the doped systems, we use a newly developed plasmon pole model accounting for both dynamical screening effects and local fields effects associated with the free carriers, which is used at both the GW and BSE levels. Further details can be found in Ref. [Champagne et al., submitted]. The doping is introduced as a shift of the Fermi energy above the bottom of the conduction band, corresponding to doping densities ranging from 0 up to $8.7\text{x}10^{12} cm^{-2}$. The dielectric matrix, kernel matrix, and BSE Hamiltonian are built for a 48x48x1 k-grid. SOC is not considered in the calculations for the doped systems. The computed intrinsic radiative linewidth is obtained from a Fermi's golden rule following Ref.[226,228].

S4.14 Computation of exciton dispersion

We construct BSE Hamiltonian for a series of center-of-mass wavevectors Q in a dense 90 × 90 k-grid. Solving for the lowest energy exciton at each Q yields the exciton dispersion with the effective mass $M_X = 0.87\ m_0$, where m_0 is the electron mass.

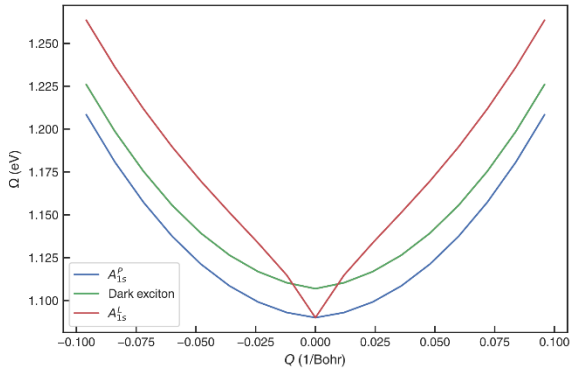

Figure S4.13. Exciton dispersion for a few lowest energy excitonic states in monolayer $MoTe_2$.

S4.15 Computed exciton absorption spectrum as a function of doping density

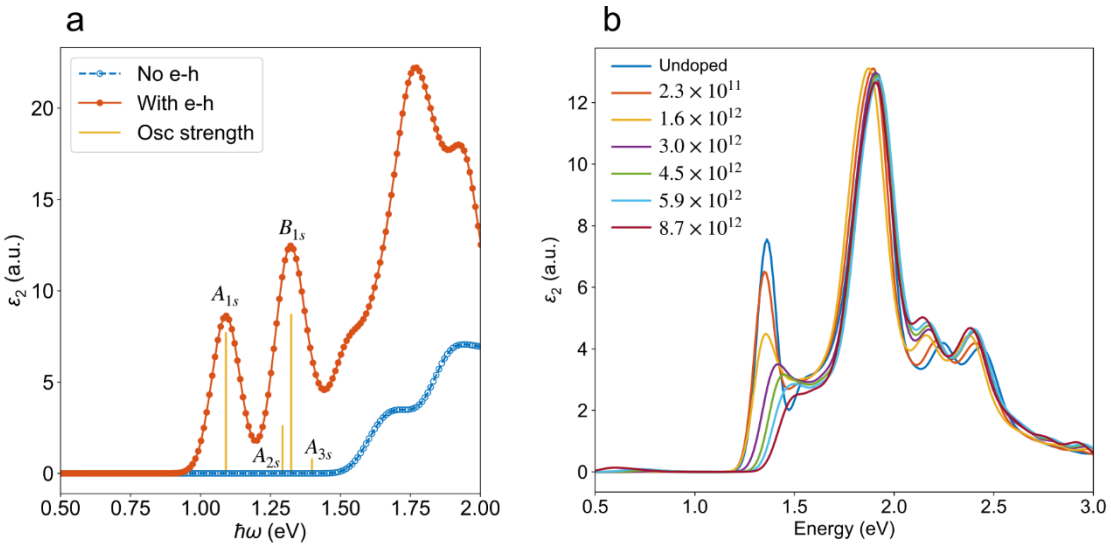

Figure S4.14. Computation of doping-dependent loss function. (a) Computed imaginary part of the dielectric function ($\epsilon_2(\hbar\omega)$) for monolayer $MoTe_2$ with and without electron-hole interactions and projected oscillator strength of the different Rydberg excitons (A1s, A2s, B1s, A3s from left to right). (b) Evolution of the imaginary part of the dielectric function as a function of doping density.

S4.16 Computation of trion binding energy

To obtain charged excitations, we obtain excited-state properties associated with N+3-particle excitations, which consist of one neutral electron-hole pair plus an additional carrier (which we restrict here to be an extra electron). We note that such a description for a trion is applicable for a vanishingly small Fermi surface; for larger carrier doping, one needs to explicitly include the hybridization with of the neutral electron-hole pair with intraband plasmons in the degenerate Fermi see.

We solve for trion excitations by writing a Dyson's equation associated with correlated 3-particle excitations, $L = LKL_0$ where L_0 is non-interacting Green's function, L is the interacting Green's function, and K is the interaction kernel. We obtain an equation of motion equivalent to that derived in a prior work[312], and which we will detail in a subsequent manuscript.

We expand our trion wave function in the electron and hole basis in the same way we constructed the exciton wave function

$$|T(n,q)\rangle = \sum_{\substack{vc_1c_2 \\ k_1k_2}} B^{n,q}_{\substack{vc_1c_2 \\ k_1k_2}} \hat{c}_{vk_1+k_2-q} \hat{c}^{\dagger}_{c_2k_2} \hat{c}^{\dagger}_{c_1k_1} |0\rangle$$

where T is a trion wavefunction with principal quantum number n and wavevector q, B are expansion coefficients, v and c label valence and conduction bands, respectively, k is a wavevector, cˆ is a fermionic destruction operator, and $|0\rangle$ is the many-body ground state. and we arrive at the Dyson's-like equation

$$\left(E_{c_1k_1} + E_{c_2k_2} - E_{vk_1+k_2-q}\right) B^{n,q}_{\substack{vc_1c_2 \\ k_1k_2}} - \sum_{n'} \langle T(n',q)|\hat{K}|T(n,q)\rangle = \Omega^{T}_{n,q} B^{n,q}_{\substack{vc_1c_2 \\ k_1k_2}}$$

where $\Omega^{T}_{n,q}$ is the energy of trion at state n and momentum q and E_{mk} is the quasiparticle energy for an electron in band m and wavevector k. From here, we found the trion binding energy $\Delta E = \Omega^{\min}_{exciton} - \Omega^{\min}_{trion}$ of 20.6 meV for the A_{1s} state. Our optical spectrum associated with the absorption of excitons and trions is shown in Fig. S4.15.

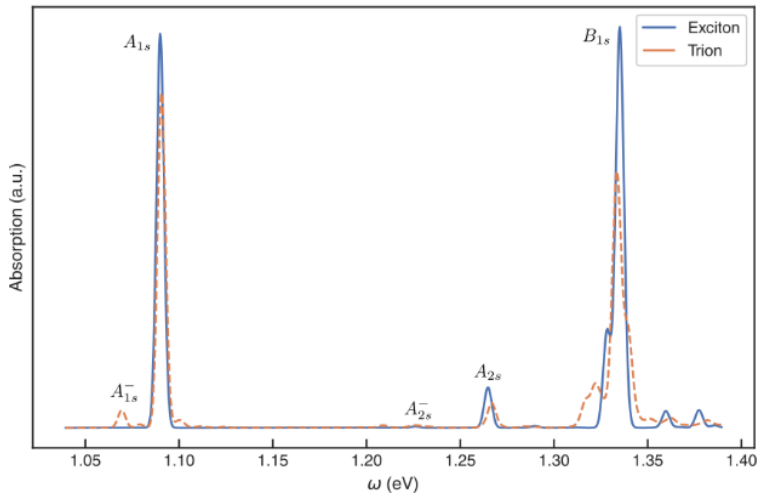

Figure S4.15. Computed imaginary part of the dielectric function for excitons and trions.

S4.17 Discussion on importance of $MoTe_2$ optical properties and its Rydberg series

Well studied TMDCs like Mo and W based sulfides and selenides have band-gaps and optical transitions in the visible spectrum (~600-760 nm). Rydberg excitons associated with these materials are thus at even higher energies. From a technology point of view wavelengths near the silicon band edge (~1.1 eV or ~1100 nm) and telecom band (~1550nm) are very important for the development of silicon-based opto-electronics. With the advent of hybrid platforms where new materials are being integrated into silicon photonics, it is important to find and expand the library of materials which have strong photo-response in these wavelengths. $MoTe_2$ is one of the few 2D materials which in its semiconducting 2H polytype exhibits a ground state excitonic optical transition in the silicon band-edge window. It has thus attracted integration into waveguide-based photonic and opto-electronic applications; for example–light emitting diode[313], waveguide-integrated high-speed[314] and strain-engineered[64] photodetector. It is evident that $MoTe_2$ has attracted significant interest, yet these studies are done for bilayer and bulk samples limiting the achievable performance because the excitonic photo-response should be maximal for a monolayer[214]. A careful and detailed understanding of the photo physics of monolayer $MoTe_2$ at low temperatures under electrostatic doping conditions is lacking which is the primary motivation of selecting this material.

Rydberg excitons in $MoTe_2$ are in a unique part of the electromagnetic spectrum (~800-1000 nm) which is exciting for a lot of applications in the near infrared such as quantum optics with rare-earth ions[315], opto-electronics for health sensing[316] and laser technology[317], including high-power applications[318]. Furthermore, Rydberg excitons provide a way to conveniently study long-range dipole-dipole interactions because of their large size. As the quantum number increases for the Rydberg exciton their average radius $\langle r_n \rangle$ increases (for a hydrogenic system) as per the formula– $\langle r_n \rangle = \frac{1}{2} a_B \left(3n^2 - l(l+1)\right)$, where a_B is the Bohr radius, n is the principal quantum number and l is the angular momentum. Such an increasing size leads to huge interaction effects and can provide insights into atomic and molecular physics at the single-particle/quantum level. They can also provide excellent sensing capabilities since their wavefunction is exceptionally large and are extra sensitive to the environment[186,201,202], as well as to their self. Furthermore, Rydberg excitons can be engineered to form an ordered array using Rydberg blockade which is very appealing for

quantum simulations. They can also play a vital role in non-linear optics when incorporated into optical cavities to form exciton-polariton modes (due to their large exciton wavefunction and strong dipole-dipole repulsion as compared to 1s excitons)[204,205].

S4.18 Atomic force microscope image of $MoTe_2$ device

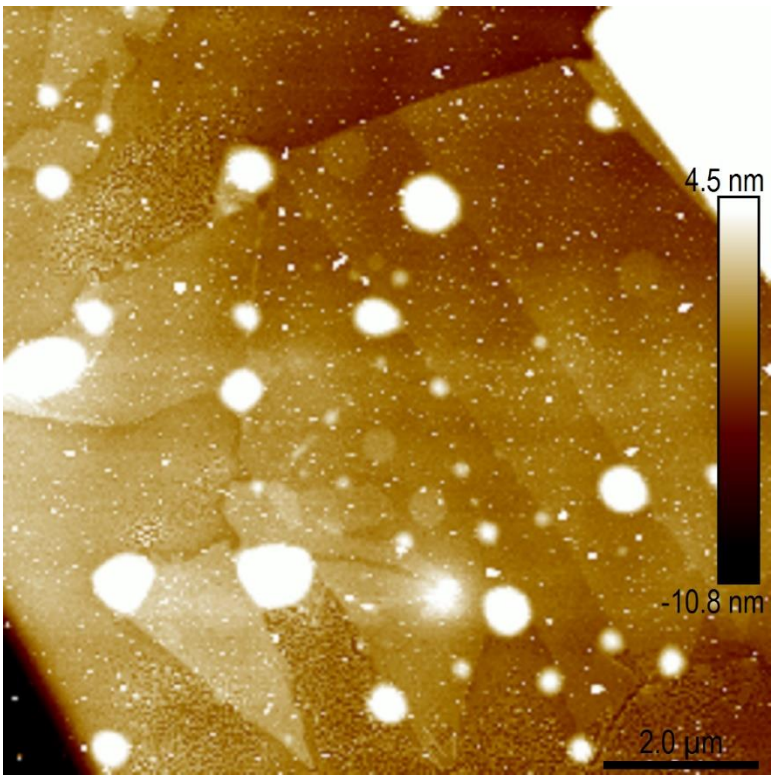

Figure S4.16. Atomic force microscope image (height sensor) of $MoTe_2$ device.

Chapter S5. Supplementary Information for Signatures of Edge-Confined Excitons in Monolayer Black Phosphorus

S5.1 Fabrication details

SiO_2 (285 nm)/Si chips were cleaned with ultrasonication in acetone and isopropanol for 30 min. each, followed by oxygen plasma treatment at 70 W, 300 mTorr for 5 min. Monolayer black phosphorus (BP) was exfoliated to polydimethylsiloxane (PDMS) stamps. Few layer hexagonal boron nitride (hBN) and graphene flakes were directly exfoliated using Scotch-tape at 100 ºC to increase the size of flakes. Monolayer thickness was initially identified using optical contrast (~7 % contrast per layer) and later verified with photoluminescence spectroscopy. hBN thickness was confirmed with atomic force microscopy. Flakes were assembled with a polycarbonate/polydimethylsiloxane (PC/PDMS) stamp with pick-up at temperatures between 80 ºC to 110 ºC. The entire heterostructure stack was dropped on prefabricated gates at 180 ºC. The polymer was washed off in chloroform overnight, followed by isopropanol for 10 min. Gates were fabricated on SiO_2 (285 nm)/Si chips with electron beam lithography (PMMA 950 A4 spun at 3500 rpm for 1 min. and baked at 180 ºC, 10 nA beam current and dosage of 1350 $\mu C/cm^2$ at 100 kV), developing in methyl isobutyl ketone: isopropanol (1:3) for 1 min., followed by isopropanol for 30 s and electron beam evaporating 5 nm Ti/95 nm Au at 0.5 $\frac{Å}{s}$ deposition rate. Liftoff was done in warm acetone (60º C) for 10 min., followed by rinse in isopropanol for 5 min. The gates were precleaned before drop-down of heterostructure by annealing in high vacuum ($2x10^{-7}$ Torr) at 300 ºC for 6 h. The chip was then wire-bonded with Aluminum wires on to a custom home-made printed circuit board.

For TEM sample fabrication first the TEM holey grid purchased from NORCADA (NH005D03 with 0.05 mm x 0.05 mm, 200 nm thick membrane, 300 nm diameter holes, 600 nm pitch, 25 x 25 array) was loaded into electron-beam evaporation chamber to deposit ~0.5 nm Ti and ~1.5 nm Au at 0.1 $\frac{Å}{s}$ deposition rate. Right after the deposition, exfoliated flakes of monolayer graphene and BP on PDMS were transferred using the dry-transfer technique at 50 ºC.

S5.2 Experimental methods

Low temperature confocal photoluminescence measurements were performed in an attoDRY800 closed-cycle cryostat at base pressures of $<2x10^{-5}$ mbar. Sample was mounted on a thermally conducting stage with Apiezon glue and stage was cooled using a closed-cycle circulating liquid helium loop. Temperature was varied between ~4K and 300K. A 532 nm (Cobolt) continuous wave laser was used as the excitation source with power ranging between 10 nW and 1 mW, focused to a diffraction limited spot. Emission was collected in a confocal fashion with a cryogenic compatible apochromatic objective with an NA of 0.82 (for the visible and NIR range, LT APO VISIR) and dispersed onto a grating-based spectrometer (with 150 grooves per mm with a Silicon CCD)–Princeton Instruments HRS 300. Polarization dependent data was acquired using a combination of linear polarizer and half wave plate on the excitation/emission channel. Voltage was applied using a Keithley 2400. Data was acquired with home-written MATLAB codes.

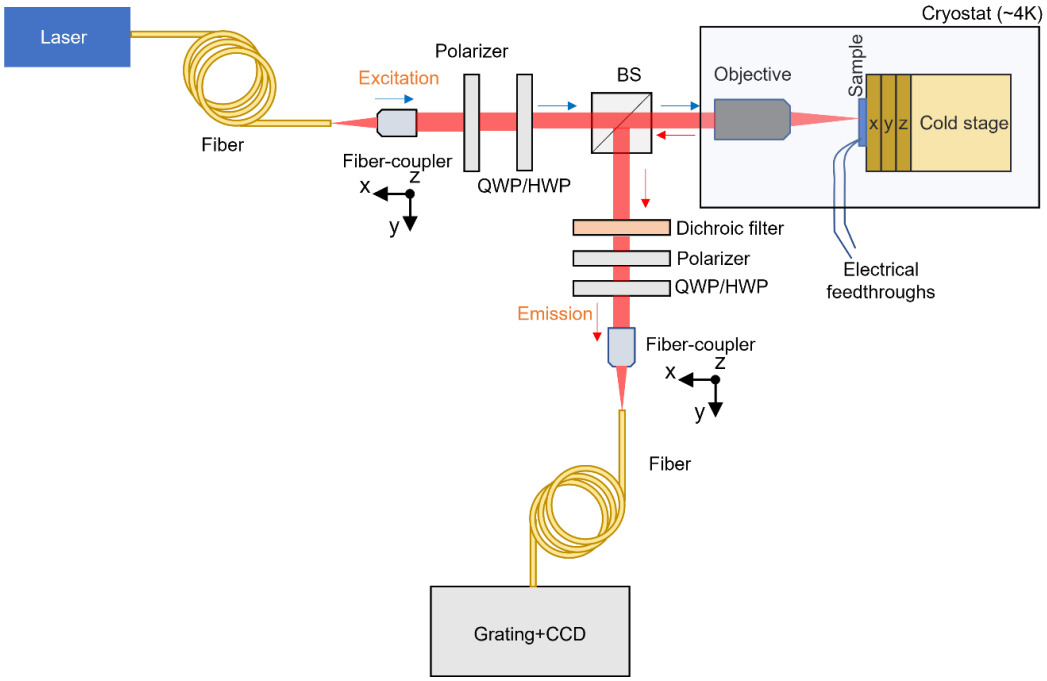

Figure S5.1. Schematic of the low-temperature confocal optical PL setup used. BS–Beam Splitter, QWP/HWP–Quarter/Half Wave Plate.

Atomic Force Microscopy was performed using Bruker Dimension Icon in tapping mode. Data analysis was performed in MATLAB.

S5.3 Image of samples studied

Multiple devices/samples were measured as part of this study. Optical microscope images of devices studied via photoluminescence are shown below.

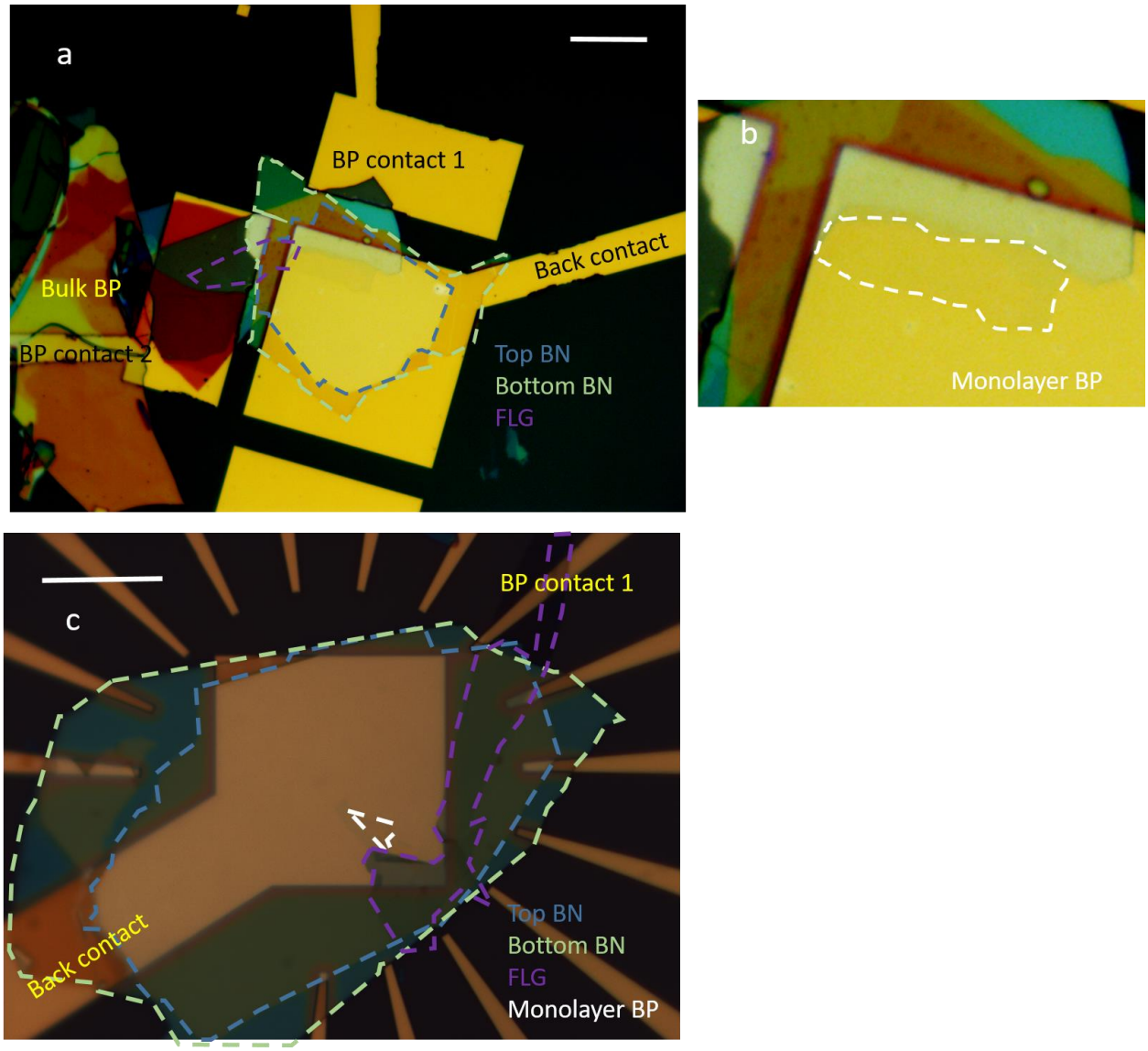

Figure S5.2. Optical microscope images of two gated heterostructures (sample (a), (b) #gateD4 and (c) #gateD1). hBN encapsulated monolayer BP is contacted with few layer graphene to gold electrodes and a back contact of optically thick gold is used as the counter electrode. Scale bar in (a) is 20 µm and (c) is 10 µm.

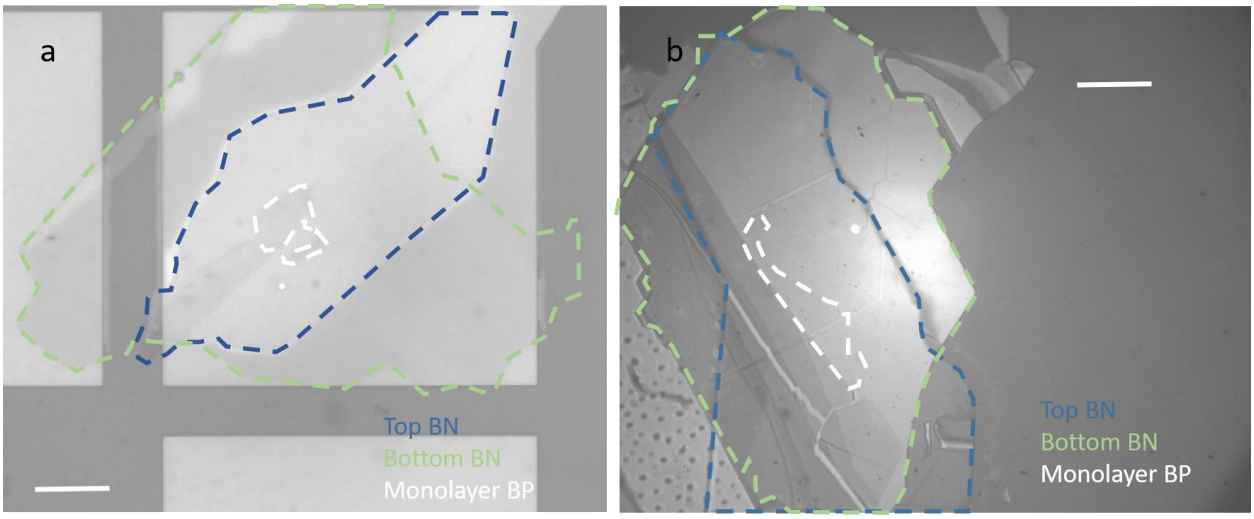

Figure S5.3. Optical microscope images of two encapsulated heterostructures (sample (a) #D6 and (b) #D2), containing top and bottom hBN and monolayer BP. Scale bars are 5 μm.

Optical microscope images of devices studied via transmission electron microscopy are shown below.

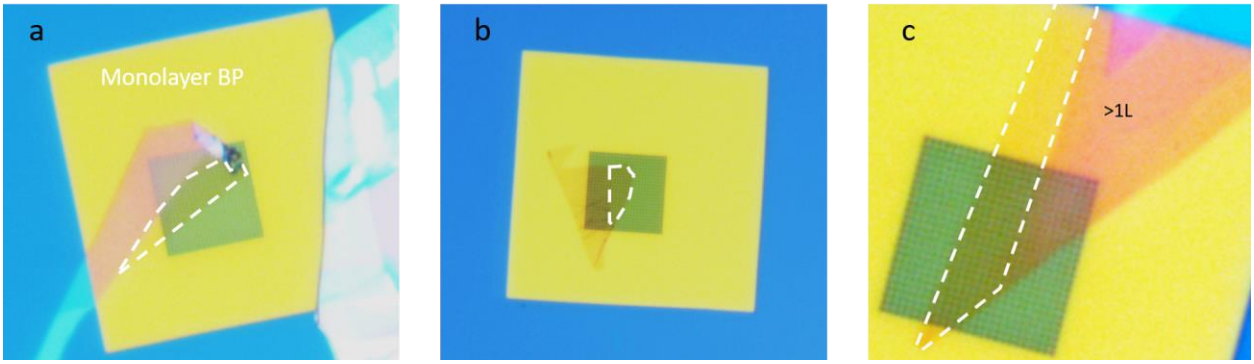

Figure S5.4. Optical microscope images of three bare monolayer samples on TEM grids (sample (a) #S1, (b) #S2 and (c) #S3). The TEM hole arrays are 15 μm x 15 μm.

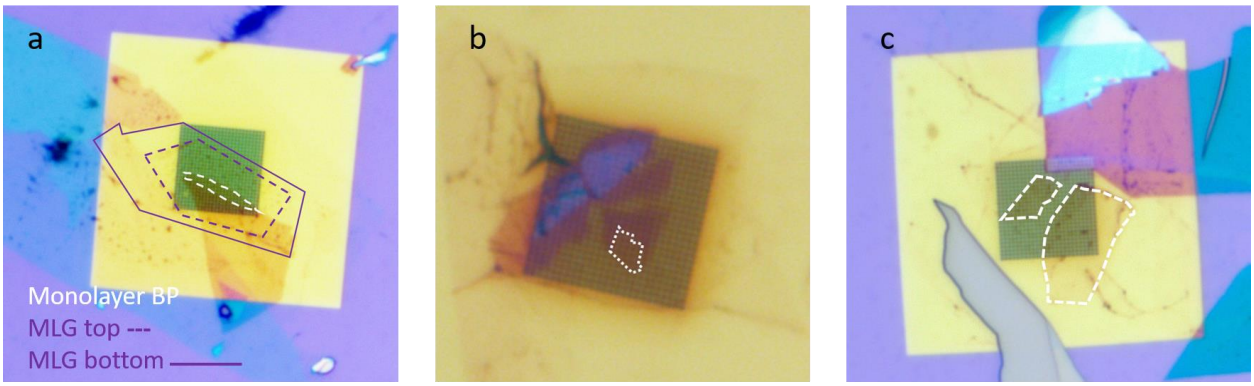

Figure S5.5. Optical microscope images of three fully encapsulated (with monolayer graphene) monolayer BP samples on TEM grids (sample (a) #H1, (b) #H2 and (c) #H3). The TEM hole arrays are 15 µm x 15 µm.

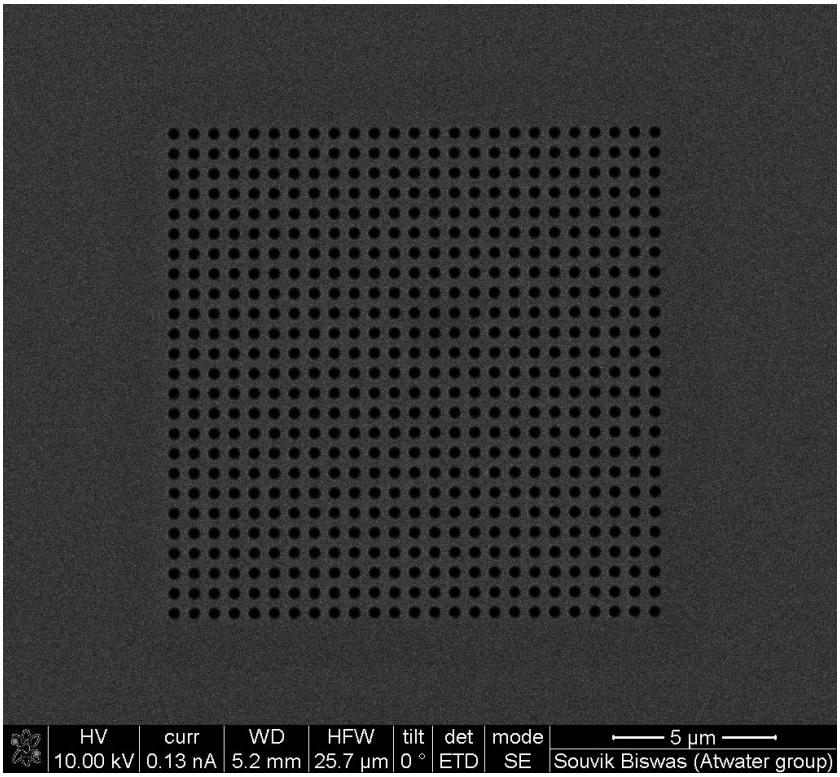

Figure S5.6. Scanning electron microscope image of a typical TEM holey grid used in measurements. To prevent charging during imaging ~0.5 nm Ti and ~1.5 nm Au were deposited right before transfer of 2D flakes.

S5.4 Visualization of strain and charge inhomogeneity in samples

We find spatial variations in the peak emission energy across different samples which indicate that there is some degree of inhomogeneous strain and charge distribution inducing during stacking of heterostructures.

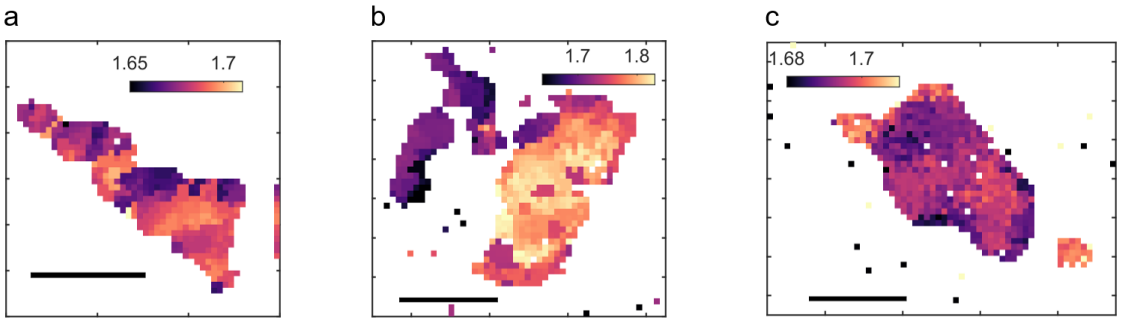

Figure S5.7. Spatial maps of energy of photoluminescence of the brightest feature (which approximately follows the exciton energy) for sample. (a) #gate D1, (b) #D6 and (c) #D2, respectively. We find ~50 meV, ~100 meV and ~20 meV variation in the PL peak energy for (a), (b) and (c), respectively.

S5.5 Polarization analysis

To acquire polarization dependent data, the emission polarizer (analyzer) was rotated in steps of 1 or 2° and photoluminescence spectra was collected at each angle. Angle-dependent false color plots are shown for some spatial spots for different devices. After fitting the PL spectrum at each emission angle to a sum of Lorentzian peaks, the PL intensity variation as a function of emission angle has been fit to the following equation–$I = I_0 \cos^2(\theta - \theta_0) + c$, where θ_0 is the azimuthal orientation of the emission and I_0, c are constants which denote the peak intensity and background intensity of emission. Following such analysis over multiple spots in different samples, a statistical set of data has been generated which shows that the emission from edge states is aligned with the local armchair axes (interior excitons), as expected from theory. Small deviations are likely due to strain-induced effects whereas a few points that show much larger deviation are likely due to reconstructions that break mirror-symmetry. Such structures have not been investigated in great details in this work and merit future studies.

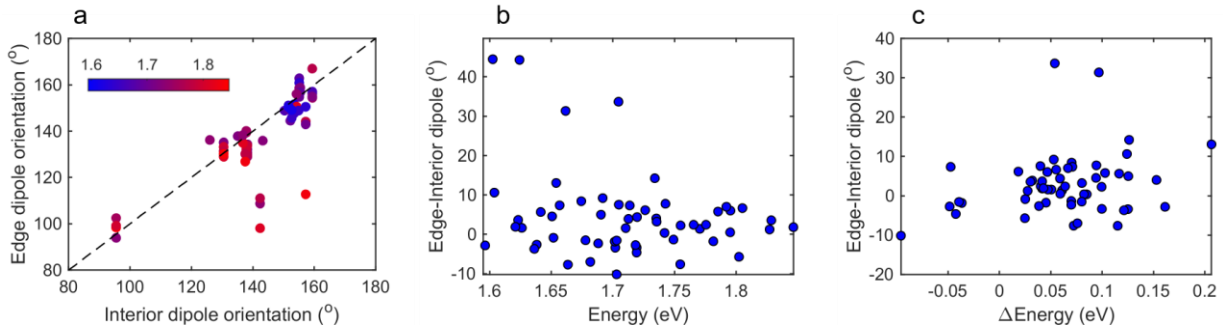

Figure S5.8. Polarization analysis-I. (a) Azimuthal orientation of edge dipole emission pattern versus interior dipole emission pattern (extracted from fitting the "interior"-like emission envelope). Color indicates peak energy of emission as noted in color bar (in eV). (b) Difference in the azimuthal dipole emission angle between the edge and the interior as a function of emission energy of the edge emission. (c) Same as (b), but plotted (on x-axis) as a function of difference in energy between the interior and edge ($\Delta E = E_{interior} - E_{edge}$).

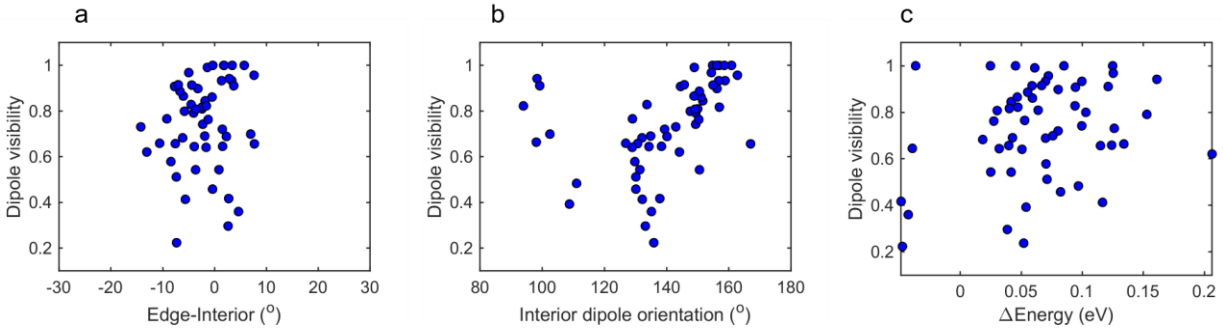

Figure S5.9. Polarization analysis-II. (a) Dipole visibility ($\frac{I_{max}-I_{min}}{I_{max}+I_{min}}$) of edge exciton emission versus difference of edge and interior dipole emission angle. (b) Dipole visibility of edge exciton emission versus interior exciton dipole orientation. (c) Same as (b), but plotted (on x-axis) as a function of difference in energy between the interior and edge ($\Delta E = E_{interior} - E_{edge}$).

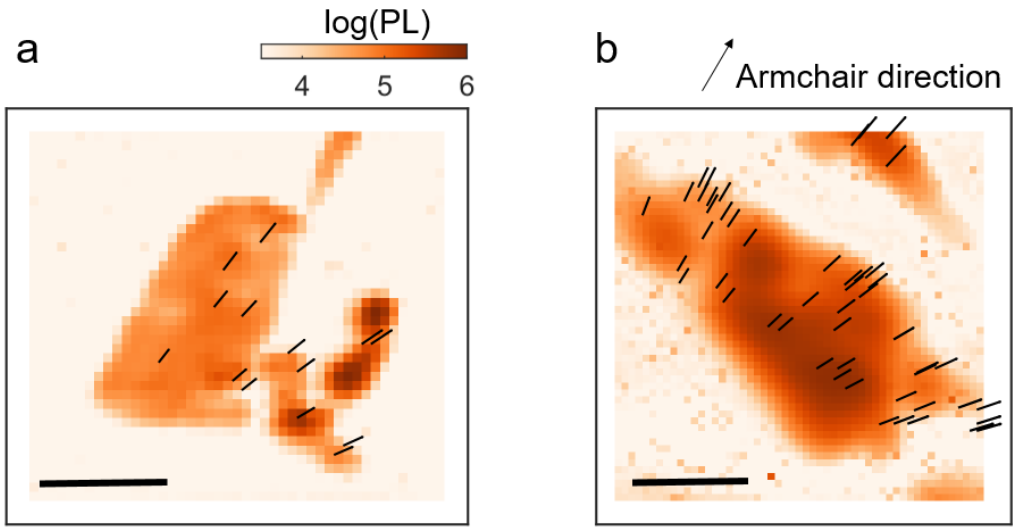

Figure S5.10. Measured armchair direction at some spatial points (direction of the arrows) superimposed on log(PL) spatial maps for sample (a)#D6 and (b)#D2, respectively. For both samples terminations along armchair and zigzag are both seen (for #D6, the longer tear is along armchair, whereas for #D2, it is along zigzag).

We estimate the macroscopic orientation of BP flakes investigated in this work by superimposing a false colormap of the emission signal with arrows pointing along the armchair direction (obtained by performing a full polarization analysis at that spot, as described previously). As can be seen, fractures along both armchair and zigzag edges are seen.

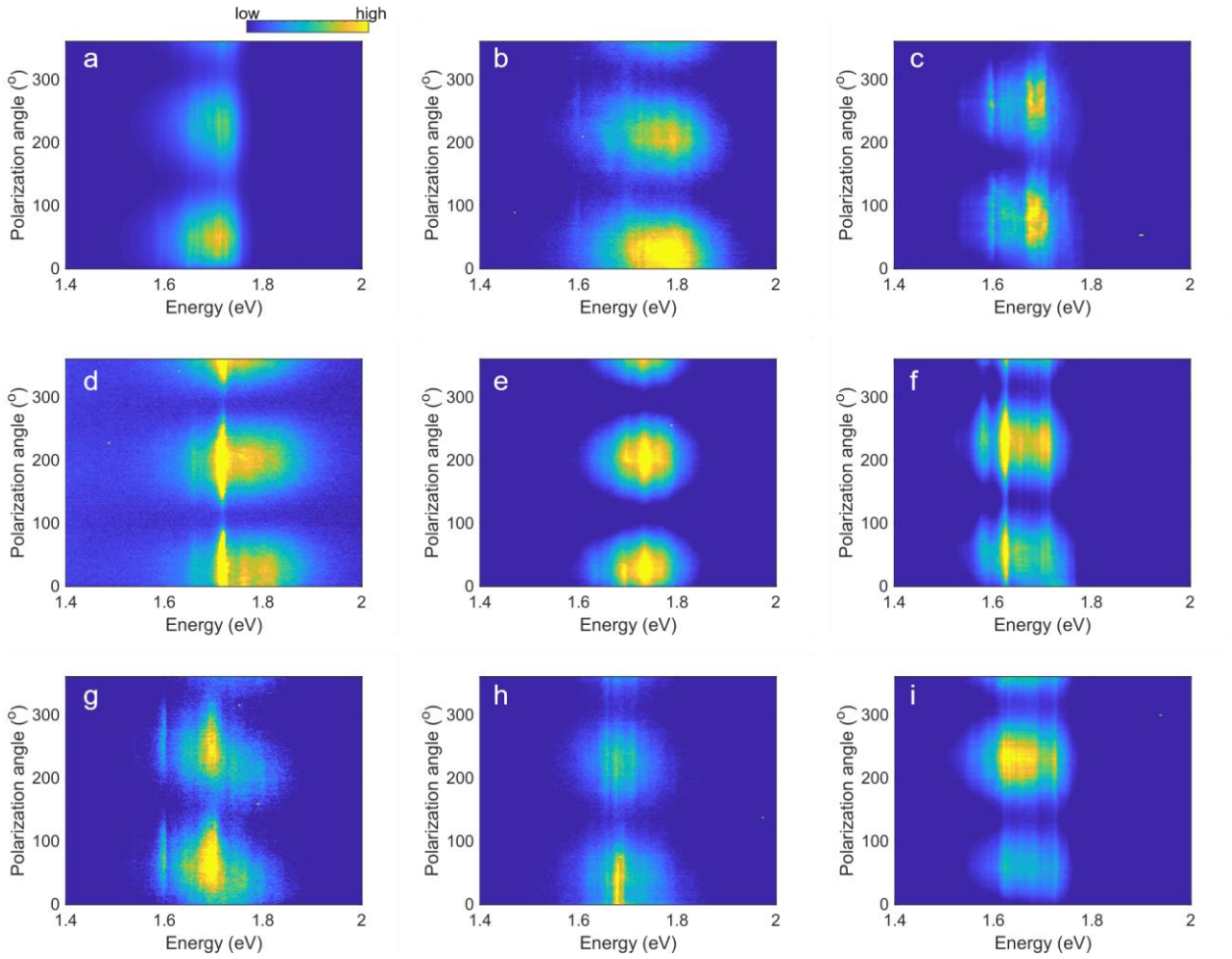

Figure S5.11. Extended polarization dataset 1. (a)-(i) False colormaps of emission spectrum as a function of collection (analyzer) polarizer angle for different spots from device D6. It can be clearly seen that for all spots (collected near physical edges of sample) signatures of both interior and edge emission is observed.

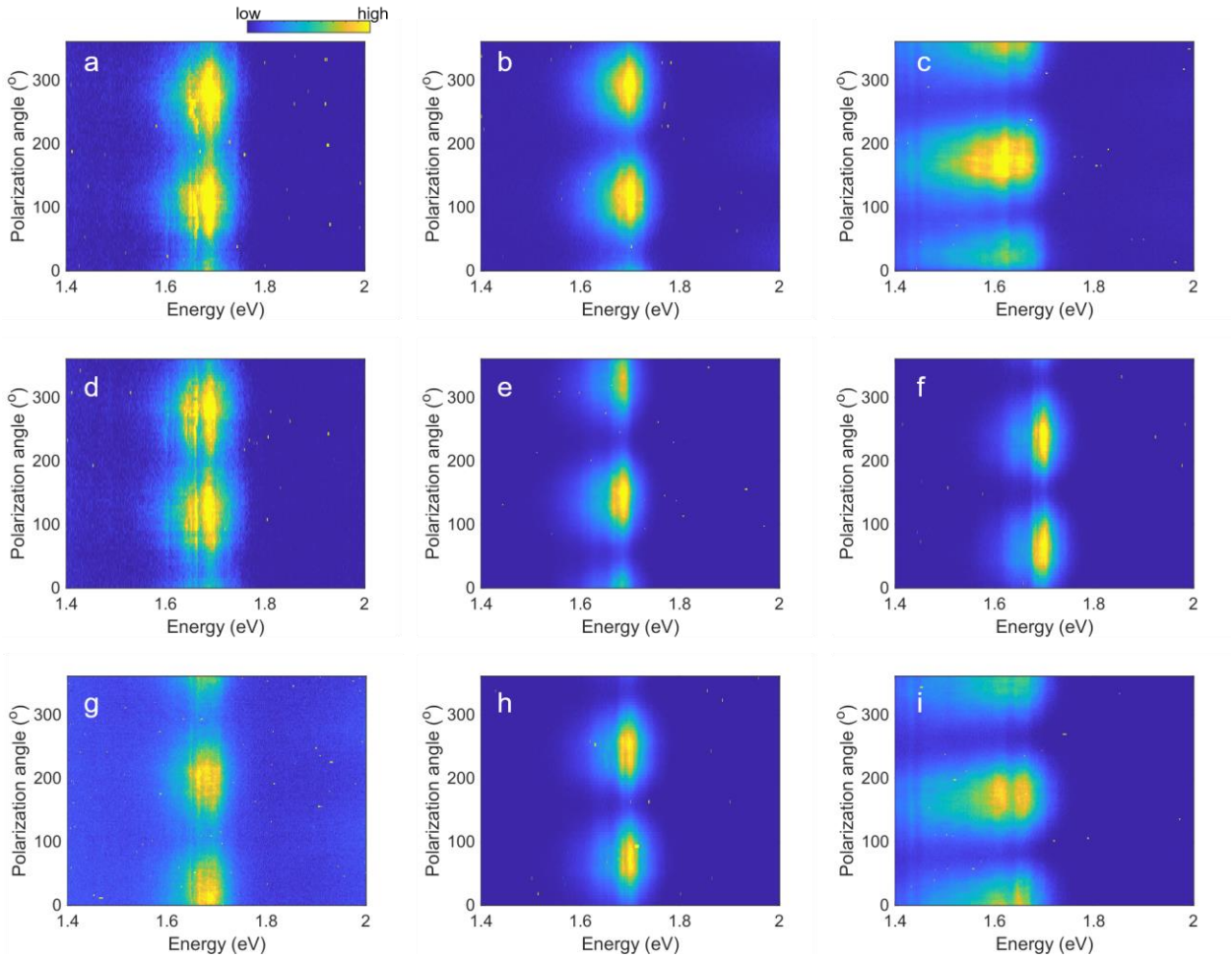

Figure S5.12. Extended polarization dataset 2. (a)-(i) False colormaps of emission spectrum as a function of collection (analyzer) polarizer angle for different spots from device #gateD1. It can be clearly seen that for all spots (collected near physical edges of sample) signatures of both interior and edge emission is observed.

S5.6 Temperature dependent PL spectra

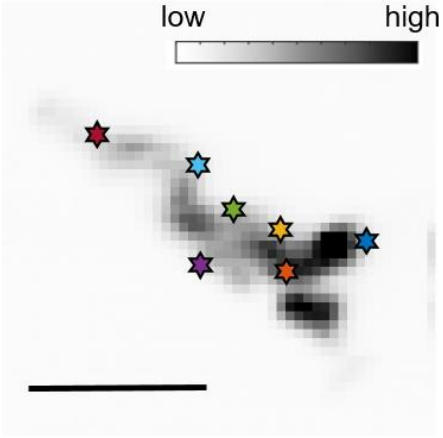

Figure S5.13. Spatial map of integrated photoluminescence spectrum. ($Int.PL = \int_{1.5\ eV}^{2\ eV} I(\omega)d\omega$) Spots are marked as stars in different colors showing temperature dependent emission Scale bar is 5 μm. This map (gate #D1) has been acquired at 5K and the same sample has been cycled from 5K to 300K to acquire temperature dependent spectrum presented next.

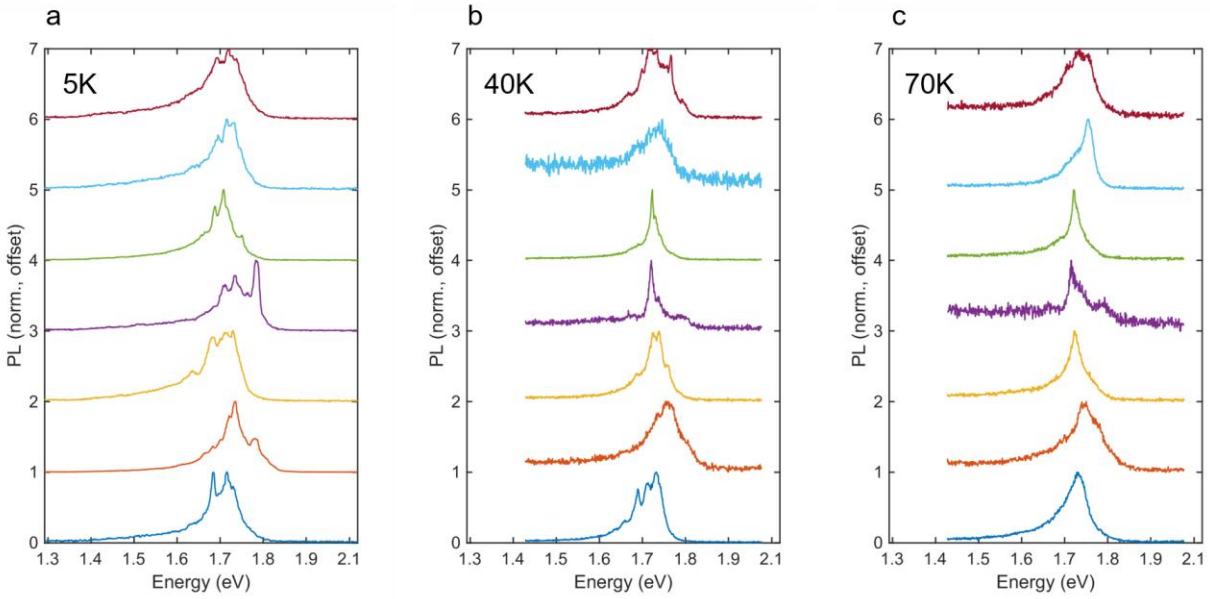

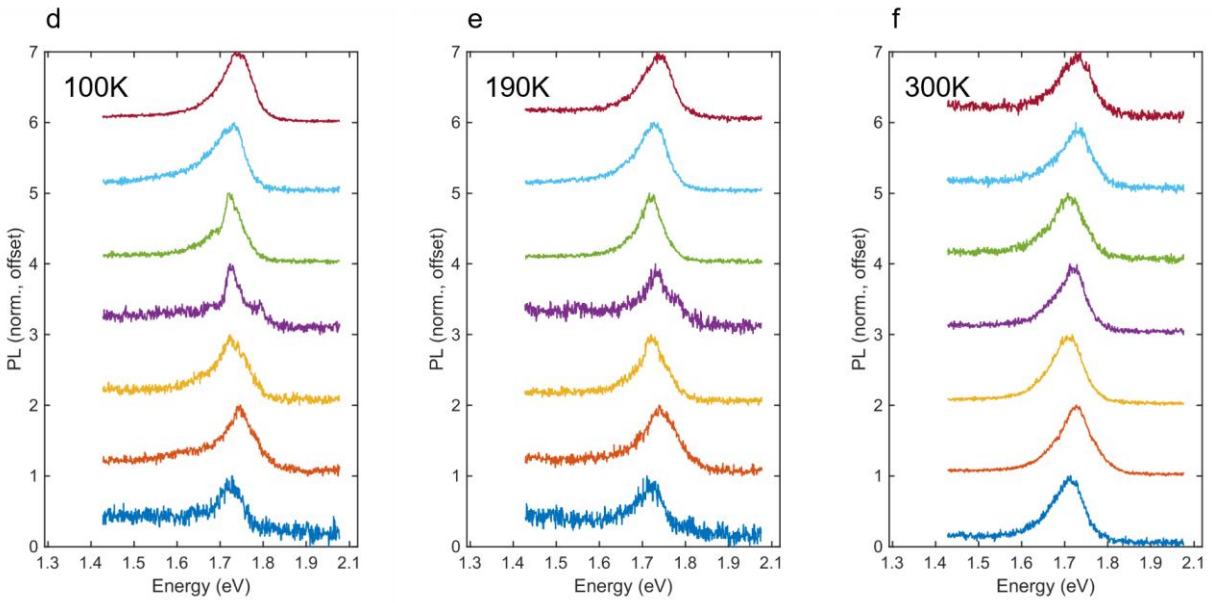

Figure S5.14. Temperature dependent (normalized and offset) photoluminescence spectrum from the selected spots (marked in S10). (a) 5K, (b) 40K, (c) 70K, (d) 100K, (e) 190K and (f) 300K showing clear broadening of edge features and eventual disappearance of the same. Interior emission profile takes over for higher temperatures.

S5.7 Power dependent spectra and statistics

Power dependence has been investigated across multiple spots and statistics have been collected. PL spectra as a function of power is shown below. Spectrum at each incident power is fit to the following set of equations–$I_{PL}(\omega) = \sum_{i=1}^{N} \frac{\frac{A_i \Gamma_i}{2}}{(\omega-\omega_i)^2+\left(\frac{\Gamma_i}{2}\right)^2}$, where A_i is the oscillator strength, Γ_i is the full-width at half maximum and ω_i is the resonance frequency/energy of each resonance), and thereafter fitting the obtained variation of integrated intensity with power to an exponent law $\int I_{PL,i}(P)\, d\omega = C_{0,i} P^{\alpha_i}$, where P_i is the incident power and α_i is the exponent for each resonance, $I_{PL,i}$ is given by equation 1 and $C_{0,i}$ is a proportionality constant. The integration is done across the full width at half-maxima for each peak.

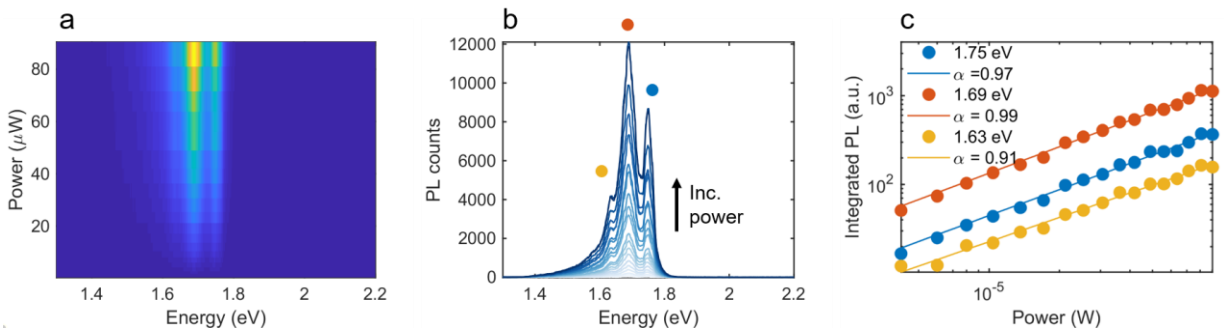

Figure S5.15. Additional pump power dependent data. (a) False color map and (b) line-cuts of power dependent photoluminescence spectrum for a specific spatial point in device D6 showing three distinct emission lines from the edge on top of a broad interior emission envelope. (c) Power-law fits of integrated photoluminescence intensity to the three aforementioned peaks showing linear behavior.

A plot of α versus ω_i is shown for sample where data was collected for 24 spots showing edge emission.

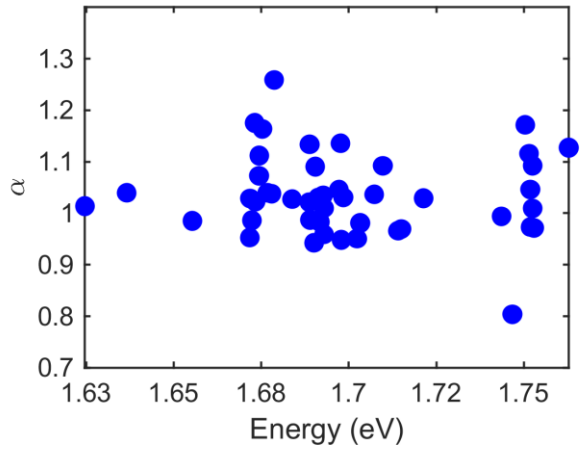

Figure S5.16. Accumulated power law fit exponents across 24 spots showing edge emission measured in sample #gateD1. Similar behavior was also seen in D6. Exponents lie between ~0.9 and ~1.1 indicating linear behavior (for the ranges of incident power measured).

S5.8 Spectral diffusion

Emission data was collected as a function of time for multiple spots out of which many showed signs of temporal fluctuation or spectral diffusion indicating high sensitivity to the environment. Such signatures allude to the fact that these states are highly localized and quantum-confined. Additional spots showing spectral diffusion are presented below, which are in stark contrast to stable emission from the interior excitons.

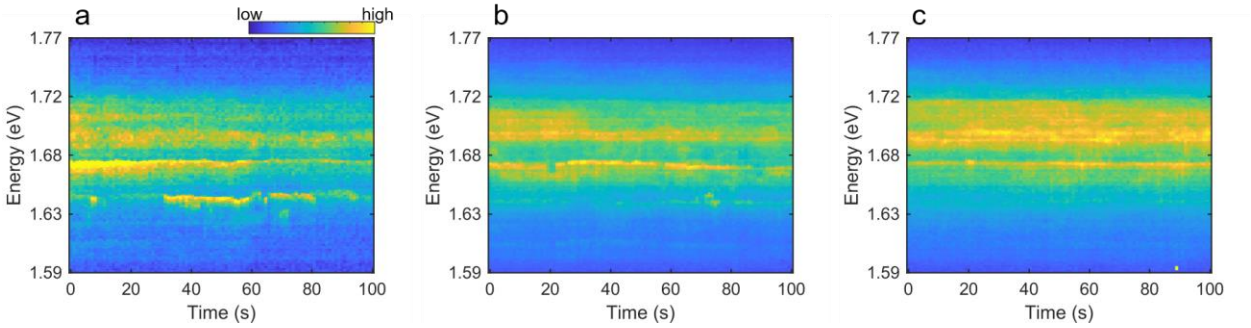

Figure S5.17. False color-maps of photoluminescence spectrum collected from three distinct spatial spots (a)-(c) showing clear signs of spectral diffusion/temporal fluctuation.

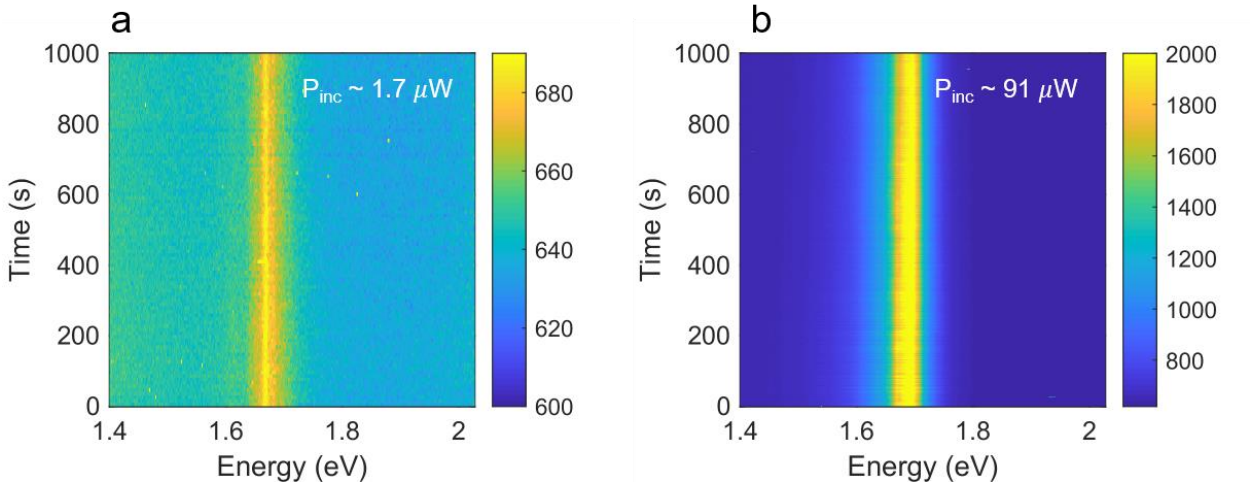

Figure S5.18. False color-maps of photoluminescence spectrum collected from interior exciton emission at an interior spatial spot showing stable emission for two different pumping powers (a) 1.7 μW and (b) 91 μW.

S5.9 Gate-dependent PL spectra of additional spots

Gate dependent PL spectra from different spots show emergence of edge emission peaks as a function of gate voltage which get quenched with added electrons/holes. In contrast, the interior emission shows a monotonic reduction indicating sample is n-doped. The details of the electrostatic landscape dictate for what voltage conditions the edge peaks line up and is sensitively linked to the amount of band-bending occurring at the edge of the sample.

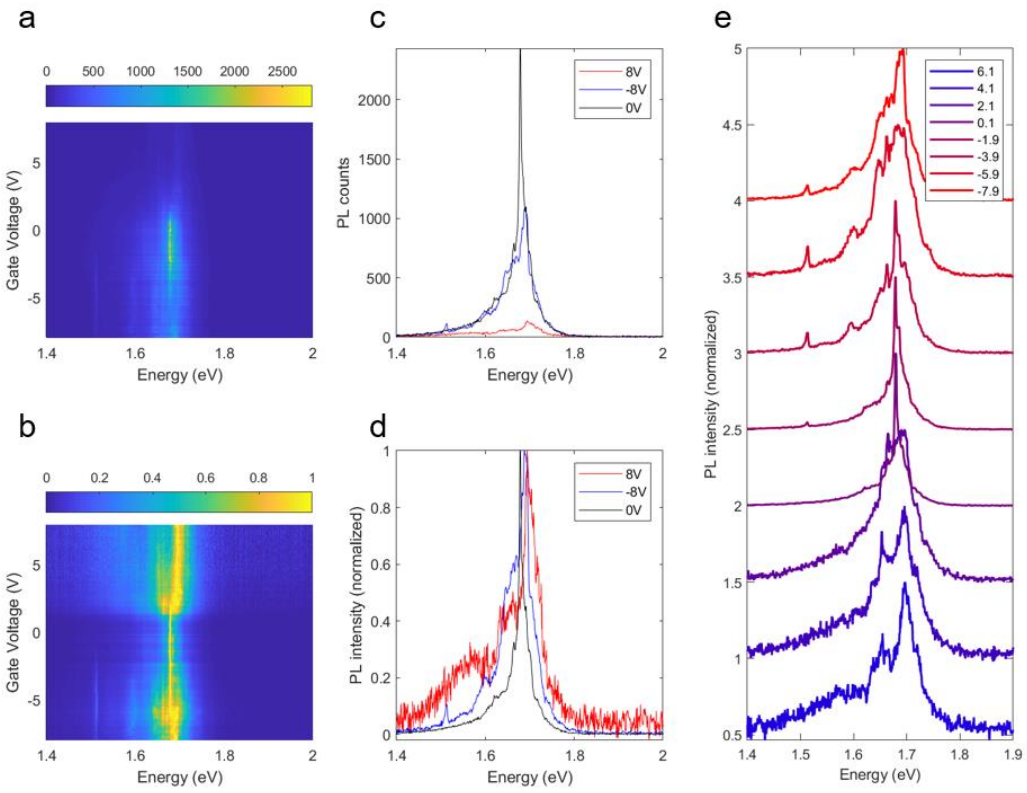

Figure S5.19. Gate dependent photoluminescence dynamics for P5 (spatial point #5) for device #gateD1. (a) False color-map of photoluminescence spectra as a function of gate voltage. (b) Same as (a) but normalized to 1, for each gate voltage. (c) Spectra from (a) at three distinct voltages (8V, 0V, -8V). (d) Spectra from (b) at three distinct voltages (8V, 0V, -8V). (e) Spectra from (b) for multiple voltages between 6.1V and -7.9V.

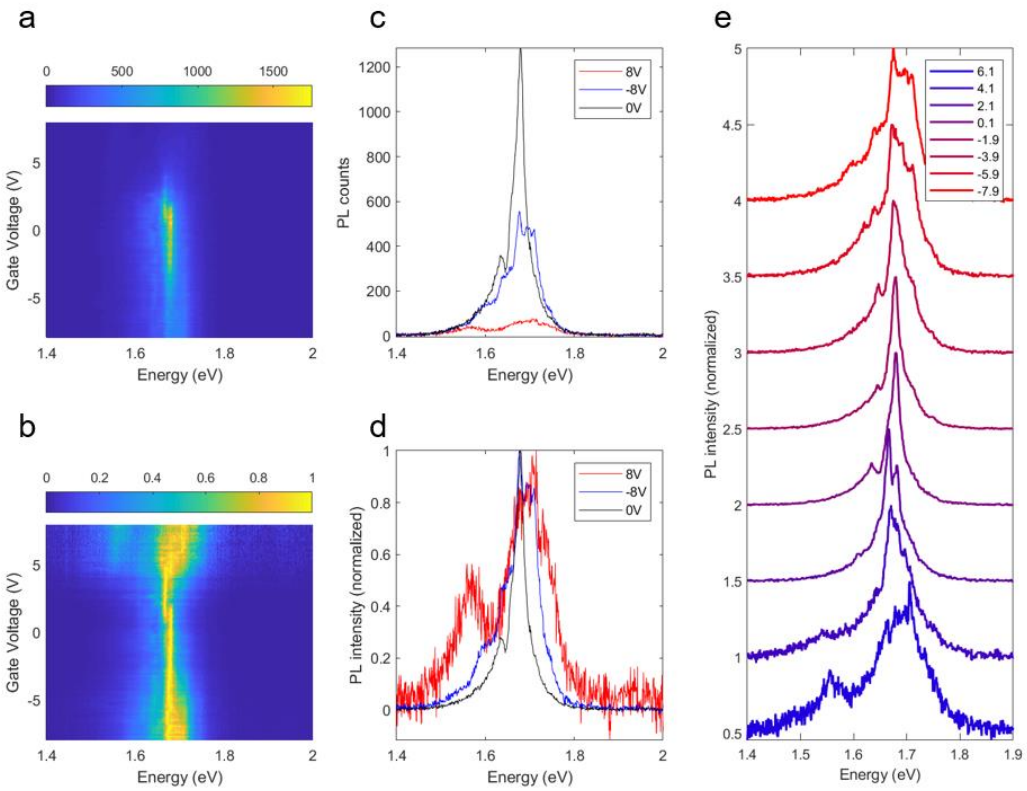

Figure S5.20. Gate dependent photoluminescence dynamics for P15 (spatial point #15) for device #gateD1. (a) False color-map of photoluminescence spectra as a function of gate voltage. (b) Same as (a) but normalized to 1, for each gate voltage. (c) Spectra from (a) at three distinct voltages (8V, 0V, -8V). (d) Spectra from (b) at three distinct voltages (8V, 0V, -8V). (e) Spectra from (b) for multiple voltages between 6.1V and -7.9V.

S5.10 Lifetime of PL emission

Time dependent emission spectra were collected both with and without filtering of the edge emission peak. The data was fit to the following equation: $I_{PL}(t) = \sum_{i=1,2,\ldots} I_i e^{-\frac{t}{\tau_1}}$, where I_i is the intensity of emission at $t = 0$ and τ_i is the time constant (lifetime) associated with that emission. Each data set was fit to a sum of three exponentials with the assumption that the first lifetime is below the resolving capability of the instrument and thus convoluted with the instrument response function, the second lifetime corresponds to the interior excitons and the third lifetime

corresponds to the edge excitons. The instrument limited lifetime is ~100 ps whereas the decay of interior excitons is ~300-500 ps which corresponds to values observed previously. A third lifetime which is on the order of 3-5 ns is seen for edge states but has very weak intensity because of significant coupling to the interior (which has a much shorter lifetime). Upon filtering most of the interior emission, an increase in the PL intensity for the longest lifetime component can be seen. To extract true lifetime of such edge states, quality of grown BP crystals must be improved such that the interior exciton is well blue-shifted and spectrally not overlapping with the edge emission - to filter out the interior emission completely.

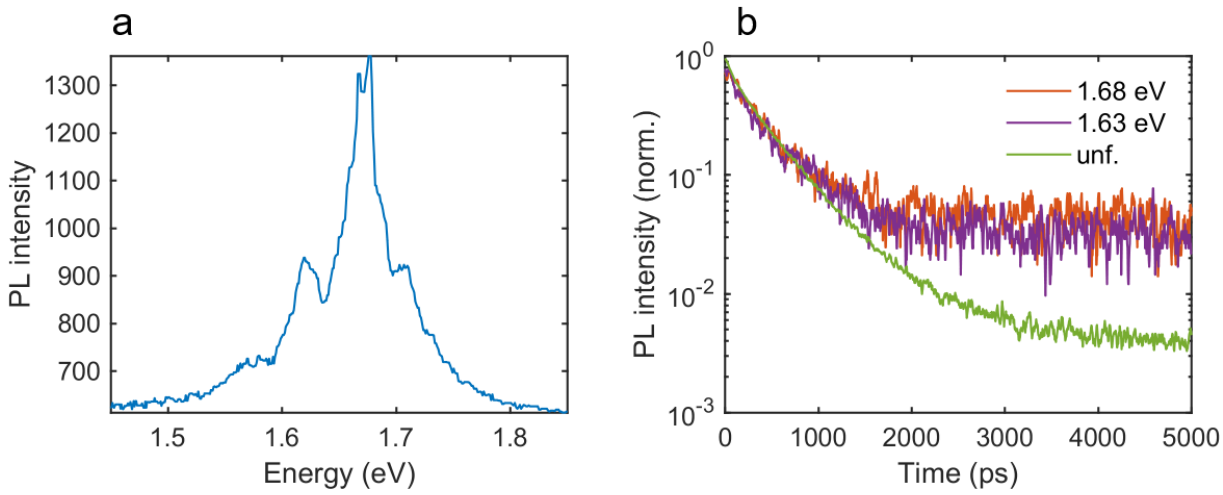

Figure S5.21. Lifetime measurements. (a) PL spectrum of a spatial location (device D6) containing edge exciton emission signatures over an envelope of interior emission. (b) Time dependent PL measurements collected without a filter and with two filters placed approximately at the two peaks from edge states at 1.63 eV and 1.68 eV. Bandwidth of the filters are ~10nm.

S5.11 Electrostatic simulations of capacitance

Finite element simulations were performed using Lumerical CHARGE module to model the electric-field profile around the BP monolayer. The thickness of each layer is as follows–hBN top 33 nm, BP monolayer 0.7 nm, bottom hBN 42 nm and bottom gold electrode 100 nm. Voltage was applied between the bottom gold and the BP sheet. A mesh size of nm was used. For BP, the following parameters were assumed (as extracted from literature)–

- DC permittivity–12.3
- Work function–5.15
- Band minimum–Γ point
- Effective mass of electron–0.17m_e
- Effective mass of hole–0.15m_e
- Band-gap–2.05 eV
- (Hole/electron) mobility–100 cm^2/Vs

Voltage was scanned from -5V to 5V in steps of 0.1V and a non-uniform adaptive mesh was used to account for edge effects and fringing fields.

The field distribution as well as line-cuts are shown below, along with a schematic for the structure simulated. A hotspot can be seen near the physical edge of the BP monolayer for the in-plane component of the electric field which is primarily responsible for the in-plane Stark effect. However, the magnitude is very sensitive to the location of the edge and as seen below, a shift on the order of a nanometer can reduce the maximal field strength by an order of magnitude. Since emission emerges from a complex set of edge configurations it is hard to pin-point the exact magnitude of the field experienced by each state under applied voltage, but the trend can be explained well from these simulations.

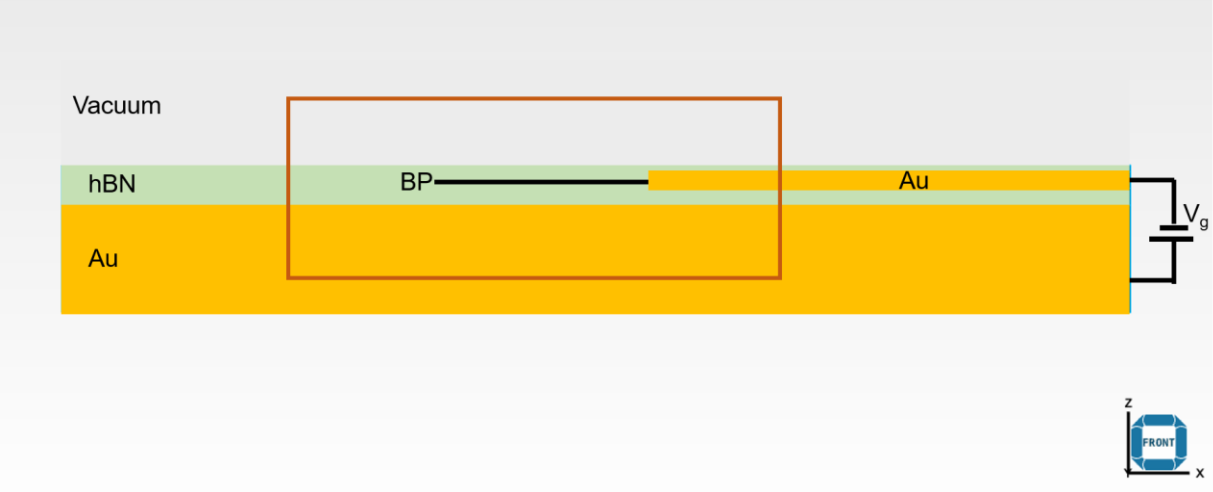

Figure S5.22. Simulation setup in Lumerical CHARGE module. hBN is modelled as a continuous medium (including the top and bottom thickness) and BP is inserted inside the hBN, such that it

matches the experimental structure of device #gateD1. Voltage is applied between the top and bottom gold. The assumption here is that graphene acts metallic enough that the Au-BP contact can yield similar results to Au-graphene-BP contact.

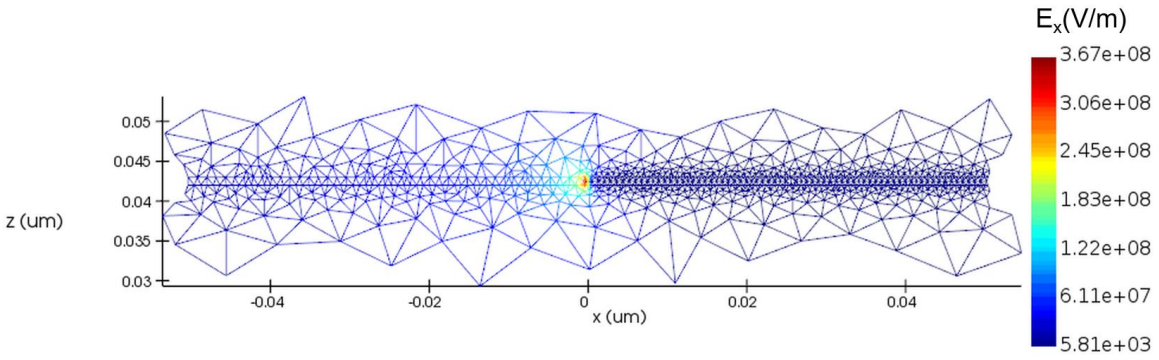

Figure S5.23. In-plane electric field component distribution cross-section at 5V. A hotspot can be seen at the BP-hBN interface at x=0 nm.

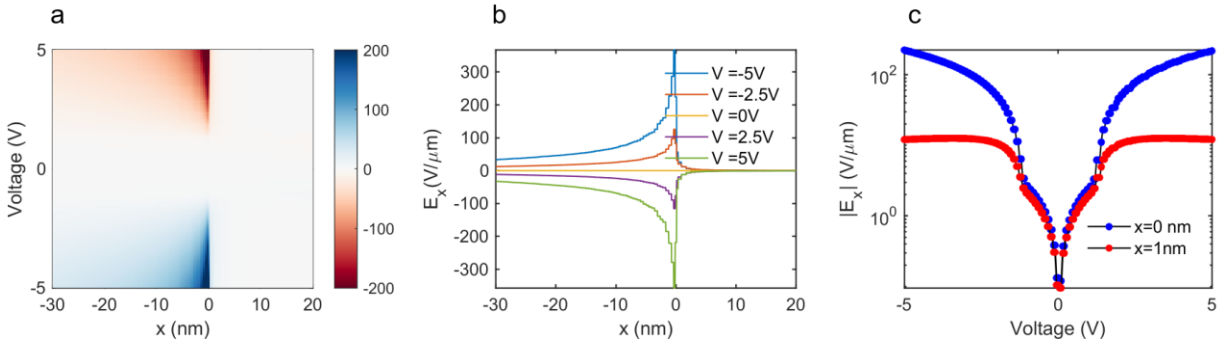

Figure S5.24. Gate dependent in-plane field simulations. (a) In-plane electric field variation as a function of spatial position (x) and gate voltage. The BP-hBN interface laterally is at x=0 nm. (b) Line-cuts of in-plane electric field for different voltages as a function of spatial position. (c) Line-cuts of in-plane electric field for two spatial positions near the BP-hBN interface, as a function of gate voltage showing the sensitivity of the field experienced by the dipole depending on its location.

S5.12 Band bending schematic

From gate dependent PL measurements, a strong band bending is seen from the interior to the edge. Here, we schematically represent the band bending to explain the shifts in the Fermi level between the interior and the edge, also supported by the gate-dependent PL measurements.

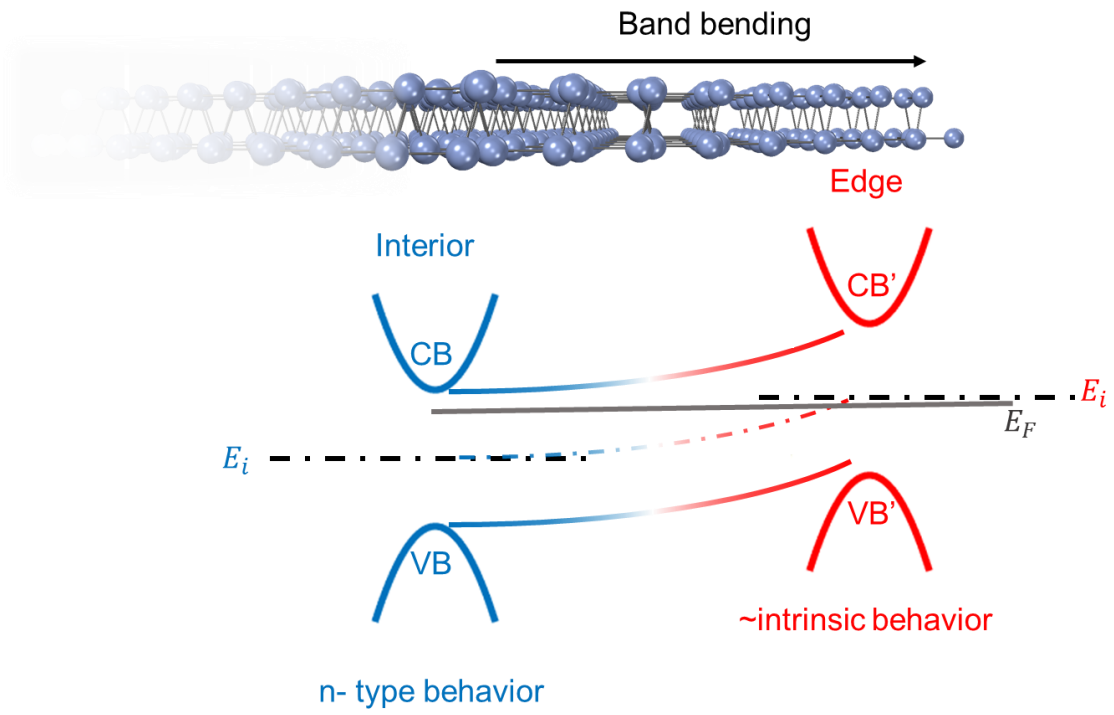

Figure S5.25. Atomic structure of monolayer black phosphorus and schematic of how band bending causes transition from n-type behavior to intrinsic at the edge.

We note that the edge excitons appear brightest at a voltage that is offset from where the interior excitons show highest luminescence. Based on a standard parallel plate capacitor model we can approximate the minimum amount of band bending that occurs for each of the edge exciton states. It is important to note that the band bending can be larger than this since we do not reach charge neutrality for the interior exciton to prevent the device from breakdown at high voltages. For device #gateD1, the bottom hBN was ~42 nm in thickness. Employing the relations for a parallel-plate capacitor we get

$\frac{C}{A} = \frac{\epsilon_0 \epsilon_{r,hBN}}{d_{hBN}}$, where $\epsilon_{r,hBN} = 3.9$ and $d_{hBN} = 42\ nm$.

$n = C(V - V_{CNP}) = \frac{\epsilon_0 \epsilon_{r,hBN}(V - V_{CNP})}{d_{hBN}}$, where $V_{CNP} > -5V$ (as estimated from PL measurements).

At $V \sim 0V$, we thus get a charge density of ~2.5x10^{12} cm^{-2}. Assuming an effective mass $m_{eff} = 0.15m_0$, for monolayer BP, we use the parabolic band approximation equation: $E_F = \frac{\pi \hbar^2 n_{2D}}{m_{eff}}$, to get a band bending lower bound of ~40 meV.

S5.13 Screening effects

Excitons in layered 2D sheets are much more prone to screening from the environment as a consequence of the Coulomb field lines being expelled out of the material itself. The difference in binding energy is striking as one approaches from a 3D to 2D limit. Strong self-screening in a 3D material renders the binding energy weaker for excitons in the medium and leads to an increased Bohr radius due to weaker Coulomb forces. Similarly, the binding energy gets larger in the 2D limit as the Bohr radius gets smaller. For monolayer black phosphorus, a similar argument holds despite its excitons being quasi 1D due to optical selection rules. Naturally, as the confinement gets tighter and the Bohr radius is further reduced at the edges, more of the Coulomb field lines are expelled outside the medium as compared to the excitons not at the edge. This makes the edge excitons more sensitive to screening from hBN dielectric environment which leads to a reduction in the energy–causing a red shift of the resonance. Since this screening is more pronounced more edges, when excitons get significantly redshifted such that their resonance energy is lower than or comparable to the interior excitons, they show up as bright peaks in photoluminescence.

In short, mathematically the exciton states can be computed using an effective-mass theory:

$$\left[-\frac{1}{2\mu}\nabla_\rho^2 - W(\rho)\right]\psi_n(\rho) = E_n\psi_n(\rho),$$

where μ is the effective mass of the exciton, ρ is the separation between the electron and hole, ψ is the wave function describing the exciton, W represents the Coulomb interaction and E is the binding energy of the corresponding eigen-state.

In the anisotropic 2D limit, the Coulomb interaction is best described by the Rytova-Keldysh potential,

$$W(\rho) = \frac{\pi e^2}{\rho_0(\epsilon_a + \epsilon_b)}\left[H_0\left(\frac{\rho}{\rho_0}\right) - Y_0\left(\frac{\rho}{\rho_0}\right)\right],$$

where Y_0, H_0 are the Bessel and Struve function of the second kind and ϵ_a and ϵ_b are the dielectric permittivities of the surround top (a) and bottom (b) medium, respectively.

However, the R-K model has unphysical divergence at $\rho \sim 0$, which is a relevant length scale in our case, as for edge excitons the Bohr radius is much smaller than the interior excitons due to stronger localization. A better approximation for the potential was shown to be as follows:

$$W(\rho) = \frac{e^2}{\epsilon_{2D}\rho} + 2\sum_{n=1}^{\infty} \frac{e^2 L_{2D,a}^n L_{2D,b}^n}{\epsilon_{2D}\sqrt{(\rho^2 + (2nd)^2}} + \left(L_{2D,a} + L_{2D,b}\right)\sum_{n=0}^{\infty} \frac{e^2 L_{2D,a}^n L_{2D,b}^n}{\epsilon_{2D}\sqrt{(\rho^2 + [(2n+1)d]^2}},$$

where $L_{2D,i} = (\epsilon_{2D} - \epsilon_i)/(\epsilon_{2D} + \epsilon_i)$ and ϵ_{2D} is the dielectric permittivity of the 2D sheet. From this expression it is clear that other factors remaining constant the Coulomb potential has an inverse dependence on the electron-hole separation–meaning edge excitons have very strong Coulomb attraction.

This analysis is derived from Ref.[157]

S5.14 Discussion on edge exciton emission

We explore the different possibilities that can give rise to discrete lines in the photoluminescence spectrum from BP edges, elaborating on why the proposed mechanism in this work is able to explain the complete set of observation.

- *Point defects*–Presence of point defects due to vacancies, interstitials, or foreign atoms are known to cause additional optical transitions. However, firstly, such defects are expected to occur in regions other than the edges as well but were found to be absent in all of the samples investigated as part of this study. Furthermore, such point defects display saturable emission and hence non-linear dependence on incident pump power, while linear scaling is seen in our

measurements–indicating more excitonic like behavior. Additionally, we find most of the emission states having aligned polarization with the local armchair axis–implying preservation of the intrinsic BP symmetry. For completeness, we list possible defects that are typically studied in phosphorene –

i. Oxygen (O)
ii. Hydrogen (H)
iii. Fluorine (F)
iv. Chlorine (Cl)
v. Hydroxyl (OH)
vi. Sulphur (S)
vii. Selenium (Se)

Of these foreign atoms, it was found that so called Family 1 edges (i.e., H, F, Cl, OH) tend to form saturated bonds with P atoms which causes the edge states to be energetically far away from the bandgap. Family 2 edges (pristine, O, S, Se) form weaker unsaturated bonds with the p_z orbital of the phosphorus atom and push edge states within the band gap of the ribbons. These calculations were reported for phosphorene nanoribbons along armchair and zigzag orientation[259]. Despite our measurements not being consistent solely with point defects, we cannot completely rule out the possibility of such states–with O being the most likely. For example, emission states which are not aligned with the local armchair orientation might arise from such states (or reconstruction that does not preserve the intrinsic BP symmetry like a (1,3) reconstruction). However, the density of such states due to defects is expected to be low as the entire processing is done in a completely inert environment (in a nitrogen purged glovebox) and immediately encapsulated with hBN. All optical measurements were performed under high vacuum. Future (optical and structural) correlated spectroscopy-based studies must be done to isolate the effect of edge reconstruction and point defects in BP.

- *Edge quantum confinement*–Since an edge is an abrupt termination of atoms, a strong confining potential well is created for excitons which can be approximately modelled as a triangular potential barrier. The Schrödinger's equation for such a system is as follows –

$$-\frac{\hbar^2}{2\mu}\nabla^2\psi_n(x) + V(x)\psi_n(x) = E_n\psi_n(x),$$

where, $V(x) = \infty$, if $x > 0$ and $V(x) = \alpha x$, if $x < 0$ and the edge is at $x = 0$. $\psi_n(x)$is the wave function, μ is the effective mass and E_n in the eigen-energy of the n^{th} bound state of the exciton. Upon solving this equation numerically, we find multiple eigen states that correspond to the quantized energy levels supported in this potential well which could, in principle, also explain the observation of peaks in our experiment. Here, we note that if this were solely the case for the observed peaks, this feature would be generic to all edges and not selected edge sites. Thus, we can assert that this is not the only mechanism leading to the formation of edge excitons.

- *Strain induced localization*–In TMDCs it is well known that strong strain gradients can cause significant reduction in the band gap leading to the formation of "defect states" that give rise to single-photon emission. To verify whether such is the case for BP, we prepared 1. An intentional strained sample by draping a sheet of monolayer BP on a fabricated nano-pillar array made of gold and 2. A serendipitous heterostructure containing a large bubble in between the layers causing strain on the BP. For sample 1, the monolayer was aligned in such a way that the only interior of BP would be strained. We saw no evidence of localized emission in the sample in either of the sample (except some of the edge sites)–ruling out strain to be the only driving factor.

S5.15 First-Principles Computation Of Optical Spectrum

In order to verify the reconstructed edge responsible for distinct emission peaks at various edges of the different sections in monolayer BP, we investigate a selected number of BP nanoribbons with different edge reconstructions, focusing on previously predicted structures that display small formation energy and displaying a gap[267]. Using these criteria, out of the 24 previously computed edge structures with an armchair and zigzag fracture orientations, we have selected 5 promising structures, as discussed earlier. We constructed nanoribbons of two unit cells along the extended direction (zigzag for AC10-ii, AC12-i, and armchair for ZZ4-i, ZZ8-i, and ZZ10-i) and 8 unit cells

along the confined direction (armchair for AC10-ii, AC12-i and zigzag for ZZ4-i, ZZ8-i, and ZZ10-i) with 13 Å out-of-plane vacuum.

We perform DFT calculations using the Quantum Espresso package with Perdew-Burke-Ernzerhof (PBE) generalized gradient approximation at an energy cutoff of 30 Ry to obtain the ground-state wave function basis for our subsequent GW and GW-BSE calculations. We perform GW calculations with the BerkeleyGW package using the Hyberten-Louie generalized plasmon-pole model (GPP). To converge the calculation of the dielectric matrix, we use a hybrid stochastic-deterministic compression of the unoccupied states following Ref. YYY, which approximately captures 170,000 bands, and evaluate the response on a 1x1x8 k-point grid with a dielectric cutoff of 12 Ry. To capture the long-range dielectric screening (q=0), we utilize the nonuniform neck subsampling (NNS) method on a 1x1x4 k-point grid with additional 32 k-points. Self-energy calculations are performed on a 1x1x4 k-point grid and interpolated to a 1x1x32 k-point grid with truncated Coulomb potential to prevent spurious interactions along both extended and out-of-plane directions. This yields quasiparticle band structure in which we project the DFT wave function to edge and bulk state by weighting the probability density with a clamp function that goes from 0 to 1 in an area of 1 unit cell from the edges. Furthermore, we project the wavefunction at each band index and k-point to the edge and interior state using a clamp function:

$$\langle edge_{n,k} \rangle = \langle \psi_{n,k} | f_{clamp}(x) | \psi_{n,k} \rangle$$

$$\langle interior_{n,k} \rangle = 1 - \langle edge_{n,k} \rangle$$

where,

$$f_{clamp}(x) = \begin{cases} 0\,, & x > x_1 + a \text{ or } x < x_2 - a \\ 1 - \frac{x - x_1}{a}\,, & x_1 + a > x > x_1 \\ 1 + \frac{x - x_2}{a}\,, & x_2 > x > x_2 - a \\ 1, \text{ otherwise.} \end{cases}$$

For x_1 and x_2 are positions of the outermost atom along the confined direction with all other atoms in the structure lie in-between x_1 and x_2, and a is the length of the primitive unit cell along the confined direction.

The matrix elements of the kernel of the BSE are computed including 20 conduction bands and 20 valence bands on a 1x1x4 k-point grid interpolated onto a 1x1x32 k-point grid.

To further distinguish between edge and interior excitons, we take the two-particle exciton amplitude $\psi_s(r_e, r_h) = \sum_{v,c,k} A^s{}_{vck}\, \psi_{ck}(r_e)\psi_{vk}(r_h)$ for each state and compute their corresponding electron, $F_e(r_e)$, and hole, $F_h(r_h)$, projection:

$$F_e(r_e) = \int d^3 r_h |\psi(r_e, r_h)|^2 = \Sigma_{v,c',c,k} A^s_{vck} A^{s^*}_{vc'k} \psi^*_{c'k}(r_e)\psi_{ck}(r_e)$$

$$F_h(r_h) = \int d^3 r_e |\psi(r_e, r_h)|^2 = \Sigma_{v,c',c,k} A^s_{vck} A^{s^*}_{vc'k} \psi^*_{c'k}(r_h)\psi_{ck}(r_h)$$

S5.16 TEM analysis of monolayer BP

A FEI Titan 80-300 STEM/TEM equipped with a probe spherical-aberration corrector was employed to conduct annular dark field scanning transmission electron microscopy (ADF-STEM) imaging analysis. The images were collected with the microscope operating at 300 kV with a probe convergence semi-angle of 14 mrad and a collection angle of 34-195 mrad.

Bibliography

1. Geim, A. K. & Grigorieva, I. v. Van der Waals heterostructures. *Nature* vol. 499 419–425.
2. Liu, Y. Van der Waals heterostructures and devices. *Nat. Rev. Mater.* **1**, 16042 (2016).
3. Yi, M. & Shen, Z. A review on mechanical exfoliation for the scalable production of graphene. *J Mater Chem A Mater* **3**, 11700–11715 (2015).
4. Ang, P. K., Wang, S., Bao, Q., Thong, J. T. L. & Loh, K. P. High-throughput synthesis of graphene by intercalation-exfoliation of graphite oxide and study of ionic screening in graphene transistor. *ACS Nano* **3**, 3587–3594 (2009).
5. Ciesielski, A. & Samorì, P. Graphene via sonication assisted liquid-phase exfoliation. *Chem Soc Rev* **43**, 381–398 (2013).
6. Wilson, J. A. & Yoffe, A. D. The transition metal dichalcogenides discussion and interpretation of the observed optical, electrical and structural properties. *Adv Phys* **18**, 193–335 (1969).
7. Novoselov, K. S. *et al.* Two-dimensional gas of massless Dirac fermions in graphene. *Nature* **438**, 197–200 (2005).
8. Armitage, N. P., Mele, E. J. & Vishwanath, A. Weyl and Dirac semimetals in three-dimensional solids. *Rev Mod Phys* **90**, 015001 (2018).
9. Stajic, J. Magnetic Weyl semimetals. *Science (1979)* **365**, 1260.3-1260 (2019).
10. Yan, B. & Felser, C. Topological Materials: Weyl Semimetals. *Annu Rev Condens Matter Phys* **8**, 337–354 (2017).
11. Cao, Y. *et al.* Unconventional superconductivity in magic-angle graphene superlattices. *Nature* **556**, 43–50 (2018).
12. Cao, Y. *et al.* Correlated insulator behaviour at half-filling in magic-angle graphene superlattices. *Nature* **556**, 80–84 (2018).
13. He, K. *et al.* Tightly bound excitons in monolayer WSe_2. *Phys Rev Lett* **113**, 026803 (2014).

14. Wang, G. *et al.* Colloquium: Excitons in atomically thin transition metal dichalcogenides. *Rev Mod Phys* **90**, 021001 (2018).

15. Chernikov, A. *et al.* Exciton binding energy and nonhydrogenic Rydberg series in monolayer WS_2. *Phys Rev Lett* **113**, 076802 (2014).

16. Mahan, G. D. Excitons in Degenerate Semiconductors. *Physical Review* **153**, 882 (1967).

17. Yang, J. *et al.* Robust Excitons and Trions in Monolayer $MoTe_2$. *ACS Nano* **9**, 6603–6609 (2015).

18. Vaquero, D. *et al.* Excitons, trions and Rydberg states in monolayer MoS_2 revealed by low-temperature photocurrent spectroscopy. *Communications Physics 2020 3:1* **3**, 1–8 (2020).

19. Chen, S. Y. *et al.* Luminescent Emission of Excited Rydberg Excitons from Monolayer WSe_2. *Nano Lett* **19**, 2464–2471 (2019).

20. Ross, J. S. *et al.* Electrical control of neutral and charged excitons in a monolayer semiconductor. *Nat Commun* **4**, 1474 (2013).

21. Wang, X. *et al.* Highly anisotropic and robust excitons in monolayer black phosphorus. *Nat Nanotechnol* **10**, 517–521 (2015).

22. Li, L. *et al.* Direct observation of the layer-dependent electronic structure in phosphorene. *Nat Nanotechnol 2016 12:1* **12**, 21–25 (2016).

23. Zhang, G. *et al.* Determination of layer-dependent exciton binding energies in few-layer black phosphorus. *Sci Adv* **4**, eaap9977 (2018).

24. Radisavljevic, B., Radenovic, A., Brivio, J., Giacometti, V. & Kis, A. Single-layer MoS_2 transistors. *Nat Nanotechnol 2011 6:3* **6**, 147–150 (2011).

25. Mak, K. Tightly bound trions in monolayer MoS_2. *Nat Mater* **12**, 207–211 (2013).

26. Chernikov, A. *et al.* Electrical Tuning of Exciton Binding Energies in Monolayer WS_2. *Phys Rev Lett* **115**, (2015).

27. Wagner, K. *et al.* Autoionization and Dressing of Excited Excitons by Free Carriers in Monolayer WSe_2. *Phys Rev Lett* **125**, 267401 (2020).

28. Chernikov, A. *et al.* Exciton binding energy and nonhydrogenic Rydberg series in monolayer WS_2. *Phys Rev Lett* **113**, 076802 (2014).

29. Hill, H. M. *et al.* Observation of excitonic rydberg states in monolayer MoS_2 and WS_2 by photoluminescence excitation spectroscopy. *Nano Lett* **15**, 2992–2997 (2015).

30. Yu, Y. *et al.* Giant Gating Tunability of Optical Refractive Index in Transition Metal Dichalcogenide Monolayers. *Nano Lett* **17**, 3613–3618 (2017).

31. Datta, I. *et al.* Low-loss composite photonic platform based on 2D semiconductor monolayers. *Nat Photonics* **14**, 256–262 (2020).

32. Karni, O. *et al.* Infrared Interlayer Exciton Emission in MoS_2/WSe_2 Heterostructures. *Phys Rev Lett* **123**, 247402 (2019).

33. Leisgang, N. *et al.* Giant Stark splitting of an exciton in bilayer MoS_2. *Nat Nanotechnol 2020 15:11* **15**, 901–907 (2020).

34. Jauregui, L. A. *et al.* Electrical control of interlayer exciton dynamics in atomically thin heterostructures. *Science (1979)* **366**, 870–875 (2019).

35. Liu, Y. *et al.* Gate-Tunable Giant Stark Effect in Few-Layer Black Phosphorus. *Nano Lett* **17**, 1970–1977 (2017).

36. Rodin, A. S., Carvalho, A. & Castro Neto, A. H. Strain-induced gap modification in black phosphorus. *Phys Rev Lett* **112**, (2014).

37. Aslan, O. Probing the optical properties and strain-tuning of ultrathin $Mo_{1-x}W_xTe_2$. *Nano Lett.* **18**, 2485–2491 (2018).

38. Huang, S. *et al.* Strain-tunable van der Waals interactions in few-layer black phosphorus. *Nat Commun* **10**, 1–7 (2019).

39. Quereda, J. *et al.* Strong Modulation of Optical Properties in Black Phosphorus through Strain-Engineered Rippling. *Nano Lett* **16**, 2931–2937 (2016).

40. Cho, C. *et al.* Highly Strain-Tunable Interlayer Excitons in MoS_2/WSe_2Heterobilayers. *Nano Lett* **21**, 3956–3964 (2021).

41. AN Grigorenko, M. P. K. N. Graphene plasmonics. *Nat Photon.* **6**, 749–758 (2012).

42. Ni, G. X. *et al.* Fundamental limits to graphene plasmonics. *Nature* **557**, 530–533 (2018).

43. Ju, L. *et al.* Graphene plasmonics for tunable terahertz metamaterials. *Nat Nanotechnol* **6**, 630–634 (2011).

44. Brar, V. W., Jang, M. S., Sherrott, M., Lopez, J. J. & Atwater, H. A. Highly confined tunable mid-infrared plasmonics in graphene nanoresonators. *Nano Lett* **13**, 2541–2547 (2013).

45. di Pietro, P. *et al.* Observation of Dirac plasmons in a topological insulator. *Nat Nanotechnol* **8**, 556–560 (2013).

46. Wang, C. *et al.* Van der Waals thin films of WTe_2 for natural hyperbolic plasmonic surfaces. *Nat Commun* **11**, 1–9 (2020).

47. Correas-Serrano, D., Gomez-Diaz, J. S., Melcon, A. A. & Alù, A. Black phosphorus plasmonics: anisotropic elliptical propagation and nonlocality-induced canalization. *Journal of Optics* **18**, 104006 (2016).

48. Lee, I. H. *et al.* Anisotropic Acoustic Plasmons in Black Phosphorus. *ACS Photonics* **5**, 2208–2216 (2018).

49. Liu, Z. & Aydin, K. Localized Surface Plasmons in Nanostructured Monolayer Black Phosphorus. *Nano Lett* **16**, 3457–3462 (2016).

50. Low, T. *et al.* Plasmons and Screening in Monolayer and Multilayer Black Phosphorus. *Phys Rev Lett* **113**, (2014).

51. Dai, S. *et al.* Tunable phonon polaritons in atomically thin van der Waals crystals of boron nitride. *Science* **343**, 1125–1129 (2014).

52. Ma, W. *et al.* In-plane anisotropic and ultra-low-loss polaritons in a natural van der Waals crystal. *Nature 2018 562:7728* **562**, 557–562 (2018).

53. Basov, D. N., Fogler, M. M. & García De Abajo, F. J. Polaritons in van der Waals materials. *Science* **354**, 6309 (2016).

54. Ling, X., Wang, H., Huang, S., Xia, F. & Dresselhaus, M. S. The renaissance of black phosphorus. *Proc Natl Acad Sci U S A* **112**, 4523–4530 (2015).

55. Chen, H. T., Taylor, A. J. & Yu, N. A review of metasurfaces: Physics and applications. *Reports on Progress in Physics* vol. 79 076401 (2016).

56. Koshelev, K. *et al.* Subwavelength dielectric resonators for nonlinear nanophotonics. *Science* **367**, 288–292 (2020).

57. Fante, R. L. & Mccormack, M. T. Reflection Properties of the Salisbury Screen. *IEEE Trans Antennas Propag* **36**, 1443–1454 (1988).

58. Park, J., Kang, J. H., Kim, S. J., Liu, X. & Brongersma, M. L. Dynamic reflection phase and polarization control in metasurfaces. *Nano Lett* **17**, 407–413 (2017).

59. Qian, K. *et al.* Under-Coupling Whispering Gallery Mode Resonator Applied to Resonant Micro-Optic Gyroscope. *Sensors 2017, Vol. 17, Page 100* **17**, 100 (2017).

60. Yu, N. & Capasso, F. Flat optics with designer metasurfaces. *Nat Mat* **13**, 139–150 (2014).

61. Yu, N. *et al.* Light propagation with phase discontinuities: Generalized laws of reflection and refraction. *Science (1979)* **334**, 333–337 (2011).

62. Wuttig, M. & Yamada, N. Phase-change materials for rewriteable data storage. *Nat Mater* **6**, 824–832 (2007).

63. Shportko, K. *et al.* Resonant bonding in crystalline phase-change materials. *Nat Mater* **7**, 653–658 (2008).

64. Maiti, R. *et al.* Strain-engineered high-responsivity $MoTe_2$ photodetector for silicon photonic integrated circuits. *Nat Photon* **14**, 578–584 (2020).

65. Xu, K. *et al.* The positive piezoconductive effect in graphene. *Nat Commun* **6**, (2015).

66. GT Reed, G. M. F. G. D. T. Silicon optical modulators. *Nat Photon* **4**, 518–526 (2010).

67. Xu, Q., Schmidt, B., Pradhan, S. & Lipson, M. Micrometre-scale silicon electro-optic modulator. *Nature* **435**, 325–327 (2005).

68. Kuo, Y.-H. *et al.* Strong quantum-confined Stark effect in germanium quantum-well structures on silicon. *Nature* **437**, 1334–1336 (2005).

69. Abel, S. *et al.* Large Pockels effect in micro- and nanostructured barium titanate integrated on silicon. *Nat Mater* **18**, 42–47 (2019).

70. Han, J.-H. Efficient low-loss InGaAsP/Si hybrid MOS optical modulator. *Nat Photon* **11**, 486–490 (2017).

71. Liu, A. A high-speed silicon optical modulator based on a metal–oxide–semiconductor capacitor. *Nature* **427**, 615–618 (2004).

72. Marris-Morini, D. Low loss and high speed silicon optical modulator based on a lateral carrier depletion structure. *Opt Express* **16**, 334–339 (2008).

73. Mak, K. F. *et al.* Tightly bound trions in monolayer MoS_2. *Nat Mat 2012 12:3* **12**, 207–211 (2012).

74. Fei, Z. *et al.* Gate-tuning of graphene plasmons revealed by infrared nano-imaging. *Nature* **486**, 82–85 (2012).

75. Li, L. *et al.* Black phosphorus field-effect transistors. *Nat Nanotechnol* **9**, 372–377 (2014).

76. Kim, J. *et al.* Observation of tunable band gap and anisotropic Dirac semimetal state in black phosphorus. *Science* **349**, 723–726 (2015).

77. Deng, B. *et al.* Efficient electrical control of thin-film black phosphorus bandgap. *Nat Commun* **8**, (2017).

78. Peng, R. *et al.* Midinfrared Electro-optic Modulation in Few-Layer Black Phosphorus. *Nano Lett* **17**, 6315–6320 (2017).

79. Youngblood, N., Chen, C., Koester, S. J. & Li, M. Waveguide-integrated black phosphorus photodetector with high responsivity and low dark current. *Nat Photon* **9**, 247–252 (2015).

80. Wang, T. *et al.* Visualizing Light Scattering in Silicon Waveguides with Black Phosphorus Photodetectors. *Advanced Materials* **28**, 7162–7166 (2016).

81. Chen, C., Youngblood, N. & Li, M. Study of black phosphorus anisotropy on silicon photonic waveguide. *2015 Optoelectronics Global Conference, OGC 2015* (2015).

82. Chen, C. *et al.* Three-Dimensional Integration of Black Phosphorus Photodetector with Silicon Photonics and Nanoplasmonics. *Nano Lett* **17**, 985–991 (2017).

83. Huang, M. *et al.* Broadband Black-Phosphorus Photodetectors with High Responsivity. *Advanced Materials* **28**, 3481–3485 (2016).

84. Zhang, G. *et al.* Infrared fingerprints of few-layer black phosphorus. *Nat Commun* **8**, (2017).

85. Wei, Q. & Peng, X. Superior mechanical flexibility of phosphorene and few-layer black phosphorus. *Appl Phys Lett* **104**, (2014).

86. Luo, Z. *et al.* Anisotropic in-plane thermal conductivity observed in few-layer black phosphorus. *Nat Commun* **6**, (2015).

87. Yuan, H. Polarization-sensitive broadband photodetector using a black phosphorus vertical p–n junction. *Nat Nanotechnol* **10**, 707–713 (2015).

88. Liao, B. *et al.* Spatial-Temporal Imaging of Anisotropic Photocarrier Dynamics in Black Phosphorus. *Nano Lett* **17**, 3675–3680 (2017).

89. Xia, F., Wang, H. & Jia, Y. Rediscovering black phosphorus as an anisotropic layered material for optoelectronics and electronics. *Nat Commun* **5**, (2014).

90. Lan, S., Rodrigues, S., Kang, L. & Cai, W. Visualizing Optical Phase Anisotropy in Black Phosphorus. *ACS Photonics* **3**, 1176–1181 (2016).

91. Qiao, J., Kong, X., Hu, Z. X., Yang, F. & Ji, W. High-mobility transport anisotropy and linear dichroism in few-layer black phosphorus. *Nat Commun* **5**, (2014).

92. Sherrott, M. C. *et al.* Experimental Demonstration of >230° Phase Modulation in Gate-Tunable Graphene-Gold Reconfigurable Mid-Infrared Metasurfaces. *Nano Lett* **17**, 3027–3034 (2017).

93. Huang, Y. W. *et al.* Gate-Tunable Conducting Oxide Metasurfaces. *Nano Lett* **16**, 5319–5325 (2016).

94. Kuo, Y. H. *et al.* Strong quantum-confined Stark effect in germanium quantum-well structures on silicon. *Nature* **437**, 1334–1336 (2005).

95. Inoue, T., Zoysa, M. de, Asano, T. & Noda, S. Realization of dynamic thermal emission control. *Nat Mater* **13**, 928–931 (2014).

96. Coppens, Z. J. & Valentine, J. G. Spatial and Temporal Modulation of Thermal Emission. *Advanced Materials* **29**, (2017).

97. Brar, V. W. *et al.* Electronic modulation of infrared radiation in graphene plasmonic resonators. *Nat Commun* **6**, 7032 (2015).

98. Wood, J. D. *et al.* Effective passivation of exfoliated black phosphorus transistors against ambient degradation. *Nano Lett* **14**, 6964–6970 (2014).

99. Wang, X. *et al.* Observation of a giant two-dimensional band-piezoelectric effect on biaxial-strained graphene. *NPG Asia Mater* **7**, e154 (2015).

100. Whitney, W. S. *et al.* Field Effect Optoelectronic Modulation of Quantum-Confined Carriers in Black Phosphorus. *Nano Lett* **17**, 78–84 (2020).

101. Low, T. *et al.* Tunable optical properties of multilayer black phosphorus thin films. *Phys Rev B* **90**, (2014).

102. Lin, C., Grassi, R., Low, T. & Helmy, A. S. Multilayer Black Phosphorus as a Versatile Mid-Infrared Electro-optic Material. *Nano Lett* **16**, 1683–1689 (2016).

103. Ling, X. *et al.* Anisotropic Electron-Photon and Electron-Phonon Interactions in Black Phosphorus. *Nano Lett* **16**, 2260–2267 (2016).

104. Hsiao, Y., Chang, P. Y., Fan, K. L., Hsu, N. C. & Lee, S. C. Black phosphorus with a unique rectangular shape and its anisotropic properties. *AIP Adv* **8**, (2018).

105. Wang, X. & Lan, S. Optical properties of black phosphorus. *Adv Opt Photonics* **8**, 618 (2016).

106. Sim, S. *et al.* Selectively tunable optical Stark effect of anisotropic excitons in atomically thin ReS_2. *Nat Commun* **7**, (2016).

107. Yuan, H. *et al.* Polarization-sensitive broadband photodetector using a black phosphorus vertical p-n junction. *Nat Nanotechnol* **10**, 707–713 (2015).

108. Dolui, K. & Quek, S. Y. Quantum-confinement and Structural Anisotropy result in Electrically-Tunable Dirac Cone in Few-layer Black Phosphorous. *Sci Rep* **5**, (2015).

109. Poddubny, A., Iorsh, I., Belov, P. & Kivshar, Y. Hyperbolic metamaterials. *Nat Photon* **7** 958–967 (2013).

110. Krishnamoorthy, H. N. S., Jacob, Z., Narimanov, E., Kretzschmar, I. & Menon, V. M. Topological Transitions in Metamaterials. *Science* **336**, 205–209 (2012).

111. Lu, D., Kan, J. J., Fullerton, E. E. & Liu, Z. Enhancing spontaneous emission rates of molecules using nanopatterned multilayer hyperbolic metamaterials. *Nat Nanotechnol* **9**, 48–53 (2014).

112. High, A. A. *et al.* Visible-frequency hyperbolic metasurface. *Nature* **522**, 192–196 (2015).

113. Liu, Z., Lee, H., Xiong, Y., Sun, C. & Zhang, X. Far-field optical hyperlens magnifying sub-diffraction-limited objects. *Science* **315**, 1686 (2007).

114. Biehs, S. A., Tschikin, M., Messina, R. & Ben-Abdallah, P. Super-Planckian near-field thermal emission with phonon-polaritonic hyperbolic metamaterials. *Appl Phys Lett* **102**, 131106 (2013).

115. Caldwell, J. D. *et al.* Sub-diffractional volume-confined polaritons in the natural hyperbolic material hexagonal boron nitride. *Nat Commun* **5**, 5221 (2014).

116. Alù, A., Silveirinha, M. G., Salandrino, A. & Engheta, N. Epsilon-near-zero metamaterials and electromagnetic sources: Tailoring the radiation phase pattern. *Phys Rev B* **75**, 155410 (2007).

117. Silveirinha, M. & Engheta, N. Tunneling of Electromagnetic Energy through Subwavelength Channels and Bends using Epsilon-Near-Zero Materials. *Phys Rev Lett* **97**, 157403 (2006).

118. Xu, T. & Lezec, H. J. Visible-frequency asymmetric transmission devices incorporating a hyperbolic metamaterial. *Nat Commun* **5**, 1–7 (2014).

119. Sun, J., Zhou, J., Li, B. & Kang, F. Indefinite permittivity and negative refraction in natural material: Graphite. *Appl Phys Lett* **98**, 101901 (2011).

120. Fei, Z. *et al.* Gate-tuning of graphene plasmons revealed by infrared nano-imaging. *Nature* **486**, 82–85 (2012).

121. Chen, J. *et al.* Optical nano-imaging of gate-tunable graphene plasmons. *Nature* **487**, 77–81 (2012).

122. Klitzing, K. v., Dorda, G. & Pepper, M. New Method for High-Accuracy Determination of the Fine-Structure Constant Based on Quantized Hall Resistance. *Phys Rev Lett* **45**, 494–497 (1980).

123. Jeckelmann, B. & Jeanneret, B. The quantum Hall effect as an electrical resistance standard. *Reports on Progress in Physics* **64**, 1603 (2001).

124. Liu, M. *et al.* A graphene-based broadband optical modulator. *Nature* **474**, 64–67 (2011).

125. Liu, M., Yin, X. & Zhang, X. Double-layer graphene optical modulator. *Nano Lett* **12**, 1482–1485 (2012).

126. Sensale-Rodriguez, B. *et al.* Broadband graphene terahertz modulators enabled by intraband transitions. *Nat Commun* **3**, 780 (2012).

127. Long, G. *et al.* Achieving Ultrahigh Carrier Mobility in Two-Dimensional Hole Gas of Black Phosphorus. *Nano Lett* **16**, 7768–7773 (2016).

128. Gillgren, N. *et al.* Gate tunable quantum oscillations in air-stable and high mobility few-layer phosphorene heterostructures. *2d Mater* **2**, 011001 (2015).

129. Chen, X. *et al.* High-quality sandwiched black phosphorus heterostructure and its quantum oscillations. *Nat Commun* **6**, 7315 (2015).

130. Li, L. *et al.* Black phosphorus field-effect transistors. *Nat Nanotechnol* **9**, 372–377 (2014).

131. Li, L. *et al.* Quantum oscillations in a two-dimensional electron gas in black phosphorus thin films. *Nat Nanotechnol* **10**, 608-613 (2015).

132. Li, L. *et al.* Quantum Hall effect in black phosphorus two-dimensional electron system. *Nat Nanotechnol* **11**, 593-597 (2016).

133. Valagiannopoulos, C. A., Mattheakis, M., Shirodkar, S. N. & Kaxiras, E. Manipulating polarized light with a planar slab of black phosphorus. *J Phys Commun* **1**, 45003 (2017).

134. Castellanos-Gomez, A. Isolation and characterization of few-layer black phosphorus. *2D Mater.* **1**, 025001 (2014).

135. Tran, V., Soklaski, R., Liang, Y. & Yang, L. Layer-controlled band gap and anisotropic excitons in few-layer black phosphorus. *Phys Rev B* **89**, 235319 (2014).

136. Qiu, D. Y., da Jornada, F. H. & Louie, S. G. Environmental Screening Effects in 2D Materials: Renormalization of the Bandgap, Electronic Structure, and Optical Spectra of Few-Layer Black Phosphorus. *Nano Lett* **17**, 4706–4712 (2017).

137. Zhang, G. *et al.* The optical conductivity of few-layer black phosphorus by infrared spectroscopy. *Nat Commun* **11**, 1847 (2020).

138. Xu, R. *et al.* Extraordinarily Bound Quasi-One-Dimensional Trions in Two-Dimensional Phosphorene Atomic Semiconductors. *ACS Nano* **10**, 2046–2053 (2016).

139. Chaves, A., Low, T., Avouris, P., Çaklr, D. & Peeters, F. M. Anisotropic exciton Stark shift in black phosphorus. *Phys Rev B* **91**, 155311 (2015).

140. Zhou, X., Lou, W. K., Zhai, F. & Chang, K. Anomalous magneto-optical response of black phosphorus thin films. *Phys Rev B* **92**, 165405 (2015).

141. Li, L. *et al.* Direct observation of the layer-dependent electronic structure in phosphorene. *Nat Nanotechnol* **12**, 21–25 (2017).

142. Lin, C., Grassi, R., Low, T. & Helmy, A. S. Multilayer Black Phosphorus as a Versatile Mid-Infrared Electro-optic Material. *Nano Lett* **16**, 1683–1689 (2016).

143. Whitney, W. S. *et al.* Field Effect Optoelectronic Modulation of Quantum-Confined Carriers in Black Phosphorus. *Nano Lett* **17**, 78–84 (2020).

144. Sherrott, M. C. *et al.* Anisotropic Quantum Well Electro-Optics in Few-Layer Black Phosphorus. *Nano Lett* **19**, 269–276 (2019).

145. Chen, C. *et al.* Widely tunable mid-infrared light emission in thin-film black phosphorus. *Sci Adv* **6**, eaay6134 (2020).

146. Peng, R. *et al.* Midinfrared Electro-optic Modulation in Few-Layer Black Phosphorus. *Nano Lett* **17**, 6315–6320 (2017).

147. Low, T. *et al.* Tunable optical properties of multilayer black phosphorus thin films. *Phys Rev B* **90**, 075434 (2014).

148. Chang, Y. C. *et al.* Realization of mid-infrared graphene hyperbolic metamaterials. *Nat Commun* **7**, 10568 (2016).

149. Gomez-Diaz, J. S., Tymchenko, M. & Alù, A. Hyperbolic Plasmons and Topological Transitions over Uniaxial Metasurfaces. *Phys Rev Lett* **114**, 233901 (2015).

150. Asahina, H. & Morita, A. Band structure and optical properties of black phosphorus. *Journal of Physics C: Solid State Physics* (1984).

151. Fan, P., Yu, Z., Fan, S. & Brongersma, M. L. Optical Fano resonance of an individual semiconductor nanostructure. *Nat Mater* **13**, 471–475 (2014).

152. Luk'Yanchuk, B. *et al.* The Fano resonance in plasmonic nanostructures and metamaterials. *Nat Mater* **9**, 707–715 (2010).

153. Scharf, B., Perebeinos, V., Fabian, J. & Avouris, P. Effects of optical and surface polar phonons on the optical conductivity of doped graphene. *Phys Rev B* **87**, 035414 (2013).

154. Principi, A. *et al.* Plasmon losses due to electron-phonon scattering: The case of graphene encapsulated in hexagonal boron nitride. *Phys Rev B* **90**, 165408 (2014).

155. Fei, Z. *et al.* Infrared nanoscopy of dirac plasmons at the graphene-SiO_2 interface. *Nano Lett* **11**, 4701–4705 (2011).

156. Mattheakis, M., Valagiannopoulos, C. A. & Kaxiras, E. Epsilon-near-zero behavior from plasmonic Dirac point: Theory and realization using two-dimensional materials. *Phys Rev B* **94**, 201404 (2016).

157. Raja, A. *et al.* Dielectric disorder in two-dimensional materials. *Nat Nanotechnol* **14**, 832–837 (2019).

158. González, J., Guinea, F. & Vozmediano, M. A. H. Unconventional Quasiparticle Lifetime in Graphite. *Phys Rev Lett* **77**, 3589–3592 (1996).

159. Liu, Y. & Ruden, P. P. Temperature-dependent anisotropic charge-carrier mobility limited by ionized impurity scattering in thin-layer black phosphorus. *Phys Rev B* **95**, 165446 (2017).

160. Fleischer, S., Zhou, Y., Field, R. W. & Nelson, K. A. Molecular orientation and alignment by intense single-cycle THz pulses. *Phys Rev Lett* **107**, 163603 (2011).

161. Crawford, G. P., Eakin, J. N., Radcliffe, M. D., Callan-Jones, A. & Pelcovits, R. A. Liquid-crystal diffraction gratings using polarization holography alignment techniques. *Journal of Applied Physics* **98**, 123102 (2005).

162. Demos, S. G. & Alfano, R. R. Optical polarization imaging. *Appl Opt* **36**, 150 (1997).

163. Schubert, M., Tiwald, T. E. & Herzinger, C. M. Infrared dielectric anisotropy and phonon modes of sapphire. *Phys Rev B* **61**, 8187–8201 (2000).

164. Ling, X. *et al.* Anisotropic Electron-Photon and Electron-Phonon Interactions in Black Phosphorus. *Nano Lett* **16**, 2260–2267 (2016).

165. Crespi, A. *et al.* Integrated photonic quantum gates for polarization qubits. *Nat Commun* **2**, 566 (2011).

166. Feigenbaum, E., Diest, K. & Atwater, H. A. Unity-order index change in transparent conducting oxides at visible frequencies. *Nano Lett* **10**, 2111–2116 (2010).

167. Niu, S. *et al.* Giant optical anisotropy in a quasi-one-dimensional crystal. *Nat Photon* **12**, 392–396 (2018).

168. Nicholls, L. H. *et al.* Ultrafast synthesis and switching of light polarization in nonlinear anisotropic metamaterials. *Nat Photon* **11**, 628–633 (2017).

169. Dorrah, A. H., Rubin, N. A., Zaidi, A., Tamagnone, M. & Capasso, F. Metasurface optics for on-demand polarization transformations along the optical path. *Nat Photon* **15**, 287–296 (2021).

170. Subkhangulov, R. R. *et al.* Terahertz modulation of the Faraday rotation by laser pulses via the optical Kerr effect. *Nat Photon* **10**, 111–114 (2016).

171. Gao, Y. *et al.* High-speed electro-optic modulator integrated with graphene-boron nitride heterostructure and photonic crystal nanocavity. *Nano Lett* **15**, 2001–2005 (2015).

172. Yang, Y. *et al.* Femtosecond optical polarization switching using a cadmium oxide-based perfect absorber. *Nat Photon* **11**, 390–395 (2017).

173. Sun, Z., Martinez, A. & Wang, F. Optical modulators with 2D layered materials. *Nat Photon* **10**, 227–238 (2016).

174. Xia, F., Wang, H., Xiao, D., Dubey, M. & Ramasubramaniam, A. Two-dimensional material nanophotonics. *Nat Photon* **8**, 899–907 (2014).

175. Chernikov, A. *et al.* Electrical Tuning of Exciton Binding Energies in Monolayer WS_2. *Phys Rev Lett* **115**, (2015).

176. van de Groep, J. *et al.* Exciton resonance tuning of an atomically thin lens. *Nat Photon* **14**, 426–430 (2020).

177. Ling, X., Wang, H., Huang, S., Xia, F. & Dresselhaus, M. S. The renaissance of black phosphorus. *Proceedings of the National Academy of Sciences of the United States of America* **112**, 4523–4530 (2015).

178. Low, T. *et al.* Tunable optical properties of multilayer black phosphorus thin films. *Phys Rev B* **90**, (2014).

179. Whitney, W. S. *et al.* Field Effect Optoelectronic Modulation of Quantum-Confined Carriers in Black Phosphorus. *Nano Lett* **17**, 78–84 (2020).

180. Sherrott, M. C. *et al.* Anisotropic Quantum Well Electro-Optics in Few-Layer Black Phosphorus. *Nano Lett* **19**, 269–276 (2019).

181. Biswas, S. *et al.* Tunable intraband optical conductivity and polarization-dependent epsilon-near-zero behavior in black phosphorus. *Sci Adv* **7**, eabd4623 (2021).

182. Zhang, G. *et al.* Infrared fingerprints of few-layer black phosphorus. *Nat Commun* **8**, (2017).

183. Çaklr, D., Sevik, C. & Peeters, F. M. Significant effect of stacking on the electronic and optical properties of few-layer black phosphorus. *Phys Rev B* **92**, 165406 (2015).

184. Youngblood, N., Chen, C., Koester, S. J. & Li, M. Waveguide-integrated black phosphorus photodetector with high responsivity and low dark current. *Nat Photon* **9**, 247–252 (2015).

185. Wu, Z. *et al.* Large-scale growth of few-layer two-dimensional black phosphorus. *Nat Mater* **20**, 1203-1209 (2021).

186. Xu, Y. *et al.* Correlated insulating states at fractional fillings of moiré superlattices. *Nature 2020 587:7833* **587**, 214–218 (2020).

187. Zhang, Z. *et al.* Correlated interlayer exciton insulator in heterostructures of monolayer WSe_2 and moiré WS_2/WSe_2. *Nat Phys 2022 18:10* **18**, 1214–1220 (2022).

188. Smoleński, T. *et al.* Signatures of Wigner crystal of electrons in a monolayer semiconductor. *Nature 2021 595:7865* **595**, 53–57 (2021).

189. Wang, X. *et al.* Light-induced ferromagnetism in moiré superlattices. *Nature 2022 604:7906* **604**, 468–473 (2022).

190. Zhu, B., Chen, X. & Cui, X. Exciton Binding Energy of Monolayer WS_2. *Scientific Reports* **5**, 1–5 (2015).

191. Qiu, D. Y., da Jornada, F. H. & Louie, S. G. Optical spectrum of MoS_2: Many-body effects and diversity of exciton states. *Phys Rev Lett* **111**, 216805 (2013).

192. Klots, A. R. *et al.* Probing excitonic states in suspended two-dimensional semiconductors by photocurrent spectroscopy. *Sci Rep* **4**, 1–7 (2014).

193. Ugeda, M. M. *et al.* Giant bandgap renormalization and excitonic effects in a monolayer transition metal dichalcogenide semiconductor. *Nat Mater* **13**, 1091–1095 (2014).

194. Raja, A. *et al.* Coulomb engineering of the bandgap and excitons in two-dimensional materials. *Nat Commun 2017 8:1* **8**, 1–7 (2017).

195. Xu, X., Yao, W., Xiao, D. & Heinz, T. F. Spin and pseudospins in layered transition metal dichalcogenides. *Nat Phys 2014 10:5* **10**, 343–350 (2014).

196. Xiao, D., Liu, G. bin, Feng, W., Xu, X. & Yao, W. Coupled spin and valley physics in monolayers of MoS_2 and other group-VI dichalcogenides. *Phys Rev Lett* **108**, 196802 (2012).

197. Cao, T. *et al.* Valley-selective circular dichroism of monolayer molybdenum disulphide. *Nat Commun 2012 3:1* **3**, 1–5 (2012).

198. Diware, M. S. *et al.* Dielectric function, critical points, and Rydberg exciton series of WSe_2 monolayer. *Journal of Physics: Condensed Matter* **30**, 235701 (2018).

199. Chernikov, A. *et al.* Exciton binding energy and nonhydrogenic Rydberg series in monolayer WS_2. *Phys Rev Lett* **113**, 076802 (2014).

200. Qiu, D. Y., da Jornada, F. H. & Louie, S. G. Screening and many-body effects in two-dimensional crystals: Monolayer MoS_2. *Phys Rev B* **93**, 235435 (2016).

201. Popert, A. *et al.* Optical Sensing of Fractional Quantum Hall Effect in Graphene. *Nano Lett* **22**, 7363–7369 (2022).

202. Xu, Y. *et al.* Creation of moiré bands in a monolayer semiconductor by spatially periodic dielectric screening. *Nat Mater 2021 20:5* **20**, 645–649 (2021).

203. Xu, Y. *et al.* Correlated insulating states at fractional fillings of moiré superlattices. *Nature 2020 587:7833* **587**, 214–218 (2020).

204. Walther, V., Johne, R. & Pohl, T. Giant optical nonlinearities from Rydberg excitons in semiconductor microcavities. *Nat Commun* **9**, 1–6 (2018).

205. Gu, J. *et al.* Enhanced nonlinear interaction of polaritons via excitonic Rydberg states in monolayer WSe_2. *Nat Commun* **12**, 1–7 (2021).

206. Goldstein, T. *et al.* Ground and excited state exciton polarons in monolayer $MoSe_2$. *J. Chem. Phys.* **153**, 071101 (2020).

207. Liu, E. *et al.* Exciton-polaron Rydberg states in monolayer $MoSe_2$ and WSe_2. *Nat Commun* **12**, 1–8 (2021).

208. Arora, A. *et al.* Excited-State Trions in Monolayer WS_2. *Phys Rev Lett* **123**, 167401 (2019).

209. Han, B. *et al.* Exciton States in Monolayer $MoSe_2$ and $MoTe_2$ Probed by Upconversion Spectroscopy. *Phys Rev X* **8**, 031073 (2018).

210. Chen, B. *et al.* Environmental changes in $MoTe_2$ excitonic dynamics by defects-activated molecular interaction. *ACS Nano* **9**, 5326–5332 (2015).

211. Froehlicher, G., Lorchat, E. & Berciaud, S. Direct versus indirect band gap emission and exciton-exciton annihilation in atomically thin molybdenum ditelluride ($MoTe_2$). *Phys Rev B* **94**, 085429 (2016).

212. Helmrich, S. *et al.* Exciton–phonon coupling in mono- and bilayer $MoTe_2$. *2d Mater* **5**, 045007 (2018).

213. Ruppert, C., Aslan, O. B. & Heinz, T. F. Optical properties and band gap of single- and few-layer $MoTe_2$ crystals. *Nano Lett* **14**, 6231–6236 (2014).

214. Lezama, I. G. *et al.* Indirect-to-Direct Band Gap Crossover in Few-Layer $MoTe_2$. *Nano Lett* **15**, 2336–2342 (2015).

215. Arora, A. *et al.* Valley Zeeman splitting and valley polarization of neutral and charged excitons in monolayer $MoTe_2$ at high magnetic fields. *Nano Lett* **16**, 3624–3629 (2016).

216. Koirala, S., Mouri, S., Miyauchi, Y. & Matsuda, K. Homogeneous linewidth broadening and exciton dephasing mechanism in $MoTe_2$. *Phys Rev B* **93**, 075411 (2016).

217. Wang, Y. *et al.* Structural phase transition in monolayer $MoTe_2$ driven by electrostatic doping. *Nature* **550**, 487–491 (2017).

218. Duerloo, K. A. N., Li, Y. & Reed, E. J. Structural phase transitions in two-dimensional Mo- and W-dichalcogenide monolayers. *Nat Commun* **5**, 1–9 (2014).

219. Sidler, M. *et al.* Fermi polaron-polaritons in charge-tunable atomically thin semiconductors. *Nat Phys* **13**, 255 (2017).

220. Lu, Y. J. *et al.* Dynamically controlled Purcell enhancement of visible spontaneous emission in a gated plasmonic heterostructure. *Nat Commun* **8**, 1–8 (2017).

221. Berghäuser, G. & Malic, E. Analytical approach to excitonic properties of MoS_2. *Phys Rev B* **89**, 125309 (2014).

222. Qiu, D. Y., da Jornada, F. H. & Louie, S. G. Environmental Screening Effects in 2D Materials: Renormalization of the Bandgap, Electronic Structure, and Optical Spectra of Few-Layer Black Phosphorus. *Nano Lett* **17**, 4706–4712 (2017).

223. Bradley, A. J. *et al.* Probing the Role of Interlayer Coupling and Coulomb Interactions on Electronic Structure in Few-Layer $MoSe_2$ Nanostructures. *Nano Lett* **15**, 2594–2599 (2015).

224. Liang, Y. & Yang, L. Carrier plasmon induced nonlinear band gap renormalization in two-dimensional semiconductors. *Phys Rev Lett* **114**, 063001 (2015).

225. Gao, S., Liang, Y., Spataru, C. D. & Yang, L. Dynamical Excitonic Effects in Doped Two-Dimensional Semiconductors. *Nano Lett* **16**, 5568–5573 (2016).

226. Katsch, F. & Knorr, A. Excitonic theory of doping-dependent optical response in atomically thin semiconductors. *Phys Rev B* **105**, 045301 (2022).

227. Brem, S. *et al.* Intrinsic lifetime of higher excitonic states in tungsten diselenide monolayers. *Nanoscale* **11**, 12381–12387 (2019).

228. Palummo, M., Bernardi, M. & Grossman, J. C. Exciton radiative lifetimes in two-dimensional transition metal dichalcogenides. *Nano Lett* **15**, 2794–2800 (2015).

229. Thureja, D. *et al.* Electrically tunable quantum confinement of neutral excitons. *Nature* **606**, 298–304 (2022).

230. Shanks, D. N. *et al.* Nanoscale Trapping of Interlayer Excitons in a 2D Semiconductor Heterostructure. *Nano Lett* **21**, 5641–5647 (2021).

231. Palacios-Berraquero, C. *et al.* Large-scale quantum-emitter arrays in atomically thin semiconductors. *Nat Commun 2017 8:1* **8**, 1–6 (2017).

232. Luo, Y. *et al.* Deterministic coupling of site-controlled quantum emitters in monolayer WSe_2 to plasmonic nanocavities. *Nat Nanotechnol* **13**, 1137–1142 (2018).

233. Yu, L. *et al.* Site-Controlled Quantum Emitters in Monolayer $MoSe_2$. *Nano Lett* **21**, 2376–2381 (2021).

234. Branny, A., Kumar, S., Proux, R. & Gerardot, B. D. Deterministic strain-induced arrays of quantum emitters in a two-dimensional semiconductor. *Nat Commun* **8**, 1–7 (2017).

235. Seyler, K. L. *et al.* Signatures of moiré-trapped valley excitons in $MoSe_2/WSe_2$ heterobilayers. *Nature* **567**, 66–70 (2019).

236. Tran, K. *et al.* Evidence for moiré excitons in van der Waals heterostructures. *Nature* **567**, 71–75 (2019).

237. Bai, Y. *et al.* Excitons in strain-induced one-dimensional moiré potentials at transition metal dichalcogenide heterojunctions. *Nat Mater* **19**, 1068–1073 (2020).

238. Baek, H. *et al.* Highly energy-tunable quantum light from moiré-trapped excitons. *Sci Adv* **6**, 8526–8537 (2020).

239. Fournier, C. *et al.* Position-controlled quantum emitters with reproducible emission wavelength in hexagonal boron nitride. *Nat Commun* **12**, 1–6 (2021).

240. Klein, J. *et al.* Site-selectively generated photon emitters in monolayer MoS_2 via local helium ion irradiation. *Nature Communications* **10**, 1–8 (2019).

241. Mak, K. F., Lee, C., Hone, J., Shan, J. & Heinz, T. F. Atomically thin MoS_2: A new direct-gap semiconductor. *Phys Rev Lett* **105**, 136805 (2010).

242. Chen, S. Y. *et al.* Luminescent Emission of Excited Rydberg Excitons from Monolayer WSe_2. *Nano Lett* **19**, 2464–2471 (2019).

243. Lundt, N. *et al.* Optical valley Hall effect for highly valley-coherent exciton-polaritons in an atomically thin semiconductor. *Nat Nanotechnol* **14**, 770–775 (2019).

244. Chang, D. E., Vuletić, V. & Lukin, M. D. Quantum nonlinear optics — photon by photon. *Nat Photon 2014 8:9* **8**, 685–694 (2014).

245. Rizzo, D. J. *et al.* Inducing metallicity in graphene nanoribbons via zero-mode superlattices. *Science* **369**, 6511 (2020).

246. Kimouche, A. *et al.* Ultra-narrow metallic armchair graphene nanoribbons. *Nat Commun* **6**, 10177 (2015).

247. Rizzo, D. J. *et al.* Topological band engineering of graphene nanoribbons. *Nature* **560**, 204–208 (2018).

248. Son, Y. W., Cohen, M. L. & Louie, S. G. Half-metallic graphene nanoribbons. *Nature* **444**, 347–349 (2006).

249. Joshi, P. P., Li, R., Spellberg, J. L., Liang, L. & King, S. B. Nanoimaging of the Edge-Dependent Optical Polarization Anisotropy of Black Phosphorus. *Nano Lett* **22**, 3180–3186 (2022).

250. Ribeiro, H. B. *et al.* Edge phonons in black phosphorus. *Nat Commun* **7**, 12191 (2016).

251. Yin, X. *et al.* Edge nonlinear optics on a MoS_2 atomic monolayer. *Science* **344**, 488–490 (2014).

252. Rodin, A. S., Carvalho, A. & Castro Neto, A. H. Strain-induced gap modification in black phosphorus. *Phys Rev Lett* **112**, 176801 (2014).

253. Quereda, J. *et al.* Strong Modulation of Optical Properties in Black Phosphorus through Strain-Engineered Rippling. *Nano Lett* **16**, 2931–2937 (2016).

254. ÇakIr, D., Sahin, H. & Peeters, F. M. Tuning of the electronic and optical properties of single-layer black phosphorus by strain. *Phys Rev B* **90**, 205421 (2014).

255. Huang, S. *et al.* Strain-tunable van der Waals interactions in few-layer black phosphorus. *Nat Commun* **10**, 1–7 (2019).

256. Surrente, A. *et al.* Excitons in atomically thin black phosphorus. *Phys Rev B* **93**, (2016).

257. Low, T. *et al.* Tunable optical properties of multilayer black phosphorus thin films. *Phys Rev B* **90**, (2014).

258. Guo, H., Lu, N., Dai, J., Wu, X. & Zeng, X. C. Phosphorene nanoribbons, phosphorus nanotubes, and van der Waals multilayers. *Journal of Physical Chemistry C* **118**, 14051–14059 (2014).

259. Peng, X., Copple, A. & Wei, Q. Edge effects on the electronic properties of phosphorene nanoribbons. *J. Appl. Phys.* **116**, 144301 (2014).

260. Tran, V. & Yang, L. Scaling laws for the band gap and optical response of phosphorene nanoribbons. *Phys Rev B* **89**, 245407 (2014).

261. de Sousa, J. S. *et al.* Substrate effects on the exciton fine structure of black phosphorus quantum dots. *Phys Rev B* **96**, 035122 (2017).

262. Liang, L. *et al.* Electronic bandgap and edge reconstruction in phosphorene materials. *Nano Lett.* **14**, 6400–6406 (2014).

263. Sorkin, V. & Zhang, Y. W. The structure and elastic properties of phosphorene edges. *Nanotechnology* **26**, 235707 (2015).

264. Yao, F. *et al. In situ* TEM study of edge reconstruction and evolution in monolayer black phosphorus. *Nanoscale* **13**, 4133–4139 (2021).

265. Lee, Y. *et al.* Atomic-scale imaging of few-layer black phosphorus and its reconstructed edge. *J Phys D Appl Phys* **50**, (2017).

266. Masih Das, P. *et al.* Controlled Sculpture of Black Phosphorus Nanoribbons. *ACS Nano* **10**, 5687–5695 (2016).

267. Liu, Y., Li, D. & Cui, T. Edge reconstructions of black phosphorene: a global search. *Nanoscale* **13**, 4085–4091 (2021).

268. Favron, A. *et al.* Photooxidation and quantum confinement effects in exfoliated black phosphorus. *Nat Mater* **14**, 826–832 (2015).

269. Wang, X. *et al.* Highly anisotropic and robust excitons in monolayer black phosphorus. *Nat Nanotechnol* **10**, 517–521 (2015).

270. Yoon, S. *et al.* Electrical control of anisotropic and tightly bound excitons in bilayer phosphorene. *Phys Rev B* **103**, L041407 (2021).

271. Watts, M. C. *et al.* Production of phosphorene nanoribbons. *Nature* **568**, 216–220 (2019).

272. Bie, Y.-Q. *et al.* A $MoTe_2$-based light-emitting diode and photodetector for silicon photonic integrated circuits. *Nat Nanotechnol* **12**, 1124–1129 (2017).

273. Lagoin, C. *et al.* Extended Bose–Hubbard model with dipolar excitons. *Nature* **609**, 485–489 (2022).

274. Andersen, T. I. *et al.* Moiré Excitons Correlated with Superlattice Structure in Twisted WSe_2/WSe_2 Homobilayers. *Nat Mat* **20**, 480-487 (2021).

275. Yang, X., Burch, K. & Ran, Y. Divergent bulk photovoltaic effect in Weyl semimetals. arXiv, 1712.09363 (2017).

276. Kotov, O. v. & Lozovik, Y. E. Giant tunable nonreciprocity of light in Weyl semimetals. *Phys Rev B* **98**, 195446 (2018).

277. Okamura, Y. *et al.* Giant magneto-optical responses in magnetic Weyl semimetal $Co_3Sn_2S_2$. *Nat Commun* **11**, 1–8 (2020).

278. Zhao, B., Guo, C., Garcia, C. A. C., Narang, P. & Fan, S. Axion-Field-Enabled Nonreciprocal Thermal Radiation in Weyl Semimetals. *Nano Lett* **20**, 1923–1927 (2020).

279. Osterhoudt, G. B. *et al.* Colossal mid-infrared bulk photovoltaic effect in a type-I Weyl semimetal. *Nat Mater* **18**, 471–475 (2019).

280. Huang, L. Waveguide-integrated black phosphorus photodetector for mid-infrared applications. *ACS Nano* **13**, 913–921 (2019).

281. Chang, T. Y. *et al.* Black Phosphorus Mid-Infrared Light-Emitting Diodes Integrated with Silicon Photonic Waveguides. *Nano Lett* **20**, 6824–6830 (2020).

282. Schmidt, P. *et al.* Nano-imaging of intersubband transitions in van der Waals quantum wells. *Nat Nanotechnol* **13**, 1035–1041 (2018).

283. Genevet, P. *et al.* Ultra-thin plasmonic optical vortex plate based on phase discontinuities. *Appl Phys Lett* **100**, (2012).

284. Wang, T. *et al.* Giant Valley-Polarized Rydberg Excitons in Monolayer WSe_2 Revealed by Magneto-photocurrent Spectroscopy. *Nano Lett* **20**, 7635–7641 (2020).

285. Cho, S. *et al.* Phase patterning for ohmic homojunction contact in $MoTe_2$. *Science (1979)* **349**, 625–628 (2015).

286. Noumbé, U. N. *et al.* Ionic Glass–Gated 2D Material–Based Phototransistor: $MoSe_2$ over LaF3 as Case Study. *Adv Funct Mater* **29**, 1907462 (2019).

287. Zhao, J. *et al.* Lithium-ion-based solid electrolyte tuning of the carrier density in graphene. *Sci Rep* **6**, 1–7 (2016).

288. Hayee, F. *et al.* Revealing multiple classes of stable quantum emitters in hexagonal boron nitride with correlated optical and electron microscopy. *Nat Mater* **19**, 534–539 (2020).

289. Hill, H. M. *et al.* Observation of excitonic rydberg states in monolayer MoS_2 and WS_2 by photoluminescence excitation spectroscopy. *Nano Lett* **15**, 2992–2997 (2015).

290. Goryca, M. *et al.* Revealing exciton masses and dielectric properties of monolayer semiconductors with high magnetic fields. *Nat Commun* **10**, 1–12 (2019).

291. Robert, C. *et al.* Optical spectroscopy of excited exciton states in MoS_2 monolayers in van der Waals heterostructures. *Phys Rev Mater* **2**, 011001 (2018).

292. Goldstein, T. *et al.* Ground and excited state exciton polarons in monolayer $MoSe_2$. *J Chem Phys* **153**, 071101 (2020).

293. Liu, E. *et al.* Exciton-polaron Rydberg states in monolayer $MoSe_2$ and WSe_2. *Nat Commun* **12**, 1–8 (2021).

294. Liu, E. *et al.* Magnetophotoluminescence of exciton Rydberg states in monolayer WSe_2. *Phys Rev B* **99**, 205420 (2019).

295. Wagner, K. *et al.* Autoionization and Dressing of Excited Excitons by Free Carriers in Monolayer WSe_2. *Phys Rev Lett* **125**, 267401 (2020).

296. Han, B. *et al.* Exciton States in Monolayer $MoSe_2$ and $MoTe_2$ Probed by Upconversion Spectroscopy. *Phys Rev X* **8**, 031073 (2018).

297. Yang, J. *et al.* Robust Excitons and Trions in Monolayer $MoTe_2$. *ACS Nano* **9**, 6603–6609 (2015).

298. Arora, A. *et al.* Valley Zeeman splitting and valley polarization of neutral and charged excitons in monolayer $MoTe_2$ at high magnetic fields. *Nano Lett* **16**, 3624–3629 (2016).

299. Xiao, K. *et al.* Many-Body Effect on Optical Properties of Monolayer Molybdenum Diselenide. *Journal of Physical Chemistry Letters* **12**, 2555–2561 (2021).

300. Perdew, J. P., Burke, K. & Ernzerhof, M. Generalized Gradient Approximation Made Simple. *Phys Rev Lett* **77**, 3865 (1996).

301. Giannozzi, P. *et al.* Advanced capabilities for materials modelling with Quantum ESPRESSO. *Journal of Physics: Condensed Matter* **29**, 465901 (2017).

302. Giannozzi, P. *et al.* QUANTUM ESPRESSO: a modular and open-source software project for quantum simulations of materials. *Journal of Physics: Condensed Matter* **21**, 395502 (2009).

303. Hamann, D. R. Optimized norm-conserving Vanderbilt pseudopotentials. *Phys Rev B* **88**, 085117 (2013).

304. Schlipf, M. & Gygi, F. Optimization algorithm for the generation of ONCV pseudopotentials. *Comput Phys Commun* **196**, 36–44 (2015).

305. Hedin, L. New Method for Calculating the One-Particle Green's Function with Application to the Electron-Gas Problem. *Physical Review* **139**, A796 (1965).

306. Strinati, G., Mattausch, H. J. & Hanke, W. Dynamical aspects of correlation corrections in a covalent crystal. *Phys Rev B* **25**, 2867 (1982).

307. Hybertsen, M. S. & Louie, S. G. Electron correlation in semiconductors and insulators: Band gaps and quasiparticle energies. *Phys Rev B* **34**, 5390 (1986).

308. Deslippe, J., Samsonidze, G., Jain, M., Cohen, M. L. & Louie, S. G. Coulomb-hole summations and energies for GW calculations with limited number of empty orbitals: A modified static remainder approach. *Phys Rev B Condens Matter Mater Phys* **87**, 165124 (2013).

309. Deslippe, J. *et al.* BerkeleyGW: A massively parallel computer package for the calculation of the quasiparticle and optical properties of materials and nanostructures. *Comput Phys Commun* **183**, 1269–1289 (2012).

310. da Jornada, F. H., Qiu, D. Y. & Louie, S. G. Nonuniform sampling schemes of the Brillouin zone for many-electron perturbation-theory calculations in reduced dimensionality. *Phys Rev B* **95**, 035109 (2017).

311. Ismail-Beigi, S. Truncation of periodic image interactions for confined systems. *Phys Rev B* **73**, 233103 (2006).

312. Deilmann, T., Drüppel, M. & Rohlfing, M. Three-particle correlation from a Many-Body Perspective: Trions in a Carbon Nanotube. *Phys Rev Lett* **116**, 196804 (2016).

313. Bie, Y. A $MoTe_2$-based light-emitting diode and photodetector for silicon photonic integrated circuits. *Nat Nanotechnol* **12**, 1124–1129 (2017).

314. Flöry, N. *et al.* Waveguide-integrated van der Waals heterostructure photodetector at telecom wavelengths with high speed and high responsivity. *Nat Nanotechnol* **15**, 118–124 (2020).

315. Kindem, J. M. *et al.* Control and single-shot readout of an ion embedded in a nanophotonic cavity. *Nature* **580**, 201–204 (2020).

316. Biswas, S., Shao, Y., Hachisu, T., Nguyen-Dang, T. & Visell, Y. Integrated Soft Optoelectronics for Wearable Health Monitoring. *Adv Mater Technol* **5**, 2000347 (2020).

317. Dalir, H. & Koyama, F. 29 GHz directly modulated 980 nm vertical-cavity surface emitting lasers with bow-tie shape transverse coupled cavity. *Appl Phys Lett* **103**, 091109 (2013).

318. Alford, W. J., Allerman, A. A. & Raymond, T. D. High power and good beam quality at 980 nm from a vertical external-cavity surface-emitting laser. *JOSA B,* **19**, 4, 663–666 (2002).